Doctoral theses at NTNU, 2021:362

Anuvansh Sharma

Magnetic and Stimuli-Responsive Nanoparticles for Environmental and Biomedical Applications

Doctoral thesis

NTNU
Norwegian University of Science and Technology
Thesis for the Degree of
Philosophiae Doctor
Faculty of Natural Sciences
Department of Materials Science and Engineering

NTNU
Norwegian University of
Science and Technology

Anuvansh Sharma

Magnetic and Stimuli-Responsive Nanoparticles for Environmental and Biomedical Applications

Thesis for the Degree of Philosophiae Doctor

Trondheim, November 2021

Norwegian University of Science and Technology
Faculty of Natural Sciences
Department of Materials Science and Engineering

NTNU
Norwegian University of
Science and Technology

NTNU
Norwegian University of Science and Technology

Thesis for the Degree of Philosophiae Doctor

Faculty of Natural Sciences
Department of Materials Science and Engineering

ISBN 978-82-326-6926-4 (printed ver.)
ISBN 978-82-326-5819-0 (electronic ver.)
ISSN 1503-8181 (printed ver.)
ISSN 2703-8084 (online ver.)

Doctoral theses at NTNU, 2021:362

Printed by NTNU Grafisk senter

This PhD Thesis Is Dedicated To My

*Nani** and *Dadi Ma***

*Maternal Grandmother / Mormor

**Paternal Grandmother / Farmor

"... दुर्गम वनों और ऊँचे पर्वतों को जीतते हुए,
जब तुम अंतिम ऊँचाई को भी जीत लोगे–
जब तुम्हें लगेगा कि कोई अंतर नहीं बचा अब,
तुममें और उन पत्थरों की कठोरता में,
जिन्हें तुमने जीता है–
जब तुम अपने मस्तक पर बर्फ़ का पहला तूफ़ान झेलोगे,
और काँपोगे नहीं–
तब तुम पाओगे कि कोई फ़र्क़ नहीं,
सब कुछ जीत लेने में,
और अंत तक हिम्मत न हारने में।"

कविता : अंतिम ऊँचाई
रचनाकार : कुँवर नारायण
पुस्तक : प्रतिनिधि कविताएँ (पृष्ठ 92)
संस्करण : 2008

"... While accomplishing difficult jungles and high mountains,
When you would win the last peak–
When you would feel there is no difference left,
Between you and the roughness of those stones,
That you have won–
When you will bear the first storm of ice on your forehead,
And you will not tremble–
Then you will find there is no difference in winning everything,
And not losing hope till the end."

Poem : Antin Unchai (Final Peak)
Author : Kunwar Narayan
Book : Representative Poems (Page 92)
Edition : 2008

Preface

This thesis has been submitted to NTNU Norwegian University of Science and Technology, in partial fulfillment of the requirement for the academic degree Philosophiae Doctor.

The doctoral studies were performed predominantly in the Functional Materials and Materials Chemistry Research Group at the Department of Materials Science and Engineering at NTNU, in Trondheim. Research work was initially performed under the supervision of Assoc. Prof. Maria Benelmekki (2016-2018) and later under the supervision of Prof. Mari-Ann Einarsrud and Assoc. Prof. Sulalit Bandyopdhyay (2018-2021).

Trondheim, September 2021
Anuvansh Sharma

Acknowledgements

Half a decade after starting my research, I find myself at the doorstep to the biggest academic milestone to date. This task would not have been possible without the support of the many to whom I owe this work. To begin with, I'd like to thank Prof. Maria Benelmekki for giving me the opportunity to pursue this PhD and begin my journey in the field of research. Further, I am particularly grateful towards Prof. Mari-Ann Einarsrud for taking over the role as my supervisor and guiding me every step of the way. All the invaluable discussions and academic insights shared with me, have gone a long way in shaping this work.

When it comes to the person who inspired me to venture into the field of nanoscience, there is none other than Assoc. Prof. Sulalit Bandyopadhyay. I had the pleasure of getting to know and work with him during my master's at NTNU. He has been a friend and a mentor from the moment I arrived in Norway and at NTNU. His ever-present influence has shaped my personality not only inside the field of academia, but far beyond-through friendly chats, cooking classes, cricketing adventures, and festivities. Together, we had the opportunity to work on innovative projects, publish articles and a book, and even work on the Corona project in 2020, developing COVID-19 test kits.

I would also like to acknowledge the behind-the-scenes crew of engineers, lab technicians and those responsible, Anita, Bjørn, Eli, Elin, Jens, Ken, Magnus and Torun for all their support and advice. The master students, Abhishek, Helena and Helene have all contributed to this work through their master theses. Guiding them during their projects has challenged my supervisory and managerial skills in the best of ways. I'd also like to extend my gratitude towards all the co-authors, contributors and collaborators to my publications.

I am thankful to the members of IMA and especially those in the FACET group, for providing an inspiring, collaborative and encouraging work environment. Having amazing colleagues at work is special. Kara, Kristine, Magnus, Nikolai, Ola and Solveig have made this journey memorable. Special mention goes to Mikalai, whose presence left a permanent mark. Over the course of our time at NTNU, we have indulged in our own side projects, ranging from 3D printing, photography, fishing to video gaming. I look forward to the adventures to come.

Making these years especially memorable, through cabin trips, dinners, board game nights, volleyball and cricket matches, bouldering, etc., Ahmad, Athul, Aravinth, Jibin, Karthik, Mandar, Martin, Prajin, Vegar, Vipin and Yash, who have been there through the good and the better during my stay in Trondheim.

Last, but not least, I owe this work to my parents as their unconditional love and support has given me the strength and confidence to pursue my studies away from home. My brother, Anujay, who is currently ascending his own academic ladder, for his genuine and sincere care.

Most importantly my wife, Simona, for tolerating my tantrums and adjusting to my weird work schedules. She has been a rock-solid pillar in my life making sure I keep on seeing the light at the end of the tunnel. Finally, to the newest addition to our family, our dog Bailey, who loyally accompanied me during my writing sessions, which he made sure to interrupt with countless walk and play sessions.

Declaration

This work has been funded by the Department of Materials Science and Engineering at NTNU. Financial support was provided by the Netherlands Organisation for Scientific Research (NWO) Grant STW14515 Water Tagging.

The work in this thesis has been published, or is ready for publishing. The author of this work has been the main contributor to the thesis, that includes planning and performing of experiments, analysis and discussion of results, as well as writing of the manuscripts. The exceptions are following, where the experiments have been performed by others under the guidance of and collaboration with the main author:

- qPCR measurements were conducted at the IHE[‖] Delft Institute for Water Education, Netherlands by Swagatam Chakraborty (PhD researcher) .
- Magnetic characterisation studies have partly been done at NTNU, the Università di Genova, Italy by Slimani Sawssen (PhD student), and Institut de Ciència de Materials de Barcelona (ICMAB-CSIC), Spain by Narcis Mestres (Senior Scientist).
- Simulations of growth kinetics have been done at the Indian Institute of Technology Bombay, India by Nirmalya Bachhar (Assistant Professor).
- Transmission electron microscopy (TEM) and energy dispersive X-ray spectroscopy (EDS) measurements for studying the growth of magneto-plasmonic dimeric nanoparticles (DNPs) (Chapter 5 – Figure 5.5), have been performed by Inger-Emma Nylund (PhD candidate, Department of Materials Science and Engineering, NTNU).
- Part of the nanoparticle synthesis, functionalisation and characterisation experiments have been carried out by Abhishek Banerjee (M.Sc., Department of Materials Science and Engineering, NTNU) and Helena Olivia Karlsen Ramsvik (M.Sc., Department of Biophysics, NTNU). Banerjee has synthesized, functionalised and characterised iron-oxide NPs (IONPs) that are further used for the synthesis of hydrological tracers in Chapter 6. He has also performed magnetic characterisation on the IONP samples using the vibrating sample magnetometer. Ramsvik has synthesised, functionalised and characterised DNPs used in investigating the effect of silver precursor concentration on the magneto-plasmonic properties of the DNPs in Chapter 5.
- Biocompatibility studies for stimuli-responsive nanogels, using the whole blood model in Chapter 7, has been performed by Helene Solhaug (M.Sc. Department of Clinical and Molecular Medicine, NTNU).

Trondheim, September 2021
Anuvansh Sharma

[‖] International Institute for Infrastructural Hydraulic and Environmental Engineering

Abstract

For the past few decades, nanomaterials have been an integral part of research involving applications in various industries, ranging from pharmaceuticals, electronics, energy, chemical, food, aviation, etc, owing to their unique optical, magnetic, mechanical, electrical, and other physico-chemical properties. Two research areas in particular, where nanomaterials have found an increased interest are environmental and biomedical sciences, as hydrological tracers and drug delivery systems, respectively. The main focus of this thesis is to synthesise, functionalise and characterise magnetic and polymeric nanoparticles (NPs) for the potential use as hydrological tracers, drug delivery systems and biosensors.

The use of tracers has been well established to monitor and manage hydrological systems such as brooks, streams and rivers. However, the availability of a limited number of potential tracers such as salts, isotopes and dyes, makes studies of hydrological processes a challenge. Furthermore, traditional tracers find limited use due to the lack of multiplexed, multipoint tracing and background noise, among others. In this regard, DNA-based tracers possess remarkable advantages including, being environmentally friendly, stable, and with high sensitivity, in addition to showing great potential in providing an ideally unlimited number of unique tracers capable of multipoint tracing. Though some studies present magnetic DNA-based tracers for hydrological applications, these utilise a single type of DNA to functionalise one type of iron-oxide NP (IONP). Therefore, there exists a gap in research that could show the possibility to produce multiple magnetic tracers by functionalising different IONPs with different DNA. Additionally, there are no reports investigating the variation of magnetic properties of the tracers with the functionalisation process.

In this work, DNA-based tracers aimed at hydrological applications were developed. To make the tracers magnetic, to facilitate recovery, IONPs were incorporated in the core of the tracers. These IONPs were synthesised using co-precipitation and thermal decomposition techniques that yielded particles with sizes ranging from 9 to 20 nm, spherical and cube shaped, with different physico-chemical properties. Particle size and shape, among other factors, have a crucial role in determining the magnetic properties of the tracers and in turn their magnetic harvesting for separation and analysis. Synthesising IONPs via thermal decomposition enables precise control over the particle's size, morphology, and eventually, their magnetic properties. Time-based growth for IONPs, synthesised via thermal decomposition of iron-oleate precursor, showed that iron-oleate started to decompose around 300 °C following burst nucleation and the reaction subsequently entered growth regime with a rapid increase in particle numbers at 310 °C. The reaction stabilised at 320 °C, where the particles underwent changes in morphology, owing to surface diffusion and Ostwald ripening.

The surface of IONPs was further modified with selected ligands to vary surface charge and hydrophilicity. Tetramethyl ammonium hydroxide and sodium citrate provided negative surface charges resulting in zeta potentials of -10 to -50 mV, while cetyltrimethylammonium bromide imparted a positive zeta potential (+30 mV). Thereafter, IONPs were functionalised with trimethoxysilylpropyl–N,N,N–trimethylammonium chloride, before DNA functionalisation, to provide a positive surface potential (>13 mV) that facilitated DNA binding. Thereafter, the IONPs were functionalised with three different double stranded DNA (T21, GM5 and GM6) to explore the possibility of producing multiple tracers, each having its unique tag. A subsequent coating of silica, encapsulated and protected the DNA from loss to the surroundings. Magnetic characterisation showed high saturation magnetisation (>75 emu/g) for the IONPs after each functionalisation step.

Further, the IONPs were used for biosensing applications, utilising the concept of magnetophoresis — motion of magnetic particles in a constant magnetic field gradient. IONPs were coupled with silver NPs that impart optical characteristics of localised surface plasmon resonance, resulting in dual magneto-plasmonic properties, into dimeric NP (DNP). Time based growth studies showed that silver nucleated heterogeneously on multiple sites on the IONP surfaces in the initial stages of the reaction, forming satellite/raspberry-like morphology. As the reaction proceeded, the particles attained a dumbbell-like shape due to the reorganisation of silver resulting from surface diffusion and Ostwald ripening. Furthermore, the effect of the silver precursor (silver acetate) concentration on the physico-chemical properties of DNPs showed increased plasmonic response and decreased magnetisation with increasing concentration. Time-based magnetic separation studies (using the concept of magnetophoresis) showed the potential of DNPs to be used as sensors. Two separate particle populations were obtained after exposing the particles to the magnetic field for 24 h. Larger particles separated after $\sim$10 h showing greater separation velocities, while the smaller particles had longer separation times. By analysing separation times for different particle populations in different samples, the presence of target analyte can be detected.

Another field, where NPs find immense use in medicine, is cancer treatment, as NP-based targeted drug delivery systems aid in reducing spread of drug toxicity to the healthy tissue, thereby increasing the effectiveness of the delivered drug in killing cancer cells. Stimuli-responsive NGs have received interest, due to their ability to swell or collapse in accordance with changes in stimuli such as temperature, pH, ionic strength, light, and electric and magnetic fields. Poly(N-isopropylacrylamide)-co-poly(acrylic acid)-based stimuli-responsive NGs, that possessed both temperature and pH-based stimuli response, were synthesised in this work, with hydrodynamic size ranging from 120 to 400 nm. NGs are usually synthesized using precipitation polymerization at temperatures above the volume phase transition temperature (VPTT) of the formed NG and these reactions are extremely sensitive to synthesis parameters, including, reactant concentrations, surfactant concentration, amount of initiator and reaction temperature. There exists a gap in research investigating the effect of oxygen in the reaction atmosphere on the synthesis of pNIPAm-pAAc-based NGs. The growth of NGs was studied via three different synthesis routes, exploring different reaction parameters, namely, surfactant amount (sodium dodecyl sulphate), reaction atmosphere (continuous and intermittent N_2 atmosphere) and stirring modes (magnet bar and impeller). A decrease in NG size was observed using continuous flow of N_2, compared to the ones where N_2 was introduced at the time of initiator addition. NGs prepared under continuous N_2 environment had a lower polydispersity index (0.2) than the ones prepared in an intermittent N_2 environment (0.6 - 0.7). The size of the NGs increased (35 to 85 % decrease in hydrodynamic size) on decreasing sodium dodecyl sulphate concentration from 4.2 to 2.1 mM.

To understand the stimuli response from temperature and pH, it is important to study the extent of incorporation of pNIPAm and pAAc in the NG matrix. Most studies investigating this are not associated with NGs, but microgels, and they do not highlight, in detail, the effect of pAAc on the physico-chemical properties of the NGs. Hence, to address this, as well as, to exploit the fact that the cancer region has an acidic microenvironment, the effect of pH response of the NG has been investigated by varying pAAc content in the NG. The size of the NGs increased (230 to 400 nm) with increasing AAc concentration from 10 to 30 mole%. Additionally, the NGs showed increased pH-based collapse (measured at synthesis and pH = 3.5) with increasing pAAc concentration from 10 mole% (6.8 % collapse) to 25 mole% (51.3 % collapse). Furthermore, loading and release studies were performed at different conditions of temperature and pH, using a model protein drug, cytochrome C (Cyt C). High loading (L.E. = 87.4 %) and encapsulation (E.E. = 254.5 μg/mg) efficiencies were measured for NGs synthesised in a continuous N_2 environment, whereas, NGs that were prepared in an intermittent N_2 environment showed low L.E. (30.8 %) and E.E. (181 μg/mg). Biocompatibility studies, conducted on the NGs using a whole blood model, showed excellent cell viability. The NGs did not activate the complement system and induced little or no release of pro-inflammatory cytokines/chemokines, suggesting good biocompatibility and potential as a candidate for drug delivery vehicles.

Both, inorganic and polymeric NPs have been produced in this work employing various synthesis techniques. One of the major challenges faced in the world of nanoscience is reproducibility of NP synthesis. High reproducibility is crucial to ensure similar production batches, thereby reducing any significant deviations in particle quality. The issue of repeatability and reproducibility was faced in this work as well, particularly with particle synthesis and functionalisation. NP quality was examined using various characterisation techniques and measurements were repeated to reduce deviation during analysis. Additionally, multiple sets of experiments were performed and optimised to reduce any undesired uncertainties. The physico-chemical properties of the NPs studied in this thesis, were mapped using a wide array of characterisation techniques. NP sizes have been measured using transmission electron microscopy and dynamic light scattering, while the zetasizer was used for measuring particle surface charge (zeta potentials). IONP surface functionalisation was measured using attenuated total reflection-Fourier transform infrared spectroscopy and the magnetic properties were investigated using a superconducting quantum interference device and vibration sample magnetometry. Ultraviolet visible spectrophotometry was used for studying the loading and release of Cyt C from NG. To examine successful functionalisation and encapsulation of the DNA with the IONPs and in silica, respectively, quantitative polymerase chain reaction analysis was conducted.

This work aimed at providing NPs that have the potential to be used in the applications of hydrological tracing and targeted drug delivery. Thus, the NPs studied within this work provide a contribution to the ever expanding search for unique materials for environmental and biomedical applications.

Publications

Publications included in the thesis

Paper I

Sharma, A., Foppen, J.W., Banerjee, A., Sawssen, S., Bachhar, N., Peddis, D., Bandyopadhyay, S., 2021. Magnetic Nanoparticles to Unique DNA Tracers: Effect of Functionalization on Physico-chemical Properties. Nanoscale research letters, 16(1), pp.1-16. https://doi.org/10.1186/s11671-021-03483-5

Paper II

Sharma, A., Raghunathan, K., Solhaug, H., Antony J., Stenvik J., Nilsen A.M., Einarsrud M-A., Bandyopadhyay S., 2021. Modulating Acrylic Acid Content of Nanogels for Drug Delivery Biocompatibility Studies. Journal of Colloid and Interface Science. https://doi.org/10.1016/j.jcis.2021.07.139

Manuscript III

Sharma, A., 2021. Growth Kinetics of Iron-Oxide – Silver Dimeric Nanoparticles & Their Potential Biomedical Applications.

Publications not included in the thesis

Paper IV

Miranti, R., Qayyum, M.S., **Sharma, A.**, Einarsrud, M-A., Mestres, N., Benelmekki, M., 2020. Spectroscopic study of partially oxidized BN nanoscrolls induced by low frequency ultrasonic irradiation. Applied Surface Science, 515, p.146055. https://doi.org/10.1016/j.apsusc.2020.146055
Contribution - Performed TEM characterisation of the BN nanoscrolls.

Book Chapters

Bandyopadhyay, S., 2019. Fabrication and Application of Nanomaterials. McGraw Hill Professional. New York, USA. ISBN: 9781260132236. Scholl, S., Khan, M. T. (Eds.).

Ch. 6 – Synthesis of Polymer-based Nanoparticles.
Authors: **Sharma, A.**; Bandyopadhyay, S.

Ch. 7 – Functionalization and Properties of Hydrogels.
Authors: Raghunathan, K; **Sharma, A.**; Bandyopadhyay, S.

Ch. 8 – Characterization of Metal Nanoparticles.
Authors: Bandyopadhyay, S.; **Sharma, A.**; Raghunathan, K.

Paper V

Raju, R., Bandyopadhyay, S., **Sharma, A.**, Gonzalez, S., Carlsen, P., Gautun, O., Glomm, W. R., 2018. Synthesis, characterization and drug loading of multiresponsive p [NIPAm-co-PEGMA](core)/p [NIPAm-co-AAc](Shell) Nanogels with Monodisperse Size Distributions. Polymers, 10(3), 309. https://doi.org/10.3390/polym10030309
Contribution - Conducted characterisation of stimuli-responsive NGs, together with drug loading experiments. Writing of the manuscript.

Paper VI

Bandyopadhyay, S., **Sharma, A.**, Glomm, W. R., 2017. The Influence of Differently Shaped Gold Nanoparticles Functionalized with NIPAM-Based Hydrogels on the Release of Cytochrome C. Gels, 3(4), 42. https://doi.org/10.3390/gels3040042
Contribution - Performed NP synthesis, functionalisation and characterisation experiments. Additionally, carried out drug loading and release experiments and participated in writing of the manuscript.

Paper VII

Bandyopadhyay, S., Alvi, M. A. A., **Sharma, A.**, Zhu, K., Kjøniksen, A. L., Nyström, B., Glomm, W. R., 2017. Influence of polymer coating on release of l-dopa from core-shell Fe@ Au nanoparticle systems. Colloid and Polymer Science, 295(2), 391-402. https://doi.org/10.1007/s00396-017-4015-y
Contribution - Performed VPTT behaviour modeling for stimuli-responsive NGs and participated in writing of the manuscript.

Note: Experimental work mentioned in papers V-VII, has been carried out over the course of my master thesis (2015-2016). Writing of the manuscripts was done during the PhD period.

Scientific Contributions

Patents

1. **Methods and products for isolating nucleic acids:** UK Patent, 2020
   Application number: 2004987.0, 2004988.8, 2010567.2 and 2010570.6
   Aas, P. A.; Bandyopadhyay, S.; Bjørås, M.; Erlandsen, S. E.; Hagen, L.; Ottesen, O.; **Sharma, A.**

2. **Covid-19 Detection:** Norway and UK Patent, 2020
   Application number: 20200427 and 20200428
   Aas, P. A.; Bandyopadhyay, S.; Bjørås, M.; Erlandsen, S. E.; Hagen, L.; Ottesen, O.; **Sharma, A.**

Table of contents

"It isn't the mountains ahead to climb that wear you down. It's the pebble in your shoe."

– Muhammad Ali

"Knowing is not enough, we must apply. Willing is not enough, we must do."

– Bruce Lee

1 Motivation

According to the Oxford English Dictionary, *'Nano'*, stemming from classical Latin – *nanus*, or its ancient Greek etonym – *nanos*, meaning "dwarf",[1] is an umbrella term encompassing several technical and scientific fields, processes, and properties at the nanoscale or microscale.[2] According to the definition given by The International Organization for Standardization (ISO), a NP is a nano-object having at least one dimension in the nanoscale, which is in the range–100 nm.[3] We, unknowingly or otherwise, encounter NPs in our daily lives in some form or another, such as, antimicrobial silver NPs in bandages, titanium oxide NPs in sun screen lotions, carbon nanotubes in sports equipment (bikes, tennis rackets, etc.), to mobile phones and other electronic gadgets.

Nanotechnology deals with the manipulation of structures of matter at the nanoscale, as stated in one of the most important lectures by physicist – *Richard Feynman*, at the American Physical Society at the California Institute of Technology in 1959, where he presented his thoughts on the ability to manipulate individual atoms and molecules.[4] This makes the field of nanoscience revolutionary, transformative, powerful, and potentially beneficial technology to help address critical international development sectors including improved water purification systems, energy systems, biomedicine, food & nutrition, and information & communications technologies.[5]

The principle motivation to perform research on NPs is founded in the so-called *quantum-size effect*. Larger accumulations of atoms and molecules behave in more of a statistical or aggregate manner, where the quantum mechanical properties get averaged away. However, at nanoscale, particles with sizes somewhere between single atoms/molecules, show pronounced size and shape dependent optical, electric and magnetic behaviour.[6] For instance, gold loses its familiar yellow colour at nanoscale as gold NPs (AuNPs) show localised surface plasmon resonance (LSPR) giving the particles their unique colours, that is dependent on particle size and morphology.[7] Thus, AuNPs can be finely tuned for medical applications of imaging and targeted laser destruction of the tumor as means to avoid harming healthy cells.[8] Similarly, IONPs show unique

magnetic property of superparamagnetism, *i.e.* having high magnetic susceptibility and zero coercivity, that is desired for various industrial applications. Furthermore, NPs have a higher percentage of surface atoms, giving a higher surface to volume ratio, which may result in an increased chemical reactivity and affect mechanical and electric properties that are desirable in catalysis.[9]

1.1 Environmental Applications

Dealing with one of the most valuable resources on the planet – *'water'*, makes hydrology an extremely important field of study. It consists not only of studying the natural distribution and movement of water, but is also concerned with the impact of human activities on water quality and with problems in water management. Furthermore, one of the crucial global challenges faced by humanity is environmental pollution, which imposes negative impacts on human health, sustainable social and economic development.[10] A prerequisite to tackling this issue is to trace the source and migration pathways of pollutants in water, soil and atmosphere.[10] For *e.g.*, human settlements are usually located in regions around or near surface water sources or an aquifer, and increasing population density and industries in these areas, often results in serious issues with regards to the quantity and quality of available water. This deems important to determine groundwater table elevation and groundwater flow direction in aquifers within and in regions surrounding residential areas. Thus, groundwater flow direction is an important parameter in investigating the pathway of pollutants originating from residential areas as well as in determining the areas to be protected.

Tracer tests are a widely used technique to investigate flow paths and travel times of solutes, particulates and contaminants in environmental waters.[11,12] However, there are a limited number of potential tracers available to hydrologists to study these dynamic processes. Traditional tracers, such as natural dissolved salts, stable isotopes, potassium bromide, and fluorescent dyes,[11,13,14] have been reported to suffer from interference of background noise, high analysis costs, potential environmental contamination, signal contamination among others. Furthermore, application of tracers at larger scales/solvent volumes results in dilution effects that pose issues with their detection limits thereby becoming an important constraint.[15]

To overcome these limitations, a new tracing systems based on DNA nanomaterials, namely DNA tracers, has already been developed. DNA tracers have been reported to be specific (*i.e.* bearing unique identifiers that do not suffer from interference due to background noise), environmentally friendly, ultrasensitive to detection and multiplex capable (*i.e.* enabling concurrent usage of a large number of species at a given time).[10,16–18] Importantly, DNA tracers can be repetitively and thus exponentially amplified, using quantitative polymerase chain reaction (qPCR), theoretically pushing the detection sensitivity down to one molecule.[19,20] Hence, tracers containing DNA require a detection amount that is orders of magnitude lower than that of traditional tracers. These tracers will pave the path for monitoring hydrological processes, currently limited by the availability of multiple unique tracers. Furthermore, the use of DNA as a tag is a precursor to ultra-high sensitivity in detection.

The rationale behind functionalising magnetic nanoparticles (MNPs) with DNA lies in – fast and easy magnetic separation, better sample handling, absence of sample volume limitations, and sample up-concentration.[15,21] To prevent the free DNA from adsorbing onto sediment particles, decay and/or biological uptake by microorganisms, the DNA needs to be protected.[21–23]. Studies have been performed that encapsulate DNA and functionalise IONPs with DNA, however, in these studies, a single type of DNA has been used for the fabrication of the tracer. More importantly, there is no report of how the magnetic properties of the tracers change during the functionalisation process. Particle size and shape of the IONPs, among other factors, have a crucial role in determining the magnetic properties of the tracers and in turn their magnetic harvesting for separation and analysis.[15] Therefore, knowing how the magnetic properties alter along the functionalisation route—from IONPs to DNA based magnetic tracers, with an aim to understand structure-properties relations for the tracers, is extremely important.

1.2 Biomedical Applications

Erik Drexler was the first scientist, who greatly believed that nanotechnology might have a great potential in medicine.[24] His vision was to utilize nanotechnology in diagnosing and treating injuries and diseases, owing to the negligible size of the molecules at nanoscale. He thought that nanotechnology might be able to help in surgery as well, especially cancer, where he stated –

> *"The immune system may not be able to recognize that a cancer cell is abnormal, because it's not able to look at enough different characteristics to identify the cell properly. If injected into the body, a nano machine with an on-board computer could look at 20 different characteristics of a cell before doing anything to it".*

Following this, there have been several drug delivery systems and diagnostic devices that have been introduced to the market, bringing a revolution in the field of medicine and medical practice. Early detection of many diseases, particularly cancers, is the key to successful treatment of the disease. However, traditional diagnostic and imaging techniques can not detect tumors in early development stages and have limited ability in differentiating benign and malignant lesions.[25] As new advancements are seen in cancer diagnostics, termination of cancerous cells is equally important. Targeted drug delivery is one possible approach in treating cancer that focuses on delivering the cancer killing drug to the intended cancerous region only, thereby avoiding healthy cells and tissue.[26]

Stimuli-responsive NGs have been shown to have great potential in biomedical applications such as drug delivery. These NGs undergo volume-based swelling or collapse on exposure to stimuli (temperature, pH, ionic charge, light, magnetic field, etc.), releasing the drug payload to the surroundings in the process. Owing to the complexity of the physiological microenvironments, NGs responding to a single stimuli might not be suitable to achieve the desired goals, therefore, materials that are responsive to dual physical or chemical stimuli are highly desired for biomedical applications. pNIPAm-pAAc-based NGs provide such dual stimuli-response with pNIPAm and pAAc providing thermal and pH-based responses, respectively.

Being one of the most widely studied thermo-sensitive polymers for bio-applications, pNIPAm-based NGs undergo entropically driven reversible coil-to-globule transition above the VPTT, that lies around 36°C for these systems, thereby making them ideal candidates for biomedical applications such as drug delivery.[27,28] pNIPAm-pAAc-based NGs are usually synthesized using precipitation polymerization at temperatures above the VPTT of the formed NG.[29–31] The reaction is complex and few studies have been conducted to understand the growth of pNIPAm-based gels.[32,33] In addition, to understand the stimuli response from temperature and pH, it is important to study the extent of incorporation of pNIPAm and pAAc in the NG matrix. However, most studies are not associated with NGs, but, microgels. Furthermore, they do not highlight in detail, the effect of pAAc on the physico-chemical properties of the NGs, as well as, release of drugs from these NGs.

Besides polymeric NPs, inorganic NPs, such as iron-oxide and silver NPs, have also been extensively used in biomedical applications owing to their superparamagnetic and plasmonic properties, respectively. In addition, magneto-plasmonic NPs combine the worlds of magnetism and photonics at nanoscale, thereby exhibiting plasmonic and magnetic phenomena simultaneously.[34] Besides their application in magnetic hyperthermia (MHT),[35–38] magnetic NPs provide other functions, such as contrast for magnetic resonance imaging (MRI)[39,40] or magnetic-based targeting and drug delivery.[41,42] On the other hand, plasmonic NPs present optical sensing ability for applications as biosensors,[43,44] and imaging agents.[8,45,46] From a theranostics approach, the magneto-plasmonic assembly has gathered particular attention over the past few years due to its multifunctional potential for biomedical applications.[35]

References

(*1*) Boholm, M. (2016). The use and meaning of nano in American English: Towards a systematic description. *Ampersand 3*, 163–173.

(*2*) Bawa, R. (2016). What's in a name? Defining "nano" in the context of drug delivery. *Handbook of Clinical Nanomedicine: Nanoparticles, Imaging, Therapy, and Clinical Applications, Pan Stanford Publishing, Singapore*, 127–169.

(*3*) Boverhof, D. R., Bramante, C. M., Butala, J. H., Clancy, S. F., Lafranconi, M., West, J., and Gordon, S. C. (2015). Comparative assessment of nanomaterial definitions and safety evaluation considerations. *Regulatory Toxicology and Pharmacology 73*, 137–150.

(*4*) Feynman, R. P. et al. (1960). There's plenty of room at the bottom. *California Institute of Technology, Engineering and Science magazine*.

(*5*) Dowling, A. P. (2004). Development of nanotechnologies. *Materials Today 7*, 30–35.

(*6*) Gul, S., Khan, S. B., Rehman, I. U., Khan, M. A., and Khan, M. (2019). A comprehensive review of magnetic nanomaterials modern day theranostics. *Frontiers in Materials 6*, 179.

(*7*) Bandyopadhyay, S., Sharma, A., and Glomm, W. R. (2017). The Influence of Differently Shaped Gold Nanoparticles Functionalized with NIPAM-Based Hydrogels on the Release of Cytochrome C. *Gels 3*, 42.

(*8*) Wu, Y., Ali, M. R., Chen, K., Fang, N., and El-Sayed, M. A. (2019). Gold nanoparticles in biological optical imaging. *Nano Today 24*, 120–140.

(*9*) Santos, C. S., Gabriel, B., Blanchy, M., Menes, O., García, D., Blanco, M., Arconada, N., and Neto, V. (2015). Industrial applications of nanoparticles–a prospective overview. *Materials Today: Proceedings 2*, 456–465.

(*10*) Liao, R., Yang, P., Wu, W., Luo, D., and Yang, D. (2018). A DNA tracer system for hydrological environment investigations. *Environmental science & technology 52*, 1695–1703.

(*11*) Leibundgut, C., Maloszewski, P., and Külls, C., *Tracers in hydrology*; John Wiley & Sons: New York, USA, 2011.

(*12*) Wilderer, P. A., *Treatise on water science*; Newnes: 2010.

(*13*) Abbott, B. W., Baranov, V., Mendoza-Lera, C., Nikolakopoulou, M., Harjung, A., Kolbe, T., Balasubramanian, M. N., Vaessen, T. N., Ciocca, F., Campeau, A., et al. (2016). Using multi-tracer inference to move beyond single-catchment ecohydrology. *Earth-Science Reviews 160*, 19–42.

(*14*) Levy, B., and Chambers, R. (1987). Bromide as a conservative tracer for soil-water studies. *Hydrological Processes 1*, 385–389.

(*15*) Sharma, A., Foppen, J. W., Banerjee, A., Sawssen, S., Bachhar, N., Peddis, D., and Bandyopadhyay, S. (2021). Magnetic Nanoparticles to Unique DNA Tracers: Effect of Functionalization on Physico-chemical Properties. *Nanoscale research letters 16*, 1–16.

(*16*) Puddu, M., Paunescu, D., Stark, W. J., and Grass, R. N. (2014). Magnetically recoverable, thermostable, hydrophobic DNA/silica encapsulates and their application as invisible oil tags. *ACS nano 8*, 2677–2685.

(*17*) Kittilä, A., Jalali, M., Evans, K. F., Willmann, M., Saar, M. O., and Kong, X.-Z. (2019). Field Comparison of DNA-Labeled Nanoparticle and Solute Tracer Transport in a Fractured Crystalline Rock. *Water Resources Research 55*, 6577–6595.

(*18*) Liao, R., Zhang, J., Li, T., Luo, D., and Yang, D. (2020). Biopolymer/plasmid DNA microspheres as tracers for multiplexed hydrological investigation. *Chemical Engineering Journal 401*, 126035.

(*19*) Wages Jr, J. (2005). Polymerase chain reaction. *Encyclopedia of Analytical Science*, 243.

(*20*) Mano, J., Hatano, S., Futo, S., Yoshii, J., Nakae, H., Naito, S., Takabatake, R., and Kitta, K. (2014). Development of a reference material of a single DNA molecule for the quality control of PCR testing. *Analytical chemistry 86*, 8621–8627.

(*21*) Sharma, A. N., Luo, D., and Walter, M. T. (2012). Hydrological tracers using nanobiotechnology: proof of concept. *Environmental science & technology 46*, 8928–8936.

(*22*) Foppen, J. W., Seopa, J., Bakobie, N., and Bogaard, T. (2013). Development of a methodology for the application of synthetic DNA in stream tracer injection experiments. *Water resources research 49*, 5369–5380.

(*23*) Foppen, J. W., Orup, C., Adell, R., Poulalion, V., and Uhlenbrook, S. (2011). Using multiple artificial DNA tracers in hydrology. *Hydrological Processes 25*, 3101–3106.

(*24*) Drexler, K. E. (1981). Molecular engineering: An approach to the development of general capabilities for molecular manipulation. *Proceedings of the National Academy of Sciences 78*, 5275–5278.

(*25*) Lin, W. (2015). Introduction: nanoparticles in medicine. *Chemical reviews 115*, 10407–10409.

(*26*) Rosenblum, D., Joshi, N., Tao, W., Karp, J. M., and Peer, D. (2018). Progress and challenges towards targeted delivery of cancer therapeutics. *Nature communications 9*, 1–12.

(*27*) Vikulina, A. S., Aleed, S. T., Paulraj, T., Vladimirov, Y. A., Duschl, C., Von Klitzing, R., and Volodkin, D. (2015). Temperature-induced molecular transport through polymer multilayers coated with PNIPAM microgels. *Physical Chemistry Chemical Physics 17*, 12771–12777.

(*28*) Nothdurft, K., Müller, D. H., Mürtz, S. D., Meyer, A. A., Guerzoni, L. P., Jans, A., Kühne, A. J., De Laporte, L., Brands, T., Bardow, A., et al. (2021). Is the Microgel Collapse a Two-Step Process? Exploiting Cononsolvency to Probe the Collapse Dynamics of Poly-N-isopropylacrylamide (pNIPAM). *The Journal of Physical Chemistry B 125*, 1503–1512.

(*29*) Meng, Z., Smith, M. H., and Lyon, L. A. (2009). Temperature-programmed synthesis of micron-sized multi-responsive microgels. *Colloid and Polymer Science 287*, 277–285.

(*30*) Hendrickson, G. R., and Lyon, L. A. (2010). Microgel translocation through pores under confinement. *Angewandte Chemie International Edition 49*, 2193–2197.

(*31*) Raju, R., Bandyopadhyay, S., Sharma, A., Gonzalez, S. V., Carlsen, P. H., Gautun, O. R., and Glomm, W. R. (2018). Synthesis, characterization and drug loading of multiresponsive p [NIPAm-co-PEGMA](core)/p [NIPAm-co-AAc](Shell) Nanogels with Monodisperse Size Distributions. *Polymers 10*, 309.

(*32*) Blackburn, W. H., and Lyon, L. A. (2008). Size-controlled synthesis of monodisperse core/shell nanogels. *Colloid and Polymer Science 286*, 563–569.

(*33*) Xia, X., and Hu, Z. (2004). Synthesis and light scattering study of microgels with interpenetrating polymer networks. *Langmuir 20*, 2094–2098.

(*34*) de Julián Fernández, C., and Pineider, F. In *New Trends in Nanoparticle Magnetism*; Springer: 2021, pp 107–136.

(*35*) Espinosa, A., Reguera, J., Curcio, A., Muñoz-Noval, Á., Kuttner, C., Van de Walle, A., Liz-Marzán, L. M., and Wilhelm, C. (2020). Janus Magnetic-Plasmonic Nanoparticles for Magnetically Guided and Thermally Activated Cancer Therapy. *Small 16*, 1904960.

(*36*) Kowalik, P., Mikulski, J., Borodziuk, A., Duda, M., Kamińska, I., Zajdel, K., Rybusinski, J., Szczytko, J., Wojciechowski, T., Sobczak, K., et al. (2020). Yttrium-doped iron oxide nanoparticles for magnetic hyperthermia applications. *The Journal of Physical Chemistry C 124*, 6871–6883.

(*37*) Soleymani, M., Velashjerdi, M., Shaterabadi, Z., and Barati, A. (2020). One-pot preparation of hyaluronic acid-coated iron oxide nanoparticles for magnetic hyperthermia therapy and targeting CD44-overexpressing cancer cells. *Carbohydrate polymers 237*, 116130.

(*38*) Chauhan, A., Midha, S., Kumar, R., Meena, R., Singh, P., Jha, S. K., and Kuanr, B. K. (2021). Rapid tumor inhibition via magnetic hyperthermia regulated by caspase 3 with time-dependent clearance of iron oxide nanoparticles. *Biomaterials science*.

(*39*) Deh, K., Zaman, M., Vedvyas, Y., Liu, Z., Gillen, K. M., O'Malley, P., Bedretdinova, D., Nguyen, T., Lee, R., Spincemaille, P., et al. (2020). Validation of MRI quantitative susceptibility mapping of superparamagnetic iron oxide nanoparticles for hyperthermia applications in live subjects. *Scientific reports 10*, 1–11.

(*40*) Jeon, M., Halbert, M. V., Stephen, Z. R., and Zhang, M. (2020). Iron oxide nanoparticles as T1 contrast agents for magnetic resonance imaging: fundamentals, challenges, applications, and prospectives. *Advanced Materials*, 1906539.

(*41*) Norouzi, M., Yathindranath, V., Thliveris, J. A., Kopec, B. M., Siahaan, T. J., and Miller, D. W. (2020). Doxorubicin-loaded iron oxide nanoparticles for glioblastoma therapy: A combinational approach for enhanced delivery of nanoparticles. *Scientific reports 10*, 1–18.

(*42*) Zhi, D., Yang, T., Yang, J., Fu, S., and Zhang, S. (2020). Targeting strategies for superparamagnetic iron oxide nanoparticles in cancer therapy. *Acta biomaterialia 102*, 13–34.

(*43*) Wang, X., Hou, T., Lin, H., Lv, W., Li, H., and Li, F. (2019). In situ template generation of silver nanoparticles as amplification tags for ultrasensitive surface plasmon resonance biosensing of microRNA. *Biosensors and Bioelectronics 137*, 82–87.

(*44*) Fan, M., Thompson, M., Andrade, M. L., and Brolo, A. G. (2010). Silver nanoparticles on a plastic platform for localized surface plasmon resonance biosensing. *Analytical chemistry 82*, 6350–6352.

(*45*) Caro, C., Castillo, P. M., Klippstein, R., Pozo, D., and Zaderenko, A. P. (2010). Silver nanoparticles: sensing and imaging applications. *Silver nanoparticles*, 201–223.

(*46*) Stensberg, M. C., Wei, Q., McLamore, E. S., Porterfield, D. M., Wei, A., and Sepúlveda, M. S. (2011). Toxicological studies on silver nanoparticles: challenges and opportunities in assessment, monitoring and imaging. *Nanomedicine 6*, 879–898.

"The task is not so much to see what no one has seen; but to think what nobody has yet thought, about that which everybody sees."

– Erwin Schrödinger

"Have no fear of perfection, you'll never reach it."

– Salvador Dali

2

Aim & Outline

The aim of this PhD work was to synthesise NPs for potential environmental application – as hydrological tracers, and biomedical application – as drug delivery systems and biosensors. As far as the environmental application is concerned, the idea focuses on producing different DNA-based tracers, each having its own DNA signature, proving the possibility to synthesise infinite number of unique tracers. Magnetic IONPs form the core of the tracers, that are further functionalised with different ligands and DNA, before being encapsulated in silica shell (to protect the DNA), as shown in Figure 2.1. Emphasis has been on the synthesis, growth and functionalisation of IONPs, together with investigating the effect of surface functionalisation, on the physico-chemical properties of the IONPs and the variation in NP magnetism with surface coating. Three different IONPs have been used to tune the magnetic properties of the tracers, in addition to using three different DNA molecules, showing the possibility to synthesise different tracers, each having their unique signature. Tracers showed magnetic separation behaviour and the successful encapsulation of the DNA within silica was measured using qPCR.

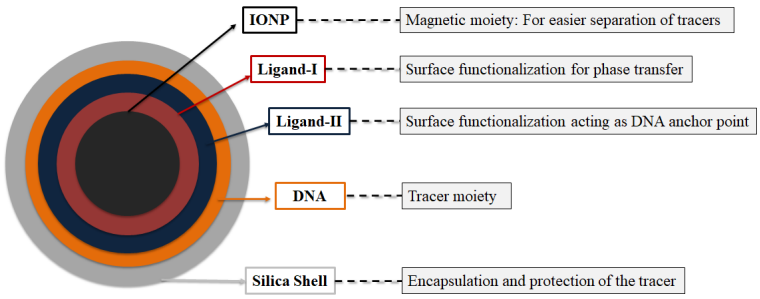

Figure 2.1: Schematic showing the hydrological tracer design, having the IONP core functionalised with DNA and encapsulation in silica shell. (Note: The image is a representation of the tracer and does not indicate that the particles will have the exact morphology.)

The IONPs were further used as seeds to grow silver on the surface via heterogeneous nucleation and epitaxial growth, resulting in dumbbell-shaped morphology of the magneto-plasmonic dimeric DNPs. These DNPs were synthesised for their potential applicability as biosensing devices. IONPs made up the magnetic part of the particles while Ag provided the plasmonic properties. The effect of concentration of silver salt precursor, on the physico-chemical properties of the particles, was studied. Separation studies were performed on the DNPs using ultraviolet visible spectrophotometry (UV-Vis), under a constant magnetic field gradient generated by a magnetophoresis set-up.

For targeted drug delivery application, stimuli-responsive NGs were synthesised using free radical precipitation polymerisation. pNIPAm and pAAc were selected as the monomers for the NGs, as they impart temperature and pH-based stimuli-response to the NG, respectively. Time-based growth study was performed to study the formation of pNIPAm-pAAc-based NGs by varying selected reaction parameters, primarily surfactant amounts and reaction atmosphere, to investigate their effects on the physico-chemical properties of the NGs. In addition, the effect of the extent of AAc incorporation in the NG matrix on the physico-chemical properties of the NG was studied, as shown in Figure 2.2. The potential of these NGs as drug delivery vehicles was evaluated by performing loading and release of Cyt C, a model protein drug, at different conditions of temperature and pH, using NGs with varying pAAc incorporation within the matrix (Figure 2.2). Furthermore, biocompatibility studies were conducted on the pNIPAm-pAAc based NGs using a human whole blood model, which is an *ex vivo* model allowing to study the complexity of complement activation by closely mimicking the *in vivo* conditions.

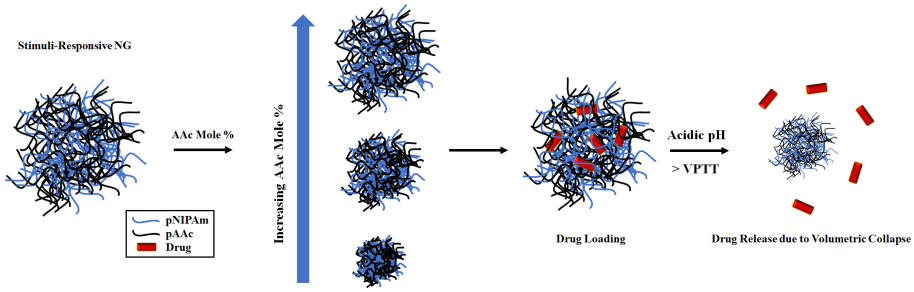

Figure 2.2: Schematic showing the effect of different amounts of pAAc incorporation on the physico-chemical properties of the pNIPAm-pAAc-based NG.

Outline

Figure 2.3 summarizes the entire outline of the thesis, that is broadly based on three NP systems, namely: *'IONPs'*, *'stimuli-responsive NGs'* and *'DNPs'* (Ag@IONPs). Within the scope of this thesis, a brief overview is given to IONPs, DNPs and NGs along with different methods to synthesise these particles and their physico-chemical properties in Chapter 3. Various NP synthesis, functionalisation and characterisation techniques employed in this work have been described in Chapter 4. Chapter 5 highlights the different mechanisms for NP nucleation and growth, together with NP functionalisation. The applicability of IONPs as hydrological tracers is mentioned in Chapter 6. Similarly, Chapter 7 focuses on biomedical applications of targeted drug delivery and biosensing using NGs and DNPs, respectively.

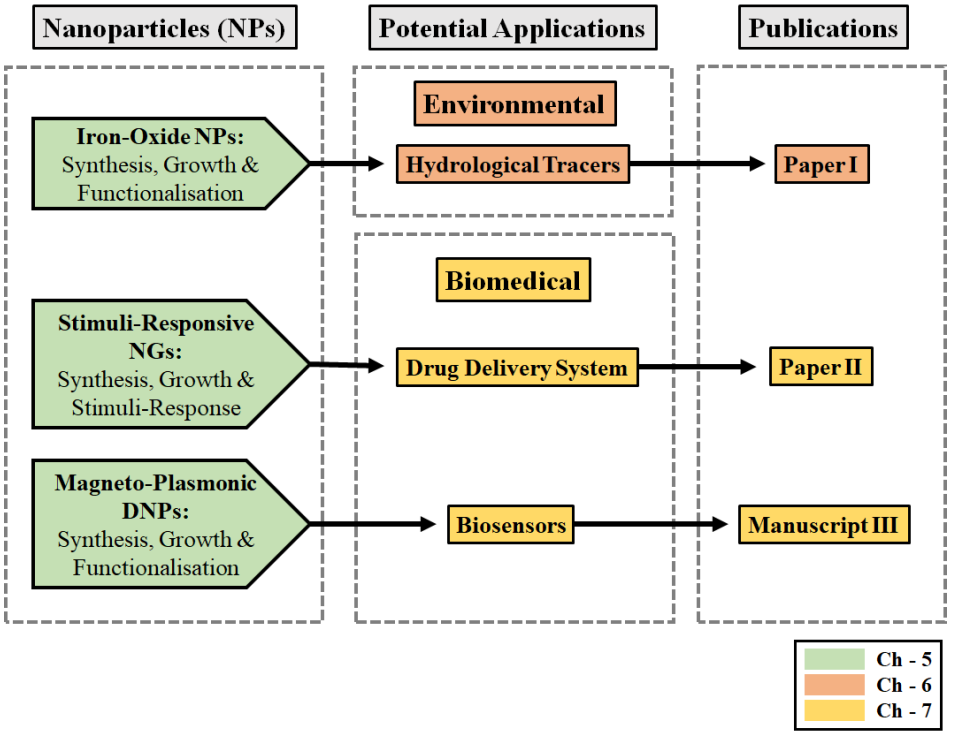

Figure 2.3: Schematic showing the outline of the entire thesis describing the NPs used in this work, as well as, their intended field of applications.

"Nothing in life is to be feared, it is only to be understood. Now is the time to understand more, so that we may fear less."

– Marie Curie

"Science is simply common sense at its best."

– Thomas Huxley

3

Introduction

The word nanotechnology was first used by a Japanese professor, Norio Taniguchi in 1974, who defined it in connection with possible applications in semiconductor processes.[1] However, the revolutionary invention of nanoscale imaging and manipulation techniques, the *Scanning Tunneling Microscope* (STM) – invented by Gerd Binning and Heinrich Rohrer in 1981, and the *Atomic Force Microscopy* (AFM) – invented by Gerd Binning, Calvin Quate and Christoph Gerber in 1986, allowed for the advancements in the field of nanoscience. These tools not only allowed the scientists to image surfaces, but also to move individual atoms as previously predicted by Richard Feynman.[2]

A nanomaterial can be defined as having at least one of its dimensions in the nanometer scale, ranging from one to normally 100 nm.[3] Hence, a *nanoparticle* has all three dimensions in the nanoscale, *nanotubes* or *nanowires* have two, while *nanofilms* have one dimension in the nanoscale. The use of metallic NPs seemed to date back to the 14^{th} and the 13^{th} centuries BC by the Egyptians and the Mesopotamians for glass-making.[4] The red colouration of the glass was analysed to result from the presence of cuprous oxide NPs and evidences of such occurrences were found until the 6^{th} century BC.

This chapter briefly describes the three different types of NPs used in the thesis, namely, iron-oxide NPs (IONPs), magneto-plasmonic dimeric NPs (DNPs) and stimuli-responsive nanogels (NGs). The formation of NPs is expressed from the viewpoint of classical theory of nucleation and growth. Different synthesis methods and NP functionalisation to obtain IONPs and NGs have been illustrated, along with their physico-chemical properties of superparamagnetism, and temperature and pH-response, respectively.

3.1 Iron-Oxide NPs

Magnetic NPs (MNPs) have an increasing interest from both fundamental and technological point of view, since the pioneering works of Louis Néel about 70 years ago. Co, Fe, Ni, Ti, iron-oxide, along with some ferrites ($BaFe_{12}O_{19}$ and $CoFe_2O_4$), are the most widely used MNPs, however, among these, IONPs (typically Fe_2O_3 or Fe_3O_4) are primarily used in biomedical field.[5,6] This stems from the fact that they possess remarkable properties, such as being superparamagnetic (*i.e.* high coercivity, low Curie temperature and high magnetic susceptibility), having low toxicity, etc., that differ greatly from the bulk material. These properties can be finely tuned through control over size, surface/interface structure, and nature and strength of interactions, allowing to design and synthesize a variety of MNPs for a wide range of applications.[7] Being superparamagnetic is of the most desirable characteristics of IONPs that has led to an increased demand for these particles in the world of nanoscience.

3.1.1 Superparamagnetism

IONPs have garnered significant interest in the biomedical field for their intrinsic magnetic and biodegradable properties.[8] These NPs are superparamagnetic as opposed to the bulk material. Bulk iron-oxide consists of multiple magnetic domains, with their own magnetic moments, that arrange themselves in a closed loop to minimize free energy, resulting in net zero magnetisation (in the absence of an external applied magnetic field). Therefore, magnetisation (M) can be expressed as a vector sum of magnetic moments of all atoms present per unit volume of any bulk ferromagnetic material. In the presence of an external magnetic field, these domains align in a particular direction, increasing the material's magnetisation with field strength till it reaches a saturation value (M_s). On removal of the external applied field, the reversal in magnetisation takes place by either Brownian motion (rotation of particle as a whole) or Neel mechanism (rotation of atomic moments inside particles collectively). However, not all domains return to their previous aligned states leading to remnant magnetisation (M_r) which can be removed by applying an opposite coercive field, giving rise to magnetization hysteresis loop. This is referred to as *ferromagnetism* – material retains magnetism after removal of magnetic field, as opposed to *paramagnetism* – material loses its magnetism on removal of magnetic field.

A single NP can be considered to contain just one domain, where the thermal energy at room temperature is sufficient to spontaneously reverse the particle's magnetisation on removal of the external field without displaying hysteresis. The particle size required to achieve superparamagnetism has been widely estimated to be below 20 nm (Figure 3.1),[10] where the barriers for magnetization reversal fall into the magnitude of thermal energy and superparamagnetic fluctuation effects. Vanishing of the remanence, coercivity and hysteresis loss is experienced when the relaxation time (τ_r) is smaller than the characteristic time of measurement (τ_m).[9], where the former is defined by Equation 3.1.

$$\tau_r = \tau_0 \exp \frac{K_a V}{k_B T} \tag{3.1}$$

where, K_a is the anisotropic constant, V is the mean particle volume, k_B is the Boltzmann constant, and T is the temperature. Therefore, as V decreases, so does the thermal energy to reverse magnetisation (i.e. $K_B T > KV$). This behaviour is termed as superparamagnetism

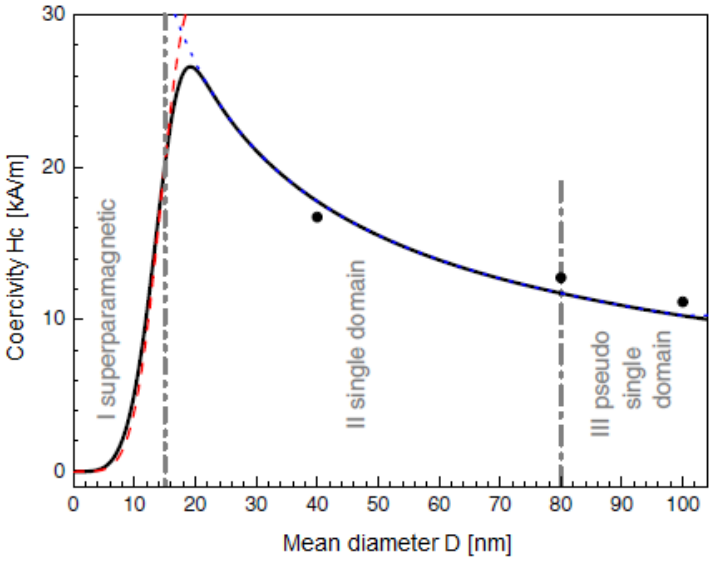

Figure 3.1: Dependence of coercivity on particle diameter with maximum coercivity being attained at a particle diameter of ∼20 nm. Adapted with permission from Hergt *et al.*[9]

and IONPs are superparamagnetic at room temperatures. This unique property allows the NPs to return back to dispersed state in suspension when the magnetic field is removed and not aggregate as there exists no residual intermagnetic force.[11] This magnetic property also makes the MNPs useful for many applications including data storage, spintronics, molecular and cellular isolation, magnetic resonance imaging (MRI) and hyperthermia treatment of cancer.[12] Having said that, IONPs might form aggregates in the absence of surface coatings due to weak magnetic forces between the particles resulting from magnetic dipole–dipole interactions or exchange interactions between particles in close proximity.[13] Therefore, the use of different ligands is important to prevent particle aggregation and obtain a homogeneously dispersed population.[14] These IONPs can further be combined with plasmonic NPs such as silver, to yield multifunctional nanomaterials exhibiting both plasmonic and magnetic phenomena.[7]

3.2 Magneto-Plasmonic NPs

Magneto-plasmonic NPs combine the worlds of magnetism and photonics at nanoscale. Plasmonic NPs present optical sensing ability for applications as biosensors[15,16] and imaging agents[17–19] owing to their unique property of localised surface plasmon resonance (LSPR). LSPR is an optical phenomenon occurring by entrapment of light wave within conductive NPs that have sizes smaller than the wavelength of incident light.[20] The interactions between the incident light (photons) and surface electrons in the conduction band produces coherent localized plasmon oscillations with a resonant frequency that is strongly dependant on the composition, size, geometry, dielectric environment and particle–particle separation distance of NPs.[21] A LSPR red shift (towards higher wavelength) is observed for Au and AgNPs as the particle size increases, while blue-shift is

observed with decreasing particle size. This is due to the increase in the distance between valence bands on increase in particle size, that further results in increase in wavelength of electromagnetic wave emitted.[22] Besides size, LSPR shift can also result from particle shape, aggregation, dielectric properties of the medium, to name a few.[23]

From a theranostic approach, the magneto-plasmonic attachment has gathered particular attention over the past few years due to its multifunctional potential for biomedical applications.[24] Magneto-plasmonic NPs, thus, combine multiple theranostic strategies in a unique structure, including multimodal photothermal therapy,[25] biosensing,[26] magnetic separation[27] and targeted therapy[28], with magnetic and plasmonic features. At nanoscale, size and surface effects play a key role in shaping NP properties that are affected by interparticle electromagnetic or magnetic dipolar interactions and intraparticle chemical, structural and electronic couplings. Studies have shown that the magnetic and plasmonic properties differ in hybrid (combination of the two) NPs and their bare counterparts.[29–32] Usually, a decrease in the magnetisation is seen in the magneto-plasmonic NPs compared to the bare NPs resulting from a '*dead layer*' or magnetic disordered layer, at the free surface or the interface of the NPs.[33–38] Thus, understanding the formation of MP NPs is critical in understanding their combined magnetic and plasmonic properties. Studies have mostly been performed with AuNPs, however, AgNPs have been shown to have better sensitivity (LSPR shift) compared to AuNPs, thereby making them suitable candidates for the application of biosensing.[39]

The formation magneto-plasmonic NPs takes place via epitaxial growth on the seed through heterogeneous nucleation.[40] The morphology of these NPs can be controlled by various reaction parameters, such as, seed size, seed concentration, solvent polarity, concentration of growth species, reaction temperature and crystalline lattice spacing, that might result in core-shell, dumbbell, flower-like morphology, as shown in Figure 3.2.[40–44] Growth of a crystalline species (Ag) on another crystalline NP (IONP) would result in a dumbbell NP given that there is a large enough lattice mismatch.[40,45]

3.3 NP Formation

The techniques to synthesise NPs is broadly classified by two approaches – '*top-down*' and '*bottom-up*'. The former consists of breaking up large pieces of material by wear to generate NPs, whereas the latter consists of building the NPs atom-by-atom or molecule-by-molecule to form larger particles. The top-down approach usually results in a broad particle size distribution (PSD) and, hence, is commonly used in the ceramic industry when size and shape are not essential for its application.[46] On the contrary, the bottom-up approach provides better control over particle size and morphology yielding NPs with narrow PSD. This is particularly important while addressing biomedical applications as the applicability of these NPs primarily depends on morphology, size, and surface properties.

The size and morphology of the IONPs can be affected by several factors, such as the presence of surfactants, reactant concentrations, reaction temperature and time.[47,48] Furthermore, particle size and morphology affects critical application aspects including blood circulation time, cellular uptake, and biodistribution. Although studies have focused on the shapes of NPs for anticancer drug delivery,[49,50] their effect on biodistribution of IONPs and their interactions with biological systems has not been extensively investigated.[51]

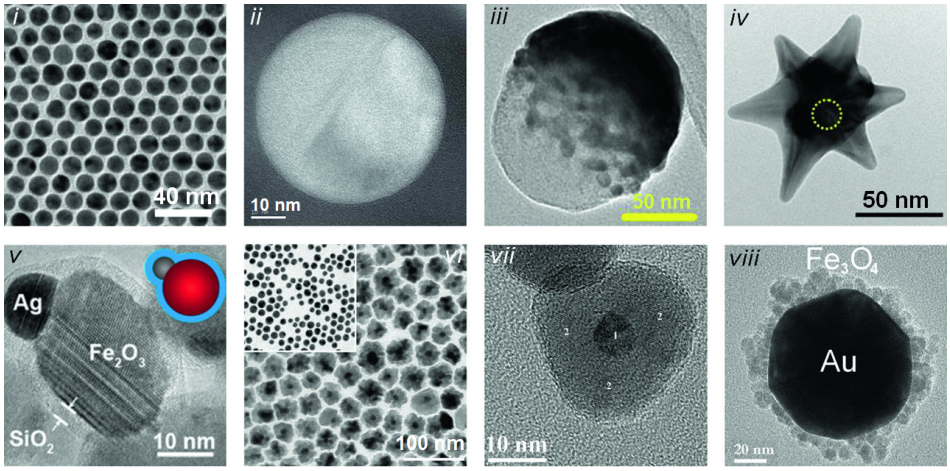

Figure 3.2: Transmission electron microscopy (TEM) images of a variety of MP nanostructures. **i** Bare Au NPs. **ii** Solid solution AuFe NP, Energy Field TEM mapping at the Au N-edge (83 eV). **iii** MP nanodome with 20 nm Fe core and 20 nm Au layer. **iv** Au nanostar with superparamagnetic core outlined by the dashed circle. **v** Asymetric SiO_2-coated Ag-Fe_2O_3 hetero-dimers. **vi** Flower-like Au@iron-oxide core-shell NPs. Inset Au nanocrystals seeds. **vii** Au@iron-oxide core-shell NPs. **viii** Fe_3O_4-decorated Au NPs. Adapted with permission from Peddis *et al.*[7] Copyright (2021) Springer Series in Materials Science.

NPs' size is another important factor determining their average circulation time followed by clearance from the body by different systems. For instance, particles having diameters <10 nm are removed by renal clearance, while particles with diameter >200 nm are concentrated in the spleen or absorbed by the phagocytic cells of the body.[52] Therefore, NPs in the range 10 to 200 nm in size are ideal for biomedical applications owing to their longer circulation times, which ease their elimination and increase the effect of permeability and retention in tumor tissues.[52] Moreover, IONPs with diameters <2 nm are not suitable for medical uses because they may induce toxic effects that can damage intracellular organelles.[48,53]

3.3.1 Supersaturation

The thermodynamic background behind nucleation lies with the reduction of free energy of the system by forming solid phase and supersaturation is the prerequisite for spontaneous crystallisation process. The system needs to be above the solubility curve for crystallisation to occur and most processes utilize the metastable zone as it allows for better control over the process (Figure 3.3). The state of supersaturation can be attained by either decreasing the temperature of the system (reducing solute solubility at a particular concentration) or increasing solute concentration in the system. Supersaturation, S, can be defined in terms of activity of the solute in the system as depicted by Equation 3.2.

$$S = \frac{a}{a^*} \tag{3.2}$$

where, a is the solute activity in an arbitrary state and a^* is the activity at equilibrium. Although the definition of supersaturation might differ from source-to-source, the basic concept of chemical potential difference between the two phases – the driving force for crystallisation, remains the point of origin. Once supersaturation is established (above solubility curve), the metastable zone allows for nucleation of the solute species.

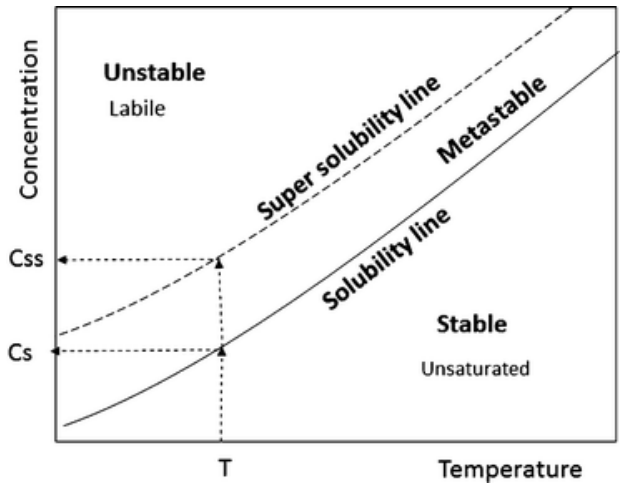

Figure 3.3: Concentration vs temperature curve for a solid showing the stable, metastable and the liable zones separated by the solubility curves. Adapted with permission from Mullin *et al.*[54] Copyright (2001) Elsevier.

3.3.2 Nucleation and Growth

LaMer and Dinegar proposed a theory, also referred as the '*classical nucleation and growth theory*', to explain crystal formation based on the mechanisms of nucleation-growth of sulfur particles.[55] The process of crystallisation starts with nucleation which is important in determining the final size and size distribution of the population. Therefore, the ability to exert any control over nucleation is necessary towards fabrication of particles with desired properties, that can be achieved by controlling supersaturation. Nucleation may occur spontaneously or it may be induced artificially by agitation, mechanical shock, friction and extreme pressures within solutions and melts, as shown by the early experiments.[56,57]

3.3.2.1 Homogeneous Nucleation

Nucleation is homogeneous when nuclei are formed in solution spontaneously. The excess free energy change (ΔG) for homogeneous nucleation can be expressed as:

$$\Delta G = \Delta G_S + \Delta G_V \tag{3.3}$$

where, ΔG_S represents the energy cost to create a solid-liquid interface and is positive, increasing proportionally to the surface area of the crystallite. ΔG_V is a negative quantity representing excess free energy of the metastable solution over the solid deposition, that

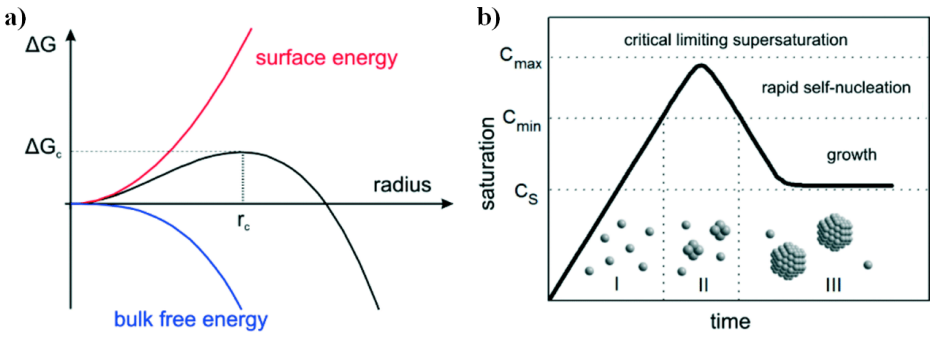

Figure 3.4: **a)** The dependence of the cluster free energy, ΔG, on the cluster radius, r, according to the classical nucleation theory (CNT). The curve has a maximum free energy ΔG at a critical cluster size, r_c, which defines the first stable particles – the nuclei. **b)** The principle of NP nucleation as per LaMer's mechanism of nucleation derived from CNT. The theoretical qualitative curve describes the monomer concentration as a function of time. Adapted with permission from Polte *et al.*[58] Copyright (2015) Royal Society of Chemistry.

is proportional to the volume of the crystallite. Thus, Equation 3.3 can be formulated as:[54]

$$\Delta G = A\gamma + V\Delta G_v = 4\pi r^2\gamma + \frac{4}{3}\pi r^3 \Delta G_v \tag{3.4}$$

Where, V is the volume of nuclei, A is the surface area of nuclei, ΔG_v is the free energy of transformation per unit volume, r is the radius of the nuclei, and γ is the interfacial tension between the developing crystalline surface and the supersaturated solution in which it is located. Since the two terms on the right-hand side of Equation 3.4 are of opposite sign and depend differently on r, the free energy of formation, passes through a maximum as seen in Figure 3.4a). This maximum value, ΔG_c, corresponds to the critical nucleus, r_c, and for a spherical cluster, is obtained by finding the maximum of ΔG as follows:

$$\frac{\Delta G}{\delta r} = 8\pi r\gamma + 4\pi r^2 \Delta G_v = 0 \tag{3.5}$$

$$r_c = \frac{-2\gamma}{\Delta G_v} \tag{3.6}$$

Thus, from Equations 3.4 and 3.6, ΔG_c can be expressed as:

$$\Delta G_c = \frac{16\pi\gamma^3}{3(\Delta G_v)^2} = \frac{4\pi\gamma {r_c}^2}{3} \tag{3.7}$$

A stable nuclei can be formed only when the excess free energy balances the energetic cost of creating a surface. As can be seen from Figure 3.4, the surface energy term is greater than the volume-dependent term, making stabilisation of clusters energetically unfavourable in the system due to overall increase in the free energy. A stable nuclei can form only when a critical size is attained resulting in negative slope of the ΔG curve. The critical size (r_c), therefore, represents the minimum size of a stable nucleus. Particles smaller than r_c will dissolve, while particles larger than r_c will continue to grow.

3.3.2.2 Heterogeneous Nucleation

In heterogeneous nucleation, nuclei are formed in the presence of foreign particles and as a result of this, the interfacial energy term has to be modified to include the contributions from both, the crystal-solution interfacial energies and the crystal-substrate interfacial energies. Typically, the interfacial energy between the crystal nucleus and the substrate is lower than the crystal in contact with the solution, resulting in lower effective interfacial energy of the system and, hence, energy barrier for nucleation. This decrease in the activation barrier depends on the contact angle, θ, between the clusters and the foreign substance surface, as given by Equation 3.8.

$$\Delta G_{crit,het} = \phi \Delta G_{crit,hom} \tag{3.8}$$

Where, ϕ is defined as:

$$\phi = \frac{(2 + cos\theta)(1 - cos\theta)^2}{4} \tag{3.9}$$

Three different scenarios can occur depending on the affinity of the crystal to the substrate (contact angle, θ) as summarised below.

Case I: θ = 180°, cosθ = -1, ϕ = 1
$\Delta G_{crit,het} = \Delta G_{crit,hom} \rightarrow$ complete non-wetting
As there is no affinity of the nucleating species towards the substrate, the energy required for nucleation is same as for homogeneous nucleation.

Case II: θ = 0 – 180°, ϕ = <1
$\Delta G_{crit,het} < \Delta G_{crit,hom} \rightarrow$ partial wetting
As some degree of affinity is shown towards the substrate, the energy required for nucleation is lower than for homogeneous nucleation.

Case III: θ = 0, ϕ = 0
$\Delta G_{crit,het} = 0 \rightarrow$ complete wetting (seeding)
This hints at the presence of pre-existing crystals (often of the same material) in the solution that provide nucleation and binding sites for the growth of the species.

Once a stable nucleus forms in a supersaturated solution, subsequent crystal growth occurs via continuous addition of building units (atoms, molecules or ions) on the surface of the crystal and their incorporation into the lattice sites.

3.3.2.3 Growth

The fundamental driving force for nucleation, as well as growth is the the same – i.e. lower chemical potential of the growth units as constituents of the solid than as corresponding solution species, however, they follow different energy landscapes. This results from the fact that solid crystals are already formed prior to growth stage, hence, further incorporation of solute species into the lattice requires lower energy than for nucleation. This phenomenon is clearly shown by LaMer diagram (Figure 3.4 b) by conceptually separating nucleation and growth stages with regards to supersaturation. Nucleation begins once critical concentration is reached followed by reduction in supersaturation as nuclei are formed. No more nuclei are formed once supersaturation falls below the critical value, but supersaturation continues to drop by the growing species until the solution reaches an equilibrium state, i.e., saturation.[59]

Crystal growth is a dynamic process with continuous attachment and detachment of growth species taking place simultaneously. The diffusion-reaction theory states the crystal growth occurs in two steps: the first involving a diffusion process by which solute molecules are transported from the bulk of the solution to the solid surface, and, the second involving first-order reaction by which these solute molecules arrange themselves into the crystal lattice. If the incorporation of the growth species is rapid, the transport of species from the bulk to the diffusion layer controls the growth process and is said to be *diffusion-controlled* denoted by Equation 3.10. Similarly, if the transport of the species is rapid, the growth is said to *reaction-controlled* denoted by Equation 3.11.

$$\frac{dm}{dt} = k_d A(C - C_i) \tag{3.10}$$

$$\frac{dm}{dt} = k_r A(C_i - C^*) \tag{3.11}$$

Where, m= mass of the solid deposited in time t, k_d = mass transfer coefficient based on diffusion, k_r = rate constant for surface reaction process, A = surface area of the crystal, C_i = solute concentration in the solution at the crystal-solution interface, C^* = equilibrium saturation concentration, C = solute concentration in the supersaturated solution.

The classical model of crystal growth assumes that growth species enter kink sites either directly from the solution or after adsorbing and diffusing through the terrace.[60] The molecules nucleate on a flat terrace generating two-dimensional islands (kinks) that further form steps as shown in Figure 3.5. As the ions incorporate on the kink sites, propagation of steps takes place and continues till the crystal edges are reached thereby, completing the surface layer. 2D nucleation, together with lateral growth of the islands on the surface, is known as '*birth and spread mechanism*' that is strongly dependant on supersaturation.[61] At sufficiently high supersaturation, multiple nucleation can occur on the surface generating high number of active sites for growth. If the lateral growth rate of the nuclei is high in comparison to the rate of nucleation, the surface is smooth. For even higher supersaturation, growth units can attach at any location (terraces, kinks or steps), resulting in rough crystal growth.

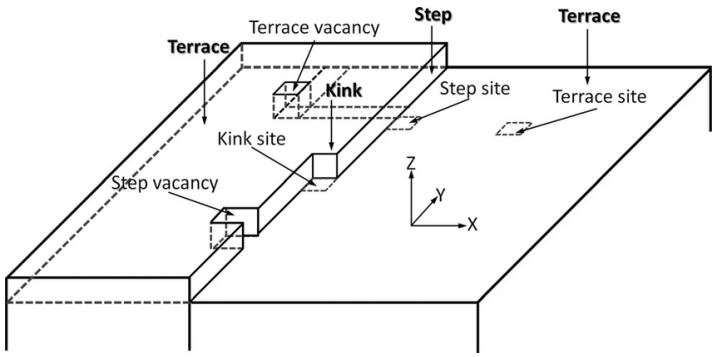

Figure 3.5: Schematic diagram of the substrate surface described by the Kossel–Stranski *"terrace–step–kink"* model showing the different nucleation sites. Adapted with permission from Bahrig *et al.*[62] Copyright (2014) Royal Society of Chemistry.

3.4 Non-classical Nucleation and Growth

Although classical nucleation theory presents a robust theoretical background, there exist some instances based on which the theory has been criticised. These arise from the lack of information on the structural characteristics of the clusters or the comprehensive insight into the pathways leading from the solution to precipitated solid.[63] It withholds certain assumptions regarding clusters, for instance, neglecting interactions between and size-dependency of surface energy, that simplify the thermodynamic framework.[64] In view of these criticisms, along with advancements in characterisation techniques (cryo-TEM, *in situ* atomic force microscopy (AFM), small-angle X-ray scattering (SAXS) and wide-angle X-ray scattering (WAXS)) and theoretical modeling (density functional theory and molecular dynamic simulations), increasing number of studies have proposed alternative nucleation hypotheses.[65]

Particle-based nucleation pathways, via aggregation and reorganisation of solution species, have been suggested that refer to these solution species as pre-nucleation clusters (PNCs). PNCs are described to comprise of either, clusters with disordered orientation, or multi-ion complexes, leading to '*cluster-mediated pathway*' and '*complex-mediated pathway*', respectively.[65] The former hypothesis states formation of small-sized clusters that subsequently interact to form stable nuclei through aggregation (Figure 3.6 b)). Whereas, in complex-mediated pathway, complexes are first formed by ionic interactions between metallic ions that have not fully reduced (Figure 3.6 c)). These further aggregate and reduce, to form nuclei. Therefore, contrary to CNT hypothesis, formation of PNCs do not lead to immediate growth, but, aid in nucleation through aggregation and reorganisation. The experimental observations of this multistep mechanism (aggregation and reorganisation) has been further supported by dynamic simulations.[66]

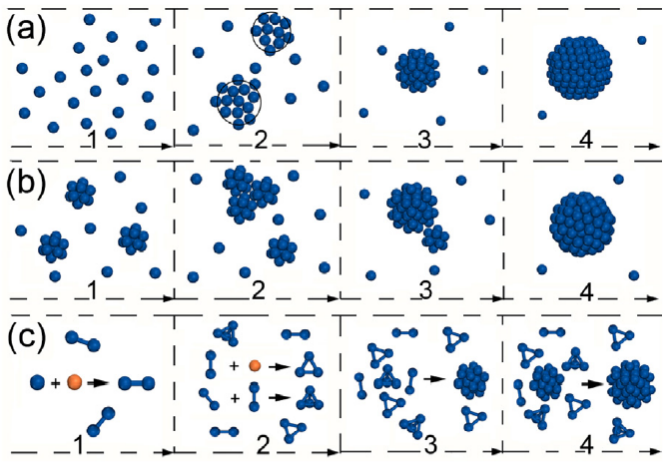

Figure 3.6: Schematic illustrations of three routes for the nucleation and seed formation of colloid metal nanocrystals. **a)** Classical 'burst''nucleation and seed formation. **b)** Cluster-aggregation mediated nucleation and seed formation. **c)** Nucleation and seed formation through aggregation of complexes. Adapted with permission from You *et al.*[65] Copyright (2016) Elsevier.

3.5 NP Synthesis

NP size, shape and morphology affect the physico-chemical properties of the IONPs, that in turn, affects their applicability in biomedicine and environmental applications.[67–69] Therefore, different novel routes are continuously researched with the aim to attain precise control over NP size and PSD. Table 3.1 lists the advantages and disadvantages of some of the synthesis methods.[70]

Table 3.1: Advantages and disadvantages of selected synthesis routes for IONPs.

Synthesis Route	Advantages	Disadvantages
Co-precipitation	Convenient, high yield, easy control of particle size and composition	Extensive agglomeration, poor morphology and particle size distribution
Thermal decomposition	High monodispersity, narrow size distribution	Expensive, organic solvents, high temperature
Hydrothermal	Easy control of particle size and shape	Long reaction times, high reaction temperature, high pressure
Microemulsion	Monodispersed particles various morphology possible	Not efficient, difficult to scale up
Sol–Gel	Energy efficient, high production rate, fast yield	Limited efficiency, high cost
Chemical vapor condensation	Small scale synthesis	Low yeild, difficult to control size and particle size distribution
Microwave	Short reaction time, high yields, excellent reproducibility, easy handling	Expensive, unsuitable for scale-up, poor reaction monitoring
Spray pyrolysis	Predictable size, shape and composition	Particle aggregation, costly
Laser pyrolysis	Small particle size, narrow size distribution	Complicated, very expensive
Biological	Selectivity and precision for nanoparticle formation, cost effective, eco-friendly	Limited knowledge, difficulty in controlling size and properties

The IONPs in this work have been synthesised using co-precipitation and thermal decomposition routes, therefore, these methods are briefly described in the sections below.

3.5.1 Co-precipitation

Co-precipitation is by far the most common route for the synthesis of magnetic iron oxide nanoparticles (IONPs), as cheap and environmentally friendly precursors and simple experimental procedures facilitate IONP production in many labs.[71] The synthesis is carried out in aqueous solution containing ferric (Fe^{3+}) and ferrous (Fe^{2+}) salts as precursors, to which a base is added at moderate temperatures, resulting in IONPs as shown by reaction below.[72]

$$Fe^{2+} + 2Fe^{3+} + 8OH^- \rightarrow Fe_3O_4 + 4H_2O \tag{3.12}$$

Even though the co-precipitation reaction is widely used, the mechanism of the reaction is still poorly understood, due to a severe lack of information on how intermediates are formed. This often leads to difficulties in obtaining reproducible syntheses, as the intermediates can remain present to a varying degree products.[72] Hence, optimising co-precipitation syntheses remains challenging as particle formation mechanisms are not well understood. This is partly due to the rapid particle formation (within seconds) providing insufficient time to characterise initial precipitates.[71] Although, some studies have been conducted to examine the growth kinetics of the process at multiple pH regimes using weaker bases that slows the reaction kinetics.[73,74] Various surfactants, such as polyethylene glycol (PEG), sodium oleate,[75] dodecylamine,[76] gluconic acid[77] and even gold shell[78] have been used to obtain uniform particle distribution.

3.5.2 Thermal Decomposition

The co-precipitation method utilises a simple and solvent-free process, yielding hydrophilic IONPs, however, low control of the synthesis process results in IONPs with a broad size distribution, and batch-to-batch inconsistency in IONP size, crystallinity, morphology, and other physico-chemical properties. To obtain precise control over the particle's size, shape and morphology, and eventually magnetic properties, IONPs can be synthesized using thermal decomposition route. This refers to the decomposition of iron precursors such as acetylacetonate, stearate, oleate or pentacarbonyl in the presence of stabilizing ligands in an organic solvent at high temperatures.[79–82] The finer control over particle size originates from temporal separation of nucleation and growth windows that promotes narrower size distributions in comparison to the more prevalent co-precipitation route.[83] Though precise control over particle shape, size and morphology is achieved thermal decomposition, the particles are in organic phase (usually toxic) that limits their use in environmental and biomedical applications.[68,84]. Hence the particle surface needs to be coated or modified with appropriate ligands before they can be utilised for further applications.

3.6 Surface Modification

NPs have a large surface-to-volume ratio resulting in high surface energies, promoting aggregate formation to minimize their surface energies. Moreover, IONPs have high chemical activity, and are readily prone to oxidation in air (especially magnetite), usually leading to loss of magnetism and dispersibility. Therefore, providing proper surface functionalisation and developing effective protection strategies to keep the stability of magnetic IONPs is extremely vital. These strategies can comprise either grafting or coating with organic molecules, including small organic molecules, surfactants, polymers, biomolecules, or with an inorganic layer, such as silica, noble metals, metal oxide or metal sulfides as shown by Figure 3.7. From a practical point of view, in most cases, the protecting shell not only stabilises the particles, but can also be used for further functionalisation steps.[85]

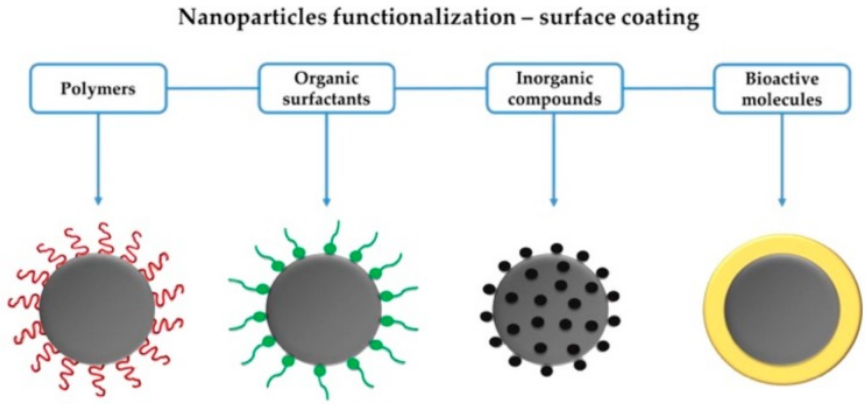

Figure 3.7: Schematic representation of the main strategies followed to modify the surface of IONPs. Adapted with permission from Wallyn *et al.*[86] Copyright (2019) MDPI.

Surface coating on IONPs can be achieved using one-step (*in situ*) or multi-step (post-synthesis modification) techniques.[68] The former involves functionalisation during NP synthesis as reported for dextran functionalised IONPs synthesised via co-precipitation.[87] Whereas, the multi-step functionalisation involves attaching the ligand onto the surface of IONPs after their synthesis.[88,89] Depending on the desired functionalisation, as well as final particle applicability, different ligands for instance, PVP,[90] chitosan,[91] CTAB,[90,92] and Na-citrate,[93] can be used. Silica is another inorganic material that has received considerable interest for IONP coating, owing to its excellent biocompatibility, non-toxicity, and stability.[94] Furthermore, silica is generally inert showing high colloidal stability due to its low isoelectric point and lower van der Waals force than other metal oxides, and allows for further conjugation with different functional groups and the potential coupling of biomolecules for biomedical applications.[95] This enables flexibility in the applicability of silica functionalised IONPs to be used as, for instance, core-shell nanocomposites for adhesion of nucleic acid,[96,97] or concurrent functionalisation with chitosan and photoluminescence: Ce^{3+}, Tb^{3+} doped GdOF luminophore, for *in vivo* toxicity assessment.[98] It is also necessary to modify the surface of IONPs to transfer them from organic to aqueous medium and vice-versa as discussed in the following sub-section.

3.6.1 Phase Transfer

Phase transfer can primarily be achieved using two pathways; partial or complete replacement of the existing hydrophobic ligand with the hydrophilic ligand referred to as '*ligand-ligand exchange*', or modification of the existing hydrophobic ligand with a hydrophilic ligand.[99] Several reports have shown that the phase transfer of these NPs may be achieved using specific ligands, such as, tetra methyl ammonium hydroxide (TMAH), hexadecyltrimethylammonium bromide (CTAB), poly-ethylene glycol (PEG), sodium citrate (Na-citrate) and so on, guided by the synthesis route and intended downstream application.[100–102]

Researchers have shown that CTAB[102] controls particle shape and size as it adsorbs on the surface of the particles reducing the surface energy by adsorbing onto the surface, along with preventing aggregation owing to electrostatic repulsion. However, CTAB is toxic and, therefore, is detrimental to cell cultures and tissues. On the contrary, Na-citrate[103] being non-toxic, biodegradable, highly soluble in several solvents, hydrophilic, and biocompatible, is a suitable ligand. Na-citrate provides anionic charge arising from the carboxylic and hydroxyl functional groups.

Other studies have used biocompatible polymers – chitosan[104] and polyvinylpyrrolidone (PVP)[105] to modify the surface of IONPs. Chitosan has one amino and two hydroxyl groups that rapidly attach onto particle surface, producing biocompatible, hydrophilic, and high stability of IONPs. In cases, where the effect of particle's size, shape and morphology on functionalisation needs to be investigated, selecting the same phase transfer methodology for all the particle types deems necessary. In order to achieve this, developing repeatable and tunable protocols becomes important.[99]

3.7 Stimuli-responsive Nanogels

The term '*nanogels*', was introduced by Kabanov *et al.* in 1999 describing them as three dimensional networks of chemically or physically cross-linked hydrophilic polymers.[106] Nanogels (NGs) are widely used as drug delivery systems owing to their extreme water retention capacity, high loading and entrapment efficiencies, good stability, along with the possibility to make them sensitive to their environment such as temperature, pH, ionic strength, electric or magnetic fields, etc.[107–109] Stimuli-responsive NGs can react in a dynamic way to a specific microenvironment and have the potential to achieve on-demand drug delivery with excellent spatial, temporal and dosage control.[110]

3.7.1 NG Synthesis

Based on the initial phase of the reaction medium, polymerisation can be classified as homogeneous (single phase) or heterogeneous (multi phase). The former represents a reaction system in which all the reaction components are soluble in the solvent, whereas, the in the latter, the formed polymer is usually insoluble in the solvent. Depending on this criteria, different types of polymerisation exist, namely, bulk, solution, suspension, emulsion, dispersion and precipitation polymerisation.[59] Among these, precipitation polymerisation is usually used for synthesising pNIPAm-based NGs as described in the following sub-section.

3.7.1.1 Precipitation Polymerisation

The synthesis of pNIPAm-based NGs via precipitation polymerisation in aqueous medium, has been extensively reported. The reason for synthesising the NGs by this method can be attributed to the thermo-responsive nature of pNIPAm, whereby it undergoes volume phase transition at temperatures above VPTT. Hence, as the polymerisation proceeds above VPTT, the formed pNIPAm precipitates out forming a heterogeneous phase (monomer dissolved in solvent phase and precipitated polymer phase). However, to prevent pNIPAm from dissolving in the solvent at T < VPTT, a crosslinker is use.[111] As the polymer is formed during the course of the reaction, it collapses on itself after attaining a critical length, creating precursor particles. These particles grow further by either aggregation with other precursor particles, incorporated into existing particles, monomer addition or capturing growing oligonucleotides. The charge provided by the initiator stabilises the precursor particles. Precipitation polymerisation also allows for high control over particle size by using a surfactant, that provides additional ionic stabilisation to the precursor particles yielding polymer-based NGs.[59]

3.7.2 Stimuli Responses

3.7.2.1 Temperature-based Response

Thermoresponsive drug delivery is among the most investigated stimuli-responsive strategies, and has been widely explored in oncology. The reason why thermoresponsive polymers are appealing, as '*smart materials*', is the fact that they apparently precipitate from a solution on either increasing or decreasing the temperature.[112] Temperature-based response is usually governed by a nonlinear sharp change in the properties of at least one component of the NP, with temperature, that can trigger the release of the drug. Ideally, thermoresponsive NGs should retain their load (drug) at body temperature ($\sim$37 °C), and rapidly cause release within a locally heated tumour ($\sim$40–42 °C) to counteract rapid blood-passage time and washout from the tumour.[110]

In particular, polymers that reveal lower critical solution temperature (LCST) behavior in water are of tremendous interest for many applications evolving from their ability to alter hydrophilic/hydrophobic behaviour upon temperature variation.[113,114] Several polymers, such as poly(N,N-diethylacrylamide)[115,116] and polyampholytes[117,118] exhibit LCST behavior, however, among these, poly(N-isopropylacrylamide) (pNIPAm) is one of the most extensively investigated polymer for its LCST behavior.[119] The increased interest in pNIPAm arises because its LCST occurs at near physiological conditions, thus, rendering this neutral water soluble polymer suitable for biotechnological applications.[120] Most widely reported value of LCST $\simeq$ 32 °C can be traced back to 1968 where Heskins and Guillet reported the LCST to be $\simeq$ 31 °C and monomer volume fraction $\phi \simeq 0.16$.[121]

In the case of NGs, the system of cross-linked polymer chains undergo volume based swelling or collapse as a response to temperature. Hence, the temperature at which this volume based transition occurs is referred to volume based transition temperature (VPTT). PNIPAm-based NGs undergo entropically driven reversible coil-to-globule phase transition above the VPTT, owing to the hydrophilic amide and hydrophobic propyl groups, that lies around 36 °C for these systems, thereby making them most widely studied thermo-sensitive polymers for biomedical applications of targeted drug delivery.[122] The VPTT of pNIPAm-based NGs can be altered by copolymerizing NIPAm with other hydrophobic or hydrophilic monomers,[123,124] and acrylic acid (AAc) is one such hydrophilic monomer that also imparts pH response to the polymer,[103,125] as discussed later.

3.7.2.2 pH-based Response

One of the conventional cancer treatment methods is chemotherapy, however, due to the multi-drug resistance of tumor cells to drugs and nonspecific drug delivery, the efficacy of this therapy is greatly limited.[126] Furthermore, nanocarriers face challenges in clinical applications, such as nonspecific release, poor tumor permeability and insufficient drug concentration that impact the effectiveness of tumor treatment.[127,128] Extensive study on stimuli-responsive nanocarriers is being going on that are designed according to the specific microenvironment of tumor tissue and among them, the pH-sensitive drug delivery system is one of the research hotspots.[129,130] Furthermore, it is seen that the biological microenvironment surrounding cancer cells tends to be acidic compared to that of normal blood (pH = 7.4), providing optimum conditions for cancer growth.[131,132] This results from the large amounts of lactic acid secreted by the tumour cells through hypoxic glycolysis, resulting in pH dysregulation in the tumor cells. Compared to normal cells (pH = 7.4), the extracellular pH values of tumor cells are lower (pH = 6.0–7.2) that are further reduced (pH = 4–6) within tumor cells.[133] Therefore, the pH gradients between the tumor microenvironment and the normal physiological environment can be used to design a pH-sensitive drug delivery system to regulate drug delivery and release.[134] Various types of pH-sensitive drug delivery systems have been developed, such as liposomes, micelles, hydrogels, and nanoparticles.[135–138]

Owing to the complexity of the physiological microenvironments, NGs responding to a single stimuli might not be suitable to achieve the desired goals, therefore, materials that are responsive to more than one physical or chemical stimuli are highly desired for biomedical applications. PNIPAm-pAAc-based NGs provide exactly such dual stimuli response with temperature and pH.[139] The pH responsiveness of pAAc stems from the carboxyl groups that at lower pH (pH < 4.5-6.0 – pK_a of AAc) resulting in NG collapse and swelling at higher pH (> pK_a) due to dissociation of carboxyl groups.[134] Additionally, pAAc is nontoxic and has high adhesion to biological tissues.[140]

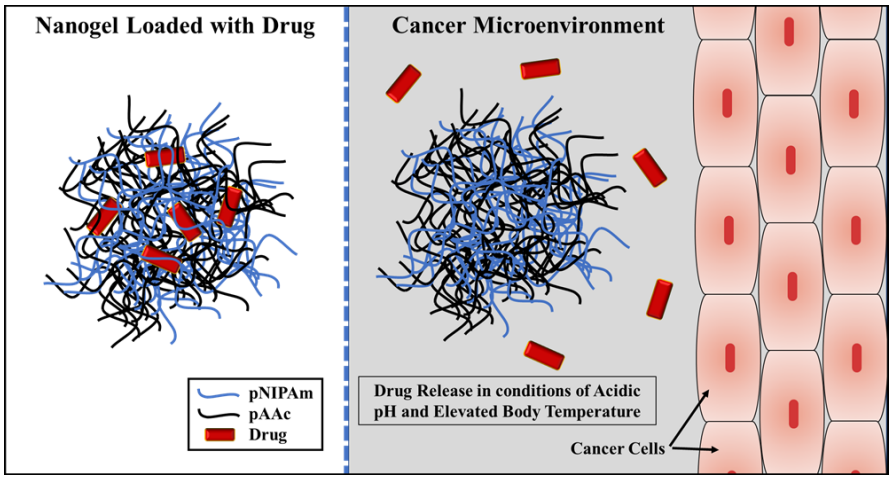

Figure 3.8: Schematic diagram showing the release of drug, loaded in dual stimuli-responsive pNIPAm-pAAc-based nanogel, to the cancer microenvironment at release conditions of elevated temperature and low pH.

3.8 Summary

This chapter gives an insight into the world of magnetic IONPs and polymeric stimuli-responsive NGs discussing their synthesis, functionalisation and physico-chemical properties. The formation of IONPs from the view of classical nucleation and growth theory has been presented, covering the concepts of supersaturation, homogeneous and heterogeneous nucleation, and crystal growth. Furthermore, various synthesis techniques to obtain IONPs were highlighted, with particular focus on the co-precipitation and thermal decomposition methods. Thereafter, surface modification techniques have been mentioned, that, not only provide particle stabilisation, but also alter the properties of the IONPs through surface functionalisation. The latter sections of the chapter capture synthesis and physico-chemical properties of stimuli-responsive NGs. Temperature and pH stimuli-responsive NGs have been mentioned, that are gaining popularity as targeted drug delivery systems.

References

(*1*) Taniguchi, N., *Proceedings of the International Conference on Production Engineering*; Japan Society of Precision Engineering Tokyo: Tokyo, Japan, 1974.

(*2*) Schaming, D., and Remita, H. (2015). Nanotechnology: from the ancient time to nowadays. *Foundations of Chemistry 17*, 187–205.

(*3*) McClements, D. J., and Xiao, H. (2017). Is nano safe in foods? Establishing the factors impacting the gastrointestinal fate and toxicity of organic and inorganic food-grade nanoparticles. *npj Science of Food 1*, 1–13.

(*4*) Brill, R. H., and Cahill, N. D. (1988). A red opaque glass from Sardis and some thoughts on red opaques in general. *Journal of Glass Studies*, 16–27.

(*5*) Li, X., Wei, J., Aifantis, K. E., Fan, Y., Feng, Q., Cui, F.-Z., and Watari, F. (2016). Current investigations into magnetic nanoparticles for biomedical applications. *Journal of Biomedical Materials Research Part A 104*, 1285–1296.

(*6*) Cardoso, V. F., Francesko, A., Ribeiro, C., Bañobre-López, M., Martins, P., and Lanceros-Mendez, S. (2018). Advances in magnetic nanoparticles for biomedical applications. *Advanced healthcare materials 7*, 1700845.

(*7*) Peddis, D., Laureti, S., and Fiorani, D., *New Trends in Nanoparticle Magnetism*; Springer: 2021.

(*8*) Jeon, M., Halbert, M. V., Stephen, Z. R., and Zhang, M. (2021). Iron oxide nanoparticles as T1 contrast agents for magnetic resonance imaging: fundamentals, challenges, applications, and prospectives. *Advanced Materials 33*, 1906539.

(*9*) Hergt, R., Dutz, S., and Röder, M. (2008). Effects of size distribution on hysteresis losses of magnetic nanoparticles for hyperthermia. *Journal of Physics: Condensed Matter 20*, 385214.

(*10*) Li, Q., Kartikowati, C. W., Horie, S., Ogi, T., Iwaki, T., and Okuyama, K. (2017). Correlation between particle size/domain structure and magnetic properties of highly crystalline Fe_3O_4 nanoparticles. *Scientific reports 7*, 1–7.

(*11*) Olsvik, O., Popovic, T., Skjerve, E., Cudjoe, K. S., Hornes, E., Ugelstad, J., and Uhlen, M. (1994). Magnetic separation techniques in diagnostic microbiology. *Clinical microbiology reviews 7*, 43–54.

(*12*) Alonso, J., Barandiarán, J. M., Barquín, L. F., and García-Arribas, A. In *Magnetic nanostructured materials*; Elsevier: 2018, pp 1–40.

(*13*) Gutiérrez, L., De la Cueva, L., Moros, M., Mazarío, E., De Bernardo, S., De la Fuente, J. M., Morales, M. P., and Salas, G. (2019). Aggregation effects on the magnetic properties of iron oxide colloids. *Nanotechnology 30*, 112001.

(*14*) Gutiérrez, L., Costo, R., Grüttner, C., Westphal, F., Gehrke, N., Heinke, D., Fornara, A., Pankhurst, Q. A., Johansson, C., Veintemillas-Verdaguer, S., et al. (2015). Synthesis methods to prepare single-and multi-core iron oxide nanoparticles for biomedical applications. *Dalton Transactions 44*, 2943–2952.

(*15*) Wang, X., Hou, T., Lin, H., Lv, W., Li, H., and Li, F. (2019). In situ template generation of silver nanoparticles as amplification tags for ultrasensitive surface plasmon resonance biosensing of microRNA. *Biosensors and Bioelectronics 137*, 82–87.

(*16*) Fan, M., Thompson, M., Andrade, M. L., and Brolo, A. G. (2010). Silver nanoparticles on a plastic platform for localized surface plasmon resonance biosensing. *Analytical chemistry 82*, 6350–6352.

(*17*) Wu, Y., Ali, M. R., Chen, K., Fang, N., and El-Sayed, M. A. (2019). Gold nanoparticles in biological optical imaging. *Nano Today 24*, 120–140.

(*18*) Caro, C., Castillo, P. M., Klippstein, R., Pozo, D., and Zaderenko, A. P. (2010). Silver nanoparticles: sensing and imaging applications. *Silver nanoparticles*, 201–223.

(*19*) Stensberg, M. C., Wei, Q., McLamore, E. S., Porterfield, D. M., Wei, A., and Sepúlveda, M. S. (2011). Toxicological studies on silver nanoparticles: challenges and opportunities in assessment, monitoring and imaging. *Nanomedicine 6*, 879–898.

(*20*) Willets, K. A., and Van Duyne, R. P. (2007). Localized surface plasmon resonance spectroscopy and sensing. *Annu. Rev. Phys. Chem. 58*, 267–297.

(*21*) Petryayeva, E., and Krull, U. J. (2011). Localized surface plasmon resonance: Nanostructures, bioassays and biosensing—A review. *Analytica chimica acta 706*, 8–24.

(*22*) Fong, K. E., and Yung, L.-Y. L. (2013). Localized surface plasmon resonance: a unique property of plasmonic nanoparticles for nucleic acid detection. *Nanoscale 5*, 12043–12071.

(*23*) Kosuda, K., Bingham, J., Wustholz, K., and Van Duyne, R. (2010). Nanostructures and surfaceenhanced Raman spectroscopy. *Handbook of Nanoscale Optics and Electronics*, 309.

(*24*) Espinosa, A., Reguera, J., Curcio, A., Muñoz-Noval, Á., Kuttner, C., Van de Walle, A., Liz-Marzán, L. M., and Wilhelm, C. (2020). Janus Magnetic-Plasmonic Nanoparticles for Magnetically Guided and Thermally Activated Cancer Therapy. *Small 16*, 1904960.

(*25*) Magadla, A., Oluwole, D. O., Managa, M., and Nyokong, T. (2019). Physicochemical and antimicrobial photodynamic chemotherapy (against E. coli) by indium phthalocyanines in the presence of silver–iron bimetallic nanoparticles. *Polyhedron 162*, 30–38.

(*26*) Chen, Y., Xianyu, Y., Dong, M., Zhang, J., Zheng, W., Qian, Z., and Jiang, X. (2018). Cascade reaction-mediated assembly of magnetic/silver nanoparticles for amplified magnetic biosensing. *Analytical chemistry 90*, 6906–6912.

(*27*) Hola, K., Markova, Z., Zoppellaro, G., Tucek, J., and Zboril, R. (2015). Tailored functionalization of iron oxide nanoparticles for MRI, drug delivery, magnetic separation and immobilization of biosubstances. *Biotechnology advances 33*, 1162–1176.

(*28*) Prucek, R., Tuček, J., Kilianová, M., Panáček, A., Kvítek, L., Filip, J., Kolář, M., Tománková, K., and Zbořil, R. (2011). The targeted antibacterial and antifungal properties of magnetic nanocomposite of iron oxide and silver nanoparticles. *Biomaterials 32*, 4704–4713.

(*29*) Vita, F., Innocenti, C., Secchi, A., Albertini, F., Grillo, V., Fiore, A., Cozzoli, P. D., and de Julián Fernández, C. (2018). Colloidal Au/iron oxide nanocrystal heterostructures: magnetic, plasmonic and magnetic hyperthermia properties. *Journal of Materials Chemistry C 6*, 12329–12340.

(*30*) Lee, Y., Garcia, M. A., Frey Huls, N. A., and Sun, S. (2010). Synthetic tuning of the catalytic properties of Au-Fe_3O_4 nanoparticles. *Angewandte Chemie International Edition 49*, 1271–1274.

(*31*) Wang, C., Wei, Y., Jiang, H., and Sun, S. (2009). Tug-of-War in Nanoparticles: Competitive Growth of Au on Au- Fe3O4 Nanoparticles. *Nano letters 9*, 4544–4547.

(*32*) George, C., Genovese, A., Qiao, F., Korobchevskaya, K., Comin, A., Falqui, A., Marras, S., Roig, A., Zhang, Y., Krahne, R., et al. (2011). Optical and electrical properties of colloidal (spherical Au)-(spinel ferrite nanorod) heterostructures. *Nanoscale 3*, 4647–4654.

(*33*) Liu, L., Cheng, S., Qi, B., Xi, Z., and Dong, D. (2015). Precision limit of atomic magnetometers in the presence of spin-destruction collisions. *Journal of Physics B: Atomic, Molecular and Optical Physics 48*, 035502.

(*34*) Kodama, R. H., Berkowitz, A. E., McNiff Jr, E., and Foner, S. (1996). Surface spin disorder in $NiFe_2O_4$ nanoparticles. *Physical Review Letters 77*, 394.

(*35*) Martínez-Boubeta, C., Simeonidis, K., Angelakeris, M., Pazos-Pérez, N., Giersig, M., Delimitis, A., Nalbandian, L., Alexandrakis, V., and Niarchos, D. (2006). Critical radius for exchange bias in naturally oxidized Fe nanoparticles. *Physical Review B 74*, 054430.

(*36*) Chandra, S., Huls, N. F., Phan, M.-H., Srinath, S., Garcia, M., Lee, Y., Wang, C., Sun, S., Iglesias, O., and Srikanth, H. (2014). Exchange bias effect in Au-Fe_3O_4 nanocomposites. *Nanotechnology 25*, 055702.

(*37*) Luchini, A., Vitiello, G., Rossi, F., De Ballesteros, O. R., Radulescu, A., D'Errico, G., Montesarchio, D., de Julián Fernández, C., and Paduano, L. (2015). Developing functionalized Fe_3O_4–Au nanoparticles: a physico-chemical insight. *Physical Chemistry Chemical Physics 17*, 6087–6097.

(*38*) Zhu, L., Deng, X., Hu, Y., Liu, J., Ma, H., Zhang, J., Fu, J., He, S., Wang, J., Wang, B., et al. (2018). Atomic-scale imaging of the ferrimagnetic/diamagnetic interface in Au-Fe_3O_4 nanodimers and correlated exchange-bias origin. *Nanoscale 10*, 21499–21508.

(*39*) Rycenga, M., Cobley, C. M., Zeng, J., Li, W., Moran, C. H., Zhang, Q., Qin, D., and Xia, Y. (2011). Controlling the synthesis and assembly of silver nanostructures for plasmonic applications. *Chemical reviews 111*, 3669–3712.

(*40*) Zhang, L., Dou, Y.-H., and Gu, H.-C. (2006). Synthesis of Ag–Fe_3O_4 heterodimeric nanoparticles. *Journal of colloid and interface science 297*, 660–664.

(*41*) Muraca, D., Sharma, S., Socolovsky, L., De Siervo, A., Lopes, G., and Pirota, K. (2012). Influence of silver concentrations on structural and magnetic properties of Ag-Fe_3O_4 heterodimer nanoparticles. *Journal of nanoscience and nanotechnology 12*, 6961–6967.

(*42*) Yu, H., Chen, M., Rice, P. M., Wang, S. X., White, R., and Sun, S. (2005). Dumbbell-like bifunctional Au-Fe_3O_4 nanoparticles. *Nano letters 5*, 379–382.

(*43*) Li, Y., Yang, S., Lu, X., Duan, W., and Moriga, T. (2019). Synthesis and evaluation of the SERS effect of Fe_3O_4–Ag Janus composite materials for separable, highly sensitive substrates. *RSC advances 9*, 2877–2884.

(*44*) Moscoso-Londono, O., Muraca, D., Tancredi, P., Cosio-Castaneda, C., Pirota, K. R., and Socolovsky, L. M. (2014). Physicochemical studies of complex silver–magnetite nanoheterodimers with controlled morphology. *The Journal of Physical Chemistry C 118*, 13168–13176.

(*45*) Sun, Y. (2015). Interfaced heterogeneous nanodimers. *National Science Review 2*, 329–348.

(*46*) Biswas, A., Bayer, I. S., Biris, A. S., Wang, T., Dervishi, E., and Faupel, F. (2012). Advances in top–down and bottom–up surface nanofabrication: Techniques, applications & future prospects. *Advances in colloid and interface science 170*, 2–27.

(*47*) Zhang, L., Dou, Y.-H., and Gu, H.-C. (2006). Sterically induced shape control of magnetite nanoparticles. *Journal of crystal growth 296*, 221–226.

(*48*) Xie, W., Guo, Z., Gao, F., Gao, Q., Wang, D., Liaw, B.-s., Cai, Q., Sun, X., Wang, X., and Zhao, L. (2018). Shape-, size-and structure-controlled synthesis and biocompatibility of iron oxide nanoparticles for magnetic theranostics. *Theranostics 8*, 3284.

(*49*) Jindal, A. B. (2017). The effect of particle shape on cellular interaction and drug delivery applications of micro-and nanoparticles. *International journal of pharmaceutics 532*, 450–465.

(*50*) Truong, N. P., Whittaker, M. R., Mak, C. W., and Davis, T. P. (2015). The importance of nanoparticle shape in cancer drug delivery. *Expert opinion on drug delivery 12*, 129–142.

(*51*) Feng, Q., Liu, Y., Huang, J., Chen, K., Huang, J., and Xiao, K. (2018). Uptake, distribution, clearance, and toxicity of iron oxide nanoparticles with different sizes and coatings. *Scientific reports 8*, 1–13.

(*52*) Chouly, C., Pouliquen, D., Lucet, I., Jeune, J., and Jallet, P. (1996). Development of superparamagnetic nanoparticles for MRI: effect of particle size, charge and surface nature on biodistribution. *Journal of microencapsulation 13*, 245–255.

(*53*) Gupta, A. K., and Wells, S. (2004). Surface-modified superparamagnetic nanoparticles for drug delivery: preparation, characterization, and cytotoxicity studies. *IEEE transactions on nanobioscience 3*, 66–73.

(*54*) Mullin, J. W., *Crystallization*; Elsevier: 2001.

(*55*) LaMer, V. K., and Dinegar, R. H. (1950). Theory, production and mechanism of formation of monodispersed hydrosols. *Journal of the american chemical society 72*, 4847–4854.

(*56*) Young, S. (1911). Mechanical Stimulus to Crystallization on Super-Cooled Liquids. *Journal of the American Chemical Society 33*, 148–162.

(*57*) Earl (1912). XX. Solubility and supersolubility from the osmotic standpoint. *The London, Edinburgh, and Dublin Philosophical Magazine and Journal of Science 24*, 254–268.

(*58*) Polte, J. (2015). Fundamental growth principles of colloidal metal nanoparticles–a new perspective. *CrystEngComm 17*, 6809–6830.

(*59*) Bandyopadhyay, S., *Fabrication and Application of Nanomaterials*; McGraw-Hill Education: 2019.

(*60*) Nielsen, A. E. (1984). Electrolyte crystal growth mechanisms. *Journal of Crystal Growth 67*, 289–310.

(*61*) Ter Horst, J. H., Schmidt, C., and Ulrich, J. In *Handbook of Crystal Growth*; Elsevier: 2015, pp 1317–1349.

(*62*) Bahrig, L., Hickey, S. G., and Eychmüller, A. (2014). Mesocrystalline materials and the involvement of oriented attachment–a review. *CrystEngComm 16*, 9408–9424.

(*63*) Schüth, F. (2001). Nucleation and crystallization of solids from solution. *Current Opinion in Solid State and Materials Science 5*, 389–395.

(*64*) Kalikmanov, V. I. In *Nucleation theory*; Springer: 2013, pp 17–41.

(*65*) You, H., and Fang, J. (2016). Particle-mediated nucleation and growth of solution-synthesized metal nanocrystals: A new story beyond the LaMer curve. *Nano Today 11*, 145–167.

(*66*) Erdemir, D., Lee, A. Y., and Myerson, A. S. (2009). Nucleation of crystals from solution: classical and two-step models. *Accounts of chemical research 42*, 621–629.

(*67*) Mahmoudi, M., Sant, S., Wang, B., Laurent, S., and Sen, T. (2011). Superparamagnetic iron oxide nanoparticles (SPIONs): development, surface modification and applications in chemotherapy. *Advanced drug delivery reviews 63*, 24–46.

(*68*) Laurent, S., Forge, D., Port, M., Roch, A., Robic, C., Vander Elst, L., and Muller, R. N. (2008). Magnetic iron oxide nanoparticles: synthesis, stabilization, vectorization, physicochemical characterizations, and biological applications. *Chemical reviews 108*, 2064–2110.

(*69*) Pathakoti, K., Manubolu, M., and Hwang, H.-M. In *Handbook of nanomaterials for industrial applications*; Elsevier: NJ, USA, 2018, pp 894–907.

(*70*) Avasthi, A., Caro, C., Pozo-Torres, E., Leal, M. P., and García-Martín, M. L. (2020). Magnetic nanoparticles as MRI contrast agents. *Surface-modified Nanobiomaterials for Electrochemical and Biomedicine Applications*, 49–91.

(*71*) Besenhard, M. O., LaGrow, A. P., Hodzic, A., Kriechbaum, M., Panariello, L., Bais, G., Loizou, K., Damilos, S., Cruz, M. M., Thanh, N. T. K., et al. (2020). Co-precipitation synthesis of stable iron oxide nanoparticles with NaOH: New insights and continuous production via flow chemistry. *Chemical Engineering Journal 399*, 125740.

(*72*) LaGrow, A. P., Besenhard, M. O., Hodzic, A., Sergides, A., Bogart, L. K., Gavriilidis, A., and Thanh, N. T. K. (2019). Unravelling the growth mechanism of the co-precipitation of iron oxide nanoparticles with the aid of synchrotron X-Ray diffraction in solution. *Nanoscale 11*, 6620–6628.

(*73*) Blanco-Andujar, C., Ortega, D., Pankhurst, Q. A., and Thanh, N. T. K. (2012). Elucidating the morphological and structural evolution of iron oxide nanoparticles formed by sodium carbonate in aqueous medium. *Journal of Materials Chemistry 22*, 12498–12506.

(*74*) Ahn, T., Kim, J. H., Yang, H.-M., Lee, J. W., and Kim, J.-D. (2012). Formation pathways of magnetite nanoparticles by coprecipitation method. *The journal of physical chemistry C 116*, 6069–6076.

(*75*) Sun, J., Zhou, S., Hou, P., Yang, Y., Weng, J., Li, X., and Li, M. (2007). Synthesis and characterization of biocompatible Fe_3O_4 nanoparticles. *Journal of biomedical materials research Part A 80*, 333–341.

(*76*) Aslam, M., Schultz, E. A., Sun, T., Meade, T., and Dravid, V. P. (2007). Synthesis of amine-stabilized aqueous colloidal iron oxide nanoparticles. *Crystal growth & design 7*, 471–475.

(*77*) Lu, W., Shen, Y., Xie, A., and Zhang, W. (2010). Green synthesis and characterization of superparamagnetic Fe_3O_4 nanoparticles. *Journal of Magnetism and Magnetic Materials 322*, 1828–1833.

(*78*) Lyon, J. L., Fleming, D. A., Stone, M. B., Schiffer, P., and Williams, M. E. (2004). Synthesis of Fe oxide core/Au shell nanoparticles by iterative hydroxylamine seeding. *Nano Letters 4*, 719–723.

(*79*) Sun, S., and Zeng, H. (2002). Size-controlled synthesis of magnetite nanoparticles. *Journal of the American Chemical Society 124*, 8204–8205.

(*80*) Baaziz, W., Pichon, B. P., Fleutot, S., Liu, Y., Lefevre, C., Greneche, J.-M., Toumi, M., Mhiri, T., and Begin-Colin, S. (2014). Magnetic iron oxide nanoparticles: reproducible tuning of the size and nanosized-dependent composition, defects, and spin canting. *The Journal of Physical Chemistry C 118*, 3795–3810.

(*81*) Park, J., An, K., Hwang, Y., Park, J.-G., Noh, H.-J., Kim, J.-Y., Park, J.-H., Hwang, N.-M., and Hyeon, T. (2004). Ultra-large-scale syntheses of monodisperse nanocrystals. *Nature materials 3*, 891–895.

(*82*) Hyeon, T., Lee, S. S., Park, J., Chung, Y., and Na, H. B. (2001). Synthesis of highly crystalline and monodisperse maghemite nanocrystallites without a size-selection process. *Journal of the American Chemical Society 123*, 12798–12801.

(*83*) Sharma, A. N., Luo, D., and Walter, M. T. (2012). Hydrological tracers using nanobiotechnology: proof of concept. *Environmental science & technology 46*, 8928–8936.

(*84*) Zhao, S., Yu, X., Qian, Y., Chen, W., and Shen, J. (2020). Multifunctional magnetic iron oxide nanoparticles: an advanced platform for cancer theranostics. *Theranostics 10*, 6278.

(*85*) Wu, W., He, Q., and Jiang, C. (2008). Magnetic iron oxide nanoparticles: synthesis and surface functionalization strategies. *Nanoscale research letters 3*, 397–415.

(*86*) Wallyn, J., Anton, N., and Vandamme, T. F. (2019). Synthesis, principles, and properties of magnetite nanoparticles for in vivo imaging applications—A review. *Pharmaceutics 11*, 601.

(*87*) Fu, C., Zhou, H., Wang, Y., Liu, D., Li, J., Deng, H., Qi, X., Chen, T., Zhang, L.-M., and Li, G. (2017). One-pot synthesis of dextran-coated iron oxide nanoclusters for real-time regional lymph node mapping. *International journal of nanomedicine 12*, 3365.

(*88*) Kim, E. H., Ahn, Y., and Lee, H. S. (2007). Biomedical applications of superparamagnetic iron oxide nanoparticles encapsulated within chitosan. *Journal of Alloys and Compounds 434*, 633–636.

(*89*) Gogoi, P., Thakur, A. J., Devi, R. R., Das, B., and Maji, T. K. (2017). Adsorption of As(V) from contaminated water over chitosan coated magnetite nanoparticle: equilibrium and kinetics study. *Environmental nanotechnology, monitoring & management 8*, 297–305.

(*90*) Jurkin, T., Gotić, M., Štefanić, G., and Pucić, I. (2016). Gamma-irradiation synthesis of iron oxide nanoparticles in the presence of PEO, PVP or CTAB. *Radiation Physics and Chemistry 124*, 75–83.

(*91*) Qu, J., Liu, G., Wang, Y., and Hong, R. (2010). Preparation of Fe_3O_4–chitosan nanoparticles used for hyperthermia. *Advanced Powder Technology 21*, 461–467.

(*92*) Khoshnevisan, K., Barkhi, M., Zare, D., Davoodi, D., and Tabatabaei, M. (2012). Preparation and characterization of CTAB-Coated Fe_3O_4 nanoparticles. *Synthesis and Reactivity in Inorganic, Metal-Organic, and Nano-Metal Chemistry 42*, 644–648.

(*93*) Cheraghipour, E., Javadpour, S., and Mehdizadeh, A. R. (2012). Citrate capped superparamagnetic iron oxide nanoparticles used for hyperthermia therapy.

(*94*) Metin, C. O., Lake, L. W., Miranda, C. R., and Nguyen, Q. P. (2011). Stability of aqueous silica nanoparticle dispersions. *Journal of Nanoparticle Research 13*, 839–850.

(*95*) Puddu, M., Paunescu, D., Stark, W. J., and Grass, R. N. (2014). Magnetically recoverable, thermostable, hydrophobic DNA/silica encapsulates and their application as invisible oil tags. *ACS nano 8*, 2677–2685.

(*96*) Li, X., Zhang, J., and Gu, H. (2011). Adsorption and desorption behaviors of DNA with magnetic mesoporous silica nanoparticles. *Langmuir 27*, 6099–6106.

(*97*) Kang, K., Choi, J., Nam, J. H., Lee, S. C., Kim, K. J., Lee, S.-W., and Chang, J. H. (2009). Preparation and characterization of chemically functionalized silica-coated magnetic nanoparticles as a DNA separator. *The Journal of Physical Chemistry B 113*, 536–543.

(*98*) Khan, L. U., da Silva, G. H., de Medeiros, A. M., Khan, Z. U., Gidlund, M., Brito, H. F., Moscoso-Londono, O., Muraca, D., Knobel, M., Perez, C. A., et al. (2019). Fe_3O_4@SiO_2 nanoparticles concurrently coated with chitosan and GdOF: Ce^{3+}, Tb^{3+} luminophore for bioimaging: toxicity evaluation in the zebrafish model. *ACS Applied Nano Materials 2*, 3414–3425.

(*99*) Sharma, A., Foppen, J. W., Banerjee, A., Sawssen, S., Bachhar, N., Peddis, D., and Bandyopadhyay, S. (2021). Magnetic Nanoparticles to Unique DNA Tracers: Effect of Functionalization on Physico-chemical Properties. *Nanoscale research letters 16*, 1–16.

(*100*) Guardia, P., Pérez, N., Labarta, A., and Batlle, X. (2010). Controlled synthesis of iron oxide nanoparticles over a wide size range. *Langmuir 26*, 5843–5847.

(*101*) Peeters, K., Lespes, G., Zuliani, T., Ščančar, J., and Milačič, R. (2016). The fate of iron nanoparticles in environmental waters treated with nanoscale zero-valent iron, FeO NPs and Fe_3O_4 NPs. *Water research 94*, 315–327.

(*102*) Kim, J., Kim, H. S., Lee, N., Kim, T., Kim, H., Yu, T., Song, I. C., Moon, W. K., and Hyeon, T. (2008). Multifunctional uniform nanoparticles composed of a magnetite nanocrystal core and a mesoporous silica shell for magnetic resonance and fluorescence imaging and for drug delivery. *Angewandte Chemie 120*, 8566–8569.

(*103*) Bandyopadhyay, S., Andersen, M. K., Alvi, M. A. A., Sharma, A., Raju, R., McDonagh, B. H., and Glomm, W. R. (2016). Incorporation of Fe@Au nanoparticles into multiresponsive pNIPAM-AAc colloidal gels modulates drug uptake and release. *Colloid and Polymer Science 294*, 1929–1942.

(*104*) Hsiao, M.-H., Mu, Q., Stephen, Z. R., Fang, C., and Zhang, M. (2015). Hexanoyl-chitosan-PEG copolymer coated iron oxide nanoparticles for hydrophobic drug delivery. *ACS macro letters 4*, 403–407.

(*105*) Yang, H., Hasegawa, D., Takahashi, M., and Ogawa, T. (2008). Facile synthesis, phase transfer, and magnetic properties of monodisperse magnetite nanocubes. *IEEE transactions on magnetics 44*, 3895–3898.

(*106*) Kabanov, A. V., and Vinogradov, S. V. (2009). Nanogels as pharmaceutical carriers: finite networks of infinite capabilities. *Angewandte Chemie International Edition 48*, 5418–5429.

(*107*) Stuart, M. A. C., Huck, W. T., Genzer, J., Müller, M., Ober, C., Stamm, M., Sukhorukov, G. B., Szleifer, I., Tsukruk, V. V., Urban, M., et al. (2010). Emerging applications of stimuli-responsive polymer materials. *Nature materials 9*, 101–113.

(*108*) Hoffman, A. S. (2013). Stimuli-responsive polymers: Biomedical applications and challenges for clinical translation. *Advanced drug delivery reviews 65*, 10–16.

(*109*) Elsabahy, M., and Wooley, K. L. (2012). Design of polymeric nanoparticles for biomedical delivery applications. *Chemical Society Reviews 41*, 2545–2561.

(*110*) Mura, S., Nicolas, J., and Couvreur, P. (2013). Stimuli-responsive nanocarriers for drug delivery. *Nature materials 12*, 991–1003.

(*111*) Oh, J. K., Drumright, R., Siegwart, D. J., and Matyjaszewski, K. (2008). The development of microgels/nanogels for drug delivery applications. *Progress in Polymer Science 33*, 448–477.

(*112*) Zhang, Q., Weber, C., Schubert, U. S., and Hoogenboom, R. (2017). Thermoresponsive polymers with lower critical solution temperature: from fundamental aspects and measuring techniques to recommended turbidimetry conditions. *Materials Horizons 4*, 109–116.

(*113*) De las Heras Alarcón, C., Pennadam, S., and Alexander, C. (2005). Stimuli responsive polymers for biomedical applications. *Chemical Society Reviews 34*, 276–285.

(*114*) Kelley, E. G., Albert, J. N., Sullivan, M. O., and Epps III, T. H. (2013). Stimuli-responsive copolymer solution and surface assemblies for biomedical applications. *Chemical Society Reviews 42*, 7057–7071.

(*115*) Aseyev, V., Tenhu, H., and Winnik, F. (2011). Self organized nanostructures of amphiphilic block copolymers II. *Adv. Polym. Sci 242*, 29–89.

(*116*) Cole, M. A., Voelcker, N. H., Thissen, H., and Griesser, H. J. (2009). Stimuli-responsive interfaces and systems for the control of protein–surface and cell–surface interactions. *Biomaterials 30*, 1827–1850.

(*117*) Das, E., and Matsumura, K. (2017). Tunable phase-separation behavior of thermoresponsive polyampholytes through molecular design. *Journal of Polymer Science Part A: Polymer Chemistry 55*, 876–884.

(*118*) Abdilla, A., Shi, S., Burke, N. A., and Stöver, H. D. (2016). Multistimuli responsive ternary polyampholytes: Formation and crosslinking of coacervates. *Journal of Polymer Science Part A: Polymer Chemistry 54*, 2109–2118.

(*119*) Rajan, R., and Matsumura, K. (2017). Tunable Dual-Thermoresponsive Core–Shell Nanogels Exhibiting UCST and LCST Behavior. *Macromolecular rapid communications 38*, 1700478.

(*120*) Halperin, A., Kröger, M., and Winnik, F. M. (2015). Poly (N-isopropylacrylamide) phase diagrams: fifty years of research. *Angewandte Chemie International Edition 54*, 15342–15367.

(*121*) Heskins, M., and Guillet, J. E. (1968). Solution properties of poly (N-isopropylacrylamide). *Journal of Macromolecular Science—Chemistry 2*, 1441–1455.

(*122*) Vikulina, A. S., Aleed, S. T., Paulraj, T., Vladimirov, Y. A., Duschl, C., Von Klitzing, R., and Volodkin, D. (2015). Temperature-induced molecular transport through polymer multilayers coated with PNIPAM microgels. *Physical Chemistry Chemical Physics 17*, 12771–12777.

(*123*) Trongsatitkul, T., and Budhlall, B. M. (2013). Temperature dependence of serum protein adsorption in PEGylated PNIPAm microgels. *Colloids and Surfaces B: Biointerfaces 103*, 244–252.

(*124*) Chen, J., Wu, L., Zhang, J., Zhang, L., Gong, D., Zhao, Y., Chen, Q., Huang, S., Yang, M., Yang, X., et al. (2020). Deep learning-based model for detecting 2019 novel coronavirus pneumonia on high-resolution computed tomography. *Scientific reports 10*, 1–11.

(*125*) Raju, R., Bandyopadhyay, S., Sharma, A., Gonzalez, S. V., Carlsen, P. H., Gautun, O. R., and Glomm, W. R. (2018). Synthesis, characterization and drug loading of multiresponsive p [NIPAm-co-PEGMA](core)/p [NIPAm-co-AAc](Shell) Nanogels with Monodisperse Size Distributions. *Polymers 10*, 309.

(*126*) Cuggino, J. C., Blanco, E. R. O., Gugliotta, L. M., Igarzabal, C. I. A., and Calderón, M. (2019). Crossing biological barriers with nanogels to improve drug delivery performance. *Journal of Controlled Release 307*, 221–246.

(*127*) Cheng, X., Zeng, X., Li, D., Wang, X., Sun, M., He, L., and Tang, R. (2019). TPGS-grafted and acid-responsive soy protein nanogels for efficient intracellular drug release, accumulation, penetration in 3D tumor spheroids of drug-resistant cancer cells. *Materials science and engineering: c 102*, 863–875.

(*128*) Zhou, D., Liu, S., Hu, Y., Yang, S., Zhao, B., Zheng, K., Zhang, Y., He, P., Mo, G., and Li, Y. (2020). Tumor-mediated shape-transformable nanogels with pH/redox/enzymatic-sensitivity for anticancer therapy. *Journal of Materials Chemistry B 8*, 3801–3813.

(*129*) Li, Q., Liang, J., You, X., Liu, X., Wu, H., Gao, W., Wen, Y., Wu, J., Xu, X., and Zhang, F. (2017). A novel reactive oxygen species triggered polymeric nanoplatform for controlled drug delivery and cancer therapy. *Journal of Biomedical Nanotechnology 13*, 513–521.

(*130*) Cheng, R., Meng, F., Deng, C., Klok, H.-A., and Zhong, Z. (2013). Dual and multi-stimuli responsive polymeric nanoparticles for programmed site-specific drug delivery. *Biomaterials 34*, 3647–3657.

(*131*) Kato, Y., Ozawa, S., Miyamoto, C., Maehata, Y., Suzuki, A., Maeda, T., and Baba, Y. (2013). Acidic extracellular microenvironment and cancer. *Cancer cell international 13*, 1–8.

(*132*) Boedtkjer, E., and Pedersen, S. F. (2020). The acidic tumor microenvironment as a driver of cancer. *Annual review of physiology 82*, 103–126.

(*133*) Mo, R., and Gu, Z. (2016). Tumor microenvironment and intracellular signal-activated nanomaterials for anticancer drug delivery. *Materials Today 19*, 274–283.

(*134*) Li, Z., Huang, J., and Wu, J. (2021). pH-Sensitive nanogels for drug delivery in cancer therapy. *Biomaterials Science 9*, 574–589.

(*135*) Raza, F., Zhu, Y., Chen, L., You, X., Zhang, J., Khan, A., Khan, M. W., Hasnat, M., Zafar, H., Wu, J., et al. (2019). Paclitaxel-loaded pH responsive hydrogel based on self-assembled peptides for tumor targeting. *Biomaterials science 7*, 2023–2036.

(*136*) Wang, Z., Deng, X., Ding, J., Zhou, W., Zheng, X., and Tang, G. (2018). Mechanisms of drug release in pH-sensitive micelles for tumour targeted drug delivery system: A review. *International journal of pharmaceutics 535*, 253–260.

(*137*) Xu, X., Wu, J., Liu, Y., Yu, M., Zhao, L., Zhu, X., Bhasin, S., Li, Q., Ha, E., Shi, J., et al. (2016). Ultra-pH-responsive and tumor-penetrating nanoplatform for targeted siRNA delivery with robust anti-cancer efficacy. *Angewandte Chemie International Edition 55*, 7091–7094.

(*138*) Zhang, X., Li, D., Huang, J., Ou, K., Yan, B., Shi, F., Zhang, J., Zhang, J., Pang, J., Kang, Y., et al. (2019). Screening of pH-responsive long-circulating polysaccharide–drug conjugate nanocarriers for antitumor applications. *Journal of Materials Chemistry B 7*, 251–264.

(*139*) Sharma, A., Raghunathan, K., Solhaug, H., Antony, J., Stenvik, J., Nilsen, A. M., Einarsrud, M.-A., and Bandyopadhyay, S. (2021). Modulating Acrylic Acid Content of Nanogels for Drug Delivery Biocompatibility Studies. *Journal of Colloid and Interface Science*.

(*140*) Das, D., Rameshbabu, A. P., Ghosh, P., Patra, P., Dhara, S., and Pal, S. (2017). Biocompatible nanogel derived from functionalized dextrin for targeted delivery of doxorubicin hydrochloride to MG 63 cancer cells. *Carbohydrate polymers 171*, 27–38.

"To improve is to change; to be perfect is to change often."

– Winston Churchill

"Everything should be made as simple as possible, but not simpler."

– Albert Einstein

4 Methodology

This chapter includes the experimental details for the synthesis, functionalisation and characterisation of the inorganic and polymeric NPs. The first part deals with the synthesis of magnetic IONPs, magneto-plasmonic dimeric NPs (DNPs) and stimuli-responsive NGs. IONPs were synthesised using co-precipitation and thermal decomposition routes, that were further used as seeds for growing Ag on the surface of IONP, yielding DNPs. Stimuli-responsive NGs were synthesised via free radical precipitation polymerisation by varying different reaction parameters such as surfactant concentration, reaction atmosphere and monomer–co-monomer mole ratios. The second part deals with the functionalisation of the above synthesised NPs. The IONPs were functionalised using various ligands to, either, make the particles hydrophilic, or modify their surface charge. The NGs were loaded with Cyt C, to further study its release from the NG matrix. The third part describes the experimental details for the characterisation of the NPs.

4.1 Synthesis of Iron-oxide NPs

4.1.1 Co-precipitation

The synthesis process has been adapted from previously reported studies and involves weighing 84.6 mg of MilliQ water (Simplicity® Millipore water purification system–Darmstadt, Germany) in a beaker and adding 15.4 mL of 25 wt% ammonia solution ($NH_4(aq)$) solution (Merck Life Sciences AS) to prepare a 1 M solution.[1] Separately, 8.0 g of iron(II)chloride tetrahydrate ($FeCl_2.4H_2O$, $\geq$99 %) and 21.6 g of iron(III)chloride hexahydrate ($FeCl_3.6H_2O$, $\geq$99 %, Acros Organics®–Geel, Belgium) were weighed and dissolved in 100 mL MilliQ water in a volumetric flask. 10 mL of this solution was added to 100 mL of 1 M ammonia solution dropwise using a burette and the reaction being kept under vigorous stirring. The NPs were obtained using magnetic separation by several washing cycles with water. These particles have been referred to as *'Mag'* in this thesis and a schematic of the experimental setup is shown in Figure 4.1.

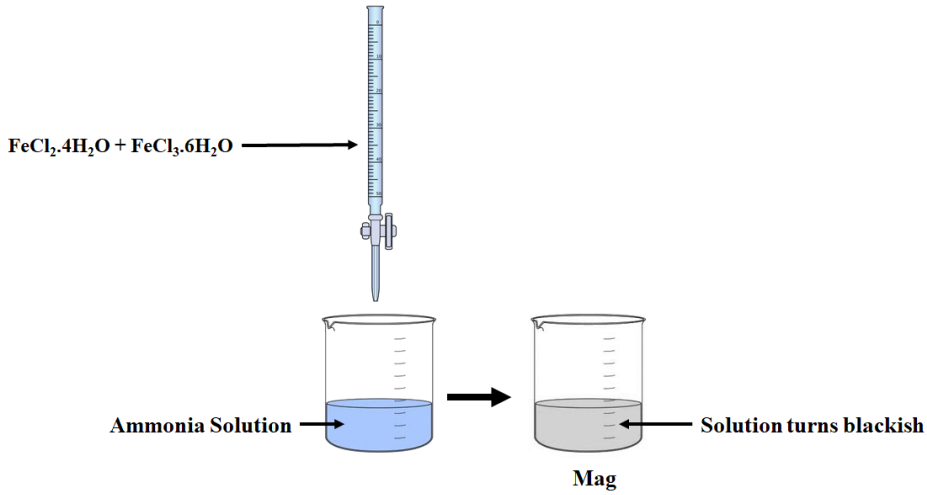

Figure 4.1: Schematic showing the co-precipitation synthesis route for iron-oxide NPs.

4.1.2 Thermal Decomposition

Spherical (SNPs) and cubic (CNPs) IONPs were synthesised using thermal decomposition of iron-oleate precursor at elevated temperatures in inert (argon) atmosphere. The temperature of the reaction was raised using a temperature controller (MRC® Heating mantle 100 mL with analog control and Digital 4 programs × 16 segment programmer) for precise control of the heating rate.

4.1.2.1 Iron Oleate Preparation

The iron-oleate complex was prepared using our previously reported protocol.[2] In essence, 5.40 g of $FeCl_3{\cdot}6H_2O$ and 18.25 g of sodium oleate (Na-oleate, >97 %, Tokyo Chemical Industry, Japan) were dissolved in a mixture of solvents consisting of ethanol (40 mL), deionized water (30 mL) and hexane (70 mL), in 250 mL round bottom flask. The resulting solution was refluxed at 70 °C for 4 h under vigorous stirring using a bar magnet. The resulting dark red organic phase, containing iron oleate complex, was transferred to a separator funnel and washed three times with MilliQ water. The remaining hexane solution was evaporated in a Heidolph rotary evaporator (T = 70 °C) to yield a highly viscous dark red liquid of iron oleate, as shown in Figure 5.2 b.

4.1.2.2 Spherical IONPs

The growth of IONPs is governed by the decomposition of iron-oleate precursor at high temperatures, which in turn influences the choice of a high boiling point solvent, octadecene (ODE, technical grade 90 %, Sigma-Aldrich®–Schnelldorf, Germany). The synthesis protocol, adapted and modified from previous works conducted by our group, utilizes oleic acid (OA, technical grade 90 %, Sigma-Aldrich®–Schnelldorf, Germany) as the reducing and stabilizing agent[2] A typical synthesis process involved mixing iron-oleate (1.6

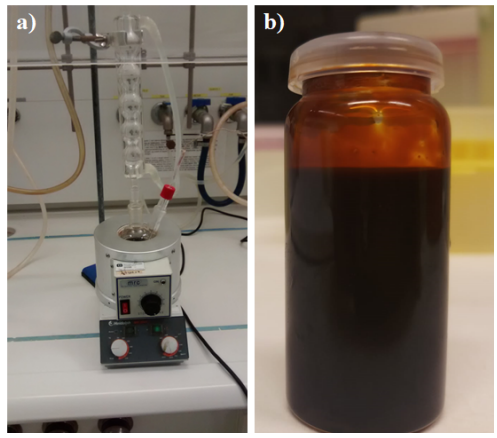

Figure 4.2: **a)** Setup for the synthesis of iron-oleate and IONPs. Image of **b)** dark red iron-oleate precursor.

g), OA (600 µL) and ODE (25 mL) in a three-necked glass reactor, placed over a heating mantle fitted with a cooling water condenser. The reaction was carried out under argon atmosphere. The temperature of the reactor was ramped from room temperature to 320 °C at 3 °C/min. The reaction was maintained at 320 °C for 45 min after which the solution was cooled to room temperature. The NPs were then washed using hexane and precipitated out using a mixture of isopropanol and hexane. The particles were magnetically separated and washed three times using acetone before finally redispersing in toluene (10 mL). A schematic of the synthesis process is shown in Figure 4.3.

4.1.2.3 Cubic IONPs

Adapted and modified from previous work, in a typical synthesis, iron-oleate (0.833 g), Na-oleate (213 mg) and ODE (14 mL), were heated in a three-necked glass reactor placed on a heating mantle, fitted with a cooling water condenser, to 325 °C at 2.8 °C/min under argon atmosphere, as shown in Figure 4.3.[3] The reaction was maintained at 325 °C for 45 min after which the NPs were cooled to room temperature. NPs were then washed using hexane and precipitated out using a mixture of isopropanol and hexane. The particles were magnetically separated and washed three times using acetone before finally redispersed in toluene (10 mL).

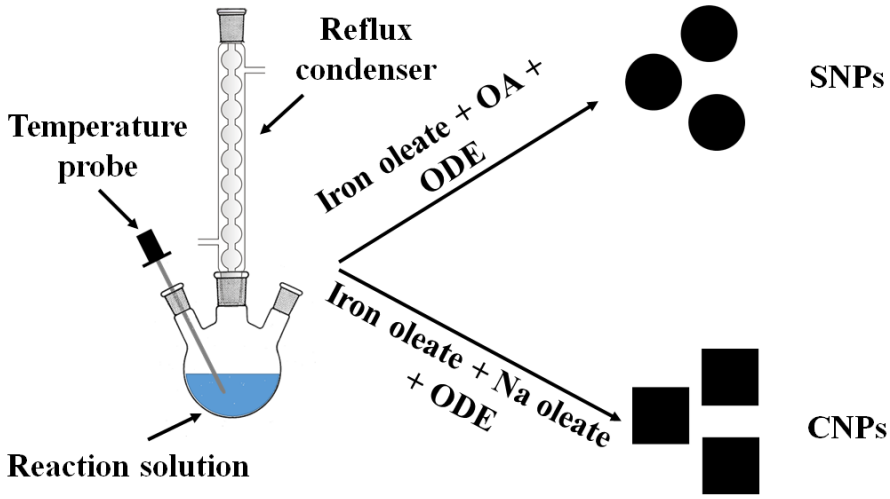

Figure 4.3: Schematic representing the synthesis route of IONPs via thermal decomposition.

4.2 Synthesis of Dimeric NPs

Both, SNPs and CNPs, were used as seeds for the growth of Ag on the surface of IONPs. DNPs, synthesised using SNPs and CNPs, are referred to as *'Ag@SNP'* and *'Ag@CNP'*, respectively. The seed-mediated synthesis of DNPs used was modified from the procedure reported by Zhang *et al.*[4] using oleylamine (99 %, Sigma-Aldrich®–Schnelldorf, Germany) as the stabilizing agent and silver acetate (AgAc, ≥99:0 %, Sigma-Aldrich®–Schnelldorf, Germany) as the reducing agent. In a typical synthesis, IONPs (10 mg), oleylamine (354 µL), toluene (10 mL) and silver acetate were mixed in a round bottom flask. The amount of AgAc was varied as shown in Table 4.1. The mixture was heated to 72 °C under inert (argon) atmosphere and the reaction was carried out overnight. The product was allowed to cool to room temperature before adding methanol in order to precipitate the particles. The particles were washed with acetone before finally redispersing them in toluene (10 mL).

Table 4.1: Varying amount of silver acetate for the synthesis of DNPs.

Seed	IONP (mg)	AgAc (mg)
SNP	10	7.7
SNP	10	11.2
SNP	10	15.7
CNP	10	11.2

4.3 Stimuli-Responsive Nanogels

PNIPAm-pAAc-based nanogels NGs were synthesised using free radical precipitation polymerisation. pNIPAm provides a temperature-based response, whereas, pAAc imparts pH responsiveness to the NGs.

4.3.1 Recrystallisation of NIPAm

To remove impurities that could inhibit the polymerisation reaction, N-isopropylacrylamide (NIPAm, Sigma-Aldrich®–Schnelldorf, Germany) was recrystallised using a previously reported protocol by our group.[5] In a typical process, 5 g of NIPAm was dissolved in 50 mL of n-hexane in a one-necked round bottom flask maintained at 110 °C using an oil bath. The reaction was allowed to proceed for 2 h following which, the reactor was put over an ice bath for 30 min, to allow recrystallisation of NIPAm. The solution was then filtered using a φ-90 mm filter paper and kept for overnight drying. After drying, the recrystallized NIPAm was stored at -20 °C to prevent absorption of moisture.

4.3.2 Synthesis of Nanogels

The NGs were synthesized using precipitation polymerization as previously reported by our group.[5] The monomers NIPAm and acrylic acid (AAc, Sigma-Aldrich®–Schnelldorf, Germany) were used to synthesize the NGs using N-N'-methylene-bisacrylamide (BIS, Sigma-Aldrich®–Schnelldorf, Germany) as cross-linker; sodium dodecyl sulphate (SDS, Sigma-Aldrich®–Schnelldorf, Germany) was used as surfactant and the reaction proceeded by adding potassium persulphate (KPS, Sigma-Aldrich®–Schnelldorf, Germany) as an initiator. In a typical reaction, NIPAm (181 mg) and BIS (14.5 mg) were added to a round bottom flask that was maintained at 70 °C. Thereafter, 10 mL of SDS, with different molarities (4.2, 3.5, 2.8 and 2.1 mM), was added to the flask and the reaction mixture was stirred for 1 h to ensure the collapse of all NIPAm monomeric units. After 1 h, AAc (124 mL of 1.46 M) and KPS (400 mL of 103 mM) were added in quick succession and the reaction was allowed to continue for 3 h.

To investigate the effect of reaction environment (atmosphere), three different modes of synthesis were applied namely, a) Continuous-Stirring – maintaining continuous flow of N_2 with stirring using a magnetic bar, b) Flashing-Stirring – N_2 purging during addition of the initiator with stirring using a magnetic bar, and c) Flashing-Impeller – N_2 purging during addition of the initiator with stirring using an impeller. Figure 4.4 represents the schematic of the three synthesis techniques used based on N_2 usage and the method of stirring. All the synthesised NGs were dialysed overnight using a molecular weight cut-off (MWCO) 14 kDa dialysis membrane, to remove any unreacted monomers and residual reactants. The dialysed NGs were further freezedried to remove the solvent and stored at 4°C for further analysis.

Furthermore, to investigate the pH stimuli response of the NGs with increased incorporation of pAAc units in the NG matrix, NGs were synthesised using continuous-stirring method. The mole ratios of the monomer (NIPAm), co-monomer (AAc) and crosslinker (BIS) were varied for the different NG samples, as shown in Table 4.2.

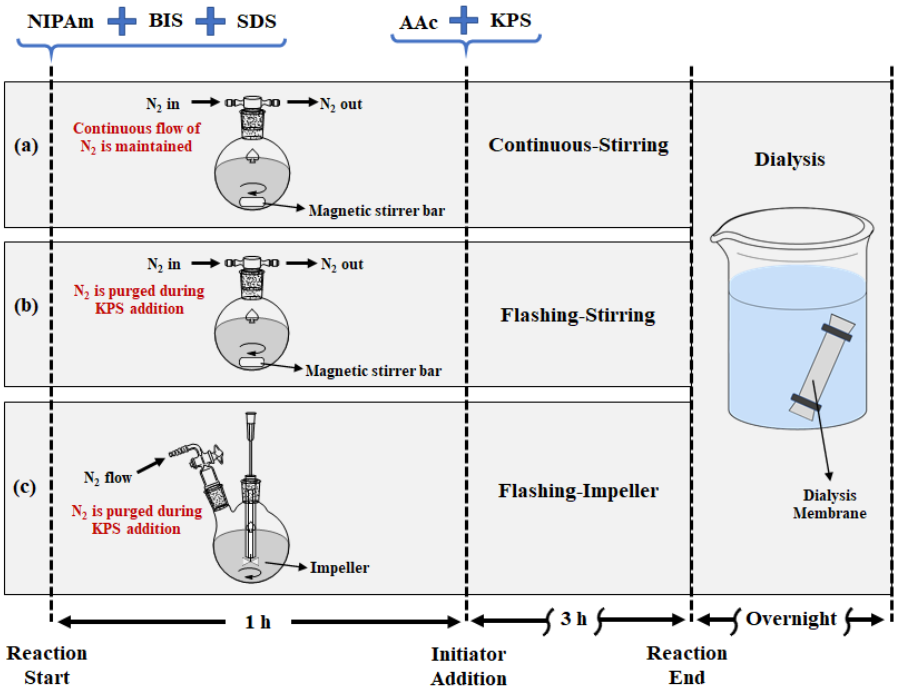

Figure 4.4: Schematic showing the synthesis of nanogels via **a)** Continuous-Stirring, **b)** Flashing-Stirring, and **c)** Flashing-Impeller techniques.

Table 4.2: Varying monomer, co-monomer and crosslinker concentrations to study the effect of incorporation of poly-acrylic acid (in the nanogel matrix) on the pH response of the nanogel

Sample	Mole Ratio NIPAm:AAc:BIS	NIPAm (mg)	AAc (µL)	BIS (mg)
AAc_10	85:10:05	181	129	14.5
AAc_12.5	82.5:12.5:05	181	166	14.9
AAc_15	80:15:05	181	205	15.4
AAc_17.5	78.5:17.5:05	181	247	15.9
AAc_20	75:20:05	181	292	16.4
AAc_22.5	72.5:22.5:05	181	340	17.0
AAc_25	70:25:05	181	391	17.6
AAc_27.5	68.5:27.5:05	181	446	18.3
AAc_30	65:30:05	181	506	19.0

4.4 NP Functionalisation

This section first describes the phase transfer of IONPs, synthesised via the thermal decomposition route, from organic to aqueous medium using different ligands. Following this, the surface charge modification of the IONPs, with trimethoxysilylpropyl-N,N,N-trimethylammonium chloride (TMAPS), is described. The NPs were further functionalised with different DNA and encapsulated in silica to produce DNA-based magnetic hydrological tracers.

4.4.1 Phase Transfer of IONPs

The synthesis and storage of IONPs, obtained via the thermal decomposition route, was done in an organic phase, that is not ideal for biomedical and environmental applications. Therefore, the NPs need to be transferred to the aqueous phase before they can be used for these applications. In order to achieve this, the NPs were functionalised with ligands, such as tetramethylammonium hydroxide solution (TMAH), cetyltrimethylammonium bromide (CTAB) and sodium citrate dihydrate (Na-citrate).

4.4.1.1 CTAB Functionalisation

CTAB was used to transfer the IONPs from toluene to water following a modified procedure previously reported by Kim *et al.*[6] In a typical process, 10 mL of the IONP solution was added to a glass vial and precipitated out by the addition of 40 mL methanol. A disc magnet was kept on the side of the vial causing the particles to separate from the solution. The supernatant was discarded and the particles were washed three times with acetone, to ensure removal of any residual solvent, and left to dry. Separately, 1 g of CTAB and 20 mL of MilliQ water was added to a 100 mL single-necked round bottom flask resulting in a milky-white mixture. The solution was stirred vigorously while heated to 40 °C to properly dissolve CTAB, that caused the liquid to turn transparent. 2 mL of chloroform was added to the dry IONPs and redispersed by ultra-sonication. The chloroform solution was then added to the CTAB solution in the round bottom flask and stirred magnetically for 30 min to ensure proper mixing. The mixture was heated to 60 °C and maintained for 10 min under stirring to evaporate the chloroform. The reaction solution was then cooled to room temperature, transferred to a glass vial and the CTAB-capped nanoparticles were separated using a disc magnet. The supernatant was discarded and the particles were washed three times with MilliQ water to remove any excess CTAB. The particles were finally redispersed in 5 mL MilliQ water for further analysis.

4.4.1.2 Na-Citrate Functionalisation

The procedure to functionalise IONPs with Na-citrate was modified from Bandyopadhyay *et al.*[5] 10 and 50 mM of Na-citrate solutions were prepared using 10 mL MilliQ water. 5 and 10 mg SNPs were separately precipitated from toluene using methanol and cleaned three times with acetone. 10 ml Na-citrate solution was added to the precipitated SNPs and the suspension was sonicated for 2 h in a bath sonicator. Afterwards, the NPs were magnetically separated and cleaned thrice with MilliQ water before redispersing them in 10 mL MilliQ water.

4.4.1.3 TMAH Functionalisation

Phase transfer of SNPs and CNPs using TMAH was performed by modifying a previously developed method.[7] Typically, 50 mg of SNPs and 25 mg of CNPs were separately precipitated from toluene using methanol and washed three times with acetone in a glass vial. 2 mL and 1 mL TMAH solution was added to the SNPs and CNPs, respectively, and the vials were placed in a bath sonicator for 10 min. Afterwards, the vials were put on shaking at 300 rpm for 2 h after which the particles were magnetically separated and cleaned three times with water. Finally, the phase transferred IONPs were redispersed in 1 mL MilliQ water in an Eppendorf tube.

4.4.2 Surface Charge Modification

Before the IONPs could be functionalised with DNA, their surface needed to be positively charged.[1] TMAH functionalised SNPs and CNPs, along with Mag, were used for DNA functionalisation. Ligand, TMAPS, was selected to functionalise the IONPs that would result in positively charged particles. In a typical process, a known amount of IONPs (Table 4.3) were taken and cleaned three times with isopropanol before finally dispersing in 1 mL isopropanol in a 1.5 mL Eppendorf tube. A known volume of TMAPS (Table 4.3) was added to the IONP solution and put on overnight shaking. The samples were collected, cleaned three times with isopropanol and redispersed in 1 mL isopropanol.

4.4.3 DNA Functionalisation and Silica Encapsulation

In a process to functionalise IONPs with three different DNA (T21, GM5 and GM6), a known quantity of IONPs, functionalised with TMAPS (Table 4.3), were added to 20 µL of DNA (100 µM) in a 1.5 mL Eppendorf tube. The solution was kept at rest and allowed to react for 4 min. The DNA functionalised NPs were then magnetically separated and cleaned three times with MilliQ water and finally redispersed in 0.5 mL MilliQ water. After successful binding of DNA, 1 µL TMAPS was added to 0.5 mL NP solution followed by 1 µL tetraethyl orthosilicate (TEOS) and the samples were left on shaking for 4 h. 8 µL of TEOS was further added to the solution after 4 h and the shaking was continued for 4 days after which the particles were magnetically separated and cleaned thrice with MilliQ water and redispersed in 0.5 mL MilliQ water.

Table 4.3: The amount of IONPs taken for surface functionalisation with TMAPS and three different DNA (20 µL for all three DNA – T21, GM5 and GM6), respectively.

	TMAPS Binding		**DNA Binding**	
IONPs	IONP Amount (mg)	TMAPS (µL)	IONP Amount (mg)	DNA (100 µM) (µL)
Mag	50	10	0.75	20
SNPs	20	40	0.36	20
CNPs	10	20	0.30	20

4.5 Drug Loading and Release

Cyt C was used to perform loading and release studies from NGs synthesized via continuous-stirring and flashing-stirring methods. Breathing in technique was used to load Cyt C inside the NGs, wherein, a freeze-dried NG sample was suspended in the drug solution.[5,8] Cyt C was absorbed in the NG matrix as the hydrophilic NG swelled in the drug solution. In a typical study, 1.7 mg of freeze-dried NG sample was measured in a glass vial and 2 mL of 0.5 mg/mL Cyt C solution was added. The mixture was kept for shaking at 300 rpm for 2 h following which the sample was dialysed for 24 h in MQ water using a 14 kDa molecular weight cut-off (MWCO) membrane tubing to remove unbound drug from the system. The sample was then re-suspended in 5 mL MilliQ water for release measurements.

The loading efficiency (L.E.) was calculated based on Equation 4.1, by obtaining the UV-Vis absorbance peaks at wavelength of 409 nm.

$$L.E. = \frac{A_{bound}}{A_{total}} \times 100 \tag{4.1}$$

where, A_{bound} and A_{total} represent the UV-Vis absorbance value of Cyt C after dialysis and before dialysis, respectively, measured at wavelength of 409 nm.

The encapsulation efficiency of the NG was calculated using Equation 4.2 as follows:

$$E.E. = \frac{L.E. \times M_{drug}}{M_{NG} \times 100} \tag{4.2}$$

where, M_{drug} and M_{NG} are the masses of Cyt C (µg) and NG (mg) used during loading experiments.

4.6 Characterisation

4.6.1 Transmission Electron Microscopy

High resolution images were recorded using a JEOL 2100 transmission electron microscope (Tokyo, Japan) operating at 200 kV. TEM grids were prepared by placing several drops of the dilute solution on a Formvar carbon-coated copper grid (Electron Microscopy Sciences, Hatfield, Pennsylvania, USA) and wiping immediately with Kimberly-Clark wipes to prevent further aggregation of the particles resulting from solvent evaporation.

4.6.2 Attenuated Total Reflection-Fourier Transform Infrared

The attenuated total reflection-Fourier transform infrared (ATR-FTIR) spectra were recorded using a Vertex 80v vacuum FTIR spectrometer and the spectra, between 600 and 4000 cm^{-1}, were recorded using OPUS software with 50 scans at a resolution of 4 cm^{-1}. The relative spectral absorbances were normalized with respect to the highest absorbance value obtained. For the growth kinetic studies of SNPs, sample aliquots were taken at defined temperatures during the reaction and the samples were analysed without further cleaning. On the other hand, for the phase transferred samples, NPs were cleaned three times using MilliQ water before analysis.

4.6.3 Super Conducting Quantum Interference Device Magnetometry

DC magnetization measurements were performed with a superconducting quantum interference device (SQUID) magnetometer (H_{max} = 5.5 T, T = 5–400 K). The sample, in the form of powder or liquid, was placed in a capsule, in order to prevent any movement of the NPs during the measurements. All the magnetic measurements were normalized by the mass of the magnetic component of the sample. Magnetization measurements were carried out as a function of temperature from 5 to 300 K using ZFC–FC (Zero Field Cooled–Field Cooled) protocols with an applied field of 25 Oe. Room temperature magnetic properties were investigated using a vibrating sample magnetometer (model 10—MicroSense, H_{max} = 20 kOe).

4.6.4 Dynamic Light Scattering and Zeta Potential Measurements

The dynamic light scattering (DLS) analysis for measuring size distribution and zeta potential of the NGs was performed using a Malvern Zetasizer Nano-ZS instrument (Malvern Instruments Ltd., Worcestershire, UK). All the NG solutions were made using MilliQ water and results were averaged over triplicate measurements.

4.6.5 Quantitative Polymerase Chain Reaction Analysis

In order to determine the amount of DNA successfully incorporated in the silica shell, sample volumes in 400 µL MilliQ water were sent to IHE Delft for qPCR analysis and stored cool upon arrival. Prior to qPCR, samples were dispersed, and vortexed three times at 3000 rpm for 30 s and sonicated for 10 s (Hielscher UP200 St Vial Tweeter sonicator). Then, MilliQ water was added to a total volume of 1000 µL. In order to remove free DNA (not covered by silica), 1.25 µL commercial bleach was added, and the mixture was vortexed for 15 s. After 1–2 min, the particles were magnetically separated, washed twice with MilliQ water, and finally resuspended in 1 mL MilliQ water. This stock solution is referred to as D0. From D0, four tenfold dilutions (D1–D4) were prepared and DNA concentrations were determined from the two most dilute samples (D3 and D4). Thereto, 20 µL D3 and D4 were taken out and, in order to dissolve particles and release DNA, 1 µL of fluoride buffer (2.3 g of $(NH_4)HF_2$ and 10 mL ammonia solution (1.9 g of ammonia in 10 mL water), called Buffered Oxide Etch (BOE) was added and allowed to stand for 10 min. From this, 4 µL of D3 or D4 was taken to which 16 µL of prepared PCR mix was added. In the case of DNA tracer T21, the PCR mix composed of 2 µL 10X PCR buffer, 0.8 µL $MgCl_2$ buffer, 1 µL dNTP mix, 1 µL Taq polymerase, 10.65 µL DEPC treated water, 0.125 µL F-primer and R-primer, and 0.3 µL of probe, composed of a FAM fluorophore and a black hole quencher. In case of the other two tracers, again 4 µL of D3 or D4 was taken and 16 µL of PCR mix was added, composed of 15.75 µL Kpap Sybr Fast qPCR Master Mix (2X) Universal (Kapa Biosystem), 0.125 µL of both F-primer and R-primer. Samples were then inserted in a qPCR apparatus (BioRad Mini-Opticon, Santa Clara, USA) and the measurement cycle of T21 was 3 min at 95 °C followed by 40 cycles of a two-step thermal profile (15 s at 95 °C, 60 s at 60 °C. The cycles of the other two tracers was 6 min and 40 s at 95 °C followed by 41 cycles of a three-step thermal profile (14 s at 95 °C, 27 s at 58 °C, 25 s at 72 °C).

4.6.6 Nuclear Magnetic Resonance

^{1}H NMR spectra were recorded in a Bruker Advance Neo 600 MHz instrument (Coventry, UK). All samples were prepared in heavy water (D_2O) keeping the reagent concentrations the same as that in the NG synthesis. 0.8 mL suspension was taken from each sample and the spectra were recorded with 128 scans at 25°C. Chemical shifts (δ) were reported in ppm and the reference peak for D_2O was locked at δ = 4.80.

4.6.7 Vibration Sample Magnetometry

Magnetic measurements of IONPs, phase transferred IONPs and NGs systems were carried out using MicroMag^{TM} 3900 Vibrating Sample Magnetometer (VSM). Magnetization measurements were performed at room temperature with maximum applied magnetic fields of 1 T. The magnetization data obtained, as a function of applied field, was normalized by the mass of the sample used for comparative study.

4.6.8 Ultraviolet Visible Spectrophotometry

Ultraviolet visible spectrophotometry (UV-Vis) was used for studying the loading and release of Cyt C from NG samples using Shimadzu® UV-2401PC Recording Spectrophotometer (Kyoto, Japan). Absorbance at 490 nm was recorded for Cyt C while performing loading and release studies of the drug from the NGs, at different temperature and pH conditions.

Additionally, UV-Vis was also used in conjunction with magnetophoresis setup, provided by SEPMAG® – Biomagnetic Separation System (Barcelona, Spain), to determine particle separation velocities during a period of 24 h, as shown in Figure 4.5. The UV-Vis based separation study was performed at two different wavelengths of 350 and 450 nm, to check for the preciseness of the technique and any ambiguity that might arise in the separation profiles.

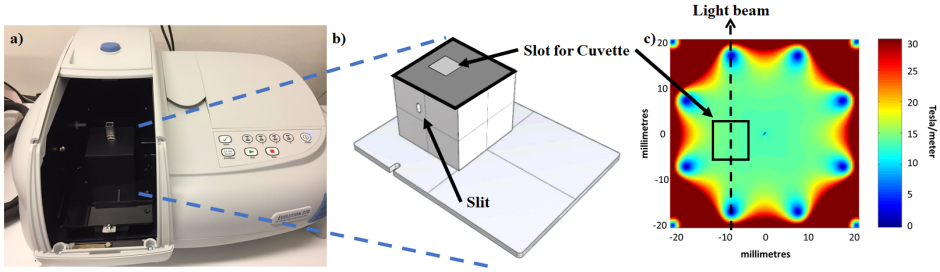

Figure 4.5: SEPMAG® magetophoresis setup in conjunction with UV-Vis **a)** Thermofisher Scientific UV-Vis Spectrophotometer fitted with the SEPMAG® magnetophoresis setup inside. **b)** SEPMAG® magnetophoresis device showing the slot for cuvette, as well as, the slit for the passage of UV beam. **c)** Distribution of magnetic field gradient, generated inside the SEPMAG® device.

References

(*1*) Puddu, M., Paunescu, D., Stark, W. J., and Grass, R. N. (2014). Magnetically recoverable, thermostable, hydrophobic DNA/silica encapsulates and their application as invisible oil tags. *ACS nano 8*, 2677–2685.

(*2*) Momtazi, L., Bagherifam, S., Singh, G., Hofgaard, A., Hakkarainen, M., Glomm, W. R., Roos, N., Mælandsmo, G. M., Griffiths, G., and Nyström, B. (2014). Synthesis, characterization, and cellular uptake of magnetic nanocarriers for cancer drug delivery. *Journal of colloid and interface science 433*, 76–85.

(*3*) Singh, G., Chan, H., Udayabhaskararao, T., Gelman, E., Peddis, D., Baskin, A., Leitus, G., Král, P., and Klajn, R. (2015). Magnetic field-induced self-assembly of iron oxide nanocubes. *Faraday discussions 181*, 403–421.

(*4*) Zhang, L., Dou, Y.-H., and Gu, H.-C. (2006). Synthesis of Ag–Fe_3O_4 heterodimeric nanoparticles. *Journal of colloid and interface science 297*, 660–664.

(*5*) Bandyopadhyay, S., Andersen, M. K., Alvi, M. A. A., Sharma, A., Raju, R., McDonagh, B. H., and Glomm, W. R. (2016). Incorporation of Fe@Au nanoparticles into multiresponsive pNIPAM-AAc colloidal gels modulates drug uptake and release. *Colloid and Polymer Science 294*, 1929–1942.

(*6*) Kim, J., Kim, H. S., Lee, N., Kim, T., Kim, H., Yu, T., Song, I. C., Moon, W. K., and Hyeon, T. (2008). Multifunctional uniform nanoparticles composed of a magnetite nanocrystal core and a mesoporous silica shell for magnetic resonance and fluorescence imaging and for drug delivery. *Angewandte Chemie 120*, 8566–8569.

(*7*) Peeters, K., Lespes, G., Zuliani, T., Ščančar, J., and Milačič, R. (2016). The fate of iron nanoparticles in environmental waters treated with nanoscale zero-valent iron, FeO NPs and Fe_3O_4 NPs. *Water research 94*, 315–327.

(*8*) Bandyopadhyay, S., Sharma, A., and Glomm, W. R. (2017). The Influence of Differently Shaped Gold Nanoparticles Functionalized with NIPAM-Based Hydrogels on the Release of Cytochrome C. *Gels 3*, 42.

"I learnt very early the difference between knowing the name of something and knowing something."

– Richard Feynman

"Real science can be far stranger than fiction and much more satisfying."

– Stephen Hawking

5 Nanoparticle Growth

This chapter summarises the results of the synthesis of inorganic and polymeric NPs from *Paper I*,[1] *Paper II*[2] and *Manuscript III*. The chapter is divided into two sub-sections. The first section deals with the synthesis of IONPs using co-precipitation and thermal decomposition routes, yielding particles with different size, shape and morphology. Nucleation and growth studies were conducted on the IONPs obtained from thermal decomposition of iron-oleate precursor, and these NPs were further used to nucleate silver on the surface, resulting in DNPs. The second sub-section deals with the synthesis of stimuli-responsive polymeric NPs, referred to as *'nanogels (NGs)'*, via free radical precipitation polymerisation.

5.1 Iron-Oxide Nanoparticles

One of the solution-based methods to synthesise IONPs is via co-precipitation of iron salts in a basic environment as described in Chapter 4 (Figure 4.1). This approach results in high particle yield without the need to use high temperatures and long reaction times. Additionally, the process utilizes water as a solvent, thereby eliminating use of any toxic organic solvents. NPs obtained from co-precipitation are referred to as *magnetite–'Mag'* and Figure 5.1 a) shows their TEM image and 5.1 b) their particle size distribution (PSD). Even though co-precipitation (without surfactant) has advantages, the process does not allow for precise control over the particle size, shape and morphology, and the magnetic properties of the particles. A more controlled particle size originates from temporal separation of nucleation and growth regimes promoting narrower size distributions in comparison to the more prevalent co-precipitation route.

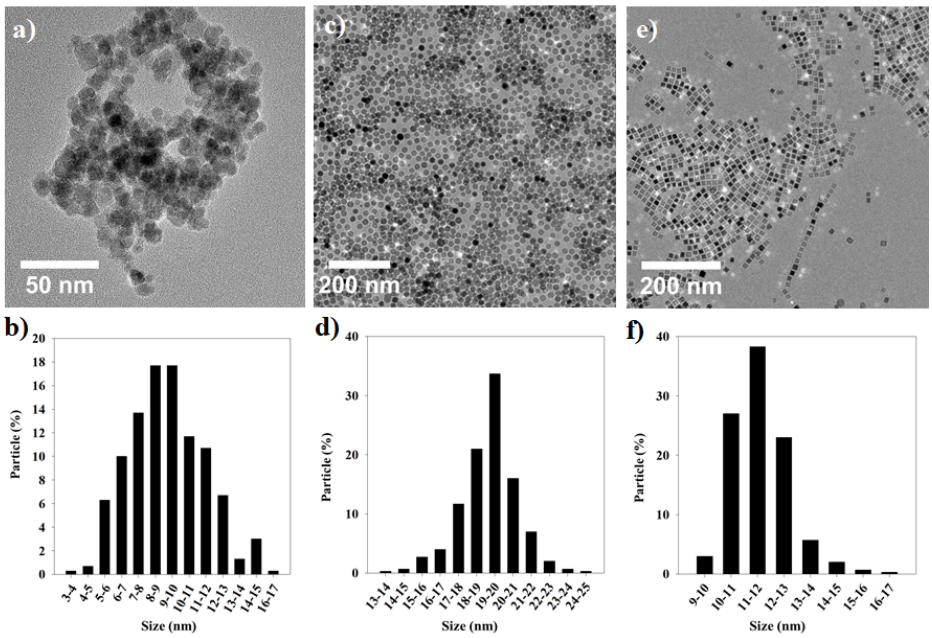

Figure 5.1: TEM images of the obtained **a)** Mag NPs (co-precipitation), **c)** spherical NPs and **e)** cubic NPs (thermal decomposition). Particle size distribution histograms for **b)** Mag, **d)** spherical and **f)** cubic NPs.

Spherical (SNPs) and cubic (CNPs) NPs were synthesised using thermal decomposition of iron-oleate precursor at elevated temperatures in an inert (argon) atmosphere. The molar ratio of the metal precursor (iron-oleate) to reducing and/or stabilizing agents [sodium oleate (Na-oleate) / oleic acid (OA) ratio] influences the size, shape and morphology evolution of the IONPs. On the other hand, the size of the NPs was clearly determined by the reaction time, temperature, and reducer/stabilizer concentrations.[3] Figures 5.1 c) and e) show the TEM images and Figures 5.1 d) and f) PSD of SNPs and CNPs, respectively. IONPs from thermal decomposition show narrower PSD, as well as, low polydispersity index (PDI) (SNP=0.08, CNP=0.09), compared to Mag (PDI=0.24), stating highly monodisperse particles.[4]

5.1.1 Growth of Spherical Iron-Oxide Nanoparticles

The synthesis of SNPs starts with the production of iron-oleate that decomposes[5] to yield a blackish dispersion of magnetic SNPs on heating in argon as shown in Figure 5.2 a). TEM images in Figures 5.3 a–e) show the evolution of SNPs as a function of reaction time and reaction temperature. No particles were seen 65 min into the reaction (220 °C) as seen in Figure 5.3 a). However, a few particles could be observed at 250 °C as shown in Figure 5.3 b). This could be attributed to stochastic growth arising from premature decomposition of iron-oleate resulting from heterogeneous nucleation at surface walls or via creation of pockets of supersaturation. Homogeneous nucleation occurs via *'Burst Mechanism'* above 300 °C, that ends rapidly as the reaction enters the growth regime. There is a rapid increase in the number of particles at 310 °C that can be distinctly seen from representative TEM image in Figure 5.3 c). As the reaction proceeds, rapid consumption of the monomer causes the supersaturation to decrease and only the nuclei larger than the critical size grow to form final NPs till the reaction temperature reaches 320 °C. The reaction is maintained

at 320 °C for 45 min (Figures 5.3 d) and e)), in which the particles grow and attain a narrower size distribution, as also shown by Hyeon *et al.*[6] Supersaturation is high enough for diffusion-controlled growth that promotes narrowing of the particle size distribution by allowing the smaller particles to grow rapidly compared to the bigger particles, owing to the higher surface energies of the smaller particles.[1]

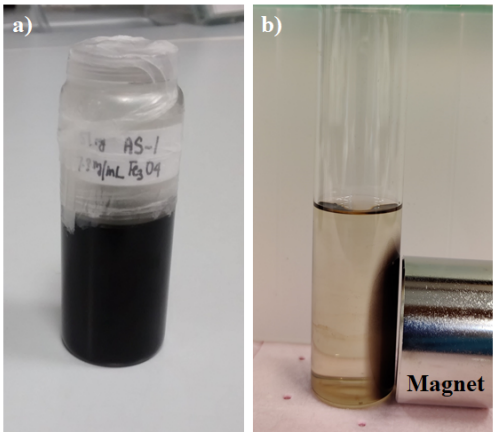

Figure 5.2: **a)** Blackish dispersion of magnetic spherical IONPs, synthesised via thermal decomposition of iron-oleate and **b)** magnetic separation of the particles under the influence of a magnet.

Narrow PSD of SNPs is obtained as a result of distinct separation of the nucleation and growth regions resulting in final particle size of $\sim$14 $\pm$ 3 nm [before cleaning (Figure 5.3 e))] and $\sim$19 $\pm$ 2 nm [after cleaning (Figure 5.1 c))]. The polydispersity of the particles is seen to decrease as NP size increases with the particles becoming more spherical with reaction time and achieving a final PDI of $\sim$0.2 (Figure 5.3 f)). The decrease in polydispersity along with the increase in mean particle size are characteristic of this growth regime. Ostwald ripening may dominate in the later stages of the growth process that acts contrary to diffusion-controlled growth as it allows larger particles to grow on the expense of the smaller ones, thereby broadening PSD.[7] The presence of Ostwald ripening was further confirmed by developing a mathematical model based on the three growth mechanisms, namely, diffusion-controlled growth, coagulation due to Brownian collisions, and Ostwald ripening. The simulation data matches well with the mean of the PSD from the experimental data and fits well when Ostwald ripening is included in the mechanism.[1]

Decomposition of iron-oleate begins around 250 °C, as observed through FTIR analysis (Figure 5.4), forming Fe^{2+}. The gradual disappearance of the carboxylate bands (1608, 1519 and 1444 cm^{-1}) as a function of reaction time culminating in complete disappearance at end of reaction, as shown in Figure 5.4 b), stating successful decomposition of the metal-oleate complex, further supporting our classical nucleation-growth model comprising burst nucleation and diffusion-controlled growth.[1]

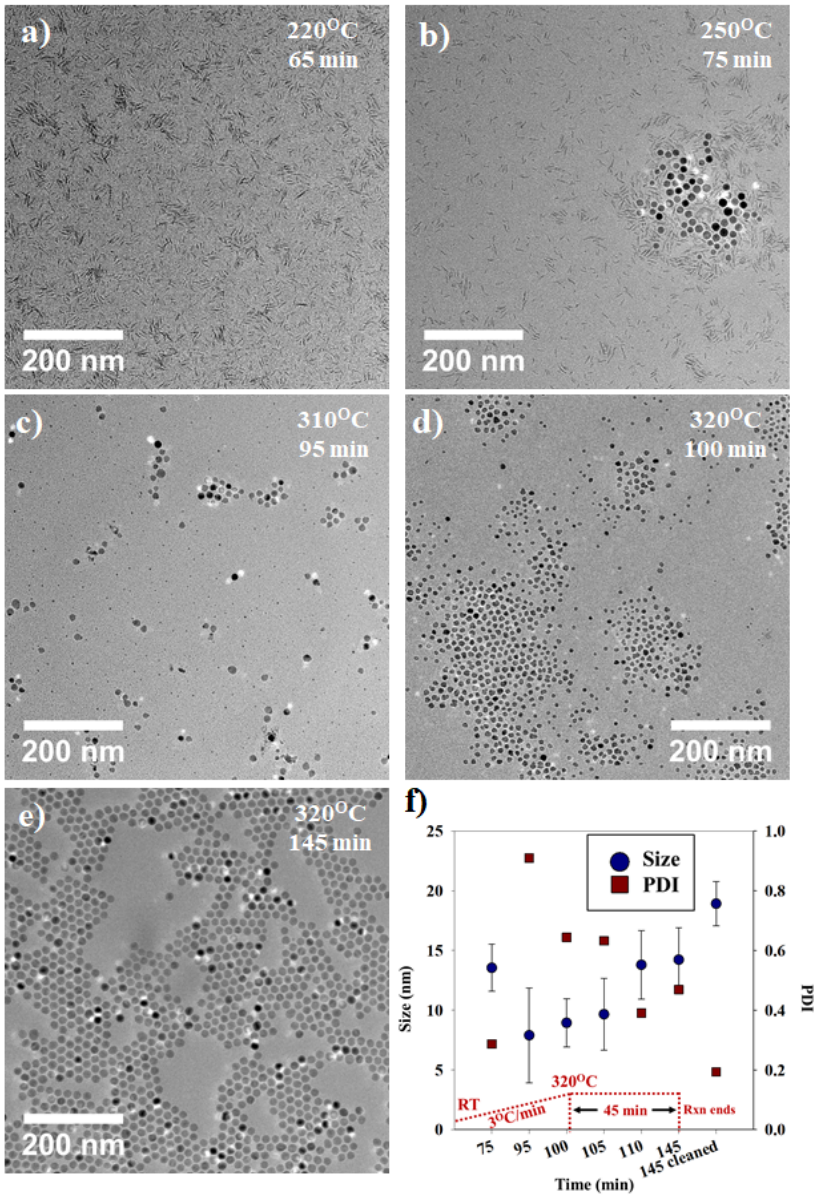

Figure 5.3: **a–e)** TEM images of spherical IONPs aliquots at different stages of the synthesis reaction. **f)** Size/PDI vs spherical IONPs synthesis reaction times. (RT = Room Temperature, Rxn = Reaction).

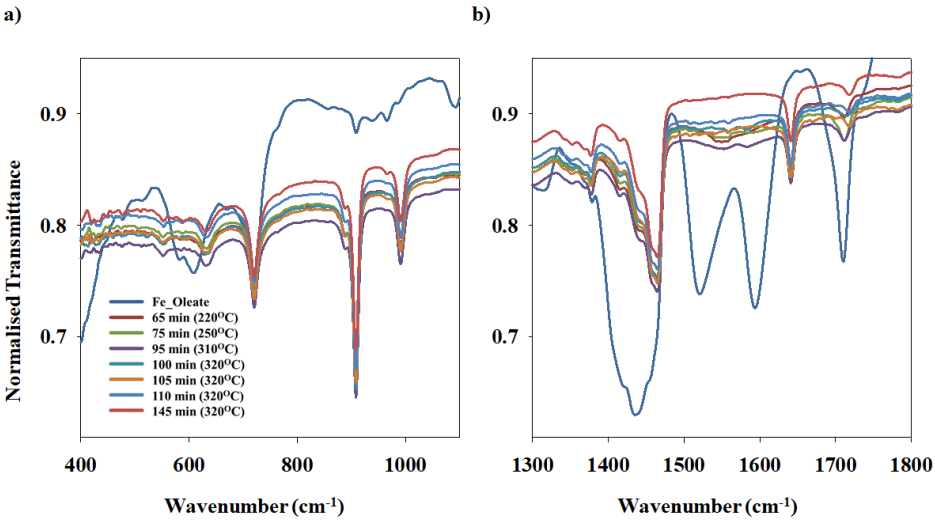

Figure 5.4: FTIR spectra showing the decomposition of iron-oleate and the growth of SNPs via thermal decomposition, at different reaction times and temperature.

5.1.2 Growth of Silver on Spherical Iron-Oxide Nanoparticles

Pre-synthesised SNPs were used as nucleating sites (seeds) for the synthesis of dimeric Ag@SNPs. To perform growth studies, aliquots of the reaction samples were taken out at intervals of 1, 3, 5, 7, 10 and 12 h, which were examined under TEM/SEM. Figures 5.5 a–f) show the formation of dimeric NPs with Ag nucleating and growing on the surface of IONPs. The deposition of Ag on the surface of IONPs was also tracked using EDS measurements. These results are included in Figures 5.5 g–i). Figure 5.5 g) shows the EDS elemental mapping data after 1 h of reaction, marking Fe, O and Ag containing regions. During the initial stages of the reaction, SNPs are seen with no dimeric growth of Ag, however, small Ag particles are scattered over the IONP surface, across the whole sample. Multiple small nodes of Ag start being visible around the SNPs, after 3 h reaction, as seen in Figure 5.5 h). The occurrence of these nodes indicates that Ag is not present as a single island but, forms multiple small islands on the surface of SNPs indicating multiple regions of deposition in contrast to one particular site (Figure 5.5 h). This is attributed to the difference in lattice spacing[8] between Fe ($\sim$0.49 nm) and Ag ($\sim$0.23 nm) as can be seen from Figure 5.6. These nodes grow further as Ag deposits on them via surface diffusion, as well as diffusion of Ag from the solvent to the particle. Figures 5.5 d–f) show the TEM images of the obtained SNP-Ag NPs after 7, 10 and 12 h of reaction, respectively. There is a homogeneous distribution of SNPs, whereas Ag nodes seem to exist in different sizes over the SNPs. The disappearance of smaller Ag nodes and growth of larger ones can be credited to Ostwald's ripening, prevalent at the later stages of the reaction. However, it should be noted that in addition to surface diffusion, Ag from smaller nodes might also redissolve in the solution and be redeposited on another SNP. Additionally, as all the particles are continuously in rigorous state of motion, Ag nodes diffusing into the solvent may contribute to different Ag@SNPs in their constantly changing vicinity. Thus, there is a non-homogeneous distribution of Ag on the SNPs.

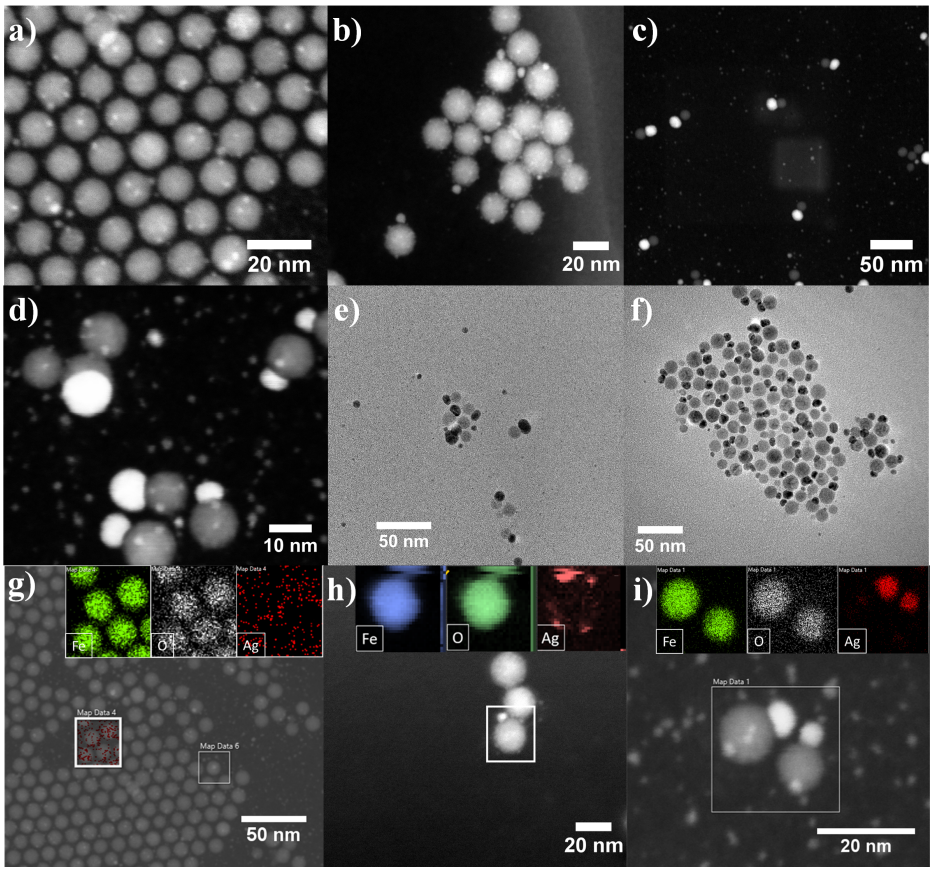

Figure 5.5: SEM images following the growth of Ag@SNPs at **a)** 1 h, **b)** 3 h, **c)** 5 h, **d)** 7 h, **e)** 10 h and **f)** 12 h. EDS elemental mapping of Ag@SNPs at time **g)** 1 h, **h)** 3 h and **i)** 5 h.

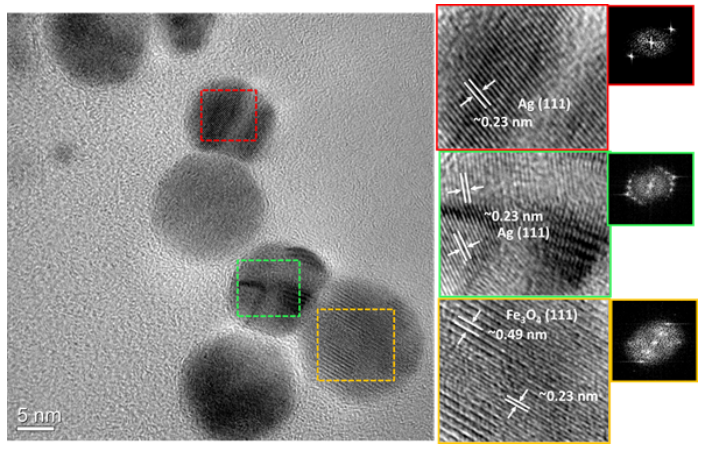

Figure 5.6: TEM image of dimeric magneto-plasmonic NPs showing lattice spacing of 0.49 nm and 0.23 nm for silver and iron-oxide NPs, respectively.

5.1.2.1 Effect of AgAc Concentration

To investigate the effect of AgAc content on the physico-chemical properties of the DNPs, AgAc amounts were varied during particle synthesis. The DNPs were characterized using VSM and UV-Vis and the respective results are shown by Figures 5.7 a) and b). VSM data suggests a decreasing saturation magnetization trend with increasing AgAc content, whereas, an increase in the UV-Vis absorbance peak is seen with greater AgAc content. These results suggest a higher degree of Ag deposition on IONPs, forming more dimeric NPs, as more AgAc is used during synthesis. A decrease in saturation magnetization (M_s), between the bare IONPs and their dimeric counterparts is seen as represented in Table 5.1. The decrease is most probably caused by the addition of non-magnetic Ag onto the IONP surface that affects particle mass but not M_s. Therefore, the higher the amount of AgAc, the greater is the decrease in M_s, and simultaneously, the plasmonic response of the particles increases due to more Ag deposition. A balance between the magnetic and plasmonic properties needs to be established to exploit the benefits of both the components of DNPs. Therefore, 11.2 mg Ag Acetate salt concentration was selected for magnetophoresis studies described in Chapter 7.

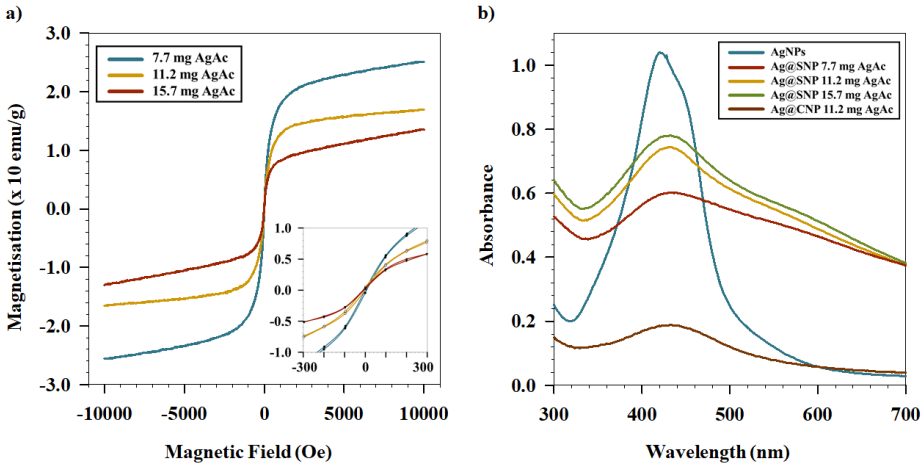

Figure 5.7: VSM and d) UV-Vis of NPs showing the decrease in magnetisation and increase in plasmon response with increasing amounts of AgAc, respectively.

Table 5.1: Saturation magnetisation and LSPR peak of IONPs and DNPs.

Particles	M_s emu/g	LSPR Peak nm
SNPs	74.33	-
CNPs	3.57	-
AgNPs	-	442
Ag@SNP 7.7 AgAc	25.13	431
Ag@SNP 11.2 AgAc	16.88	432
Ag@SNP 15.7 AgAc	13.6	432
Ag@CNP 11.2 AgAc	-	432

5.2 Stimuli-Responsive Nanogels

The synthesis of pNIPAm-pAAc-based NGs using free radical precipitation polymerisation is reported in this section. To study the effect of different reaction parameters on the growth of the NGs, the concentration of dodecyl sulphate (SDS), as well as, nitrogen atmosphere, were varied during the NG synthesis. Furthermore, the effect of increasing pAAc content in the NGs on their physico-chemical properties was also investigated.

5.2.1 Growth of Nanogels

Figure 5.8 a) shows the variation of NGs' hydrodynamic size with synthesis temperature at different SDS concentrations. NGs synthesized by the three methods – continuous-stirring method (NGs_CS), flashing-stirring (NGs_FS) and flashing-impeller (NGs_FI), show an increasing hydrodynamic size on decreasing the SDS amount from 4.2 to 2.1 mM. SDS provides colloidal stability to the precursor particles during nucleation by electrostatic stabilization.[9] Additionally, higher concentration of SDS led to denser packing around the incipient nucleation (oligomer) centers, thus, limiting the growth of NGs. This finding is also in agreement with the results obtained in previous studies conducted by our group, where SDS concentration was one of the central factors determining the size of the NGs.[10]

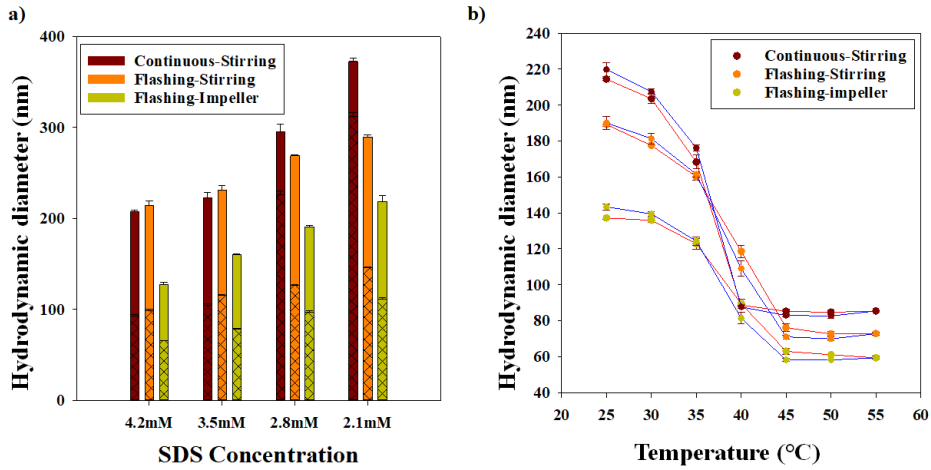

Figure 5.8: Variation of synthesized nanogel sizes as a function of **a)** SDS concentration and **b)** temperature (at 4.2 mM SDS).

The heating and cooling phase transition curves, shown in Figure 5.8 b), are used to determine the VPTTs of the respective NG systems (at 4.2 mM SDS), presented in Table 5.2. The curves have a sigmoidal fit, showing collapse from 25 to 40 – 45°C, owing to the shift in the balance of hydrophilic and hydrophobic forces that cause coil-to-globule transition upon the increase in temperature. At elevated temperatures, entropically-driven release of bound water takes place due to breakage of hydrogen bonds, and water is excluded from the molecular aggregates as polymer-polymer interactions exceed polymer-solvent interactions. The polymer chains, thus collapse, attaining a globular structure resulting in phase separation.[10] NGs_CS, among the three systems, show collapse over a narrower temperature window. Low PDI for NGs_CS (Table 5.2) infers narrower PSD and monodisperse population compared to NGs_FS and NGs_FI, that might result in more uniform and consistent volumetric collapse of the NG system as a whole.

Table 5.2: VPTT and PDI of NGs synthesized by different methods using 4.2 mM SDS.

Nanogels	VPTT (°C)	PDI
NGs_CS	36.3 ± 0.1	0.2 ± 0.0
NGs_FS	37.8 ± 0.1	0.7 ± 0.1
NGs_FI	37.7 ± 0.1	0.6 ± 0.2

Figure 5.9 a) shows the size of the NGs synthesised by the three synthesis methods. An initial increase in size is seen, for all the methods, before stabilizing at the final particle size. On the contrary, PDI shows a decreasing trend as the reaction proceeds (Figure 5.9 b)) showing that the samples achieve monodisperse population at the end of the reaction.

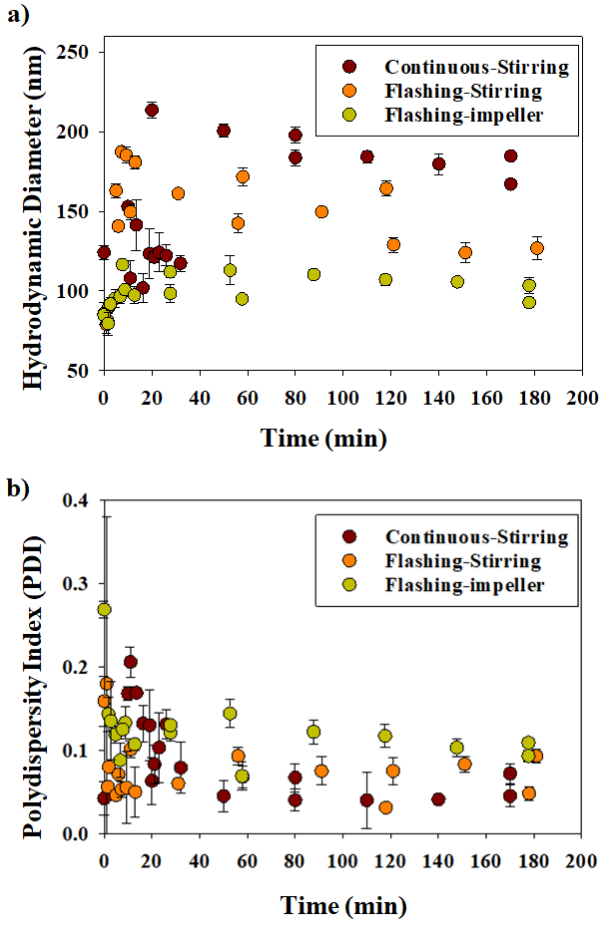

Figure 5.9: Variation of **a)** size and **b)** PDI, as a function of reaction duration for NGs synthesised via the Continuous-Stirring (CS), Flashing-Stirring (FS), and Flashing-Impeller (FI) methods.

5.2.2 Effect of Acrylic Acid

Figures 5.10 a and b show the variation of NG sizes and zeta potentials with respect to mole% of AAc. An increasing trend is observed in NG size with increasing AAc mole% (from 10 to 30 mole%), indicating a higher relative incorporation of AAc in the NGs. Figure 5.11 shows the ^{1}H NMR spectra of NGs synthesized with increasing mole % of AAc. As the amount of AAc mole % increases, corresponding increase is seen for NMR peaks around 2.2 and 1.8 that correspond to pAAc incorporated in the NGs.

The size of the NGs show collapse with change in pH on going from basic towards acidic pH (Figure 5.10 b)). As AAc deprotonates at higher pH and becomes negatively charged, repulsion between the polymeric chains occurs. The maximum stretching of the polymeric chain with deprotonation depends on the percent ionization of the carboxylic groups. Therefore, a higher amount of AAc in the NG matrix is expected to promote swelling of the structure.

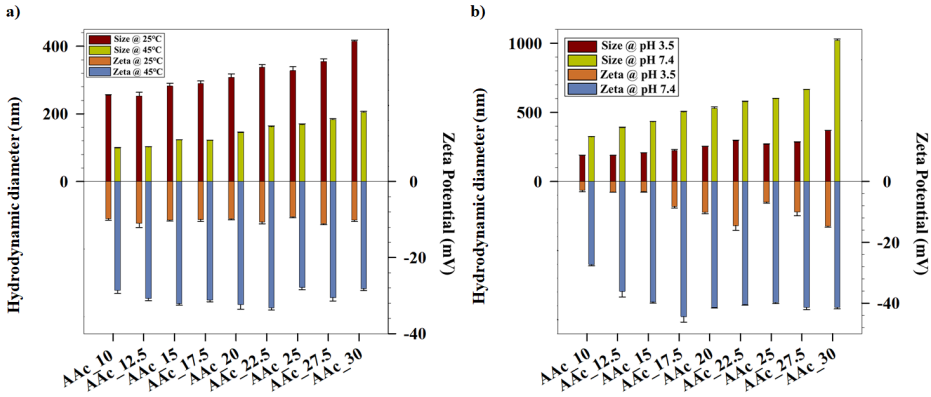

Figure 5.10: Hydrodynamic diameter and zeta potential of the NGs_CSs at **a)** 25 and 45°C, and **b)** pH = 3.5 and 7.4.

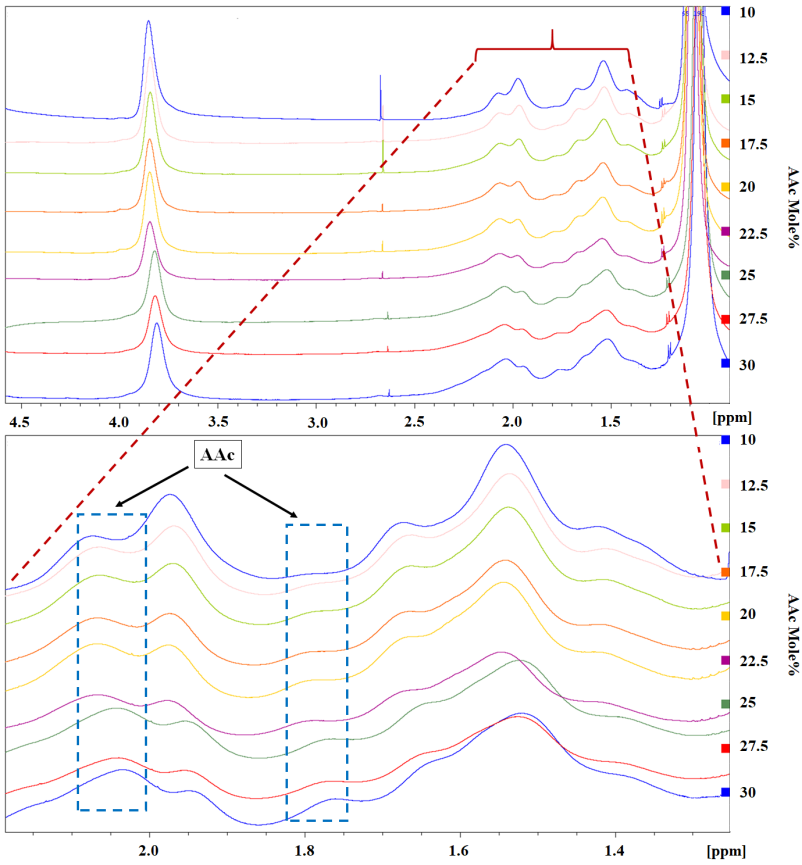

Figure 5.11: ^{1}H NMR spectra of NGs_CS synthesized with increasing mole% of AAc from 10 to 30.

5.3 Summary

Different inorganic and polymeric NPs were synthesised and their growth was studied by varying selected reaction parameters. IONPs were primarily synthesised via the co-precipitation and thermal decomposition (of iron-oleate) routes resulting in IONPs with different morphology, with a size range of 10–20 nm. SNPs and CNPs, synthesised using thermal decomposition of iron-oleate precursor, resulted in particles having narrow PSD and low PDI (SNP=0.08, CNP=0.09). Whereas, IONPs from co-precipitation (Mag) had broader PSD and higher PDI of 0.24, implying higher polydisperse population than both, SNPs and CNPs.

Nucleation and growth of SNPs occurs via burst nucleation, with the decomposition of iron-oleate precursor around 300 °C, following which the reaction quickly enters the growth regime. Diffusion-controlled growth dominates during the early stages (high supersaturation) of the reaction, while Ostwald ripening takes over in the later stages of the reaction (low supersaturation). On using SNPs as seed for the nucleation and growth of silver on the surface of IONPs, results is dimeric NPs. AgNPs nucleate on SNPs via heterogeneous nucleation and subsequent epitaxial growth leads to dumbbell morphology, owing to the lattice mismatch between Fe ($\sim$0.49 nm) and Ag ($\sim$0.23 nm).

Free radical precipitation polymerization was used to synthesise stimuli-responsive, pNIPAm-pAAc-based nanogels NGs. The effect of surfactant (SDS) concentration and reaction atmosphere, on the growth of NGs was investigated. Smaller sizes were obtained with 4.2 mM SDS concentration and the size increased with decreasing amounts of SDS, until 2.1 mM concentration. Furthermore, the effect of increasing mole% of AAc on the physico-chemical properties of the NG was also studied. An increase in the size was observed with increasing AAc mole%, ranging from 256 $\pm$ 2 nm to 415 $\pm$ 3 nm for AAc mole% of 10 and 30, respectively. The potential applicability of these NPs as hydrological tracers and targeted drug delivery systems will be explored in the following chapters.

References

(*1*) Sharma, A., Foppen, J. W., Banerjee, A., Sawssen, S., Bachhar, N., Peddis, D., and Bandyopadhyay, S. (2021). Magnetic Nanoparticles to Unique DNA Tracers: Effect of Functionalization on Physico-chemical Properties. *Nanoscale research letters 16*, 1–16.

(*2*) Sharma, A., Raghunathan, K., Solhaug, H., Antony, J., Stenvik, J., Nilsen, A. M., Einarsrud, M.-A., and Bandyopadhyay, S. (2021). Modulating Acrylic Acid Content of Nanogels for Drug Delivery Biocompatibility Studies. *Journal of Colloid and Interface Science*.

(*3*) Situ-Loewenstein, S. F., Wickramasinghe, S., Abenojar, E. C., Erokwu, B. O., Flask, C. A., Lee, Z., and Samia, A. C. S. (2018). A novel synthetic route for high-index faceted iron oxide concave nanocubes with high T2 relaxivity for *in vivo* MRI applications. *Journal of Materials Science: Materials in Medicine 29*, 1–10.

(*4*) Pusey, P. (1987). The effect of polydispersity on the crystallization of hard spherical colloids. *Journal de physique 48*, 709–712.

(*5*) Kwon, S. G., Piao, Y., Park, J., Angappane, S., Jo, Y., Hwang, N.-M., Park, J.-G., and Hyeon, T. (2007). Kinetics of monodisperse iron oxide nanocrystal formation by "heating-up" process. *Journal of the American Chemical Society 129*, 12571–12584.

(*6*) Kwon, S. G., and Hyeon, T. (2008). Colloidal chemical synthesis and formation kinetics of uniformly sized nanocrystals of metals, oxides, and chalcogenides. *Accounts of chemical research 41*, 1696–1709.

(*7*) Chang, H., Kim, B. H., Jeong, H. Y., Moon, J. H., Park, M., Shin, K., Chae, S. I., Lee, J., Kang, T., Choi, B. K., et al. (2019). Molecular-level understanding of continuous growth from iron-oxo clusters to iron oxide nanoparticles. *Journal of the American Chemical Society 141*, 7037–7045.

(*8*) Li, Y., Yang, S., Lu, X., Duan, W., and Moriga, T. (2019). Synthesis and evaluation of the SERS effect of Fe_3O_4–Ag Janus composite materials for separable, highly sensitive substrates. *RSC advances 9*, 2877–2884.

(*9*) Smith, M. H., and Lyon, L. A. (2012). Multifunctional nanogels for siRNA delivery. *Accounts of chemical research 45*, 985–993.

(*10*) Bandyopadhyay, S., Andersen, M. K., Alvi, M. A. A., Sharma, A., Raju, R., McDonagh, B. H., and Glomm, W. R. (2016). Incorporation of Fe@Au nanoparticles into multiresponsive pNIPAM-AAc colloidal gels modulates drug uptake and release. *Colloid and Polymer Science 294*, 1929–1942.

"Water and air, the two essential fluids on which life depends, have become global garbage cans"

– Jacques-Yves Cousteau

"We never know the worth of water until the well is dry."

– Thomas Fuller

6 Hydrological Tracers

This chapter summarises the results of *Paper I*,[1] describing the functionalisation of IONPs for their use as potential hydrological tracers. The three different IONPs, namely, SNP, CNP and Mag, were used to make the tracers magnetic. Furthermore, the synthesised IONPs were functionalised using different ligands before they could be functionalised with DNA (tracer moiety). In the case of IONPs synthesised using thermal decomposition of iron oleate (SNPs and CNPs), the particles needed to be transferred from organic to aqueous phase before they could be used for environmental applications. Furthermore, the charge on the surface of IONPs had to be adjusted before they could be functionalised with DNA. In order to protect the DNA from degradation and loss to the surroundings, the DNA functionalised IONPs were encapsulated in a silica shell.

This chapter, thus, highlights the functionalisation of IONPs with various ligands as well as DNA resulting in tracers that can be used for hydrological applications as depicted in Figure 6.1. The first part focuses on the surface functionalisation of IONPs, the second on DNA functionalisation, while the third focuses on silica encapsulation.

6.1 Surface Functionalisation of IONPs

Using DNA as the tracer moiety allows for the synthesis of a potentially unlimited number of unique tracers, each having its own bar code. Using magnetic IONPs in the tracers enables for easy recovery of the tracers downstream, thereby minimizing losses. Mag, SNPs and CNPs have been used as the magnetic components forming the core of the tracer particle. Each type of IONP provides different magnetic and surface properties, thus, allowing flexibility in tracer design.

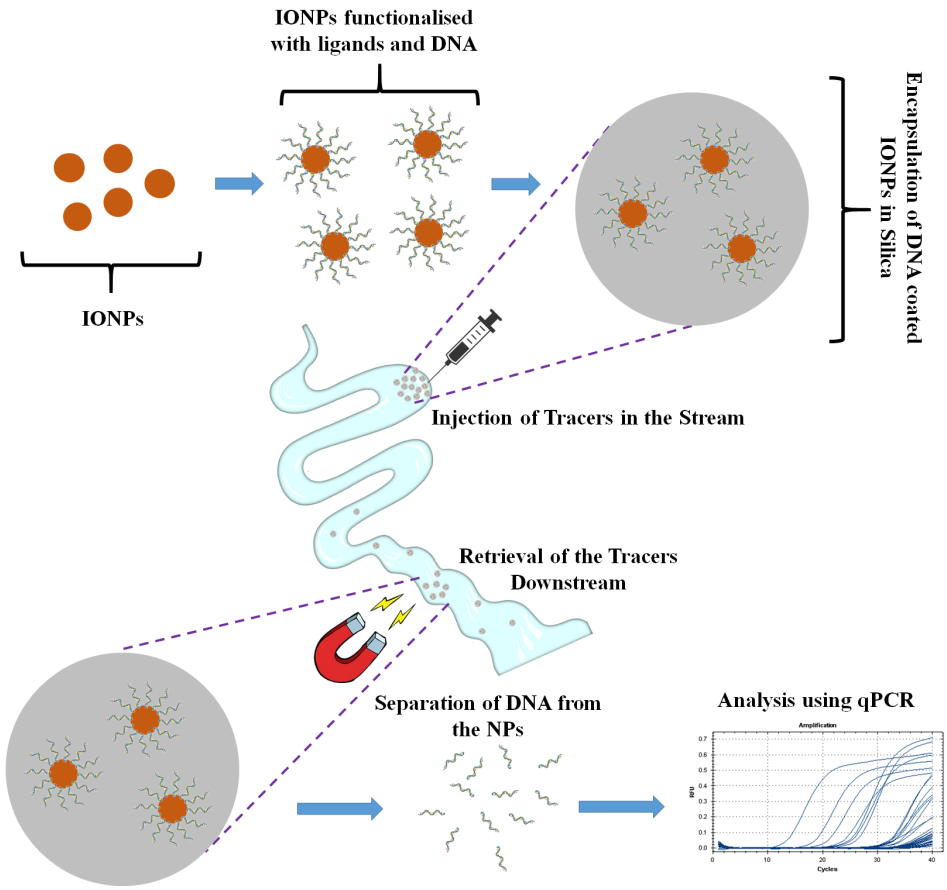

Figure 6.1: Schematic representing the potential applicability of DNA-based magnetic tracers for hydrology.

6.1.1 Phase transfer of SNPs and CNPs

Typically, there are two pathways by which IONPs can be functionalised with a hydrophilic ligand; the first one involves complete replacement of the hydrophobic ligand with a hydrophilic ligand (*'ligand-ligand exchange'*), and the second involves modification of the hydrophobic ligand by the hydrophilic one.

As both SNPs and CNPs were synthesised and stored using organic solvents, they needed to be transferred to aqueous phase before they could be used in hydrological applications. Various functionalisation strategies were used that further required application of different ligands to transfer the IONPs into aqueous phase. Three different ligands, namely, tetramethyl ammonium hydroxide (TMAH), sodium citrate (Na-citrate) and cetyltrimethylammonium bromide (CTAB) were used to make SNPs and CNPs hydrophilic, with their sizes and zeta potentials provided in Table 6.1. Although CTAB provided positive potential, it is usually avoided due to its toxicity.[2]

Table 6.1: DLS results showing the size and zeta potentials of the different phase transferred SNPs using TMAH, Na-citrate and CTAB.

Iron-Oxide NPs	Ligand	Size (nm)	Zeta Potential (mV)
SNPs	Na-citrate	343 ± 5	-49.7 ± 0.1
	CTAB	364 ± 10	$+32.0 \pm 0.0$
	TMAH	495 ± 11	-10.0 ± 2.5
CNPs	TMAH	272 ± 20	-38.6 ± 2.8

To further understand the surface properties of the phase transferred NPs and the functionalisation mechanism using Na-citrate and CTAB, a series of FTIR measurements were conducted as shown in Figure 6.2 (TMAH study is discussed in the Section 6.1.2). CTAB results in a positive zeta potential while Na-citrate and TMAH impart negative surface charge to the NPs. The sharp absorption bands at 1383 and 1584 cm^{-1} for pure Na-citrate show the stretching of asymmetric and symmetric carbonyl groups (C=O) respectively.[1] These vibrations are greatly reduced for the Na-citrate functionalised SNPs showing interaction of the C=O groups with the surface of the SNPs. Concurrently, the absence of characteristic bands of the surface bound oleic acid (OA) asymmetric and symmetric stretching of C–H at 2850 and 2923 cm^{-1}, in the case of SNPs with Na-citrate, further suggest complete replacement of OA. Therefore, this results in ligand-ligand exchange whereby a small molecule (Na-citrate) easily displaces longer hydrocarbon chains of the surface bound OA, leading to negative surface charge in an aqueous medium. The driving force for ligand exchange and more effective binding of Na-citrate might be attributed to the presence of multiple functional groups (or sites) in a Na-citrate molecule compared to just one functional group in OA.[3]

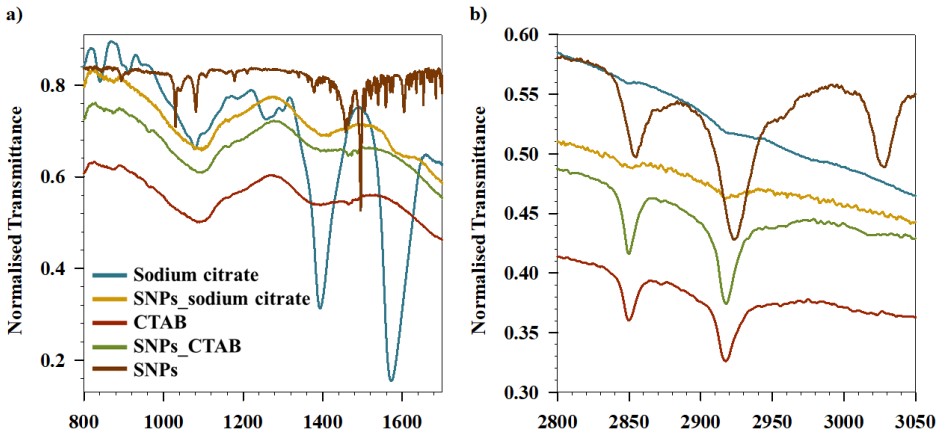

Figure 6.2: ATR-FTIR spectra of Na-citrate, CTAB and SNPs functionalised with Na-citrate and CTAB in **a)** region 800–1600 cm^{-1} and **b)** region 2800–3200 cm^{-1}.

The absorbance bands for pure CTAB observed at 942 and 980 cm^{-1} are assigned to C–N bond and C–H stretching, respectively (Figure 6.2 a)). For SNPs coated with CTAB, the bands at 942 and 980 cm^{-1} are highly reduced and shifted in comparison to pure CTAB. This might be caused by the interacting N^+ of CTAB with SNPs leading to reduced absorbance of its own C–N bond stretching, thereby confirming SNPs' functionalisation with CTAB. Although

the intensity of the C–H stretching bands at 2850 and 2923 cm^{-1} from surface bound OA, is reduced, these overlap with CTAB C–H stretching bands in the same range. Therefore, chemisorption of CTAB molecules on the SNP surface might happen, either via complete removal of the OA, or by formation of inclusion complexes with OA.[4]

6.1.2 Surface Charge Modification

Once IONPs are successfully phase transferred to water, the surface charge needs to be altered to positive before they can further be functionalised with DNA. Phase transfer of SNPs and CNPs was first achieved with TMAH, to transfer the particles from the toxic organic solvent (toluene) to aqueous phase, followed by functionalisation with TMAPS (imparting positive surface charge to the NPs) as shown in Figure 6.3. As Mag NPs use aqueous-based synthesis route (co-precipitation), there is no need to functionalise them with TMAH and, hence, they can directly be functionalised with TMAPS.

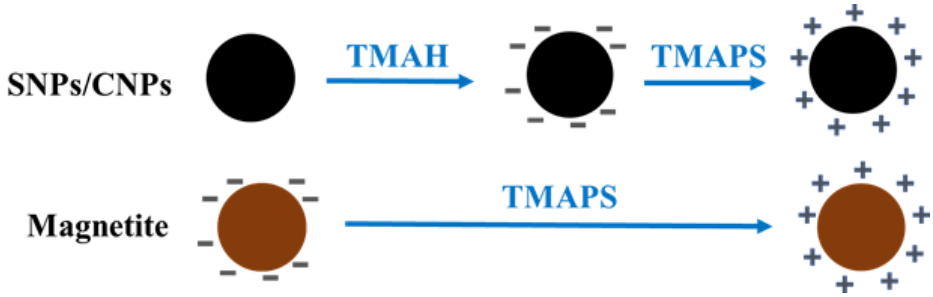

Figure 6.3: Schematic representing the surface functionalisation of different IONPs with TMAH and TMAPs.

The ATR-FTIR spectra of TMAH and TMAPS functionalised NPs are shown in Figure 6.4. The absorbance band at 1031 cm^{-1} for TMAPS corresponds to the stretching of –Si–O–C–.[5] This vibration is absent for both SNPs and CNPs functionalised with TMAH and TMAPS owing to the interaction of the $–N^{+}(CH)_4$ groups of TMAH with –Si–O– of TMAPS during the modification. Complete removal of OA can be concluded from the disappearance of the asymmetric and symmetric C–H stretching band of OA at 2850 and 2923 cm^{-1} (Figure 6.4 a)).

The sharp band at 920 cm^{-1} for CNPs (Figure 6.4 c)) can be attributed to the out-of-plane angular deformation of –C–OH of Na-oleate (present on the surface of CNPs).[6] Complete disappearance of this peak is observed for spectra of CNPs functionalised with TMAH and TMAPS showing removal of Na-oleate, which is in accordance with phase transferred SNPs (where OA was removed). Other bands, observed at 1031 (Figure 6.4 c), 2876 and 2972 cm^{-1} (Figure 6.4 d), for CNPs functionalised with TMAH and TMAPS have similar characteristics as of SNPs functionalised with TMAH and TMAPS, showing analogous surface interactions during phase transfer. From the FTIR spectra, it is however difficult to conclude if TMAPS replaces TMAH completely for both SNPs and CNPs. However, it can be inferred that TMAPS is the outermost ligand providing positive zeta potential after TMAPS coating for Mag, SNPs and CNPs as shown in Table 6.2, arising from the amine functional group of TMAPS.

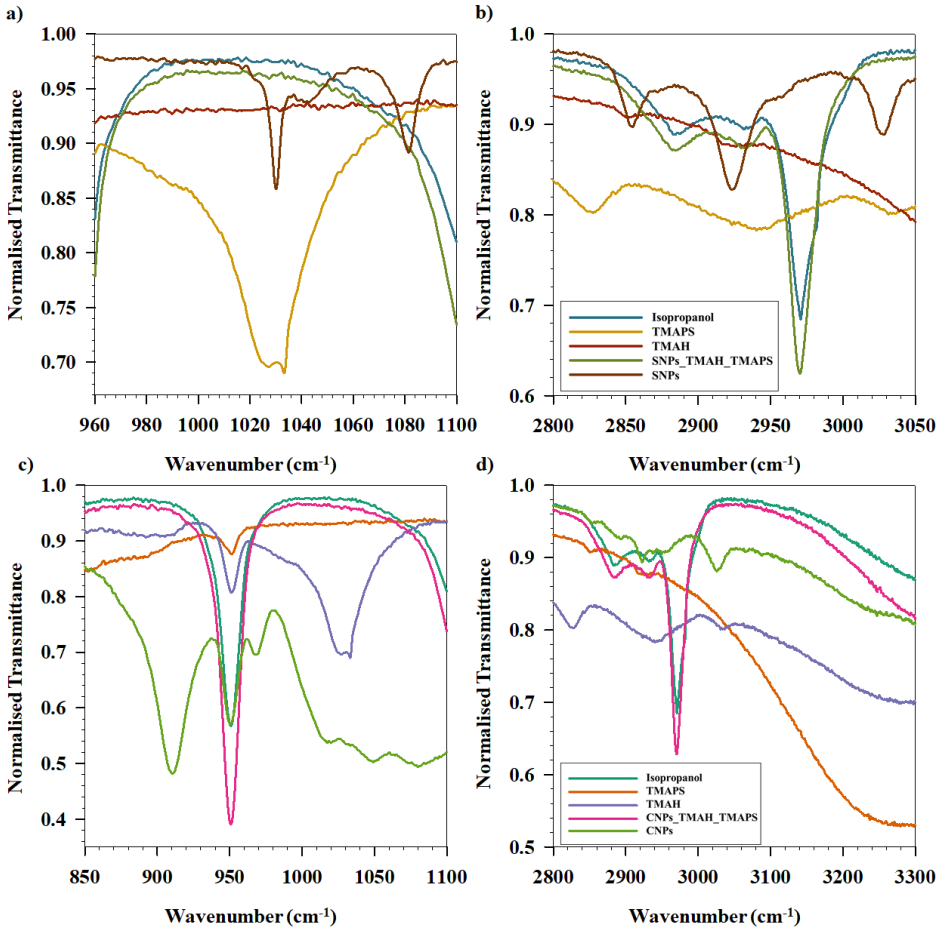

Figure 6.4: FTIR spectra of pure isopropanol, TMAH, pure TMAPS and the surface functionalized **a)**, **b)** spherical NPs and **c)**, **d)** cubic NPs, with TMAH and TMAPS.

Table 6.2: DLS results showing the size and zeta potentials of the different phase transferred SNPs using various TMAH and TMAPS.

IONPs	Before TMAPS (mV)	After TMAPS (mV)
Mag	-37.0 ± 4.3	+21.7 ± 7.0
SNP	-39.3 ± 17.1	+13.8 ± 1.4
CNP	-33.2 ± 4.9	+15.0 ± 0.0

6.2 DNA Functionalisation and Silanization

With the aim to fabricate tracers bar-coded with unique double-stranded DNA (dsDNA), three different dsDNA molecules, namely, T21, GM5 and GM6, were selected. Charge density mapping between the TMAPS functionalized IONPs and the dsDNA is a precursor to the successful binding of the dsDNA to the IONPs. Through a series of preliminary experiments, the ratio of NPs to dsDNA was optimised to facilitate effective DNA binding as shown in Figure 6.5 a). As more DNA is added to the TMAPS functionalised IONPs, the positive potential starts to decrease and ultimately becomes negative with higher amount of DNA (DNA has negatively charged due to its phosphate backbone). Successful binding of DNA reverses the surface charge of the IONPs in all the cases as reported in Figure 6.5 b). This shows the robustness and adaptability of our protocol that can be applied to different particle types as well as different DNA strands. A final coating of silica was deposited after this step to ensure a protective shell around the DNA. The silica coated NPs containing specific dsDNA and specific iron oxide NP cores were all found to have high colloidal stability, indicated by high zeta potential values (< -30 mV) as shown in Figure 6.5 b).

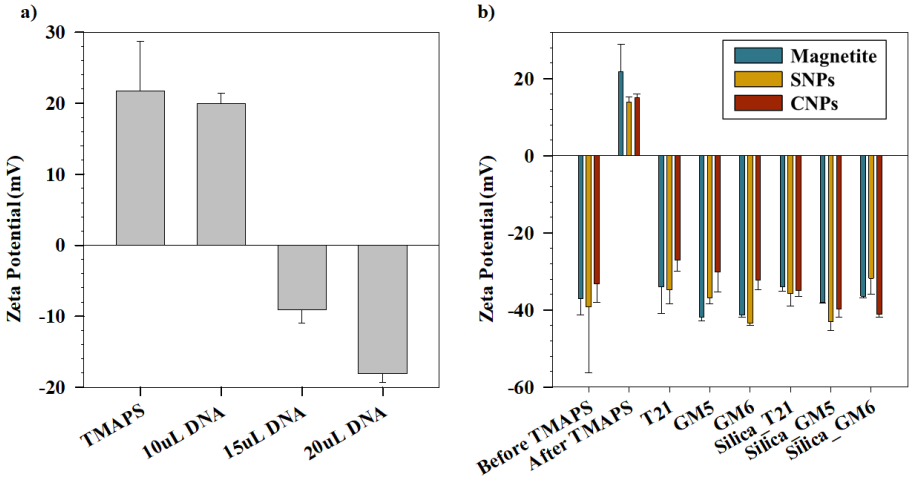

Figure 6.5: **a)** Variation of zeta potential for Mag NPs with different amounts of T21 dsDNA. **b)** Zeta Potential of Mag, SNPs and CNPs after functionalisation with 20 μL DNA (T21, GM5, GM6) and encapsulation with silica (Silica_T21, Silica_GM5, Silica_GM6).

6.3 Magnetic Properties

Ligands bonded to the surface of IONPs might influence their magnetic properties by modifying the electronic structure and as a result, magnetic properties.[7,8] In order to investigate the effect of molecular coating on magnetic properties, field and temperature dependence of magnetisation were investigated on bare magnetite (Mag) and at every stage of functionalisation *i.e.* TMAPS (Mag_TMAPS), DNA (Mag_DNA) and silica (Mag_Silica). Even though SNPs and CNPs possess higher structural uniformity that might lead to superior magnetic properties, the discussion of magnetic properties is limited to Mag, as these NPs provide higher saturation magnetisation (77 $\pm$ 8 emu/g) compared to SNPs and CNPs.

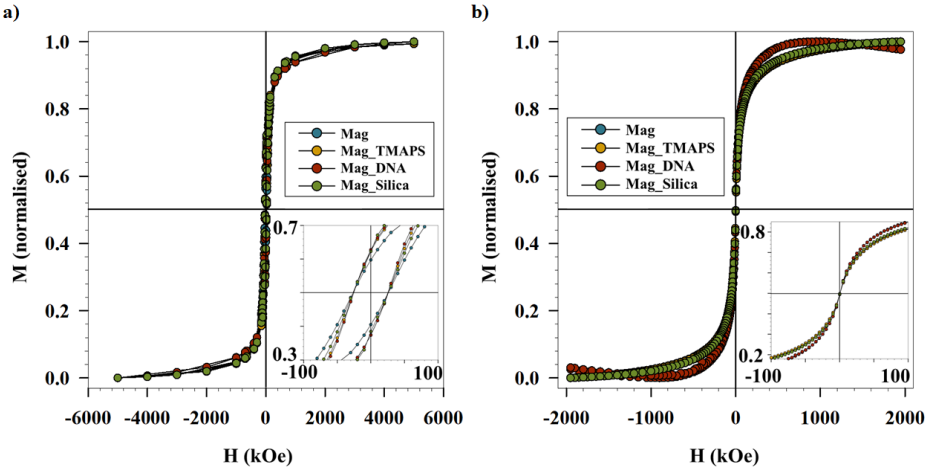

Figure 6.6: Field dependence of magnetisation for Mag, Mag_TMAPS, Mag_DNA and Mag_Silica at **a)** 5 K and **b)** 300 K.

Field dependence of magnetisation recorded at 5 K (Figure 6.6 a) indicates that the coating of Mag was successfully achieved without affecting the magnetic characteristics of the magnetic core and both bare and coated samples present similar saturation magnetisation (M_s) values, and coercivity (H_c). M vs H at 300 K (Figure 6.6 b) shows superparamagnetic behaviour (i.e. remanence magnetisation, M_r = 0, and H_c = 0) for all the samples.

To comment on the interparticle interaction in the Mag samples, the variation of interparticle interaction intensity (δm) vs magnetic field (at 5 K) was plotted as shown in Figure 6.7.[9] Negative values (δm intensity) are indicative of dipolar interactions in all the samples, that tend to slightly decrease with NP functionalisation.[1] In a sample of randomly distributed NPs with average magnetic moment, μ_p (i.e. $M_s \times V_p$), the relationship between average separation distance, d, and dipolar energy, E_d, is approximately given by Equation 6.1.

$$E_d \sim \frac{\mu_0 (M_s \times V_p)^2}{4\pi d^3} \tag{6.1}$$

where μ_0 is permeability, M_s saturation magnetization and V_p volume of nanoparticles. Assuming that M_s and V_p are equal in all the samples, the observed reduction of dipolar interactions (i.e. dipolar energy, E_d) means an increase of interparticle distance, indicating the efficiency for the coating process.

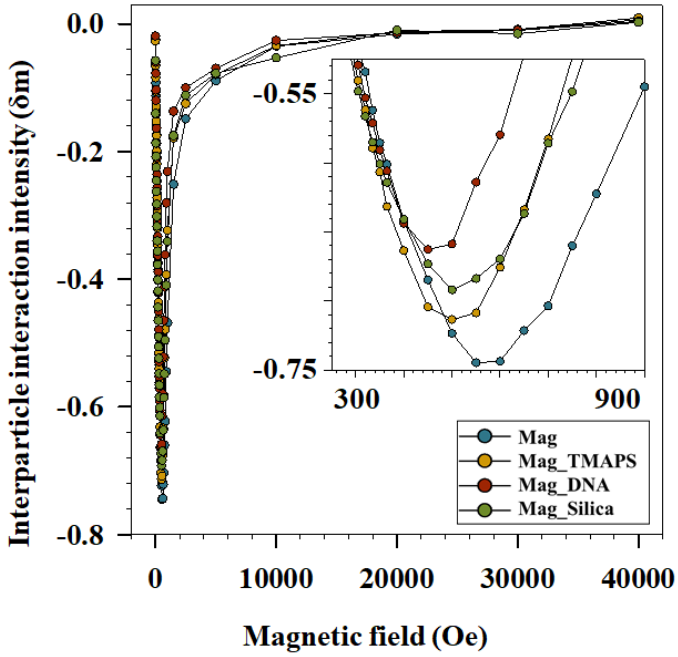

Figure 6.7: Interparticle interaction intensity (δm) at 5 K of Mag and functionalised Mag samples.

6.4 qPCR Measurements

In order to assess the dsDNA loads in the tracer particles, qPCR measurements were performed after bleaching any surface bound dsDNA (Figure 6.8).[1] Both, the silica and IONPs, were dissolved in etch solution to release the encapsulated DNA.[10] A low cycle threshold (C_t) value, during dsDNA run (described in Chapter 4), indicates high DNA concentration. The presence of large detectable quantities of DNA is therefore verified for all the tracer types, indicated by statistically significant lower C_t values compared to NTC (negative control) as shown in Figure 6.8. The results shown are for samples diluted 30 times (starting concentration = 1.5 mg/mL), whereby further proving the applicability of such tracers with high ultrasensitivity and negligible dilution problems.

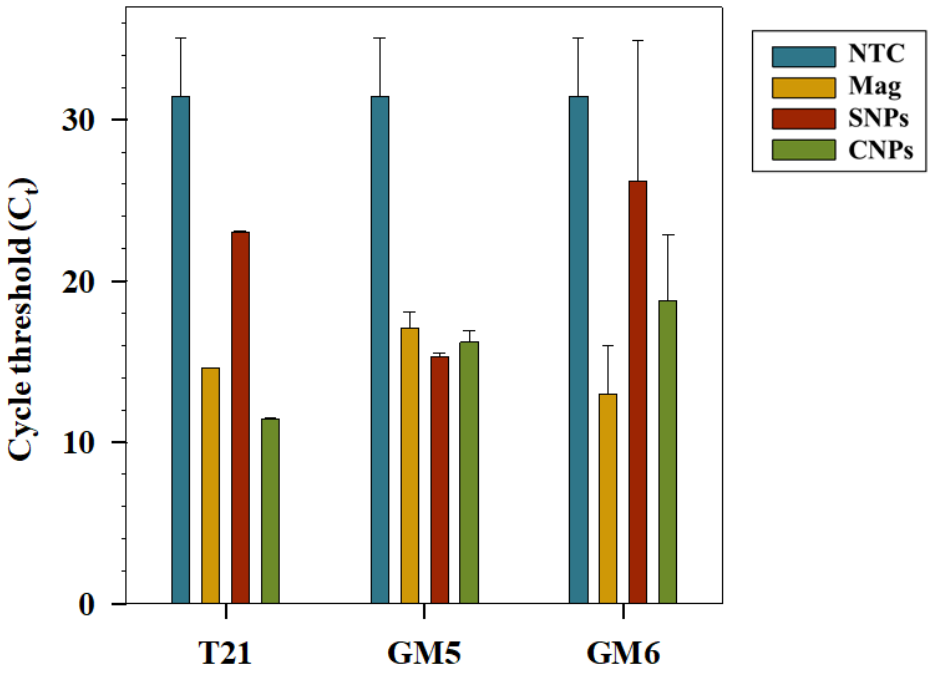

Figure 6.8: Cycle threshold (C_t) value, measured using qPCR, for different IONPs functionalized with different dsDNA.

6.5 Summary

DNA-based magnetic hydrological tracers were successfully synthesised having different magnetic cores, involving Mag, SNPs and CNPs, as well as, three different dsDNA (T21,GM5, GM6). SNPs and CNPs were phase transferred to water using TMAH, CTAB and Na-citrate. The functionalised NPs show high stability denoted by high absolute values of the zeta potentials, +32.0 $\pm$ 0.0 mV for CTAB, -49.7 $\pm$ 0.1 mV for Na-citrate and -38.6 $\pm$ 2.8 mV (CNP) for TMAH. Furthermore, the surfaces of all three IONPs were made positively charged using TMAPS and subsequently functionalised with T21, GM5 and GM6 dsDNAs. DNA functionalised IONPs were encapsulated in silica to protect the DNA from degradation and loss to surrounding media. The obtained tracers had high electrostatic stability, shown by high absolute values of the zeta potentials (< -30 mV) and retained their magnetic properties after several functionalisation steps. qPCR data proved successful DNA binding and encapsulation in silica shell, thereby pointing at, not only, the possibility to produce infinite unique tracers, but also, aiming at multipoint tracing. DNA from all the systems was detected even at 30-fold dilution stating the high ultrasensitivity of the system to overcome dilution challenges.

References

(*1*) Sharma, A., Foppen, J. W., Banerjee, A., Sawssen, S., Bachhar, N., Peddis, D., and Bandyopadhyay, S. (2021). Magnetic Nanoparticles to Unique DNA Tracers: Effect of Functionalization on Physico-chemical Properties. *Nanoscale research letters 16*, 1–16.

(*2*) Jia, Y. P., Shi, K., Liao, J. F., Peng, J. R., Hao, Y., Qu, Y., Chen, L. J., Liu, L., Yuan, X., Qian, Z. Y., et al. (2020). Effects of cetyltrimethylammonium bromide on the toxicity of gold nanorods both in vitro and in vivo: molecular origin of cytotoxicity and inflammation. *Small Methods 4*, 1900799.

(*3*) Davis, K., Cole, B., Ghelardini, M., Powell, B. A., and Mefford, O. T. (2016). Quantitative measurement of ligand exchange with small-molecule ligands on iron oxide nanoparticles via radioanalytical techniques. *Langmuir 32*, 13716–13727.

(*4*) Wang, Y., Wong, J. F., Teng, X., Lin, X. Z., and Yang, H. (2003). "Pulling" nanoparticles into water: phase transfer of oleic acid stabilized monodisperse nanoparticles into aqueous solutions of α-cyclodextrin. *Nano Letters 3*, 1555–1559.

(*5*) Oh, T., and Kim, C. H. (2010). Study on characteristic properties of annealed SiOC film prepared by inductively coupled plasma chemical vapor deposition. *IEEE transactions on plasma science 38*, 1598–1602.

(*6*) Kumar, T. V., Prabhakar, S., and Raju, G. B. (2002). Adsorption of oleic acid at sillimanite/water interface. *Journal of colloid and Interface Science 247*, 275–281.

(*7*) Vasilakaki, M., Ntallis, N., Yaacoub, N., Muscas, G., Peddis, D., and Trohidou, K. (2018). Optimising the magnetic performance of Co ferrite nanoparticles via organic ligand capping. *Nanoscale 10*, 21244–21253.

(*8*) Tanaka, Y., Saita, S., and Maenosono, S. (2008). Influence of surface ligands on saturation magnetization of FePt nanoparticles. *Applied Physics Letters 92*, 093117.

(*9*) Peddis, D., Jönsson, P. E., Laureti, S., and Varvaro, G. In *Frontiers of Nanoscience*; Elsevier: 2014; Vol. 6, pp 129–188.

(*10*) Paunescu, D., Puddu, M., Soellner, J. O., Stoessel, P. R., and Grass, R. N. (2013). Reversible DNA encapsulation in silica to produce ROS-resistant and heat-resistant synthetic DNA'fossils'. *Nature protocols 8*, 2440–2448.

"Always laugh when you can, it is cheap medicine."

– Lord Byron

"Isn't it a bit unnerving that doctors call what they do 'practice'."

– George Carlin

7

Drug Delivery Systems & Biosensors

This chapter summarises the results of *Paper II*[1] and *Manuscript III*, looking into the potential applicability of NGs and IONPs for drug delivery and biosensing applications. This chapter is divided into into two sections describing each of the two biomedical applications. For drug delivery systems, loading and release studies were performed using a model protein drug – cytochrome *C* (Cyt C), with the NGs. The NGs were synthesised via the continuous-stirring and flashing-stirring methods, with varying degrees of AAc in the NG matrix. To mimic cancerous regions and elevated body temperatures, the release of Cyt C from the NGs was observed at 40 °C and at acidic pH. The second section of the chapter deals with the application of biosensing, where SNPs and Ag@SNPs, were characterised using the principles of *'Magnetophoresis'*.

7.1 Drug Delivery

This section highlights the potential of pNIPAm-pAAc-based NGs as drug delivery systems. The biocompatibility of the NG was studied, followed by the loading and release studies of Cyt C, and finally the drug release models commenting on the kinetics of drug release from these NGs.

7.1.1 Biocompatibility Studies

NGs, synthesised using the continuous-stirring method (NGs_CS), were used for biocompatibility studies using a whole blood model. Inflammatory responses in blood during exposure to potential drug carriers and NPs can be determined by quantifying pro-inflammatory cytokine production, the formation of the complement activation product soluble Terminal Complement Complex (TCC) and activation of the Complement Receptor 3 (CR3).[2,3] Release of cytokines, such as chemokine IL-8 and pro-inflammatory cytokines IL-1β, IL-6 and TNF-α, have been suggested as potent biomarkers for predicting the immunotoxic potential of NPs, due to high levels of induction being closely related

to change in cellular mechanisms and toxicity.[4] Therefore, biocompatibility studies were conducted on the pNIPAm-pAAc-based NGs using a human whole blood model, which is an *ex vivo* model allowing to study the complexity of complement activation by closely mimicking the *in vivo* conditions.[5]

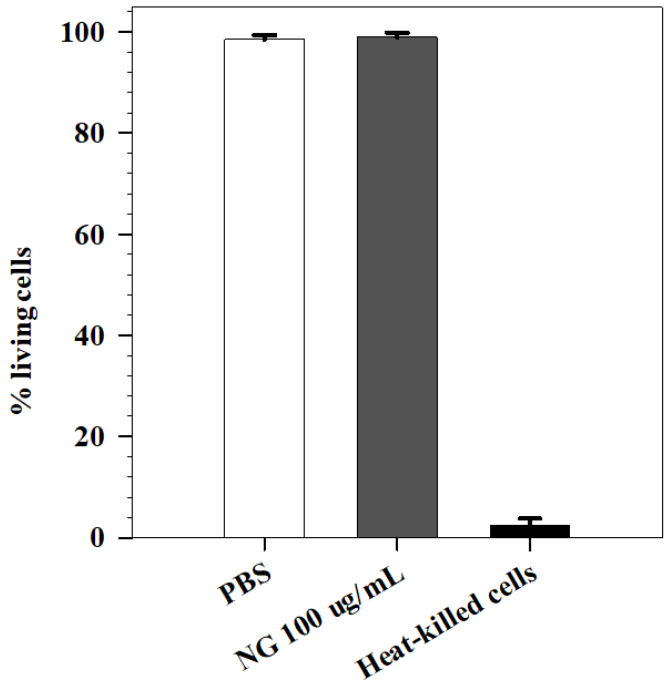

Figure 7.1: Cell viability of monocytes and granulocytes was maintained after NG incubation in human whole blood cells. Loss of cell viability is accompanied by disruption of plasma membrane integrity and increased PI permeability and nuclear staining. Quantification of dead versus viable cells (PI intensity) was done by flow cytometry with gating for the respective cell types.

Cell viability of monocytes and granulocytes in human whole blood was maintained after exposure to the NGs, as compared to the PBS control and heat-killed cells, as shown in Figure 7.1. TCC and CR3 activation was examined by measuring soluble TCC formation as shown in Figure 7.2 a). Neither did NG exposure significantly increase the formation of TCC in human whole blood cells nor activation of CR3 (Figure 7.2 b)). Therefore, it appears that the NGs do not significantly activate the complement system in human whole blood during the conditions examined.

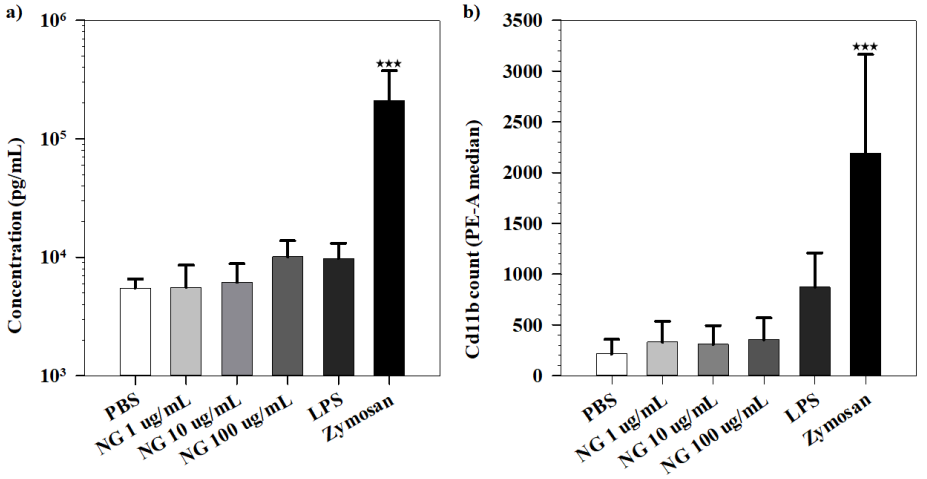

Figure 7.2: **a)** There was no significant increase in TCC formation during incubation of NGs in blood, as determined by ELISA for soluble TCC in the plasma. **b)** Assessment of CR3 activation in human whole blood cells by NGs as determined by Cd11b count. Error bars represent standard deviation, statistical significance (***P < 0.001) compared to the PBS control found by one-way ANOVA.

NGs also showed low production of cytokines, IL-1β, IL-6, IL-8 and TNF-α, compared to the baseline phosphate buffered saline (PBS) values and positive controls – Lipopolysaccharide (LPS). However, a minor, but not significant, increase of IL-6 was noted with the highest NG dose (100 μg/mL), and minimal, but statistically significant, reduction in IL-8 and TNF-α was found for the intermediate NG doses (1 and 10 μg/mL). Previous research has reported similar data using other cell based models,[6–8] however, whether the minimal decrease in IL-8 and TNF-α, relative to the PBS control is biologically relevant, can not be determined without vastly increasing the number of donors to exclude potential statistical sampling errors. Minimal effects on complement activation, cytotoxicity and production of pro-inflammatory cytokines in human whole blood cells, suggests that the NGs have good biocompatibility. On the other hand, there could be molecular processes induced by the NGs that are not accounted for by this model, such as, production of other cytokines or increased cellular stress mechanisms, coagulation effects and tissue reactions during prolonged exposure *in vivo*. Hence, further investigation of these properties may be considered in order to fully develop these NGs as drug carriers.

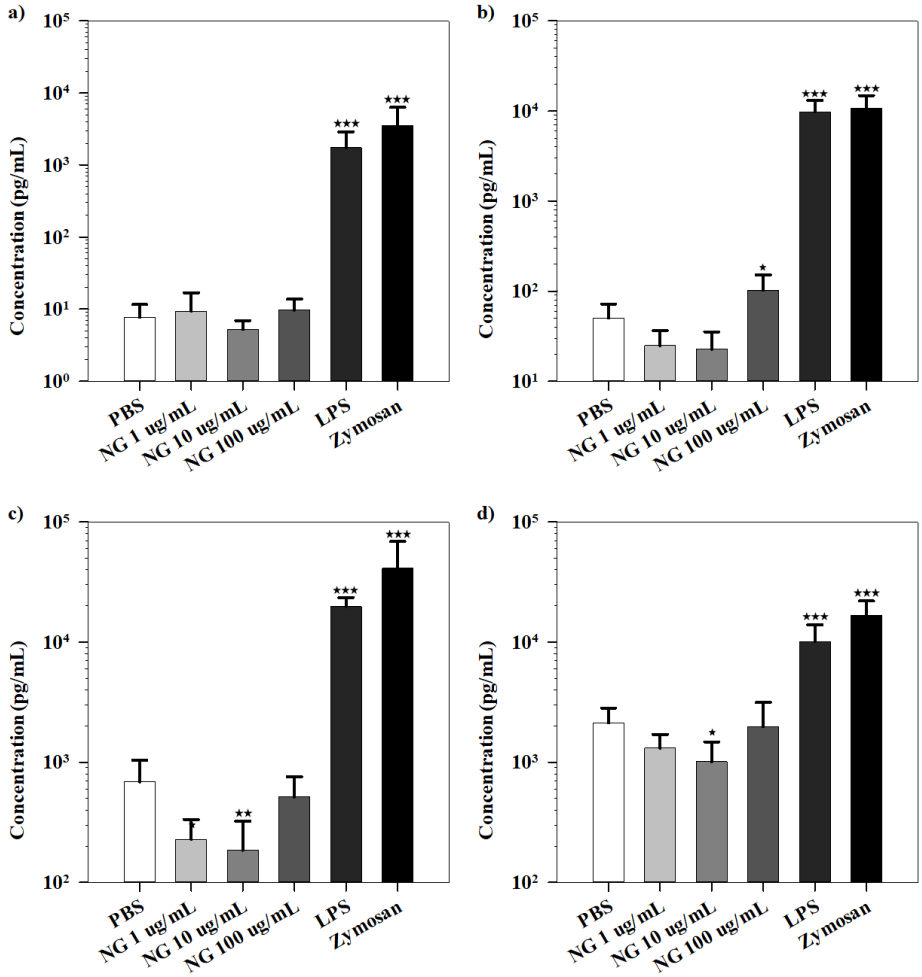

Figure 7.3: Plasma levels of pro-inflammatory cytokines **a)** IL-1β, **b)** IL-6, **c)** TNF-α, and **d)** chemokine IL-8. Error bars represent standard deviations. Statistical significance (*P<0.05, **P<0.1, ***P<0.1) compared to the PBS control found by one-way RM-ANOVA with Dunette post-test on log-transformed data (assuming log-normal distribution).

7.1.2 Drug Loading & Release

Cyt C was loaded in the NGs by *breathing-in technique*, where the NG incorporates the drug in the matrix as it swells on coming in contact with the drug solution. NGs with larger sizes have the capacity to imbibe more drug inside their matrix as they swell on coming in contact with drug solution, as shown in Figure 7.4. NGs, synthesised via the continuous-stirring (NGs_CS) and flashing-stirring (NGs_FS) methods, were used to study loading and release of Cyt C from the matrix. High loading (L.E.) and encapsulation (E.E.) efficiencies of 87.4 $\pm$ 12.2 % and 254.5 $\pm$ 36.4 μg/mg, respectively, was obtained for NGs_CS. Whereas, for NGs_FS, L.E. and E.E. increased with increasing AAc mole% reaching 70.3 $\pm$ 7.8 % and 414.0 $\pm$ 46.0 μg/mg, respectively, for 25 mole% AAc, as shown in Figure 7.5 a).

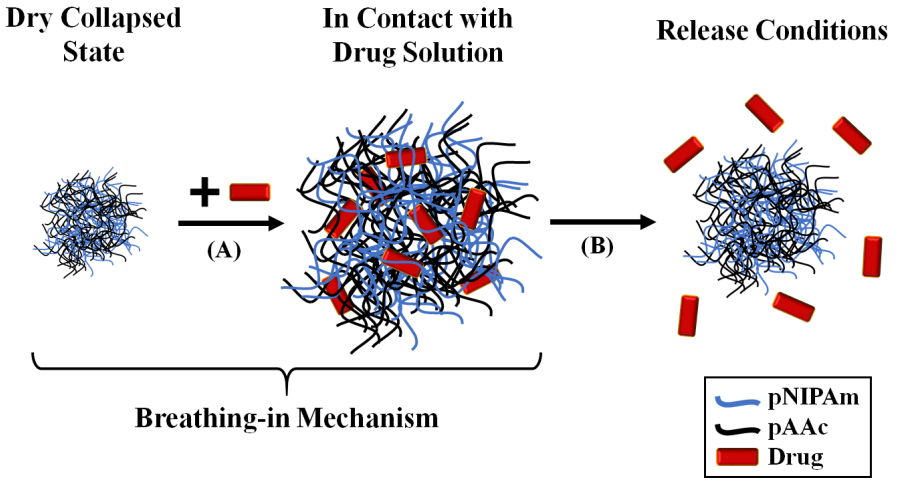

Figure 7.4: Schematic showing drug loading via the **(A)** breathing-in mechanism and **(B)** drug release via collapse of the stimuli-responsive NG.

Previous research has shown that the heme ligand, located in the lysine-rich region of Cyt C, interacts with the negatively charged hydrogel units via Coulombic forces, resulting in polymer-protein complex formation.[9] Therefore, increasing the number of carboxylic acid groups (as more AAc units are incorporated in the NG matrix) might lead to a higher number of binding sites for Cyt C thereby increasing drug loading.

As mentioned earlier, to mimic cancerous regions and elevated body temperatures, the release of Cyt C from the NGs was observed at 40 °C and acidic pH, as shown in Figure 7.5 b). NGs_CS particles were continuously exposed to 40°C, while NGs_FS particles were first subjected to pH = 3 for 30 h, followed by 40 °C and pH = 3. In the case of NGs_CS samples, the Cyt C release profiles at 40 °C and at 40 °C with pH = 3.5 coincided to a significant extent. It was seen that NGs_FS followed the release profile of NGs_CS for the initial part and almost plateaued out after 2 h. Drug release from NGs_CS was observed to be faster than NGs_FS with 50 % of Cyt C being released in the first 10 h as opposed to 27 % and 24 % for NGs_FS@AAc_10 and NGs_FS@AAc_15, respectively. The high release could be attributed to a higher amount of Cyt C in NGs_CS (L.E. = 87.4 $\pm$ 12.2 %) resulting in a larger drive for diffusion because of a larger concentration gradient.

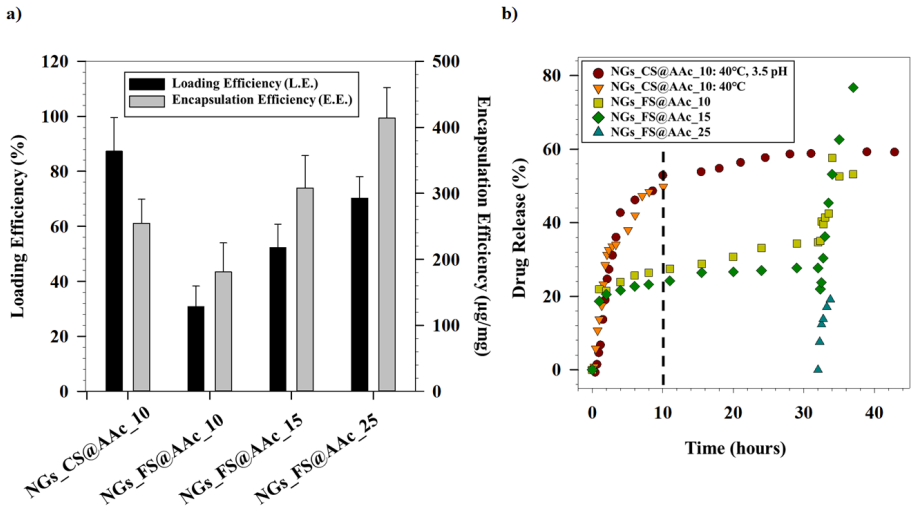

Figure 7.5: **a)** Loading and encapsulation effciencies of NGs_CS and NGs_FS. **b)** Release profiles of Cyt C from NGs_CS and NGs_FS at different temperatures and pH values.

Table 7.1: Extent of collapse of NGs_CS with temperature and pH stimuli.

Sample	Temperature-based collapse 25 – 40 °C [%]	pH-based collapse synthesis pH – ph = 3.5 [%]
NGs_CS@AAc_10	93.4 ± 1.7	6.8 ± 2.2
NGs_CS@AAc_15	91.9 ± 2.9	41.7 ± 1.1
NGs_CS@AAc_25	88.6 ± 2.3	51.3 ± 2.5

The temperature induces a greater collapse in the NGs compared to pH, as shown in Table 7.1. Therefore, as the release for NGs_CS is induced by temperature and pH, there is a higher driving force (expelling the drug from the NG matrix) owing to greater NG collapse. On the contrary, no Cyt C release is seen for NGs FS@AAc_25 when the system is exposed to just acidic pH conditions, even though the system had higher L.E. The release from this system occurs only after the temperature was raised above VPTT, to 40 °C. This fact, together with the similar release profiles for NGs_CS (40 °C and at 40 °C with pH = 3.5), further support the hypothesis that temperature has a greater impact on drug release than pH. Furthermore, the diffusion of Cyt C progresses in three probable zones. The first being transport of the drug from the NG matrix to the NG surface, second being transport of the drug from the NG's surface to the dialysis membrane, and the third, diffusion across the dialysis membrane into the sink. Owing to the larger size of the AAc_25 NGs, the drug needs to travel a larger distance (than for AAc_10 and AAc_15) to reach the NG surface before it can diffuse out of the NG matrix. Thus, an additional driving force is needed to drive the drug out of the NG matrix, provided by the temperature stimuli.

7.2 Biosensors

Magnetic NPs (MNPs) have been used for separation processes in biomedical applications, where magnetic-activated cell sorting (MACS) provides the means to separate cells of interest from mixed cell populations. Particularly, two techniques can be used to separate target cells from the medium,[10] as mentioned below.

- *Direct method*: MNPs are first functionalised with appropriate affinity ligands before being exposed to the target cells, where the NPs become bound to the target cells and the solution containing the complexes is allowed to flow through a separating column to which a magnetic field is applied.
- *Indirect method*: The affinity ligand is first added to the cell suspension that is subsequently captured by the MNPs (bearing an affinity ligand against the primary label) that can further be separated using an appropriate magnetic separator.

The magnetophoresis technique can be used for biosensing applications using MNPs that have high surface functionality. On application of an external magnetic field, MNPs move in the direction of the field with separation time depending on factors such as solvent viscosity, NP size and magnetic field strength. For a constant field and solvent viscosity, the velocity of separation varies directly with MNP size. These NPs can be functionalized with a ligand having functional groups that are complementary to the targeted antigen, thereby enabling attachment of the antigen to the MNPs and resulting in NP self-assembly. Once the self-assembled NPs are exposed to the magnetic field, they would separate out of the solvent with a particular separation velocity, compared to the non-self-assembled NPs. The variation in separation time would be an indicator of the presence of the antigen. Preliminary magnetic separation studies were conducted using a modified magnetophoretic set-up inside UV-Vis spectrophotometer over a period of 24 h.

7.2.1 Magnetic Separation Studies

Figure 7.6 a) shows the magnetic Ag@SNPs aqueous solution in the UV-Vis cuvette prior to exposure to the magnetic field. Due to the constant magnetic field gradient generated by the magnetophoretic instrument, Ag@SNPs were attracted and started separating in the UV-Vis cuvette, as shown in Figure 7.6 b). As the NPs started to separate, their UV-Vis absorbance decreased simultaneously, thereby further confirming NP separation in the presence of the magnetic field (Figures 7.6 c) and d)). Similar separation profiles were obtained at 350 and 450 nm, having two distinct separation zones (Zone 1 and Zone 2), whereby Zone 2 appeared $\sim$1 h after exposure to the magnetic field. The magnetic field acted more on larger particles, thus pulling them with greater velocities as compared to smaller ones. Therefore, larger particles have lower separation times than smaller particles, that have lower separation velocities. Hence, over a period of time, the UV-Vis separation spectra formed two distinct zones, resulting in two distinct sets of NP population consisting of larger (Figure 7.6 e)) and smaller NPs (Figure 7.6 f)), found in Zones 1 and 2 respectively.

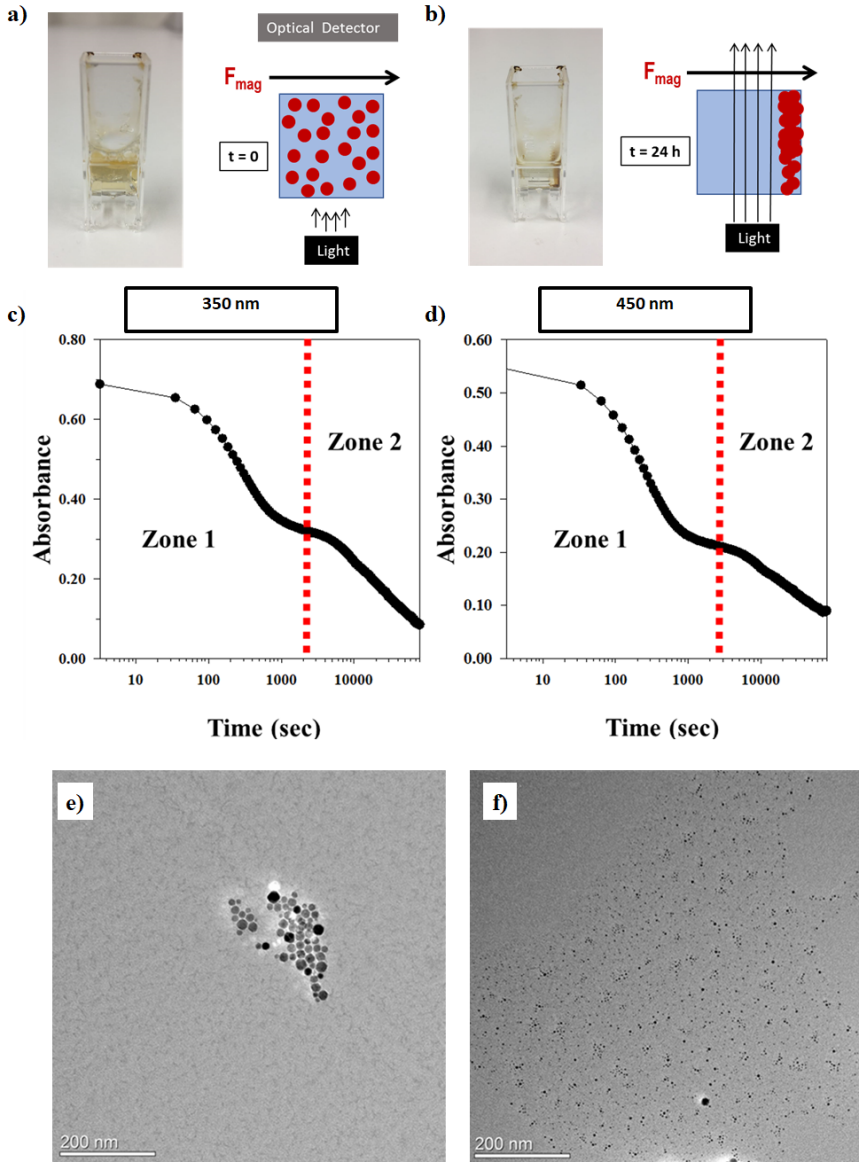

Figure 7.6: Schematic of Ag@SNPs **a)** before and **b)** after being exposed to the magnetophoretic setup. UV-Vis spectra of Ag@SNPs measured over 24 h at **c)** 350 nm and **d)** 450 nm. TEM images of Ag@SNPs taken from magnetophoresis study in **e)** Zone 1 and **f)** Zone 2.

7.3 Summary

The potential applicability of stimuli-responsive nanogels (NGs) and dimeric NPs in the field of biomedicine was described in this chapter. NGs, synthesised using continuous-stirring (NGs_CS) and flashing-stirring (NGs_FS) methods were loaded with a model protein drug, Cyt C, with loading efficiencies (L.E.) of 87.4 $\pm$ 12.2 % and 30.8 $\pm$ 7.4 % for NGs_CS and NGs_FS, respectively. The L.E. of NGs_CS can, however, be increased with increasing acrylic acid mole% in the NG system, from 10 to 25 mole%, as Cyt C interacts with the negatively charged hydrogel units via Coulombic forces, resulting in polymer-protein complex formation. Therefore, an increasing number of carboxylic acid groups (as more AAc units are incorporated in the NG matrix) might lead to a higher number of binding sites for Cyt C, thereby, increasing drug loading. The release of Cyt C from the NGs, conducted at 40 °C and acidic pH (pH= 3.5), showed similar release profiles for NGs_CS and NGs_FS for the first 2 h, following which, 50 % drug release was observed for the continuous-stirring system, whereas the NGs_FS showed only 27 %, in 10 h. The low release could reciprocate from lower L.E. of the flashing-stirring system providing lower concentration dependant drive for diffusion of Cyt C.

The magneto-plasmonic DNPs were used to demonstrate the magnetophoresis-based separation, to investigate their potential in biosensing applications. The separation of Ag@SNPs, carried out using the magnetophoresis-UV setup, resulted in two sets of particle populations based on particle sizes (zone 1 and zone 2). The larger particles are separated in the first hour of exposure to the magnetic field, while smaller particles separate with a lower velocity. These NPs can be used for the purpose of biosensing by studying the change in separation velocities (or time) of the bare IONPs and the IONPs attached to the analyte (antigen).

References

(*1*) Sharma, A., Raghunathan, K., Solhaug, H., Antony, J., Stenvik, J., Nilsen, A. M., Einarsrud, M.-A., and Bandyopadhyay, S. (2021). Modulating Acrylic Acid Content of Nanogels for Drug Delivery Biocompatibility Studies. *Journal of Colloid and Interface Science*.

(*2*) Fara, A., Mitrev, Z., Rosalia, R. A., and Assas, B. M. (2020). Cytokine storm and COVID-19: a chronicle of pro-inflammatory cytokines. *Open biology 10*, 200160.

(*3*) Halperin, J. A., Taratuska, A., Nicholson-Weller, A., et al. (1993). Terminal complement complex C5b-9 stimulates mitogenesis in 3T3 cells. *The Journal of clinical investigation 91*, 1974–1978.

(*4*) Elsabahy, M., and Wooley, K. L. (2013). Cytokines as biomarkers of nanoparticle immunotoxicity. *Chemical Society Reviews 42*, 5552–5576.

(*5*) Mollnes, T. E., Brekke, O.-L., Fung, M., Fure, H., Christiansen, D., Bergseth, G., Videm, V., Lappegård, K. T., Köhl, J., and Lambris, J. D. (2002). Essential role of the C5a receptor in E coli–induced oxidative burst and phagocytosis revealed by a novel lepirudin-based human whole blood model of inflammation. *Blood, The Journal of the American Society of Hematology 100*, 1869–1877.

(*6*) Bartlett, R. L., and Panitch, A. (2012). Thermosensitive nanoparticles with pH-triggered degradation and release of anti-inflammatory cell-penetrating peptides. *Biomacromolecules 13*, 2578–2584.

(*7*) Bridges, A. W., Singh, N., Burns, K. L., Babensee, J. E., Lyon, L. A., and García, A. J. (2008). Reduced acute inflammatory responses to microgel conformal coatings. *Biomaterials 29*, 4605–4615.

(*8*) Giulbudagian, M., Yealland, G., Hönzke, S., Edlich, A., Geisendörfer, B., Kleuser, B., Hedtrich, S., and Calderón, M. (2018). Breaking the barrier-potent anti-inflammatory activity following efficient topical delivery of etanercept using thermoresponsive nanogels. *Theranostics 8*, 450.

(*9*) Jain, P. K., Lee, K. S., El-Sayed, I. H., and El-Sayed, M. A. (2006). Calculated absorption and scattering properties of gold nanoparticles of different size, shape, and composition: applications in biological imaging and biomedicine. *The journal of physical chemistry B 110*, 7238–7248.

(*10*) Kang, J. H., Hahn, Y. K., Kim, K. S., and Park, J.-K. (2009). Magnetophoretic Biosensing and Separation Using Magnetic Nanomaterials. *Magnetic Nanomaterials*.

"Whatever you do in life, it's not legendary unless your friends are there to see it."

– Neil Patrick Harris

"Happiness can be found, even in the darkest of times, if one only remembers to turn on the lights."

– Albus Dumbledore

8 Papers & Manuscripts

8.1 Paper I

Sharma, A., Foppen, J.W., Banerjee, A., Sawssen, S., Bachhar, N., Peddis, D., Bandyopadhyay, S., 2021. Magnetic Nanoparticles to Unique DNA Tracers: Effect of Functionalization on Physico-chemical Properties. Nanoscale research letters, 16(1), pp.1-16. https://doi.org/10.1186/s11671-021-03483-5

Sharma *et al. Nanoscale Res Lett* (2021) 16:24
https://doi.org/10.1186/s11671-021-03483-5

Nanoscale Research Letters

NANO EXPRESS

Open Access

Magnetic Nanoparticles to Unique DNA Tracers: Effect of Functionalization on Physico-chemical Properties

Anuvansh Sharma[1], Jan Willem Foppen[2], Abhishek Banerjee[1], Slimani Sawssen[3,4], Nirmalya Bachhar[5], Davide Peddis[3,4] and Sulalit Bandyopadhyay[6,7*]

Abstract: To monitor and manage hydrological systems such as brooks, streams, rivers, the use of tracers is a well-established process. Limited number of potential tracers such as salts, isotopes and dyes, make study of hydrological processes a challenge. Traditional tracers find limited use due to lack of multiplexed, multipoint tracing and background noise, among others. In this regard, DNA based tracers possess remarkable advantages including, environmentally friendly, stability, and high sensitivity in addition to showing great potential in the synthesis of ideally unlimited number of unique tracers capable of multipoint tracing. To prevent unintentional losses in the environment during application and easy recovery for analysis, we hereby report DNA encapsulation in silica containing magnetic cores (iron oxide) of two different shapes—spheres and cubes. The iron oxide nanoparticles having size range 10–20 nm, have been synthesized using co-precipitation of iron salts or thermal decomposition of iron oleate precursor in the presence of oleic acid or sodium oleate. Physico-chemical properties such as size, zeta potential, magnetism etc. of the iron oxide nanoparticles have been optimized using different ligands for effective binding of dsDNA, followed by silanization. We report for the first time the effect of surface coating on the magnetic properties of the iron oxide nanoparticles at each stage of functionalization, culminating in silica shells. Efficiency of encapsulation of three different dsDNA molecules has been studied using quantitative polymerase chain reaction (qPCR). Our results show that our DNA based magnetic tracers are excellent candidates for hydrological monitoring with easy recoverability and high signal amplification.

Keywords: Hydrological tracers, Magnetic iron oxide nanoparticles, DNA encapsulation, Phase transfer, Silica nanoparticles

Introduction

Tracer tests are a widely used technique to investigate flow paths and travel times of solutes, particulates and contaminants in environmental waters [1, 2]. However, there are limited number of potential tracers available to hydrologists to study these dynamic processes. Traditional tracers, such as natural dissolved salts, stable isotopes, bromide, and fluorescent dyes [1, 3], have been reported to suffer from interference of background noise, high analysis costs, potential environmental contamination, signal contamination among others. Furthermore, application of tracers at larger scales/solvent volumes results in dilution effects that pose issues with their detection limits thereby becoming an important constraint.

DNA tracers have been reported to be specific, (i.e. bearing unique identifiers that do not suffer from interference due to background noise) environmentally friendly, ultrasensitive to detection and multiplex capable (i.e. enabling concurrent usage of a large number of species at a given time) [4–7]. Importantly, DNA tracers can be repetitively and thus exponentially amplified, using quantitative polymerase chain reaction (qPCR),

*Correspondence: ratnavo@gmail.com; sulalit.bandyopadhyay@ntnu.no
[6] Department of Water Management, Delft University of Technology, PO Box 5048, 2600 GA Delft, The Netherlands
Full list of author information is available at the end of the article

theoretically pushing the detection sensitivity down to one molecule [8, 9]. Hence, tracers containing DNA require a detection amount that is orders of magnitude lower than that of traditional tracers.

Foppen et al. and Sharma et al. were the first to test DNA as an applied tracer in surface water. Foppen et al. [10–12] compared the breakthrough and recovery rates of six different free DNA tracers and a conservative tracer in several stream channel experiments. These DNA tracers showed consistent advective–dispersive transport properties, but low mass recovery for the free DNA tracers (3–53%) compared with the conservative tracer (67–106%) [10]. This mass loss of the free DNA tracers was attributed to adsorption onto sediment particles, decay and/or biological uptake by microorganisms. Encapsulating DNA inside a protective shell was therefore suggested in order to enhance the longevity of the tracer.

To our knowledge, there are four types of encapsulated DNA tracers reported in the literature—(1) DNA wrapped and stabilized by a combination of polyamidoamine (PAA), a cationic homopolymer and a poly(ethylene) glycol (PEG)-poly(amidiamine) (PAA)-PEG copolymer (Garnett particle) [13], (2) iron oxide nanoparticles (IONPs) plus DNA, encapsulated by polylactic acid (PLA) (Sharma particle) [12], (3) silica core, surrounded by a layer of DNA and protected again by silica (Paunescu particle) [14, 15] and (4) magnetite with DNA wrapped around them and protected by silica cover (Puddu particle) [4]. In case of the latter two, DNA is encapsulated within silica shells, that have been shown to be heat and radical resistant, whereby isolating the DNA completely from the environment. However, in these studies, a single type of DNA has been used for fabrication of the tracer. More importantly, there is no report of how the magnetic properties of the tracers change during the functionalization process. This is important to understand since the rationale behind incorporating magnetic nanoparticles (MNPs) lies in fast and easy magnetic separation, better sample handling, absence of sample volume limitations and up-concentration. Studies so far have focussed only on magnetite as the core of the tracer. Particle size and shape of the IONPs among other factors have a crucial role in determining the magnetic properties of the tracers and in turn their magnetic harvesting for separation and analysis.

To obtain a precise control over the particle's size, shape and morphology and eventually, their magnetic properties, IONPs can be synthesized using thermal decomposition route. This refers to decomposition of iron precursors such as acetylacetonate, stearate, oleate or pentacarbonyl in the presence of stabilizing ligands in an organic solvent at high temperatures [16–19]. The finer control over particle size originates from temporal separation of nucleation and growth windows that promotes narrower size distributions in comparison to the more prevalent co-precipitation route. However, the obtained nanoparticles (NPs) in the former case are in organic phase that limits their use in environmental and biomedical applications [20–22]. Several reports have shown that the phase transfer of these NPs may be achieved using specific ligands such as tetra methyl ammonium hydroxide (TMAH), hexadecyltrimethylammonium bromide (CTAB), poly-ethylene glycol (PEG), sodium citrate (Na-citrate) and so on, guided by the synthesis route and application downstream [23–25]. Phase transfer however influences subsequent functionalization steps of tracer synthesis, such as binding of the DNA to the core, tracer encapsulation, etc. In cases, where the effect of particle's size, shape and morphology on functionalization needs to be investigated, selecting the same phase transfer methodology for all the particle types deems necessary. In order to achieve this, developing repeatable and tunable protocols becomes utmost important.

Further, functionalization steps can impact the magnetic properties of the final tracer particle, whereby affecting their applicability downstream. In fact, the molecular coating can strongly influence surface magnetism of the particles, altering the magnetic properties [26, 27]. An understanding of how the physico-chemical properties vary subsequently with the functionalization route is believed to be a precursor in understanding the final functional properties of the tracers. However, such reports are missing in literature. Herein, we report a robust approach to synthesize spinel IONPs via co-precipitation and thermal decomposition routes, followed by functionalization with three different types of double-stranded DNA (dsDNA). The type of the dsDNA used for functionalization provides for the uniqueness of the tracer. Thereafter, we silanize the DNA functionalized IONPs to encapsulate the DNA inside a protective shell, thereby producing customizable, hydrological tracers bearing unique DNA tracer moieties. Our work reports, for the first time, how the magnetic properties alter along the functionalization route—from IONPs to DNA based magnetic tracers, with an aim to understand structure-properties relations for the tracers.

Method Section

Iron(II)chloride tetrahydrate ($FeCl_2.4H_2O, \geq 99\%$), 1-octadecene (ODE, technical grade 90%), oleic acid (OA, technical grade 90%), sodium citrate dihydrate (Na-citrate, $\geq 99\%$), tetramethylammonium hydroxide solution (TMAH, ACS reagent) and tetraethyl orthosilicate (TEOS, reagent grade 98%) were purchased from Sigma-Aldrich® (Schnelldorf, Germany).

Cetyltrimethylammonium bromide (CTAB, ≥ 99%) and iron(III)chloride hexahydrate ($FeCl_3.6H_2O$, ≥ 99%) were bought from Acros Organics® (Geel, Belgium). Trimethoxysilylpropyl-N,N,N-trimethylammonium chloride (TMAPS, in 50% methanol) and sodium oleate (> 97%) were purchased from abcr® (Karlsruhe, Germany) and Tokyo Chemical Industry (TCI, Japan), respectively. Ammonium hydroxide solution (25 wt%) was bought from Merck Life Sciences AS. The 3 dsDNA namely, T21, GM5 and GM6 were supplied by Biolegio B.V. (Nijmegen, Netherlands) and further details regarding the dsDNA can be found in the Additional information 1 (SI, Materials and Methods). All the chemicals were used as received without any further purification or modification. All solutions were prepared using distilled de-ionized water (MilliQ water), having a resistivity ~ 18.2 MΩ/cm at 25 ℃, taken from Simplicity® Millipore (Darmstadt, Germany) water purification system.

Synthesis of IONPs

Co-precipitation

The synthesis process has been adapted from previously reported studies and involves weighing 84.6 mg of MilliQ water in a beaker and adding 15.4 mL of 25% (wt) NH_4OH solution to prepare a 1 M solution [4]. Separately, 8.0 g of FeCl2.4H2O and 21.6 g of $FeCl_3{\cdot}6H_2O$ were weighed and dissolved in 100 mL MilliQ water in a volumetric flask. 10 mL of this solution was added to 100 mL of 1 M ammonia solution dropwise (using a burette), the reaction being kept under vigorous stirring. The NPs were obtained using magnetic separation by several washing cycles with water. These particles have been referred to as 'Mag' in this report.

Thermal Decomposition

Spherical and cubic IONPs were synthesised using thermal decomposition of Fe oleate precursor at elevated temperatures in inert (argon) atmosphere. The temperature of the reaction was raised using a temperature controller (MRC® Heating mantle 100 mL with analog control and Digital 4 programs × 16 segment programmer) for precise control of the heating rate.

Iron Oleate The iron-oleate complex was prepared using our previously reported protocol [28]. In essence, 5.40 g of $FeCl_3{\cdot}6H_2O$ and 18.25 g of sodium oleate were dissolved in a mixture of solvents consisting of 40 mL ethanol, 30 mL deionized water and 70 mL hexane, in 250 mL round bottom flask. The resulting solution was refluxed at 70 °C for 4 h under vigorous stirring using a bar magnet. The resulting dark red organic phase, containing iron oleate complex, was transferred to a separator funnel and washed three times with MilliQ water. The remaining hexane solution was evaporated in a Heidolph rotary evaporator ($T = 70$ °C) to yield a highly viscous dark red liquid of iron oleate.

Iron Oleate: Spheres (SNPs) The synthesis protocol, adapted and modified from previous works conducted by our group, involved mixing 1.6 g of iron oleate, 600 µL OA and 25 mL 1-octadecene (ODE) in a three-necked glass reactor, placed over a heating mantle fitted with a cooling water condenser [28]. The reaction was carried out under argon atmosphere. The temperature of the reactor was ramped from room temperature to 320 ℃ at 3 ℃/min. The reaction was maintained at 320 ℃ for 45 min after which the solution was cooled down to room temperature. NPs were then washed using hexane and precipitated out using a mixture of isopropanol and hexane. The particles were magnetically separated and washed thrice using acetone before finally redispersing in a known volume of toluene.

Iron Oleate: Cubes (CNPs) Adapted and modified from our group's work, in a typical synthesis, 0.833 g of iron oleate, 213 mg sodium oleate and 14 mL ODE were heated in a three-necked glass reactor placed on a heating mantle, fitted with a cooling water condenser, to 325 ℃ at 2.8 ℃/min under argon atmosphere [29]. The reaction was maintained at 325 ℃ for 45 min after which the NPs were cooled to room temperature. NPs were then washed using hexane and precipitated out using a mixture of isopropanol and hexane. The particles were magnetically separated and washed thrice using acetone before finally redispersing in a known volume of toluene.

Growth Kinetics

We characterized the growth of SNPs obtained from the decomposition of iron oleate precursor in ODE. Small sample volumes were taken at defined time intervals and analysed using transmission electron microscopy (TEM) and Fourier transform infrared (FTIR) spectroscopy without further cleaning.

We have developed a mechanistic model and carried out kinetic Monte Carlo simulation to understand the growth kinetics of the NPs following our previous work [30]. Our simulation data matched the mean of the particle size distribution (PSD) obtained from analysing the TEM images of SNPs presented in this work. The details of the simulation are reported in the Additional information 1 (Sect. 2).

Phase Transfer and Functionalization of IONPs

Phase transfer of SNPs and CNPs was carried out using either CTAB, Na-Citrate or TMAH. The detailed procedure can be found in the Additional information 1

(Sect. 3). Once the NPs were successfully phase transferred, they were redispersed either in MilliQ water or isopropanol before further analysis or functionalization. For Mag, direct functionalization was carried out, since the NPs were already dispersed in aqueous phase.

A known amount of IONPs in water (Mag, SNPs and CNPs) were taken and cleaned thrice with isopropanol before finally dispersing in 1 mL isopropanol in a 1.5 mL Eppendorf tube. 10 µL of TMAPS was added to the IONP solution and put on overnight shaking. The samples were collected afterwards, cleaned thrice with isopropanol and redispersed in 1 ml isopropanol.

In a process to functionalize IONPs with dsDNA, a known quantity of IONPs functionalized with TMAPS (Table 1) was added to a predetermined amount of dsDNA (optimized through preliminary experiments) in a 1.5 mL Eppendorf tube. The solution was kept at rest and allowed to react for 4 min. The DNA functionalised NPs were then magnetically separated and cleaned three times with MilliQ water and finally redispersed in 0.5 mL MilliQ water.

After successful binding of dsDNA, 1 µL TMAPS was added to 0.5 mL NP solution followed by 1 µL TEOS and the samples were left on shaking for 4 h. 8 µL of TEOS was further added to the solution after 4 h and the shaking was continued for 4 days after which the particles were magnetically separated and cleaned thrice with MilliQ and redispersed in known volume of MilliQ water.

Characterization Techniques

Transmission Electron Microscopy (TEM)

High resolution images were taken using the JEOL 2100 transmission electron microscope (Tokyo, Japan) operating at 200 kV. TEM grids were prepared by placing several drops of the dilute solution on a Formvar carbon-coated copper grid (Electron Microscopy Sciences) and wiping immediately with Kimberly-Clark wipes to prevent further aggregation owing to evaporation at room temperature.

Table 1 Showing the amount of IONPs taken for surface functionalization with TMAPS and dsDNA respectively

	IONP amount (mg)	TMAPS (µl)	IONP amount (mg)	dsDNA (T21, GM5, GM6) (µl)
Mag	50	10	0.75	20
SNPs	20	40	0.36	20
CNPs	10	20	0.30	20

Attenuated Total Reflection-Fourier Transform Infrared (ATR-FTIR)

The attenuated total reflection-Fourier transform infrared (ATR-FTIR) spectra were obtained using a Vertex 80v vacuum FTIR spectrometer. OPUS software was used to record spectra between 600 and 4000 cm^{-1} using 50 scans at a resolution of 4 cm^{-1}. The spectral absorbances were normalized with respect to the highest absorbance value obtained. In case of the growth kinetic studies of SNPs, sample aliquots were taken at defined temperatures during the reaction and the samples were analysed without further cleaning. On the other hand, for the phase transferred samples, NPs were cleaned thrice using MilliQ water before analysis.

Dynamic Light Scattering (DLS)

The size distribution and zeta potential of the NPs were measured using a Malvern Zetasizer Nano-ZS instrument (Malvern Instruments Ltd., Worcestershire, UK) and the manufacturer's own software. The solvent used for all the NPs was MilliQ water.

Super Conducting Quantum Interference Device (SQUID) Magnetometry

DC magnetization measurements were performed with superconducting quantum interference device (SQUID) magnetometer (H_{max} = 5.5 T, T = 5–400 K). The sample, in the form of powder or liquid, was placed in a capsule, in order to prevent any movement of the NPs during the measurements. All the magnetic measurements were normalized by the mass of the magnetic component of the sample. Magnetization measurements were carried out as a function of temperature from 5 to 300 K using ZFC–FC (Zero Field Cooled–Field Cooled) protocols with an applied field of 25 Oe. Room temperature magnetic properties were investigated using a vibrating sample magnetometer (model 10—MicroSense, H_{max} = 20 kOe).

Thermogravimetric Analysis

The mass of ligand on the IONPs was calculated using thermogravimetric analysis of the samples using the SDT Q600 Thermogravimetric Analyser (TA® Instruments, Delaware, USA) and the manufacture's inbuilt software.

qPCR Analysis

In order to determine DNA, samples in 400 µL MilliQ water were sent to IHE Delft and stored cool upon arrival. Prior to qPCR, samples were dispersed, and vortexed 3 times @ 3000 rpm for 30 s and sonicated for 10 s (Hielscher UP200 St Vial Tweeter sonicator). Then, MilliQ water was added to a total volume of 1000 µL. In order to remove free DNA, not covered by silica,

1.25 µL commercial bleach was added, and the mixture was vortexed for 15 s. After 1–2 min, the particles were magnetically separated, washed twice with MilliQ water, and finally resuspended in 1 mL MilliQ water. This was the stock solution or D0. From D0, four tenfold dilutions (D1–D4) were prepared and DNA concentrations were determined from the two most dilute samples (D3 and D4). Thereto, 20 µL D3 and D4 were taken out and, in order to dissolve particles and release DNA, 1 µL of fluoride buffer (2.3 g of $(NH_4)HF_2$ and 1.9 gm of NH_4F in 10 mL water), called Buffered Oxide Etch (BOE) was added and allowed to stand for 10 min. From this, 4 µL of D3 or D4 was taken to which 16 µL of PCR mix was added. In case of DNA tracer T21, the PCR mix composed of 2 µL 10X PCR buffer, 0.8 µL $MgCl_2$ buffer, 1 µL dNTP mix, 1 µL Taq polymerase, 10.65 µL DEPC treated water, 0.125 µL F-primer and R-primer, and 0.3 µL of probe, composed of a FAM fluorophore and a black hole quencher. In case of the other two tracers, again 4 µL of D3 or D4 was taken and 16 µL of PCR mix was added, composed of 15.75 µL KAPA SYBR FAST qPCR Master Mix (2X) Universal (Kapa Biosystem), 0.125 µL of both F-primer and R-primer. Samples were inserted in a qPCR apparatus (BioRad Mini-Opticon). The protocol of T21 was 3 min at 95 ℃, followed by 40 cycles of a two-step thermal profile (15 s at 95 ℃, 60 s at 60 ℃). The protocol of the other two tracers was 6 min and 40 s at 95 ℃, followed by 41 cycles of a three-step thermal profile (14 s at 95 ℃, 27 s at 58 ℃, 25 s at 72 ℃).

Results and Discussion

In order to develop DNA based magnetic tracers for hydrology, three important aspects need to be considered—controlling the size and shape of the magnetic core, protection of the DNA (unique tracer moiety) through robust functionalization procedures and understanding how sequential functionalization influences the magnetic properties of the final tracer particles.

Controlling the Particle Size and Shape

The magnetic cores in the DNA based tracers have been synthesized using co-precipitation and thermal decomposition routes. The IONPs synthesized using co-precipitation are referred to as 'Mag', while the spherical and cubic IONPs synthesised using thermal decomposition of Fe oleate precursor are named as 'SNPs' and 'CNPs' respectively.

Figure 1a, b show the schematics of the synthesis routes of different IONPs via co-precipitation and thermal decomposition respectively. The ratio of the metal precursor (Iron oleate) to reducing/stabilizing (Na-oleate/OA ratio) agents influences the size, shape and morphology evolution of the IONPs. The growth of IONPs is governed by the decomposition of iron oleate precursor at high temperatures, which in turn influences the choice of solvent. On the other hand, the size of the NPs is clearly determined by the reaction time, temperature, and concentration [31]. TEM images in Fig. 1c–f, show the evolution of the spherical IONPs as a function of reaction time and reaction temperature. Nucleation starts at temperatures above 300 ℃ via 'burst mechanism' that ends quickly as the reaction enters growth regime and the NPs undergo sustained growth resulting in narrow particle size distribution as reported by others [32, 33]. However, we found the presence of some fully formed particles at 250 ℃ (Additional file 1: Figure S1a) that we attribute to stochastic growth arising from some premature decomposition of iron oleate resulting from heterogeneous nucleation at surface walls or via creation of pockets of supersaturation.

This burst nucleation along with the rapid increase in the number of particles can be distinctly seen from representative TEM images of the aliquot at the reaction temperature of 310 ℃ (Fig. 1d). Subsequently, the rapid consumption of the monomer causes the supersaturation to decrease and only the nuclei bigger than the critical size grow to form final NPs as the reaction time increases up to 320 ℃, after which the reaction is maintained for 45 min. (Fig. 1e, f) However, the supersaturation is high enough for diffusion-controlled growth that focuses on narrowing particle size distribution by allowing the smaller particles to grow rapidly compared to the bigger particles, owing to the higher surface energies of the smaller particles. The decrease in polydispersity along with the increase in mean particle size are characteristic of this growth regime and can be seen in Fig. 1g. Ostwald ripening may dominate in the later stages of the growth process that acts contrary to the diffusion-controlled growth as it allows bigger particles to grow on the expense of the smaller ones, thereby broadening the particle size distribution (PSD).

To further verify the mechanism discussed above, we have developed a model of particle formation which consists of an instantaneous reaction followed by nucleation and subsequent growth of nuclei (Additional file 1: Sect. 2). The growth consists of three main mechanisms, namely diffusion-controlled growth, coagulation due to Brownian collisions and Ostwald ripening. The simulation data matches well with the mean of the PSD from the experimental data of SNPs (Additional file 1: Figure S1b), however the standard deviation of the distribution is being overestimated from the model. We observe that the experimental data matches better (Additional file 1: Figure S1c) when Ostwald ripening is included in the mechanism. However, such a simplified model with several assumptions (viz. instantaneous reaction, lumped

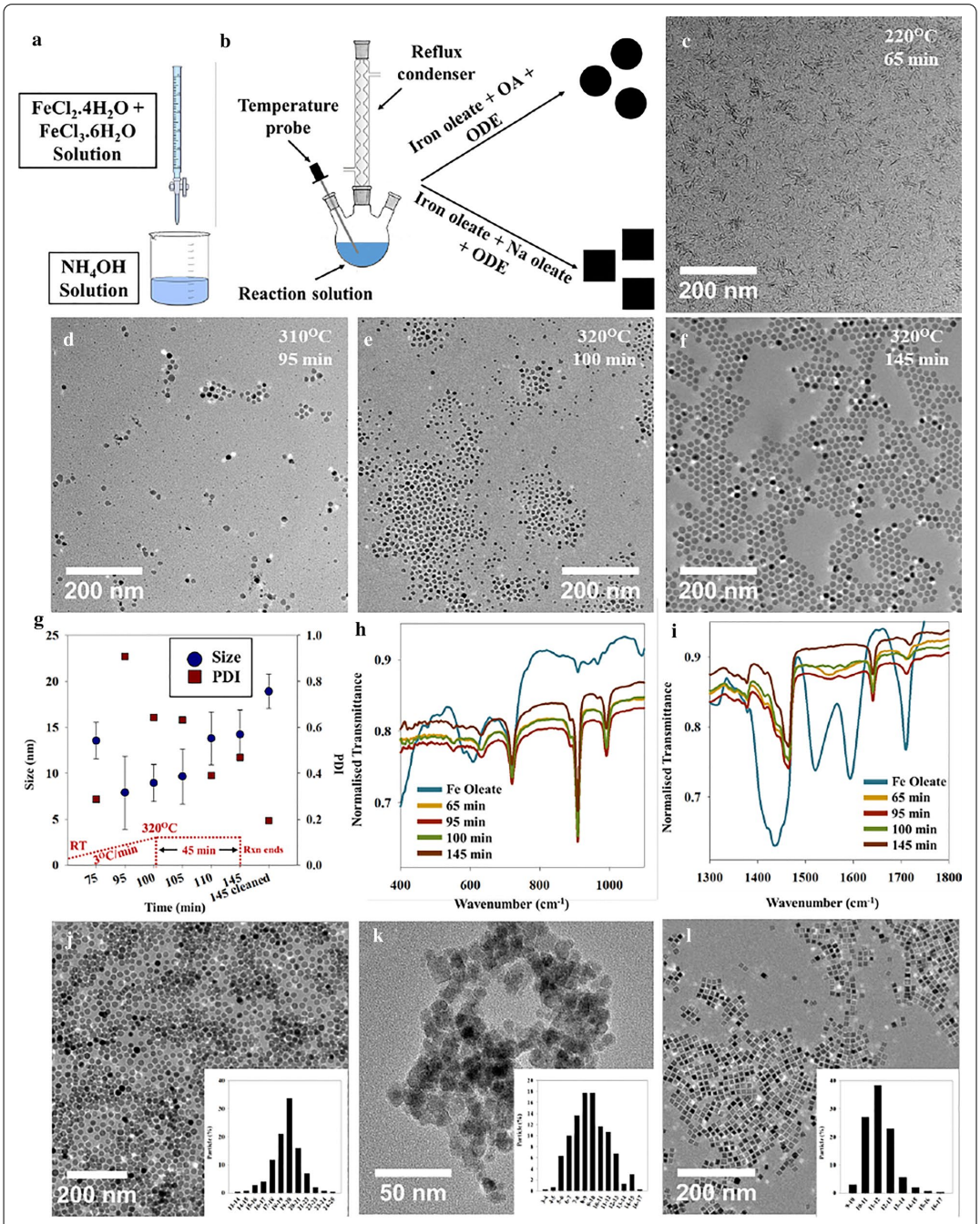

Fig. 1 Schematic representing the synthesis route of IONPs via **a** co-precipitation and **b** thermal decomposition. **c**–**f** TEM images and **g** size/PDI, vs SNPs synthesis reaction times (RT = room temperature, Rxn = reaction). **h**, **i** FTIR spectra showing the development of SNPs with the decomposition of iron oleate. TEM images and size distribution histograms of the finally obtained IONPs **j** SNPs, **k** Mag and **l** CNPs

coagulation parameter, onset of Ostwald ripening) may not be adequate to capture the entire growth kinetics (Additional file 1: Sect. 4.1). For this reason, we leave the effect of Ostwald ripening on growth mechanism, as an open question that should be addressed through future experiments and simulations.

A monodisperse particle size distribution of SNPs is obtained as a result of distinct separation of the nucleation and growth regions resulting in final particle size of ~ 14 ± 3 nm [before cleaning (Fig. 1f)] and ~ 19 ± 2 nm [after cleaning (Fig. 1j)] [34]. The polydispersity of the particles is seen to decrease as NP size increases with the NPs becoming more spherical with reaction time and achieving a final PDI of ~ 0.2 (Fig. 1g). ImageJ software was used to calculate the particle sizes from the TEM images (i.e. Fig. 1c–f). 300–1000 particles were analysed per image and the average size and standard deviation of these have been plotted in Fig. 1g. Further, we investigated the growth mechanism by following the evolution of the FTIR spectra of the reaction aliquots taken out at specific time intervals as shown in Fig. 1h, i.

The bands around 1711 cm^{-1} can be attributed to the carbonyl group of the oleic acid (OA) whereas the vibrational frequencies at 1608, 1519, and 1444 cm^{-1} belong to carboxylate groups, characteristic of the oleate complex (Fig. 1i). In addition, the region between 1300 and 1700 cm^{-1} can be used to deduce the carboxylate coordination mode and the presence of these distinctive FTIR bands indicate that the structure of our oleate complex is bidentate as has also been reported by Bronstein et al. [33]. The removal of (OA) surrounding iron oleate starts around 170 ℃ and is followed by decomposition of the first oleate chain at 250 ℃, forming Fe^{2+} attached to two other oleate chains. Pure metal carboxylates decompose at temperatures near to or higher than 300 ℃ resulting in the formation of thermal free radicals [33]. The synthesis reaction for generating iron oxide nanocrystals is carried out by heating the solution of iron-oleate complex in a high boiling, long-chain hydrocarbon solvent, 1-octadecene (ODE). The gradual disappearance of the carboxylate peaks as a function of reaction time culminating in complete disappearance at end of reaction, as shown in Fig. 1i, stating successful decomposition of the metal-oleate complex, further supports our classical nucleation-growth model comprising burst nucleation and diffusion-controlled growth.

To gain information about the type of iron oxide formed in our system, FTIR of SNPs in the range 400–750 cm^{-1} were analysed (Fig. 1h). The absorption bands in the range 400–750 cm^{-1} are attributed to Fe–O vibration modes. IONPs can exist mainly in different polymorphs, magnetite (Fe_3O_4), hematite (α-Fe_2O_3), maghemite (γ-Fe_2O_3), as well as others designated as β-Fe_2O_3 which is rarely found. For Fe_3O_4, only one band exists around 574 cm^{-1} whereas, two and three bands can be seen for α-Fe_2O_3 and γ-Fe_2O_3 in the range 500–700 cm^{-1} respectively. From the XRD pattern (Additional file 1: Figure S1d), very broad features are observed confirming the small size of the NPs. Diffractions at 2θ values around 30°, 35°, 42° and 63° correspond to the lattice planes {220}, {311}, {400} and {440} respectively, of the cubic spinel z of magnetite [35, 36]. It is difficult to make a concrete distinction between the inverse cubic spinel magnetite (Fe_3O_4) and tetragonal maghemite (Fe_2O_3) phases from XRD due to their similar crystal structures. Furthermore, presence of maghemite could be attributed to oxidation on exposure to air during NP drying. The broad peak around $2\theta = 20°$ could be due to OA, suggesting the coating of OA on NPs, acting as a stabilizing agent preventing agglomeration [36].

In the current study, besides the spherical IONPs discussed above (SNPs), two other IONPs were also synthesized, one using co-precipitation route (Mag) and other using the thermal decomposition route in the presence of sodium oleate (instead of OA) resulting in cubic IONPs (CNPs). Figure 1j–l, show representative TEM images of SNPs, Mag and CNPs respectively with 300 particles analysed for each respectively. Even though the co-precipitation route provides high product purity without unwanted organic solvents and use of high synthesis temperatures, this method produces NPs having a broader size distribution (without stabilizing agent). This is reflected by a higher poly dispersity index (PDI) of 0.24 in comparison to SNPs (PDI = 0.08) and CNPs (PDI = 0.09), synthesized via thermal decomposition methods. The higher degree of control of NP size in case of the latter method can primarily be attributed to temporal separation of nucleation and growth windows during the particle formation phase, leading to monodispersity. Further, thermal decomposition helps in controlling the shape of the IONP in the presence of stabilizing ligands (such as sodium oleate) as is reported here and in our previous studies [29]. Sodium oleate preferentially binds to the {100} facet over {111} preventing growth in that direction, allowing the {111} to grow faster leading to the formation of cube shaped NPs [37]. However, both SNPs and CNPs, being synthesized in organic solvents cannot be directly applied for hydrological applications which require the use of water dispersible tracers, thereby, necessitating phase transfer and subsequent functionalization of SNPs and CNPs.

Phase Transfer and Functionalization of IONPs

Phase Transfer

In an attempt to transfer the SNPs and CNPs synthesized via thermal decomposition from organic solvent to water, functionalization strategies using various ligands are reported here. Table 2 shows the sizes and zeta potentials of the phase transferred SNPs and CNPs using different ligands. The phase transfer can primarily be achieved using two pathways; partial or complete replacement of the existing hydrophobic ligand with the hydrophilic ligand referred to as 'ligand-ligand exchange', or modification of the existing hydrophobic ligand with a hydrophilic ligand. The choice of ligands has been optimized through preliminary studies (not shown here) with an aim to control the surface charge of the phase-transferred NPs.

Both the NPs are seen to have hydrodynamic diameters, which are at least one order of magnitude higher than their respective TEM particle sizes (SNPs: ~ 19 ± 2 nm; CNPs: 12 ± 1 nm) before phase transfer. This suggests that during the process of functionalization, the ligand forms weak interactions among several NPs, resulting in larger hydrodynamic diameters. The reported functionalization strategies have been shown to be reproducible and robust (Additional file 1: Figure S2a and S2b), thereby allowing tunability of the surface functional groups, particle size and surface charge. Further, all the NPs show high electrostatic stabilities represented by high zeta potential values (positive or negative). The relative differences in zeta potentials among the samples reported can be traced back to different particle sizes, ligands, treatment conditions among others.

To further understand the surfaces of our phase transferred NPs and the functionalization mechanism, we performed a series of FTIR studies (Additional file 1: Figure S2c and S2d). Na-citrate functionalized SNPs are found to be anionic [38]. The sharp absorption bands at 1383 and 1584 cm^{-1} for pure Na-citrate show the stretching of asymmetric and symmetric carbonyl groups (C=O) respectively. These vibrations are greatly reduced for the Na-citrate functionalised SNPs showing interaction of C=O groups with the surface of SNPs. Concurrently, the absence of characteristic peaks of surface bound OA (stretching of asymmetric and symmetric hydrocarbon chains at 2850 and 2923 cm^{-1}) in the case of SNPs with Na-citrate, further suggest complete replacement of OA. Therefore, ligand-ligand exchange happens whereby a small molecule (Na-citrate) easily displaces longer hydrocarbon chains that of surface bound OA, leading to negative surface charge in water. On the other hand, SNPs functionalized with CTAB are observed to be cationic. The absorbance bands for pure CTAB seen at 942 and 980 cm^{-1} depict C–N bond and $–CH_3$ groups stretching respectively (Additional file 1: Figure S2c and S2d). For SNPs coated with CTAB, the vibrations at 942 and 980 cm^{-1} are highly reduced and shift in comparison to CTAB. This is due to the interaction of the N^+ group with SNPs leading to reduced absorbance of its own C–N bond stretching, confirming SNPs' functionalization with CTAB. Although the intensity of the surface bound OA bands at 2850 and 2923 cm^{-1} is reduced, these overlap with CTAB hydrocarbon bands in the same range. Therefore, we believe that chemisorption of CTAB molecules on the SNP surface happens either via complete removal of the surface bound OA or formation of inclusion complexes with OA, characteristic of a quaternary amine, reported in case of other quaternary amines such as α-cyclodextrin [38].

Unlike the CTAB functionalized SNPs, for successful binding of negatively charged DNA to the surface of phase transferred IONPs, it is imperative to decorate the surface with positive charges. This is achieved by first phase transferring SNPs and CNPs with TMAH (as described above), and subsequently functionalizing with TMAPS. On the other hand, this phase transfer protocol is not needed for Mag NPs (synthesized via co-precipitation) which are directly functionalized with TMAPS. A schematic representation is shown in Fig. 2a.

Table 2 DLS results showing the size and zeta potentials of the different phase transferred SNPs using various ligands

Iron precursor	Ligand	Size (nm)	Zeta potential (mV)
SNPs	Na-citrate	343 ± 5	− 49.7 ± 0.1
	CTAB	364 ± 10	32.0 ± 0.0
	TMAH	495 ± 11	− 10.0 ± 2.5
CNPs	TMAH	272 ± 20	− 38.6 ± 2.8

Surface Charge Modification

Figure 2b shows the ATR-FTIR spectra obtained for studying the surface modification of SNPs and CNPs functionalized with THAH and further with TMAPS. The absorbance at 1031 cm^{-1} for TMAPS corresponds to the stretching of –Si–O–C– [39]. This vibration is absent in case of both SNPs and CNPs functionalized with TMAH and TMAPS (Fig. 2b, c) owing to the interaction of $–N(CH)_3$ group of TMAH with –Si–O– of TMAPS during the modification process. Complete removal of OA can be concluded from the disappearance of the asymmetric and symmetric long chain hydrocarbon vibrations of OA at 2850 and 2923 cm^{-1} (Fig. 2b). Appearance of a sharp absorbance band at 2972 cm^{-1} in case of SNPs functionalized with TMAH and TMAPS (shown in Fig. 2b) is due to singly bonded –C–H groups of isopropanol, TMAPS and TMAH.

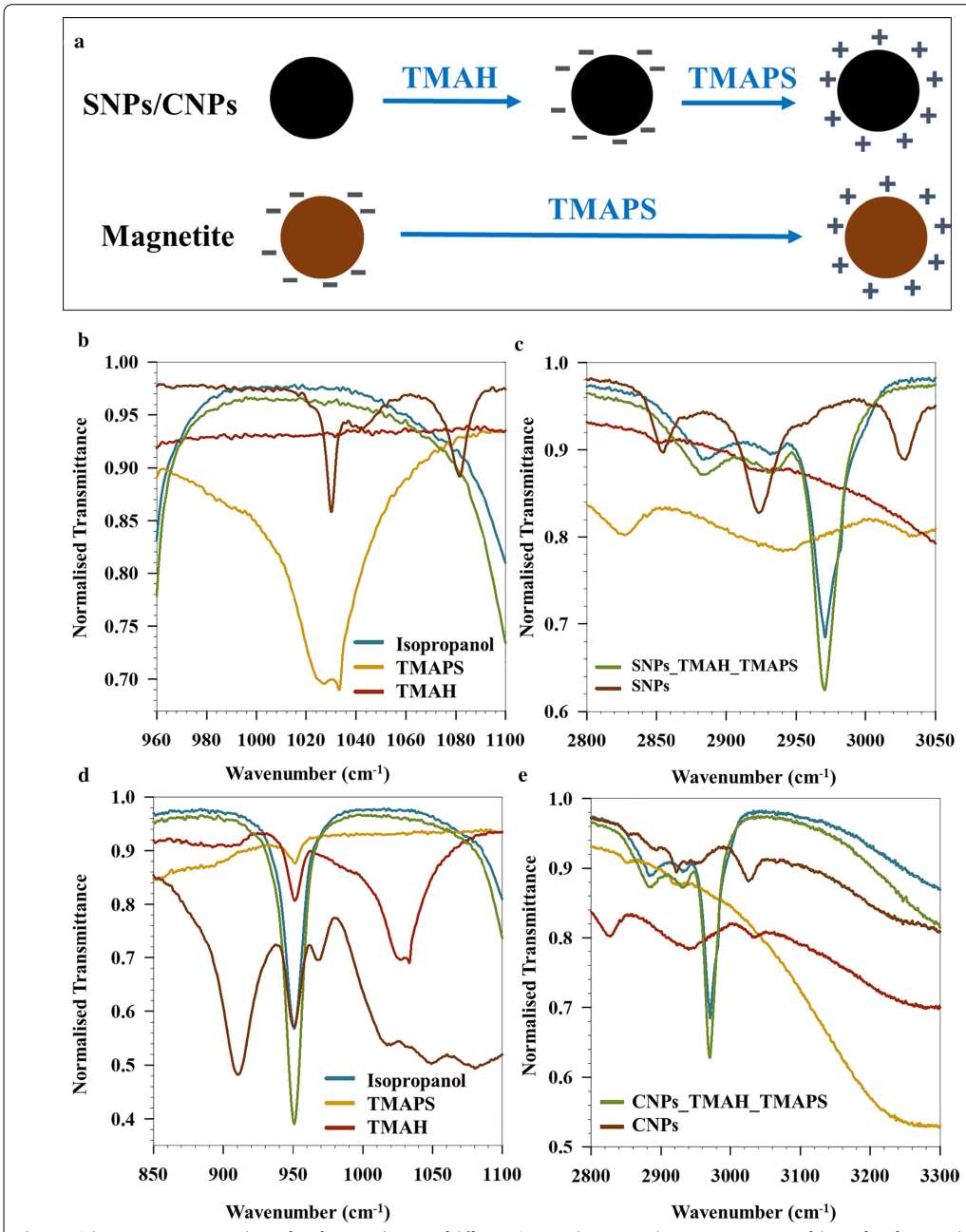

Fig. 2 **a** Schematic representing the surface functionalization of different IONPs with TMAH and TMAPs. FTIR spectra of the surface functionalized **b**, **c** SNPs and **d**, **e** CNPs with TMAH and TMAPS

The sharp peak seen at 920 cm^{-1} for CNPs (Fig. 2d) can be attributed to out-of-plane angular deformation of –C–OH of Na-oleate (present on the surface of CNPs) [40]. Complete disappearance of this peak is seen for spectra of CNPs functionalized with TMAH and TMAPS showing removal of Na-oleate which is in sync with phase transferred SNPs (where OA was removed). Other spectral features at 1031 (Fig. 2d), 2876 and 2972 cm^{-1} (Fig. 2e) for CNPs functionalized with TMAH and TMAPS have similar characteristics as of SNPs functionalized with TMAH and TMAPS, showing analogous surface interactions during phase transfer. From the FTIR data, it is however difficult to conclude if TMAPS replaces TMAH completely for either SNPs or CNPs. However, it can be inferred that TMAPS is the outermost ligand providing positive zeta potential after TMAPS coating in case of Mag, SNPs and CNPs as shown in Fig. 3a, arising from the amine functional group of TMAPS.

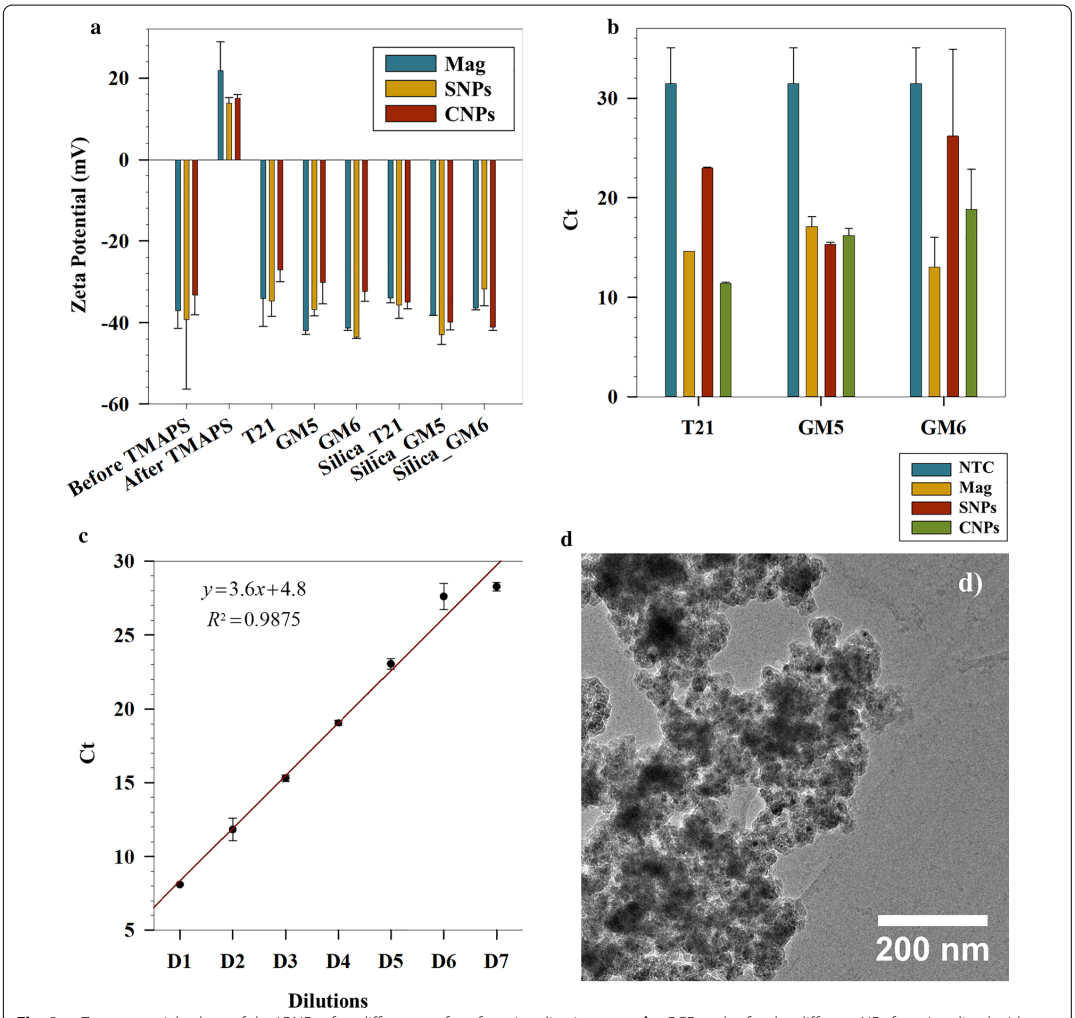

Fig. 3 **a** Zeta potential values of the IONPs after different surface functionalization steps. **b** qPCR cycles for the different NPs functionalized with different dsDNA. **c** Dilution curve for GM5 functionalized SNPs up to 7 dilution cycles. **d** TEM image of T21 functionalized Mag NPs encapsulated in silica. (The error bars represent the standard deviation calculated from the triplicate measurement of the particular sample)

Silanization and Binding of DNA

After successful functionalization of the particles yielding in cationic surfaces, the three NPs viz. Mag, SNPs and CNPs were loaded with dsDNA. Figure 3a shows the variation in zeta potentials at each surface functionalization step for all the IONPs. TMAPS was successfully bound to the respective NP surface, represented by positive zeta potentials after TMAPS functionalization (Mag: 21 ± 7 mV, SNPs: 13 ± 1 mV, CNPs: 15 ± 1 mV).

With an intent to fabricate tracers, bar-coded with unique dsDNA, we chose three different dsDNA molecules, namely, T21, GM5 and GM6. Charge density mapping between the TMAPS functionalized IONPs and the dsDNA is a precursor to the successful binding of the dsDNA to the IONPs. Through a series of preliminary experiments, we optimized the ratio of NPs to dsDNA to facilitate effective binding. Successful binding of DNA reverses the surface charge of the IONPs in all the cases as reported in Fig. 3a. This shows the robustness and adaptability of our protocol to different particle types and different DNA strands. A final coating of silica was carried out after this step to ensure a protective shell around the DNA. The silica coated NPs containing specific dsDNA and specific iron oxide core are all found to have high colloidal stabilities indicated by high zeta potential values (Fig. 3a).

In order to assess the dsDNA loads in our tracer particles, qPCR measurements were done after bleaching any surface bound dsDNA. To release the encapsulated DNA, the tracer particles were dissolved in buffered oxide etch—a fluoride buffer, containing $(NH_4)HF_2$ and NH_4F, which has been shown to etch away the silica (shell) and iron oxide (core), without affecting the dsDNA [14]. In addition, the presence of this buffer in the qPCR samples has been previously shown neither to influence the signal to noise ratio nor inhibit the primers during amplification cycles [14]. The cycle threshold (Ct) values obtained from qPCR runs for the respective tracer particles are shown in Fig. 3b. A lower C_t value indicates that the fluorescent signal required to cross the threshold (exceed background level) is defined by a smaller number of cycles, in turn representing high DNA concentrations. The presence of large detectable quantities of DNA is therefore verified for all the tracer types, indicated by statistically significant lower C_t values compared to NTC (negative control). The results shown are for D3 diluted samples (tenfold dilution with each cycle), whereby further proving the applicability of such tracers with high ultrasensitivity and negligible dilution problems. To further substantiate our claim, we performed a dilution series for the SNP tracers functionalized with GM5 as shown in Fig. 3c. The PCR efficiency is determined by means of a standard curve involving generating a dilution series of the concentrated stock solution. This series of samples, with controlled relative amounts of targeted template, is most frequently diluted using tenfold dilution steps that are analysed by qPCR measuring the quantification cycle (C_t) using standard procedures. An efficiency of 100% follows the assumption of perfect doubling of the number of DNA template molecules in each step of the PCR. The PCR efficiency (E) can be calculated from the slope of the C_t versus the logarithm of the target concentrations as follows [41]:

$$E = (10^{(1/\text{slope})} - 1) \times 100\% \tag{1}$$

$$E = (10^{(1/3.6)} - 1) \times 100\% = 89.6\% \tag{2}$$

with $R^2 = 0.9875$.

Also, D6 and D7 show similar C_t values that are close to the NTC of the assay. Hence, there could still be some particles left in D7, however, the C_t value is obscured by the NTC.

Figure 3d shows a representative TEM image of T21 functionalized Mag tracers, Although, several Mag NPs can be distinctively seen throughout a mesh of silica, our results show that several Mag NPs are encapsulated within single silica shells. However, how sequential functionalization affects the magnetic properties of IONPs needs to be studied in order to assess their applications in tracer hydrology and subsequent magnetic separation prior to analysis. We report here for the first time an in-detail magnetic characterization of our magnetic DNA tracers at each stage of functionalization.

Influence of Magnetic Properties upon Functionalization

Molecular coating can strongly influence magnetic properties of NPs both restoring the bulk saturation magnetization and influencing the local effective magnetic anisotropy, (i.e. coercive field). This effect can be attributed to the influence of different ligands bonded at the IONPs surface that modify electronic structure and then magnetic properties of the NPs [26, 27, 42]. In order to investigate the effect of molecular coating on magnetic properties, field and temperature dependence of magnetization has been investigated on bare magnetite (Mag) and at every stage of functionalization (Mag_TMAPS, Mag_DNA and Mag_Silica) particles. Even though SNPs and CNPs possess higher structural uniformity that might lead to superior magnetic properties, we limit our discussion of magnetic measurements to Mag, as these NPs provide higher saturation magnetization with respect to CNPs ($M_s = 39$ (3) $Am^2\ kg^{-1}$) in our case (Additional file 1: Figure S5). In addition, Mag provides the most consistent qPCR results (Fig. 3b) across the 3 variants of dsDNA used. Furthermore, studies conducted

on Mag have not shown any magnetic data to stress on the effect of surface functionalization and encapsulation on the magnetic properties of these NPs.

Field dependence of magnetization recorded at 5 K (Fig. 4a) indicates that the coating of Mag was successfully achieved without affecting the magnetic characteristics of the magnetic core and both bare sample and coated samples present very close saturation magnetization (M_s) values, and coercivity field, H_c (inset Fig. 4a, Table 3). M vs H at 300 K (Fig. 4b) shows superparamagnetic behaviour (i.e. Mr = 0 and Hc = 0) for all the samples. Thermal dependence of magnetization measured according to zero field cooled (ZFC) and field cooled (FC) protocols in DC field of 25 Oe and in the temperature range of 5–300 K are shown in Fig. 4c. All the coated samples show comparable magnetic behaviour that are different from bare NP counterparts. In this view, in order to draw a clearer picture, a comparison among Mag and Mag_Silica particles will be shown as an example and ZFC FC measurements for all the samples is reported in Additional file 1: (Sect. 4.3). According to ZFC protocol, the sample was at first cooled down from 300 to 5 K in zero field, then a small field of 25 Oe was applied and the data was collected during the warming up from 5 to 300 K. The applied field was maintained as the sample was cooled down again to 5 K and M_{FC} magnetization was measured during the cooling process. As an example, Fig. 4c shows the ZFC–FC of Mag and Mag_Silica samples. ZFC–FC exhibit a blocking process typical of an ensemble of single-domain magnetic particles with a distribution of blocking temperatures [43]. Both MZFC of Mag and Mag_Silica sample clearly show a maximum that can be considered proportional to the mean blocking temperature:

$$T_{\max} = \beta T_B \tag{3}$$

where β can be considered in the range 1.5–2.5 for log normal size distribution [44].

Both samples show also irreversibility between FC and ZFC up to quite high temperature. The temperature below this irreversibility is observed (T_{irr}) and can be associated with the blocking of the biggest particles. Looking at values of T_{max} and T_{irr} (Table 2), it appears clear that all the samples show similar values within experimental errors.

It is worth to note that M_{FC} shows temperature independent behaviour at low temperature, suggesting the presence of relevant interparticle interaction among the particles [45].

In order to better understand the effect of the molecular coating on the magnetization dynamics of the NPs, the temperature dependence of the difference $M_{FC} - M_{ZFC}$ has been plotted (Fig. 4d) ($M_{FC} - M_{ZFC}$ of the other samples are reported in Additional file 1: Figure S3a). For a NP ensemble, it can be demonstrated that

$$M_{TRM}(H,T,t) = M_{FC}(H,T,t) - M_{ZFC}(H,T,t) + M_{IRM}(H,T,t) \tag{4}$$

where M_{IRM} is isothermal remnant magnetization. However, as M_{IRM} is negligible in the IONP assemble, $M_{FC} - M_{ZFC}$ can be considered as a good approximation of M_{TRM} [46, 47]. For both samples, $M_{FC} - M_{ZFC}$ shows a decrease with increasing temperature, as expected for an assembly of magnetic monodomain particles. The derivative of $M_{FC} - M_{ZFC}$ (Fig. 4e) can be considered as only a rough estimation of the ΔE_a distribution due to the presence of interparticle interactions in our samples. The distribution of magnetic anisotropy energies shows the presence of two maxima centered at around 20 K (T_{Low}) and 100 K (T_{high}) respectively. Following previous detailed investigation of magnetic properties in iron oxides, T_{low} can be ascribed to the freezing of non-collinear spin present in the particle surface, while T_{high} is related to superparamagnetic transition of monodomain particles [48–50].

Within the Néel model, the blocking temperature can be defined as the temperature for which the relaxation time is equal to the measuring time of the experimental technique. In a real system of NPs, where a finite size distribution always exists, T_B is often defined as the temperature at which 50% of the sample is in the superparamagnetic state. The T_B distribution can be obtained from the ΔE_a distribution by evaluating the temperature at which 50% of the particles overcome their anisotropy energy barriers. Blocking temperature for all the samples show equal values within experimental errors, suggesting that molecular coating is not influencing the magnetization dynamics of superspin. It is interesting to observe that data reported in Table 3 is in good agreement with Eq. 3: considering the values of T_{max} and T_{irr}, β are in the expected range. This suggests that despite interparticle interaction being present between particles, the magnetization dynamics of superspin is governed by magnetic anisotropy of single particles [43, 51].

In order to shed some light on the interparticle interactions in our samples, the variation of δm versus field at 5 K according to DCD (Direct Current Demagnetization) and IRM (Isothermal Remnant Magnetization) protocols (Additional file 1: Sect. 4.3), are presented in Fig. 4f [52]. As an example, positive value in δm is an indication of exchange interactions among nanoparticles while negative peak indicates the prevalence of dipolar interactions. Thus, it can be clearly seen from Fig. 4f, that the dipolar interaction is dominating in our samples, before coating as well. After coating with DNA, a slight, but evident, reduction in the intensity of δm (as absolute value) was

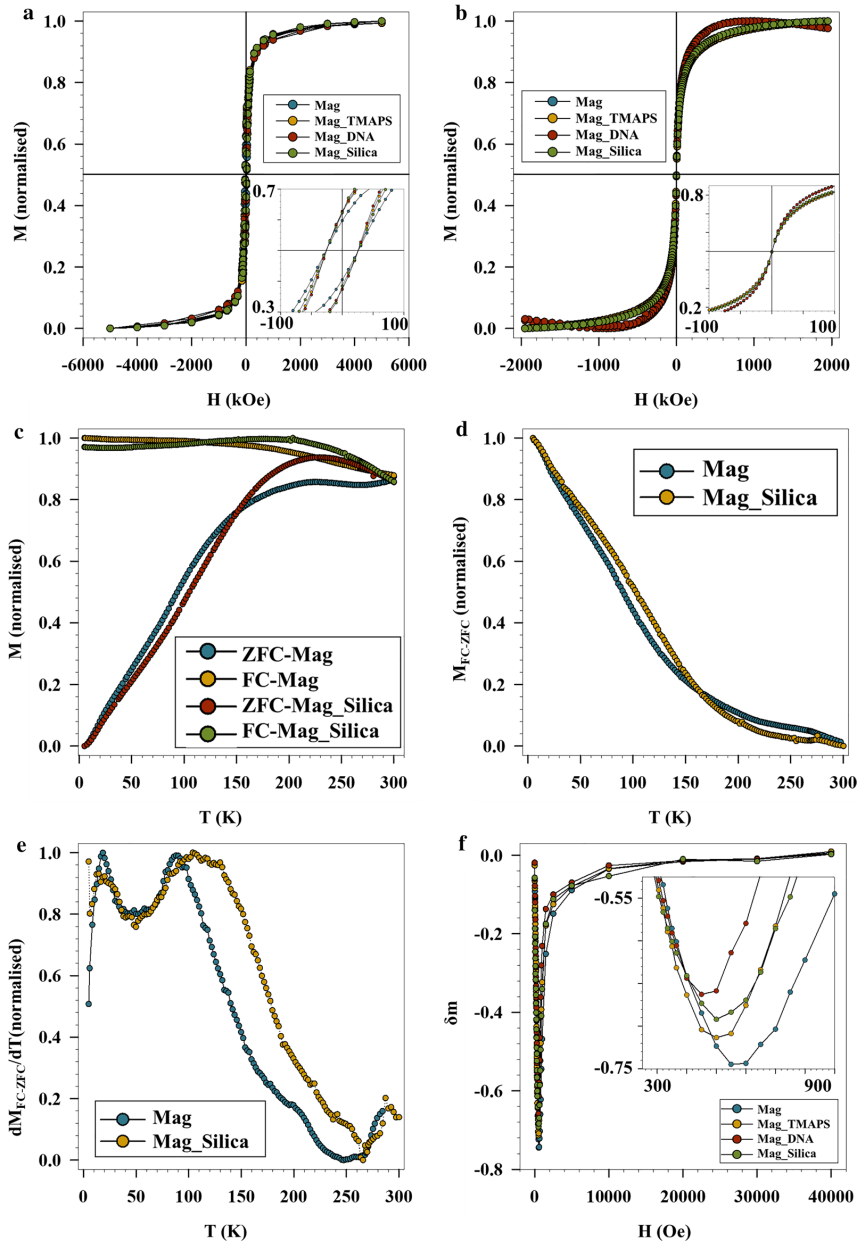

Fig. 4 Field dependence of magnetization for Mag, Mag_TMAPS, Mag_DNA and Mag_Silica at **a** 5 K and **b** 300 K. **c** ZFC–FC measurements, **d** M_{FC}–M_{ZFC} plots and **e** derivative of M_{FC}–M_{ZFC} plots for Mag and Mag_Silica. **f** δm plots at 5 K Mag and functionalized Mag samples

Table 3 Coercive Field (H_c), saturation magnetization at 5 K (M_S). Temperature corresponding to the maximum in ZFC curve (T_{max}), irreversibility temperature (T_{irr}), and blocking temperature (T_B). Uncertainties on the last digit are given in parentheses

Sample	Hc (Oe)	*Ms* 5 K (emu/g)	T_{max} (K)	T_B (K)	T_{irr} (3%) (K)
Mag	260 (25)	77 (8)	228 (22)	90 (9)	283 (28)
Mag_TMAPS	255 (20)	75 (8)	236 (23)	92 (9)	243 (24)
Mag_DNA	250 (20)	85 (9)	202 (20)	92 (9)	207 (20)
Mag_Silica	200 (20)	83 (9)	228 (22)	102 (10)	242 (24)

observed (inset, Fig. 4f). In a sample of randomly distributed nanoparticles with average magnetic moment μ_p (i.e. $M_s \times V_p$,) and average separation d, dipolar energy (E_d) is approximately, given by

$$E_d \sim \frac{\mu_0 (M_s \times V_p)^2}{4\pi d^3} \quad (5)$$

where μ_0 is permeability, M_s saturation magnetization, V_p volume of nanoparticles, d is the distance between particles. Considering M_s and V_p equal in all the samples, the observed reduction of dipolar interactions (i.e. dipolar energy) means an increase of interparticle distance, indicating the efficiency for the coating process.

The magnetic properties (i.e. saturation magnetization and magnetic anisotropy) of Mag remain intact after surface functionalization with DNA and encapsulation in silica proving the efficiency of magnetic core and the possibility of magnetic separation of these NPs thereby improving the recovery of the tracer moieties downstream.

Conclusion

Conventional hydrological tracers show limitations due to lack of multiplexed, multipoint tracing and interference of background noise. DNA based tracers eliminate most of these challenges by enabling synthesis of ideally unlimited number of unique tracers that are stable and highly sensitive to detection. Herein, we synthesised DNA based tracers having a magnetic core encapsulated in a protective silica shell. We report for the first time encapsulation of three different types of DNA using three different magnetic cores, thereby showing the uniqueness of the tracers. Superparamagnetic IONPs, with a size range of 10–20 nm, were synthesized using the methods of co-precipitation and thermal decomposition for the purpose of producing magnetic hydrological tracers. The surface of the IONPs were functionalized using different ligands such as CTAB, Na-citrate, TMAH and TMAPS, thus, providing different surface functionalities and surface charges to IONPs. The functionalized nanoparticles show high stability denoted by high zeta potential values, above > 30 mV (CTAB) and < − 30 mV (Na-citrate and TMAH). Spherical and cube shaped IONPs, synthesized via co-precipitation or thermal decomposition routes, were thereafter successfully functionalized with three different dsDNA (T21, GM5 and GM6) followed by encapsulation in silica shell. The effect of surface functionalization of IONPs on the physicochemical properties and especially magnetic properties of IONPs was investigated. In the latter context, we track for the first time, the effect of functionalization on the magnetic properties. It was observed that the magnetic core retained most of its magnetic properties even after encapsulation in silica. Successful DNA binding to the IONPs was verified using qPCR for all the different magnetic cores and the three different dsDNAs studied herein. Our results show robust and repeatable synthesis and functionalization protocols capable of producing magnetic tracers with unique DNA tags that retain relevant magnetic properties of the cores even after silica encapsulation. The tracers show detection at extremely low concentrations, thereby proving their non-susceptibility to dilution effects under application conditions. These tracers will pave the path for monitoring several hydrological processes, currently limited by the availability of multiple unique tracers. Further, the use of DNA as a tag is a precursor to ultra-high sensitivity in detection and the magnetic core will facilitate easy separation of tracers after applications downstream.

Supplementary Information

The online version contains supplementary material available at https://doi.org/10.1186/s11671-021-03483-5.

Additional file 1: Supporting information.

Abbreviations

qPCR: Quantitative polymerase chain reaction; PAA: Polyamidoamine; PEG: Poly(ethylene) glycol; NPs: Nanoparticles; IONPs: Iron oxide nanoparticles; PLA: Polylactic acid; TMAH: Tetra methyl ammonium hydroxide; CTAB: Hexadecyltrimethylammonium bromide; ODE: 1-Octadecene; OA: Oleic acid; TEOS: Tetraethyl orthosilicate; TMAPS: Trimethoxysilylpropyl-*N,N,N*-trimethylammonium chloride; Mag: Magnetite NPs synthesised by co-precipitation; SNPs: Iron oleate: spheres; CNPs: Iron oleate: cubes; TEM: Transmission electron microscopy; FTIR: Fourier transform infrared; PSD: Particle size distribution; DLS: Dynamic light scattering; SQUID: Super conducting quantum interference device; XRD: X-ray diffraction; ZFC–FC: Zero field cooled–field cooled; BOE: Buffered oxide etch.

Acknowledgements

We thank Prof. Mari-Ann Einarsrud (NTNU) and the Functional Materials and Materials Chemistry (FACET) group for all the valuable insights and discussions. We thank Assoc. Prof. Thom Bogaard as well as the Water Tagging Project team for their inputs and fruitful scientific discussions. Financial support was provided by the Netherlands Organisation for Scientific Research (NWO) Grant STW14515 Water Tagging. The authors would like to thank NorFab for the financial support in connection to the use of NTNU Nanolab and the Faculty

of Natural Sciences and Technology, NTNU, for the financial support. We thank the Department of Material Sciences and Engineering (NTNU), NORTEM/Gemini Centre (NTNU) and Nanolab (NTNU), for all their financial, technical and laboratory support.

Authors' Contributions

All of the tracer synthesis and functionalization experiments, starting from the iron oxide NPs, their functionalization and surface modification with different ligands, DNA and silica, have been performed at the Norwegian University of Science and Technology, Norway. The applicability qPCR tests of the tracers have been conducted at the IHE Delft Institute for Water Education, Netherlands, whereas, the magnetic characterization studies have been done at the Università di Genova, Italy. Simulations of the growth kinetics have been done at Indian Institute of Technology Bombay, India. Study Concepts: SB, AS, JWP. Study Design: SB, JWP. Literature Research: AS, AB, SB. Data Acquisition: AS, AB, JWP, SB, SS, NB, DP. Data Analysis/Interpretation: SB, AS, JWP, SS, NB, DP. Statistical Analysis: AB, AS, SB, NB. Manuscript Preparation:AS, SB, AB, JWP, SS, NB, DP. Manuscript Revisions: AS, SB. All authors read and approved the final manuscript.

Funding

The authors received no specific funding for this work.

Availability of Data and Supporting Materials

All additional and relevant data can be found with the Supporting Information.

Competing Interests

The authors declare that they have no competing interests.

Author details

[1] Department of Materials Science and Engineering, Norwegian University of Science and Technology (NTNU), 7491 Trondheim, Norway. [2] Department of Water Science and Engineering, IHE Delft Institute for Water Education, PO Box 3015, Delft, The Netherlands. [3] Dipartimento di Chimica e Chimica Industriale, Università di Genova, Genoa, Italy. [4] Istituto di Struttura della Materia – CNR, Area della Ricerca di Roma1, 00015 Monterotondo Scalo, RM, Italy. [5] Department of Chemical Engineering, Indian Institute of Technology Jodhpur, Jodhpur 342037, India. [6] Department of Water Management, Delft University of Technology, PO Box 5048, 2600 GA Delft, The Netherlands. [7] Department of Chemical Engineering, Norwegian University of Science and Technology (NTNU), 7491 Trondheim, Norway.

Received: 26 September 2020 Accepted: 18 January 2021
Published online: 06 February 2021

References

1. Leibundgut C, Maloszewski P, Külls C (2011) Tracers in hydrology. John Wiley, New York
2. Wilderer PA (2010) Treatise on water science. Newnes, Oxford
3. Abbott BW, Baranov V, Mendoza-Lera C, Nikolakopoulou M, Harjung A, Kolbe T, Balasubramanian MN, Vaessen TN, Ciocca F, Campeau A (2016) Using multi-tracer inference to move beyond single-catchment ecohydrology. Earth Sci Rev 160:19–42
4. Puddu M, Paunescu D, Stark WJ, Grass RN (2014) Magnetically recoverable, thermostable, hydrophobic DNA/silica encapsulates and their application as invisible oil tags. ACS Nano 8(3):2677–2685
5. Liao R, Yang P, Wu W, Luo D, Yang D (2018) A DNA tracer system for hydrological environment investigations. Environ Sci Technol 52(4):1695–1703
6. Kittilä A, Jalali M, Evans KF, Willmann M, Saar MO, Kong XZ (2019) Field comparison of DNA-labeled nanoparticle and solute tracer transport in a fractured crystalline rock. Water Resour Res 55(8):6577–6595
7. Liao R, Zhang J, Li T, Luo D, Yang D (2020) Biopolymer/plasmid DNA microspheres as tracers for multiplexed hydrological investigation. Chem Eng J 401:126035
8. Wages Jr J (2005) Polymerase chain reaction. In: Encyclopedia of analytical science, p 243. ISBN 978-0-12-369397-6. https://www.sciencedirect.com/referencework/9780123693976/encyclopedia-of-analytical-science#book-info
9. Mano J, Hatano S, Futo S, Yoshii J, Nakae H, Naito S, Takabatake R, Kitta K (2014) Development of a reference material of a single DNA molecule for the quality control of PCR testing. Anal Chem 86(17):8621–8627
10. Foppen JW, Seopa J, Bakobie N, Bogaard T (2013) Development of a methodology for the application of synthetic DNA in stream tracer injection experiments. Water Resour Res 49(9):5369–5380
11. Foppen JW, Orup C, Adell R, Poulalion V, Uhlenbrook S (2011) Using multiple artificial DNA tracers in hydrology. Hydrol Process 25(19):3101–3106
12. Sharma AN, Luo D, Walter MT (2012) Hydrological tracers using nanobiotechnology: proof of concept. Environ Sci Technol 46(16):8928–8936
13. Rackstraw BJ, Stolnik S, Davis SS, Bignotti F, Garnett MC (2002) Development of multicomponent DNA delivery systems based upon poly (amidoamine)–PEG co-polymers. Biochim Biophys Acta (BBA) Gene Struct Exp 1576(3):269–286
14. Paunescu D, Puddu M, Soellner JO, Stoessel PR, Grass RN (2013) Reversible DNA encapsulation in silica to produce ROS-resistant and heat-resistant synthetic DNA'fossils'. Nat Protoc 8(12):2440
15. Grass RN, Schälchli J, Paunescu D, Soellner JO, Kaegi R, Stark WJ (2014) Tracking trace amounts of submicrometer silica particles in wastewaters and activated sludge using silica-encapsulated DNA barcodes. Environ Sci Technol Lett 1(12):484–489
16. Sun S, Zeng H (2002) Size-controlled synthesis of magnetite nanoparticles. J Am Chem Soc 124(28):8204–8205
17. Baaziz W, Pichon BP, Fleutot S, Liu Y, Lefevre C, Greneche J-M, Toumi M, Mhiri T, Begin-Colin S (2014) Magnetic iron oxide nanoparticles: reproducible tuning of the size and nanosized-dependent composition, defects, and spin canting. J Phys Chem C 118(7):3795–3810
18. Park J, An K, Hwang Y, Park J-G, Noh H-J, Kim J-Y, Park J-H, Hwang N-M, Hyeon T (2004) Ultra-large-scale syntheses of monodisperse nanocrystals. Nat Mater 3(12):891–895
19. Hyeon T, Lee SS, Park J, Chung Y, Na HB (2001) Synthesis of highly crystalline and monodisperse maghemite nanocrystallites without a size-selection process. J Am Chem Soc 123(51):12798–12801
20. Colombo M, Carregal-Romero S, Casula MF, Gutiérrez L, Morales MP, Böhm IB, Heverhagen JT, Prosperi D, Parak WJ (2012) Biological applications of magnetic nanoparticles. Chem Soc Rev 41(11):4306–4334
21. Laurent S, Forge D, Port M, Roch A, Robic C, Vander Elst L, Muller RN (2008) Magnetic iron oxide nanoparticles: synthesis, stabilization, vectorization, physicochemical characterizations, and biological applications. Chem Rev 108(6):2064–2110
22. Zhao S, Yu X, Qian Y, Chen W, Shen J (2020) Multifunctional magnetic iron oxide nanoparticles: an advanced platform for cancer theranostics. Theranostics 10(14):6278
23. Guardia P, Pérez N, Labarta A, Batlle X (2010) Controlled synthesis of iron oxide nanoparticles over a wide size range. Langmuir 26(8):5843–5847
24. Peeters K, Lespes G, Zuliani T, Ščančar J, Milačič R (2016) The fate of iron nanoparticles in environmental waters treated with nanoscale zero-valent iron, FeONPs and Fe_3O_4NPs. Water Res 94:315–327
25. Kim J, Kim HS, Lee N, Kim T, Kim H, Yu T, Song IC, Moon WK, Hyeon T (2008) Multifunctional uniform nanoparticles composed of a magnetite nanocrystal core and a mesoporous silica shell for magnetic resonance and fluorescence imaging and for drug delivery. Angew Chem Int Ed 47(44):8438–8441
26. Vasilakaki M, Ntallis N, Yaacoub N, Muscas G, Peddis D, Trohidou K (2018) Optimising the magnetic performance of Co ferrite nanoparticles via organic ligand capping. Nanoscale 10(45):21244–21253
27. Tanaka Y, Saita S, Maenosono S (2008) Influence of surface ligands on saturation magnetization of FePt nanoparticles. Appl Phys Lett 92(9):093117
28. Momtazi L, Bagherifam S, Singh G, Hofgaard A, Hakkarainen M, Glomm WR, Roos N, Mælandsmo GM, Griffiths G, Nyström B (2014) Synthesis, characterization, and cellular uptake of magnetic nanocarriers for cancer drug delivery. J Colloid Interface Sci 433:76–85
29. Singh G, Chan H, Udayabhaskararao T, Gelman E, Peddis D, Baskin A, Leitus G, Král P, Klajn R (2015) Magnetic field-induced self-assembly of iron oxide nanocubes. Faraday Discuss 181:403–421
30. Bachhar N, Bandyopadhyaya R (2016) Role of coating agent in iron oxide nanoparticle formation in an aqueous dispersion: experiments and simulation. J Colloid Interface Sci 464:254–263
31. Situ-Loewenstein SF, Wickramasinghe S, Abenojar EC, Erokwu BO, Flask CA, Lee Z, Samia ACS (2018) A novel synthetic route for high-index

faceted iron oxide concave nanocubes with high T 2 relaxivity for in vivo MRI applications. J Mater Sci Mater Med 29(5):58
32. Hufschmid R, Arami H, Ferguson RM, Gonzales M, Teeman E, Brush LN, Browning ND, Krishnan KM (2015) Synthesis of phase-pure and monodisperse iron oxide nanoparticles by thermal decomposition. Nanoscale 7(25):11142–11154
33. Bronstein LM, Huang X, Retrum J, Schmucker A, Pink M, Stein BD, Dragnea B (2007) Influence of iron oleate complex structure on iron oxide nanoparticle formation. Chem Mater 19(15):3624–3632
34. Tartaj P, Morales MP, Veintemillas-Verdaguer S, Gonzalez-Carreño T, Serna CJ (2006) Synthesis, properties and biomedical applications of magnetic nanoparticles. Handb Magn Mater 16(5):403–482
35. Fleet ME (1986) The structure of magnetite: symmetry of cubic spinels. J Solid State Chem 62(1):75–82
36. Shukla S, Jadaun A, Arora V, Sinha RK, Biyani N, Jain V (2015) In vitro toxicity assessment of chitosan oligosaccharide coated iron oxide nanoparticles. Toxicol Rep 2:27–39
37. Sharma K, Ningthoujam R, Dubey A, Chattopadhyay A, Phapale S, Juluri R, Mukherjee S, Tewari R, Shetake NG, Pandey B (2018) Synthesis and characterization of monodispersed water dispersible Fe_3O_4 nanoparticles and in vitro studies on human breast carcinoma cell line under hyperthermia condition. Sci Rep 8(1):1–11
38. Wang Y, Wong JF, Teng X, Lin XZ, Yang H (2003) "Pulling" nanoparticles into water: phase transfer of oleic acid stabilized monodisperse nanoparticles into aqueous solutions of α-cyclodextrin. Nano Lett 3(11):1555–1559
39. Oh T, Kim CH (2010) Study on characteristic properties of annealed SiOC film prepared by inductively coupled plasma chemical vapor deposition. IEEE Trans Plasma Sci 38(7):1598–1602
40. Kumar TV, Prabhakar S, Raju GB (2002) Adsorption of oleic acid at sillimanite/water interface. J Colloid Interface Sci 247(2):275–281
41. Svec D, Tichopad A, Novosadova V, Pfaffl MW, Kubista M (2015) How good is a PCR efficiency estimate: recommendations for precise and robust qPCR efficiency assessments. Biomol Detect Quantif 3:9–16
42. Vestal CR, Zhang ZJ (2003) Effects of surface coordination chemistry on the magnetic properties of MnFe2O4 spinel ferrite nanoparticles. J Am Chem Soc 125(32):9828–9833
43. Muscas G, Yaacoub N, Concas G, Sayed F, Hassan RS, Greneche J-M, Cannas C, Musinu A, Foglietti V, Casciardi S (2015) Evolution of the magnetic structure with chemical composition in spinel iron oxide nanoparticles. Nanoscale 7(32):13576–13585
44. Gittleman J, Abeles B, Bozowski S (1974) Superparamagnetism and relaxation effects in granular Ni–SiO_2 and Ni–Al_2O_3 films. Phys Rev B 9(9):3891
45. Cannas C, Musinu A, Peddis D, Piccaluga G (2004) New synthesis of ferrite–silica nanocomposites by a sol–gel auto-combustion. J Nanopart Res 6(2):223–232
46. Muscas G, Cobianchi M, Lascialfari A, Cannas C, Musinu A, Omelyanchik A, Rodionova V, Fiorani D, Mameli V, Peddis D (2019) Magnetic interactions vs. magnetic anisotropy in spinel ferrite nanoparticles. IEEE Magn Lett 10:1–5. https://doi.org/10.1109/LMAG.2019.2956908
47. Chantrell RW, El-Hilo M, O'Grady K (1991) Spin-glass behavior in a fine particle system. IEEE Trans Magn 27(4):3570–3578
48. Muscas G, Concas G, Cannas C, Musinu A, Ardu A, Orrù F, Fiorani D, Laureti S, Rinaldi D, Piccaluga G (2013) Magnetic properties of small magnetite nanocrystals. J Phys Chem C 117(44):23378–23384
49. Guardia P, Batlle-Brugal B, Roca A, Iglesias O, Morales MdP, Serna C, Labarta A, Batlle X (2007) Surfactant effects in magnetite nanoparticles of controlled size. J Magn Magn Mater 316(2):e756–e759
50. Salafranca J, Gazquez J, Pérez NS, Labarta A, Pantelides ST, Pennycook SJ, Batlle X, Varela M (2012) Surfactant organic molecules restore magnetism in metal-oxide nanoparticle surfaces. Nano Lett 12(5):2499–2503
51. Peddis D, Rinaldi D, Ennas G, Scano A, Agostinelli E, Fiorani D (2012) Superparamagnetic blocking and superspin-glass freezing in ultra small δ-(Fe 0.67 Mn 0.33) OOH particles. Phys Chem Chem Phys 14(9):3162–3169
52. Peddis D, Jönsson PE, Laureti S, Varvaro G (2014) Magnetic interactions: a tool to modify the magnetic properties of materials based on nanoparticles. In: Frontiers of nanoscience, vol 6. Elsevier, pp 129–188

Publisher's Note

8.2 Paper II

Sharma, A., Raghunathan, K., Solhaug, H., Antony J., Stenvik J., Nilsen A.M., Einarsrud M-A., Bandyopadhyay S., 2021. Modulating Acrylic Acid Content of Nanogels for Drug Delivery Biocompatibility Studies. Journal of Colloid and Interface Science. https://doi.org/10.1016/j.jcis.2021.07.139

Journal of Colloid and Interface Science 607 (2022) 76–88

Contents lists available at ScienceDirect

Journal of Colloid and Interface Science

journal homepage: www.elsevier.com/locate/jcis

Modulating acrylic acid content of nanogels for drug delivery & biocompatibility studies

Anuvansh Sharma [a], Karthik Raghunathan [b], Helene Solhaug [c], Jibin Antony [b], Jørgen Stenvik [d,e], Asbjørn Magne Nilsen [e], Mari-Ann Einarsrud [a], Sulalit Bandyopadhyay [b,*]

[a] Department of Materials Science and Engineering, NTNU Norwegian University of Science and Technology, Norway
[b] Department of Chemical Engineering, NTNU Norwegian University of Science and Technology, Norway
[c] Department of Clinical and Molecular Medicine, Faculty of Medicine and Health Sciences, NTNU Norwegian University of Science and Technology, Trondheim, Norway
[d] Centre of Molecular Inflammation Research, NTNU Norwegian University of Science and Technology, Trondheim, Norway
[e] Department of Clinical and Molecular Medicine, NTNU Norwegian University of Science and Technology, Trondheim, Norway

GRAPHICAL ABSTRACT

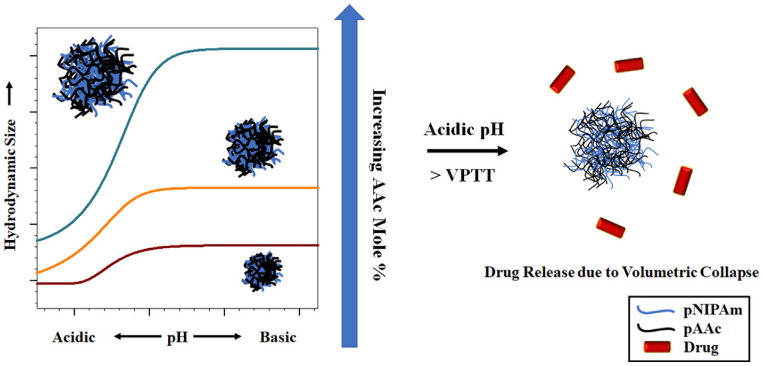

ARTICLE INFO

Article history:
Received 26 May 2021
Revised 18 July 2021
Accepted 27 July 2021
Available online 5 August 2021

Keywords:
Nanogels
Stimuli-responsive NGs
Poly-acrylic acid
Drug delivery
Biocompatibility

ABSTRACT

Dual stimuli-responsive nanogels (NGs) have gained popularity in the field of bio medicine due to their versatile nature of applicability. Poly(N-isopropylacrylamide)-co-poly(acrylic acid) (pNIPAm-pAAc)-based NGs provide such dual stimuli-response with pNIPAm and pAAc providing thermal and pH-based responses, respectively. Studying the growth of these NGs, as well as, understanding the effect of the incorporation of pAAc in the NG matrix, is important in determining the physico-chemical properties of the NG. Studies have been conducted investigating the effect of increasing pAAc content in the NGs, however, these are not detailed in understanding its effects on the physico-chemical properties of the pNIPAm-pAAc-based NGs. Also, the biocompatibility of the NGs have not been previously reported using human whole blood model. Herein, we report the effect of different reaction parameters, such as surfactant amount and reaction atmosphere, on the growth of pNIPAm-pAAc-based NGs. It is shown that the size of the NGs can be precisely controlled from ~130 nm to ~400 nm, by varying the amount of surfactant and the reaction atmosphere. The effect of increasing incorporation of pAAc in the NG matrix on its physico-chemical properties has been investigated. The potential of these NGs as drug delivery vehicles is investigated by conducting loading and release studies of a model protein drug, cytochrome

* Corresponding author.
E-mail address: sulalit.bandyopadhyay@ntnu.no (S. Bandyopadhyay).

https://doi.org/10.1016/j.jcis.2021.07.139

Abbreviations

AAc	Acrylic acid
BIS	N-N′-methylene-bisacrylamide
CR3	Complement Receptor 3
CS	Continuous-Stirring
Cyt *C*	Cytochrome *C*
DLS	Dynamic light scattering
E.E.	Encapsulation efficiencies
FI	Flashing-Impeller
FS	Flashing-Stirring
KPS	Potassium persulphate
LPS	Lipopolysaccharide
L.E.	Loading efficiency
NGs	Nanogels
NIPAm	N-isopropylacrylamide
NMR	Nuclear magnetic resonance
PFA	Paraformaldehyde
PSD	Particle size distribution
PBS	Phosphate buffered saline
pAAc	Poly(acrylic acid)
PDI	Polydispersity index
pNIPAm	Poly(N-isopropylacrylamide)
PI	Propidium iodide
SDS	Sodium dodecyl sulpahate
TCC	Terminal complement complex
TMB	Tetramethylbenzidine
TEM	Transmission electron microscopy
VCE	Volumetric collapse efficiency
VPTT	Volume phase transition temperature

C (Cyt *C*) from the NGs at temperature above the volume phase transition temperature (VPTT) and acidic pH. An *ex vivo* human whole blood model was used to investigate biocompatibility of the NGs by quantifying inflammatory responses during NG exposure. The NGs did not induce any significant production of chemokine IL-8 or pro-inflammatory cytokines (IL-1β, IL-6, TNF-α), and the cell viability in human whole blood was maintained during 4 h exposure. The NGs did neither activate the complement system, as determined by low Terminal Complement Complex (TCC) activation and Complement Receptor 3 (CR3) activation assays, thereby overall suggesting that the NGs could be potential candidates for biomedical applications.

1. Introduction

Stimuli-responsive nanogels (NGs) have been shown to have great potential in biomedical applications, such as drug delivery [1] and tissue engineering [2]. Owing to the complexity of the physiological microenvironments, NGs responding to a single stimuli might not be suitable to achieve the desired goals, therefore, materials that are responsive to more than one physical or chemical stimuli are highly desired for biomedical applications [3]. Poly (N-isopropylacrylamide)-co-poly(acrylic acid) (pNIPAm-pAAc)-based NGs provide exactly such dual stimuli response with temperature and pH [4,5]. pNIPAm-based NG undergoes entropically driven reversible coil-to-globule phase transition above the volume phase transition temperature (VPTT), owing to the hydrophilic amide and hydrophobic propyl groups, that lies around 36 °C for these systems, thereby making them most widely studied thermosensitive polymers for biomedical applications of targeted drug delivery [6,7]. The VPTT of pNIPAm-based NGs can be altered by copolymerizing NIPAm with other hydrophobic or hydrophilic monomers [8,9] and acrylic acid (AAc) is one such hydrophilic monomer that also imparts pH response to the polymer, as previously shown by our group [10,4].

PNIPAm-pAAc-based NGs are usually synthesized using precipitation polymerization at temperatures above the VPTT of the formed NG [11,12,4]. A surfactant, such as sodium dodecyl sulphate (SDS), is generally added to avoid NG agglomeration and control the population size [13–15]. These reactions are extremely sensitive to synthesis parameters, including, reactant concentrations, surfactant concentration, amount of initiator and reaction temperature. Studies conducted by Lyon et al. and our group, have shown the effect of these parameters on the size of NGs [10,16]. The presence of oxygen has been shown to hamper radical polymerization reactions by reacting with either the initiator, primary or the growing polymer radical units forming peroxides that hinder further chain growth [17–19]. However, the effect of oxygen atmosphere has not yet been investigated for the synthesis of pNIPAm-pAAc based NGs. Furthermore, polymerization occurs rather fast upon addition of the initiator, thereby shortening the nucleation window. Thereafter, chain growth takes place, where the polymer and co-polymer are incorporated within the NG matrix. The reaction is complex and few studies have been conducted to understand the growth of pNIPAm-based gels [15,20]. In addition, to understand the stimuli response from temperature and pH, it is important to study the extent of incorporation of pNIPAm and pAAc in the NG matrix. Studies have shown the effect of increasing amounts of AAc on the physico-chemical properties [21–23], as well as, the loading efficiencies of the NGs with cytochrome *C* (Cyt *C*) [10,24] and l-dopa [25,26]. Our group, among others, have shown loading and release of drugs from pNIPAm-pAAc based gels at different conditions of temperature and pH [10,25,24,27]. However, most of these studies are not associated with NGs, but, microgels and they do not highlight in detail, the effect of pAAc on the physico-chemical properties, such as swelling/collapse and VPTT of the NGs, as well as, release of drug from these NGs. Although, NGs and microgels share similar structures, NGs pose an advantage owing to their smaller size and responsiveness to deliver payloads to target areas, together with high drug encapsulation, large surface area, and stable interior network structure [28–30].

As the effect of drug carriers increases with circulation time in the blood stream, investigating inflammatory responses in a blood model can be important to gain information on the biocompatibility of the system [31]. Inflammatory responses in blood during exposure to potential drug carriers and NPs can be determined by quantifying pro-inflammatory cytokine production, the formation of the complement activation product soluble Terminal Complement Complex (TCC) and activation of the Complement Receptor 3 (CR3) [32,33]. Previous studies suggests that NGs with AAc as comonomers, have low cytotoxicity and do not induce production of pro-inflammatory cytokines [34,35]. However, the models used are often solely based on *in vitro* cell mono-cultures, i.e.

monocytes lacking the complex interaction between different cell types and plasma cascades involved in an *in vivo* response scenario, as can be modelled using human whole blood [36]. Release of cytokines, such as chemokine IL-8 and pro-inflammatory cytokines IL-1β, IL-6 and TNF-α, have been suggested as potent biomarkers for predicting the immunotoxic potential of NPs, due to high levels of induction being closely related to change in cellular mechanisms and toxicity [37].

In this study, we performed time-based growth experiments to study the formation of pNIPAm-pAAc-based NGs by varying selected reaction parameters, primarily surfactant amounts and reaction atmosphere, to investigate their effects on the physico-chemical properties of the NGs. In addition, the effect of the extent of AAc incorporation in the NG matrix on the physico-chemical properties of the NG was studied. The potential of these NGs as drug delivery vehicles was evaluated by performing loading and release of Cyt *C*, a model protein drug, at different conditions of temperature and pH, and for the first time, using NGs with varying pAAc incorporation in the matrix. Furthermore, biocompatibility studies were conducted on the pNIPAm-pAAc based NGs using a human whole blood model, which is an *ex vivo* model allowing to study the complexity of complement activation by closely mimicking the *in vivo* conditions [36].

2. Experimental section

N-isopropylacrylamide (NIPAm, 97%), N-N′-methylene-bisacrylamide (BIS, 99%), acrylic acid (AAc, 99%), sodium dodecyl sulphate (SDS, 99%), potassium persulphate (KPS, >99%), phosphate buffered saline (PBS, suited for cell culture, endotoxin tested, and supplemented with Ca^{2+}/Mg^{2+}, Zymosan (A crude cell wall extract from the yeast *Saccharomyces cerevisiae*) and propidium iodide (PI) solution suitable for hematology ($\geqslant$94%) were purchased from Sigma–Aldrich® (Schnelldorf, Germany). Ethylenediaminetetraacetic acid (EDTA, ultrapure grade, 0.5 M) was purchased from Invitrogen (Waltham, MA, USA). Ultrapure lipopolysaccharide (LPS) from *Escherichia coli* serotype O111:B4 was purchased from InvivoGen (San Diego, CA, USA). Sterile Refludan for injection or infusion containing the thrombin inhibitor Lepirudin (50 mg/mL) was purchased from Pharmion (Windsor, UK). Lysis buffer and anti-CD11b labelled with phycoerythrin (PE) for flow cytometry were purchased from BD Biosciences (Franklin Lakes, NJ, USA). Paraformaldehyde aqueous solution for cell fixation (PFA, 16%, methanol free and microfiltered) was purchased from VWR (Radnor, PA, USA). All the chemicals (except NIPAm) were used as received without any further purification or modification. Solutions for whole blood experiments were prepared in PBS with Ca^{2+}/Mg^{2+}, which are essential for normal complement activation. All other solutions were prepared using distilled de-ionized water (MQ-water), having a resistivity ~18.2 MΩ.cm at 25 °C, taken from Simplicity® Millipore (Darmstadt, Germany) water purification system.

2.1. Recrystallization of NIPAm

To remove impurities that could inhibit the polymerization reaction, NIPAm was recrystallized using a previously reported protocol by our group [10]. In a typical process, 5 g of NIPAm was dissolved in 50 mL of n-hexane in a one-necked round bottom flask maintained at 110 °C using an oil bath. The reaction was allowed to proceed for 2 h following which, the reactor was placed over an ice bath for 30 min, to allow recrystallization of NIPAm. The solution was then filtered using a ϕ−90 mm filter paper and kept for overnight drying. After drying, the recrystallized NIPAm was stored at −20 °C to prevent absorption of moisture.

2.2. Synthesis of nanogels

The NGs were synthesized using precipitation polymerization as previously reported by our group [10]. The monomers NIPAm and AAc were used to synthesize the NGs using BIS as cross-linker; SDS was used as surfactant and the reaction proceed by adding KPS, as an initiator. In a typical reaction, NIPAm (181 mg) and BIS (14.5 mg) were added to a round bottom flask maintained at 70 °C. 10 mL of SDS, with different molarities (4.2, 3.5, 2.8 and 2.1 mM), were added to the flask and the reaction mixture was stirred for 1 h to ensure the collapse of all NIPAm monomeric units. After 1 h, AAc (124 μL of 1.46 M) and KPS (400 μL of 103 mM) were added in quick succession and the reaction was allowed to continue for 3 h.

To investigate the effect of reaction environment (atmosphere), three different modes of synthesis were applied, namely, a) Continuous-Stirring (CS) – maintaining continuous flow of N_2 with stirring using a magnetic bar stirrer, b) Flashing-Stirring (FS) – N_2 purging during addition of the initiator with stirring using a magnetic bar stirrer, and c) Flashing-Impeller (FI) – N_2 purging during addition of the initiator with stirring using an impeller. Fig. 1 represents the schematic of the three synthesis techniques used based on N_2 usage and the method of stirring. All the synthesised NGs were dialysed overnight using a 14 kDa molecular weight cut-off (MWCO) dialysis membrane, to remove any unreacted monomers and residual reactants. The dialysed NGs were freezedried to remove the solvent and stored at 4 °C for further analysis.

Furthermore, to investigate the pH stimuli response of the NGs with increased incorporation of pAAc units in the NG matrix, NGs were synthesised using CS method. The mole ratios of the monomer (NIPAm), co-monomer (AAc) and crosslinker (BIS) were varied for the different NG samples, as shown in Table 1.

2.3. VPTT Calculation

VPTT of the NGs was calculated by plotting the swelling/collapse of the NGs over a temperature range for both, the heating and cooling cycles. The sizes of these NGs were measured using dynamic light scattering (DLS), between 25 and 55 °C with an interval of 5 °C. Using the NG sizes at different temperatures, relative swelling of the NGs (α_T) was calculated as described in Eq. 1.

$$\alpha_T = \left\{\frac{D}{D_0}\right\}^3 \tag{1}$$

where, D is the NG's hydrodynamic diameter at a given temperature and D_0, is the diameter at 25 °C. α_T was plotted against temperature for heating and cooling cycles and a sigmoidal 5 parameter equation (Eq. 2) was fit, using SigmaPlot® version 14.0, to the obtained curves to find the VPTT described in our previous work [38].

$$y = y_0 + \frac{a}{\left[1 + e^{-\left(\frac{x-x_0}{b}\right)}\right]^c} \tag{2}$$

where, a, b, c, x_0 and y_0 are the 5 constant parameters obtained from SigmaPlot®. An in-house developed MATLAB® code was used to calculate the system's VPTT by equating the areas under the heating and cooling curves, measured by Simpson's $1/3^{rd}$ rule [38].

2.4. VCE_{temp} and VCE_{pH} Calculations

At temperatures above VPTT and acidic pH, NGs undergo volume based collapse. Drug release studies involving polymeric NPs were conducted at different temperature conditions that are usually above the transition temperatures of the material (~37 – 45 °C) [39–42]. Furthermore, it is seen that the biological microenvironment surrounding cancer cells tends to be acidic compared to

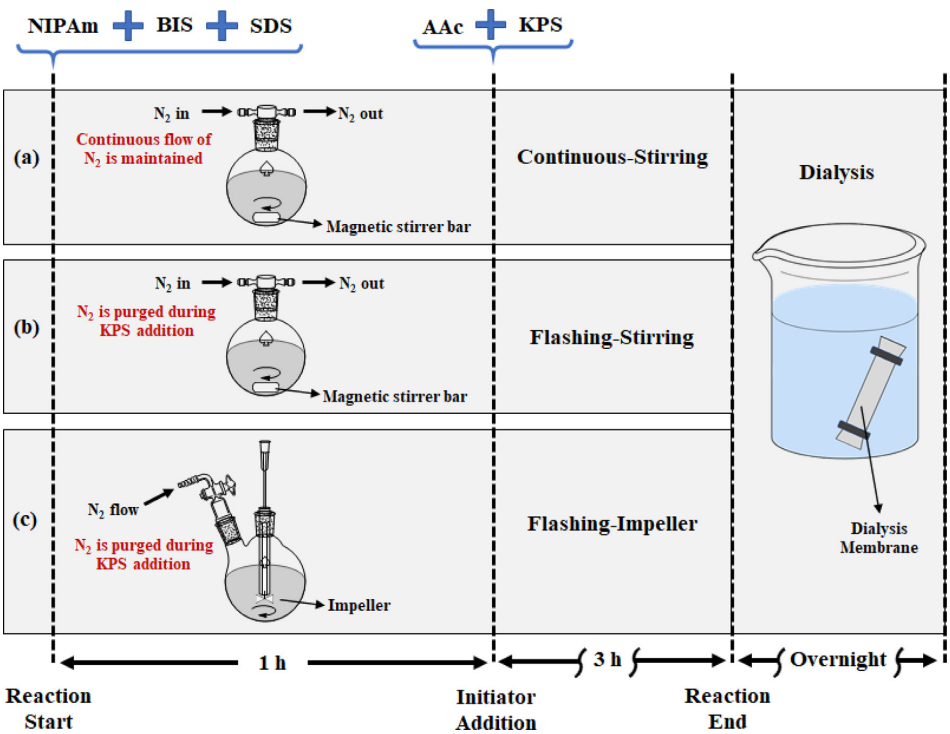

Fig. 1. Schematic representation of the synthesis of NGs via a) Continuous-Stirring, b) Flashing-Stirring, and c) Flashing-Impeller techniques, showing the different nitrogen and stirring modes used in the three synthesis methods.

Table 1
Varying monomer, co-monomer and crosslinker concentrations to study the effect of incorporation of pAAc (in the NG matrix) on the pH response of the NG.

Sample	Mole Ratio NIPAm:AAc:BIS	NIPAm (mg)	AAc (μL)	BIS (mg)
AAc_10	85:10:05	181	129	14.5
AAc_12.5	82.5:12.5:05	181	166	14.9
AAc_15	80:15:05	181	205	15.4
AAc_17.5	78.5:17.5:05	181	247	15.9
AAc_20	75:20:05	181	292	16.4
AAc_22.5	72.5:22.5:05	181	340	17.0
AAc_25	70:25:05	181	391	17.6
AAc_27.5	68.5:27.5:05	181	446	18.3
AAc_30	65:30:05	181	506	19.0

that of normal blood (pH = 7.4), providing optimum conditions for cancer growth [43–45]. Hence, the volumetric collapse efficiencies (VCE) of the NGs, with respect to temperature (25 and 45 °C – maximum collapse of NGs) and pH (3.5 and 7.4), were calculated based on Eqs. 3 and 4 respectively.

$$VCE_{temp} = \frac{{D_{25}}^3 - D_{45}^3}{D_{25}^3} \times 100\% \quad (3)$$

$$VCE_{pH} = \frac{{D_{7.4}}^3 - D_{3.5}^3}{D_{7.4}^3} \times 100\% \quad (4)$$

where, VCE_{temp} is the volumetric collapse efficiency based on the temperature response of the NG (measured at normal pH) and VCE_{pH} is the volumetirc collapse efficiency based on the pH response of the NG (measured at 25 °C). D_{25} and D_{45}, are NG's hydrodynamic diameters at 25 and 45 °C, respectively. $D_{3.5}$ and $D_{7.4}$ are the hydrodynamic diameters at pH = 3.5 and 7.4, respectively.

2.5. Drug loading and release

A model protein drug, Cyt *C*, was used to perform loading and release studies from NGs synthesized via CS and FS methods. Breathing in technique was used to load Cyt *C*, wherein, a freeze-dried NG sample was suspended in the drug solution to allow absorption of Cyt *C* in the NG matrix as the hydrophilic NG swells in solution. In a typical study, 1.7 mg of freeze-dried NG sample was taken in a glass vial and 2 mL of 0.5 mg/mL Cyt *C* solution was added. The mixture was kept for shaking at 300 rpm for 2 h following which the sample was dialysed for 24 h in MQ water using a 14 kDa molecular weight cut-off (MWCO) membrane tubing to remove unbound drug from the system. The sample was then re-suspended in 5 mL water for release measurements. The absorbance value of Cyt *C* was measured using UV–vis spectrophotometer at 409 nm and loading efficiency (L.E.) of the NGs was calculated using Eq. 5.

$$L.E.(\%) = \frac{Abs_{dia}}{Abs_{CytC}} \times 100\% \quad (5)$$

where, Abs_{dia} and Abs_{CytC} are the absorbance values of Cyt *C* of the dialysed sample and that of the drug solution time = 0 and at a particular time 'i', respectively.

Cyt *C* release studies was performed at different temperature (above VPTT of NGs) and pH (acidic) conditions over a period of

time. Absorbance value of Cyt *C* at 409 nm was measured and the drug release % was calculated using Eq. 6.

$$Release(\%) = \frac{Abs_{t0} - Abs_{ti}}{Abs_{t0}} \times 100\% \quad (6)$$

where, Abs_{t0} and Abs_{ti} are the absorbance values of Cyt *C* at time = 0 and at a particular time 'i', respectively.

2.6. Whole blood model

Human whole blood, from voluntary healthy donors, was collected in low-activating polypropylene vials (Nunc 4.5 mL) containing thrombin inhibitor/anti-coagulant lepirudin (50 μg/mL). Immediately after collection, 500 μL blood and controls were incubated with 200 μL NGs in 1.8 mL Nunc propylene vials. Phosphate buffered saline (PBS) was used as the negative control while Zymosan and Lipopolysaccharide (LPS) served as positive controls with final concentrations of 10 μg and 100 ng/mL, respectively. The NGs were added with final concentrations of 1, 10 and 100 μg/mL. The tubes were then incubated at 37 °C in a Rock'n Roller (Labinco B.V., The Netherlands) providing continuous, slow rotation around the axis of the tubes at a fixed angle. Samples were extracted from the tubes after a given incubation time according to the response parameters that were examined; TCC: 30 min, cytokine production and cell viability: 240 min. For TCC and cytokine analysis, EDTA (final concentration = 10 mM) was added to stop further potential complement activation. Plasma was then separated by centrifuging the whole blood samples at 1800 times *g* for 15 min. Plasma was stored at −20 °C until analysis.

2.6.1. TCC activation

TCC formation analysis were performed using a TCC ELISA kit (Human Terminal Complement Complex HK328, Hycult Biotech, Netherlands), according to the instructions from the manufacturer. In brief, plasma samples and controls were added to the antibody-covered 96-well plate and incubated for 1 h at room temperature, followed by washing with wash buffer. Biotinylated tracer was added followed by another 1 h incubation step. After washing with the wash buffer, streptavidin-peroxidase conjugate was added and the plate was further incubated for 1 h. The wells were then washed again before tetramethylbenzidine (TMB) was added and incubated for 30 min. Kit stop solution was added before the plate was read at 450 nm using a UV–vis spectrophotometer (Unico, Dayton, OH, USA).

2.6.2. Cytokine production

The concentrations of the pro-inflammatory cytokines IL-1β, IL-6, IL-8 and TNF-α were determined using Bio-Plex Pro Human Cytokine Screening Panel assay kit (BioRad, Hercules, CA, USA). The assay was performed per the manufacturers instructions. In brief, assay bead solution was diluted and added to a Bio-Plex Pro 96-well assay plate. Plasma samples and recombinant reference cytokines (standards) were diluted in Bio-Plex sample dilution buffer and added to the beads. The assay plate was then incubated on a shaker for 30 min at 850 ± 50 rpm before it was washed three times. Detection antibody was added, followed by another 30 min of incubation on the shaker. After washing, streptavidin-peroksidase was added to the plate followed by 10 min incubation on the shaker. After another washing step, Bio-Plex assay buffer was added and the plate was shaken for 30 s. The beads were analysed using Bio-Plex 200 with Bio-Plex Manager Software.

2.6.3. Cell viability

25 μL whole blood samples were transferred to separate flow vials after 4 h incubation. Non-treated fresh blood was used as negative control of cell death, while as positive control blood cells were killed by heating the blood for 2 min at 70 °C followed by 3 min on ice. 2.5 μL propidium iodide (PI) was added shortly before flow cytometry analysis with BD FACSCanto II (BD BioSciences, Franklin Lakes, NJ, USA). NG induced cytotoxicity in monocytes and granulocytes was quantified by, first gating living and dead cell populations in the negative and positive controls according to their forward- and side scatter, and then applying the same gating for the NG treated samples. This data analysis was done using FlowJo software (BD BioSciences).

2.7. Characterization techniques

2.7.1. Dynamic Light Scattering (DLS) and zeta potential measurements

The size distribution and zeta potential of the NGs were measured using a Malvern Zetasizer Nano-ZS instrument (Malvern Instruments Ltd., Worcestershire, UK). All the NG solutions were made using MilliQ water and results were averaged over triplicate measurements.

2.7.2. Transmission Electron Microscopy (TEM)

TEM characterization was performed using JEOL JEM-1011 with tungsten filament, with accelerated voltage of 80 kV. Images were captured with MORADA CCD camera (3392 x 2248 x 16bit). NGs were stained using uranyl acetate. The NGs were diluted to 0.2 mg/mL suspension and equilibrated at room temperature for 5 h before sonication for 1 min. Uranyl acetate solution (1 mL, 4%) was added to 1 mL NG suspension and equibrilated for 15 min. Drops were placed on sterile copper grids with formvar and allowed to rest for 5 min before carefully dried on the edges using filter paper. The grid was air dried for 24 h before characterization.

2.7.3. Nuclear Magnetic Resonance (NMR)

^{1}H NMR spectra were recorded in a Bruker Advance Neo 600 MHz instrument. All samples were prepared in heavy water (D_2 O) keeping the reagent concentrations the same as that in the NG synthesis. 0.8 mL suspension was taken from each sample and the spectra were recorded with 128 scans at 25 °C. The reference peak was locked at 4.80 for D_2O. Chemical shifts (δ) were reported in ppm.

3. Results and discussion

3.1. NG synthesis methods and growth kinetics

The hydrodynamic sizes presented in Fig. 2a, show the temperature dependent size change of the NGs at different SDS concentrations. NGs synthesized by continuous-stirring method (NGs_CS) show an increasing hydrodynamic diameter from 208 ± 2 nm to 373± 4 nm when the SDS amount was decreased from 4.2 to 2.1 mM, respectively. Similar trend can also be observed for the NGs synthesized by flashing-stirring (NGs_FS) and flashing-impeller (NGs_FI) methods. In the course of NG formation, SDS provides colloidal stability to the precursor particles during nucleation by electrostatic stabilization [46]. In addition to providing charge stabilization, a higher concentration of SDS results in denser packing around the incipient nucleation (oligomer) centers, thereby limiting the growth of NGs. These data confirm results obtained in previous studies conducted by our group, where SDS concentration was one of the central factors determining the size of the NGs [10]. Furthermore, all the NGs show temperature stimulated volume based transition when exposed to temperatures above their

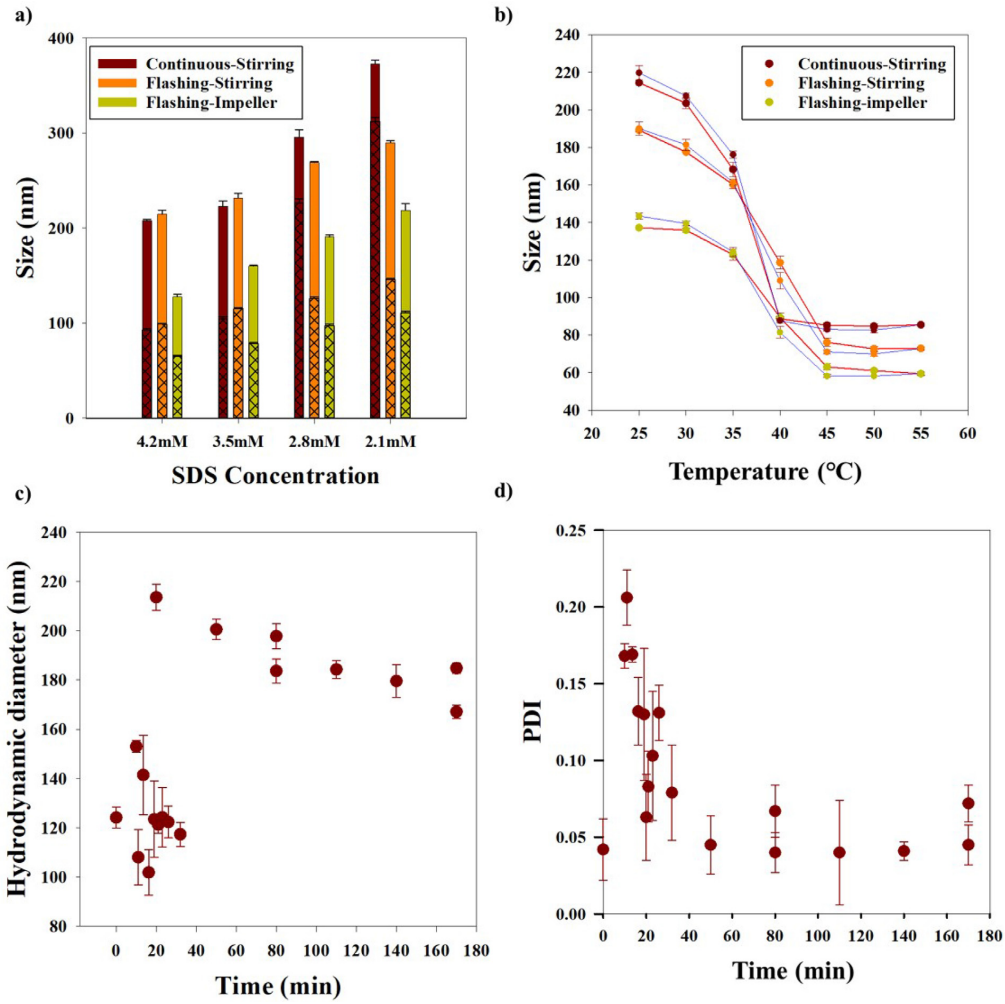

Fig. 2. Variation in the sizes of NGs, synthesized via continuous-stirring, flashing-stirring and flashing-impeller methods, as a function of a) surfactant (SDS) concentration (black crosshatches represent the sizes of NGs at 45 °C) and b) temperature (at 4.2 mM SDS). Variation of c) size and d) PDI, as a function of reaction duration for NGs synthesised using continuous-stirring method, showing the progress of the reaction, with the size increasing and PDI decreasing as the reaction proceeds. The error bars represent the standard deviation calculated from the triplicate measurement of the particular sample.

VPTT. The reduction in NG sizes at 45 °C have been shown by an overlay (black grids) on the corresponding NGs bar curves in Fig. 2a. An entropy driven release of bound water molecules takes place at elevated temperatures due to breaking of hydrogen bonds. Thus, polymer–polymer interactions become stronger than polymer–solvent interactions leading to phase separation and collapse of the NGs.

The heating and cooling phase transition curves, shown in Fig. 2b, are used to determine the VPTTs of the respective NG systems, presented in Table 2. All the NGs showed collapse above VPTT, leading to visible colour change from transparent to pale whitish as the solution turned turbid. The curves in Fig. 2b have a sigmoidal shape, however the collapse for NGs_CS was more abrupt than for the other two systems. Low PDI, measured using Eq. 7 [47] for NG_CS depicts more monodisperse particles than NGs_FS and NGs_FI (Table 2).

Table 2
VPTT and PDI of NGs synthesized by different methods using 4.2 mM SDS.

Method Used	VPTT (°C)	PDI
Continuous-stirring	36.3 ± 0.1	0.2 ± 0.0
Flashing-stirring	37.8 ± 0.1	0.7 ± 0.1
Flashing-impeller	37.7 ± 0.1	0.6 ± 0.2

$$\sigma = \frac{\left(\overline{a^2} - \overline{a}^2\right)^{1/2}}{\overline{a}} \tag{7}$$

where, $\overline{a^2}$ is the NG's mean size and $\overline{a}$ is the NG size.

Having a narrower particle size distribution (PSD) might lead to a more uniform and consistent collapse of the entire system as a whole. In the case of NGs_FS and NGs_FI, with a broader PSD, non-uniform collapse of all the particles at a particular tempera-

ture will occur, resulting in a gradual slope in size collapse (Fig. 2b). The three NGs have temperature-based volumetric collapse efficiencies (VCE_{temp}) that follow the order; NGs_CS > NGs_FS > NGs_FI (for 4.2 mM SDS), as seen in Table 3. Low VCE_{temp} was also witnessed in our previous studies for NGs_CS method [10], however, low VCE_{temp} was not seen in the case of NGs_FS > NGs_FI in this study. High VCE_{temp} highlights the fact that the hydrophobic tails of the SDS chains interfere constructively in increasing the hydrophobicity of the NGs above VPTT, whereby causing a more efficient collapse. Low VCE_{temp}, in the case of NGs_CS, at low SDS concentrations reflects lower incorporation of SDS in the NGs, thereby making the system more hydrophilic with lower collapse. NGs have smaller sizes at 2.8 and 2.1 mM SDS for FS and FI methods, indicating the possibility of higher SDS present in the NG, resulting in more efficient volume collapse at lower SDS concentrations.

Fig. 2c and 2d show the variation of particle size and PDI with respect to reaction time for NGs_CS. Time 't = 0' represents the time of initiator addition and the reaction continued for 3 h after the addition. Smaller particle sizes and high PDI were observed in the initial stages of polymerization. The size and PDI values vary a lot in the initial stages of polymerization with high standard deviation which stabilize as the reaction proceeds. A rapid increase in the size of the particles was observed corresponding to the transfer to the pale whitish colour of the reaction medium. This increase in size was different for the three systems with NGs_FI having the fastest increase while NGs_CS having the slowest increase (Fig. S1). ^{1}H NMR of the different NGs showed similarity in the polymer matrix regardless of the synthesis method used, with the typical characteristic proton peaks, ascribed to pNIPAm and the overlapping peaks of pAAc, as can be seen Fig. S3 [48]. NGs from the three methods showed peaks at around 1.0 ppm and 3.8 ppm for the free $-CH_3$ and $-CH_2-$ groups of pNIPAm, respectively. The peaks for the protons of pNIPAm and pAAc, that are present in the polymer backbone, were overlapping in the region 1.4–2.2 ppm. Thus, the differences in the NG structures from ^{1}H NMR could not be predicted.

The reaction medium in the case of NGs_CS is maintained under oxygen-free atmosphere throughout the whole reaction. For the NGs_FS and NGs_FI, nitrogen was purged for 5 min after initiator (KPS) addition, however, the reaction was further maintained under sealed atmosphere (reactor) in the former case, thereby shielding the medium from oxygen for the initial stages of the reaction involving, initiator (KPS) activation and commencement of polymerization. Whereas, in the case of NGs_FI, the seal at the reactor neck, where the impeller rod enters the reactor, doesn't make an airtight seal, thereby having a possibility of air entering the reactor and exposing the reaction mixture to oxygen. The presence of oxygen might be responsible for reducing the efficiency of the initiator as well as cause untimely polymer chain terminations, thereby resulting in smaller polymer chains. This further result in smaller sizes of the NGs (Fig. S1), together with higher PDI for these systems, as compared to NGs_CS and NGs_FS, despite showing structure similarity from ^{1}H NMR (Fig. S3). Fig. 2d shows the variation of PDI of NG_CS as a function of reaction time. PDI follows a similar trend as NG size with high degree of deviation during the initial stages of the reaction and stabilizing as polymerization proceeds. Also, the impeller creates a greater shear as opposed to stirring with a bar magnet, that might result in more reaction nuclei being formed thereby reducing the final NG size. The reaction kinetics of NGs_CS is slowest among the three methods and the final particle size is reached after an hour of KPS addition. NGs_FI are the fastest at attaining the final particle size, whereas the kinetics of NGs_FS lies in between the other two methods. Therefore, less number of nuclei form for NGs_CS, leading to greater growth of NGs and larger particle size. Stirring by impeller could also assist in capturing oligomers more efficiently resulting in earlier onset of polymerization, as seen by the earlier colour change of the reaction mixture. It can further assist in stabilizing these nuclei by providing better access to SDS in the reaction mixture.

As NGs_CS had the highest VCE_{temp} (91.9 ± 0.7) (Table 3), this system was selected to study the effect of increased incorporation of pAAc in the NG, on its physico-chemical properties.

Table 3
VCE_{temp} of NGs_CS, NGs_FS and NGs_FI, synthesized using continuous and flashing methods at different SDS concentrations.

SDS mMole	Continuous-stirring %	Flashing-stirring %	Flashing-impeller %
4.2	92 ± 0	90 ± 1	87 ± 1
3.5	90 ± 1	88 ± 1	88 ± 0
2.8	55 ± 8	90 ± 1	87 ± 1
2.1	41 ± 5	87 ± 1	87 ± 1

Table 4
Extent of collapse of NGs_CS with temperature and pH stimuli.

Sample	Temperature-based collapse 25–40 °C [%]	pH-based collapse synthesis pH – ph = 3.5 [%]
NGs_CS@AAc_10	93.4	6.8
NGs_CS@AAc_15	91.9	41.7
NGs_CS@AAc_25	88.6	51.3

3.2. Effect of Acrylic Acid (AAc)

To investigate the effect of increasing number of pAAc chains in the NG matrix, the mole% of AAc monomers, in the NG_CS samples, was increased from 10 to 30 with an interval of 2.5 (Table 1).

Fig. 3a and b show the variation in the hydrodynamic diameter and zeta potentials for different mole% of AAc (Table 1) with respect to temperature (25 and 45 °C) and pH (3.5 and 7.4). The NGs show collapsing trend with increasing temperature in contrast to swelling behaviour when transferring from acidic to basic medium. The collapse of the NGs above their VPTTs (between 34 and 36 °C in our case (Table S1), is primarily due to a shift in the balance of hydrophilic/ hydrophobic forces that cause coil-to-globule transition upon increase in temperature. At elevated temperatures, entropically-driven release of bound water takes place due to breakage of hydrogen bonds, and water is excluded from the molecular aggregates as polymer–polymer interactions exceed polymer–solvent interactions. The polymer chains, thus collapse, attaining a globular structure resulting in phase separation [10].

The hydrophobicity of AAc increases below pKa of ≈4.26 due to protonation of the carboxylic (–COOH) groups, leading to the formation of hydrogen bonds between the carboxylic groups. This increases the crosslinking within the NG thereby reducing the diffusion of water into the NG matrix making them denser. As AAc deprotonates at higher pH and becomes negatively charged, repulsion between the polymeric chains occurs. The maximum stretching of the polymeric chain with deprotonation depends on the percent ionization of the carboxylic groups. Therefore, a higher amount of AAc in the NG matrix is expected to promote swelling of the structure.

The variations in VCE of the NGs with temperature and pH are shown in Fig. 3c. VCE_{temp} and VCE_{pH}, show a decreasing and an increasing trend with the varying amounts of initial AAc content, respectively. The increase in VCE_{pH} can be attributed to the increasing number of AAc units being incorporated in the NG matrix, thereby occupying more sites within the network. Hence,

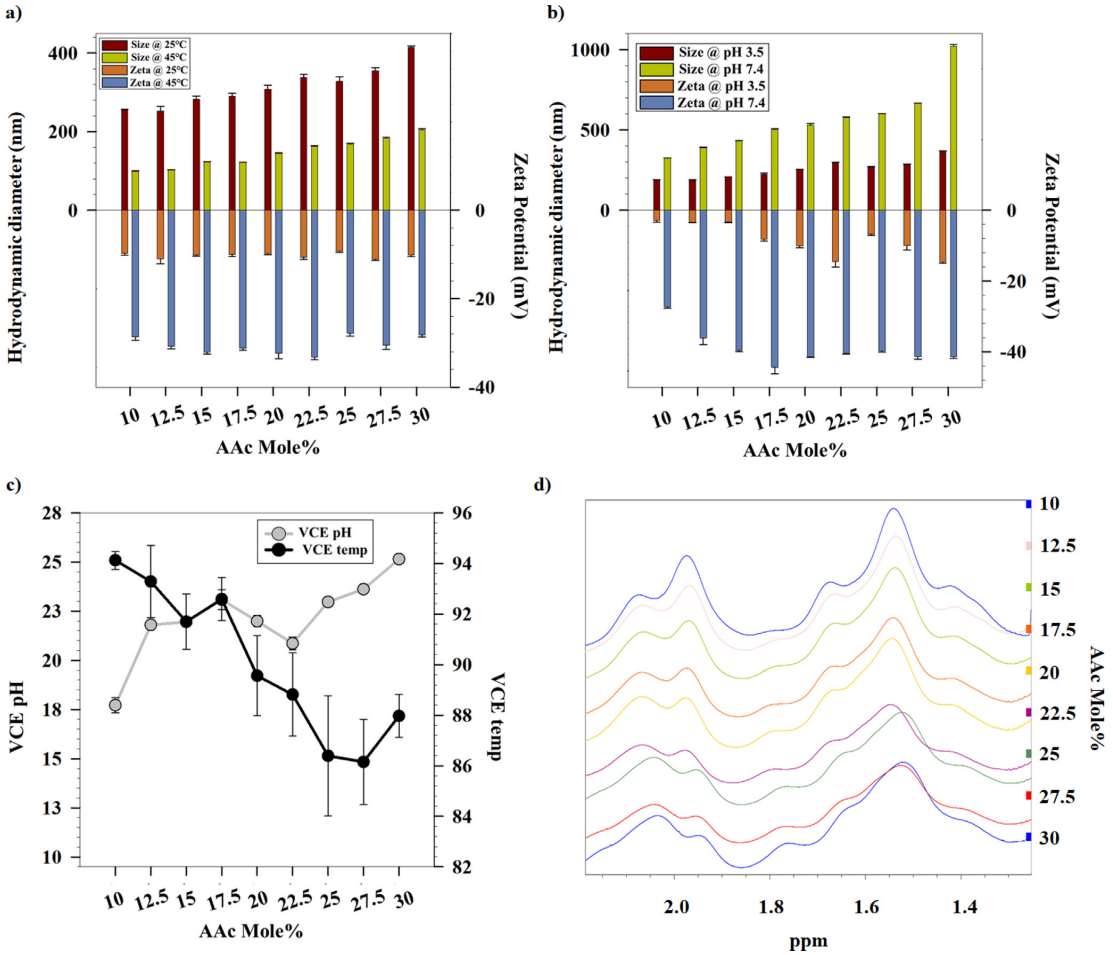

Fig. 3. Hydrodynamic diameter and zeta potentials of the NGs, synthesised via the continuous-stirring method (NGs_CS) with different mole% of AAc, at a) 25 and 45 °C (at neutral pH), and b) pH = 3.5 and 7.4 (at 25 °C), showing the collapse of NGs at elevated temperature (above VPTT) and acidic pH conditions. c) Volumetric collapse efficiency of the NGs_CS with respect to pH and temperature, suggesting a decrease in temperature-based collapse and increase in pH-based collapse with increasing AAc mole%. The error bars represent the standard deviation calculated from the triplicate measurement of the particular sample. d) ^{1}H NMR spectra of NGs synthesized with increasing mole% of AAc, with the increase in peaks for pAAc with increasing AAc mole%, suggesting increased incorporation of pAAc in the NGs.

the protonation in acidic medium leads to greater amount of water extrusion from the NG pores due to breaking of hydrogen bonds resulting in greater collapse and, thus, higher VCE_{pH} when transitioning from pH = 7.4 to 3.5. An inverse trend in VCE_{temp} with increasing initial AAc content is observed. As the temperature dependent collapse is brought about by pNIPAm, the increased incorporation of AAc units in the NGs might suppress the temperature response to some extent thereby reducing the degree of collapse with increasing amounts of AAc units. In addition, the deprotonation of AAc might increase with temperature resulting in intermolecular repulsion that will additionally hinder collapse (opposing the collapse caused by pNIPAm). The effect of the presence of AAc units is evident for samples AAc_25, AAc_27.5 and AAc_30, where the VCE_{temp} tends to stabilize and even showing a slight increase in the case of AAc_30. To observe the higher content of pAAc in the NG matrix with increasing mole ratio of AAc reagent, ^{1}H NMR was performed. As the proton chemical shifts for pNIPAm and pAAc in the polymer backbone overlap in the region 1.4–2.2 ppm, similar result was observed with these NGs. However, increased intensity could be seen at around 2.1 ppm and 1.75 ppm for the protons of pAAc (Fig. 3d). This increase could be due to the higher relative incorporation of AAc in the NG with increasing mole%.

Fig. 4a and b show the variation of hydrodynamic diameter of the NG with temperature and pH, respectively. The NGs show greater response with increasing initial AAc mole%, as is evident from the heating and cooling cycle curves for AAc_10, AAc_20 and AAc_30. This might be due to the lower content of NIPAm monomer units being incorporated in the NGs relative to the AAc. AAc_10 might have longer pNIPAm chains before being interrupted by pAAc chains (system has lower amount of AAc in the reaction mixture). For AAc_30, more AAc is present in the reaction mixture, facilitating pNIPAm co-polymerizing with pAAc, resulting in shorter pNIPAm chains (interpenetrated with pAAc). The range of collapse of the NGs depends on similar chain lengths formed by consecutive pNIPAm units before being interrupted by pAAc

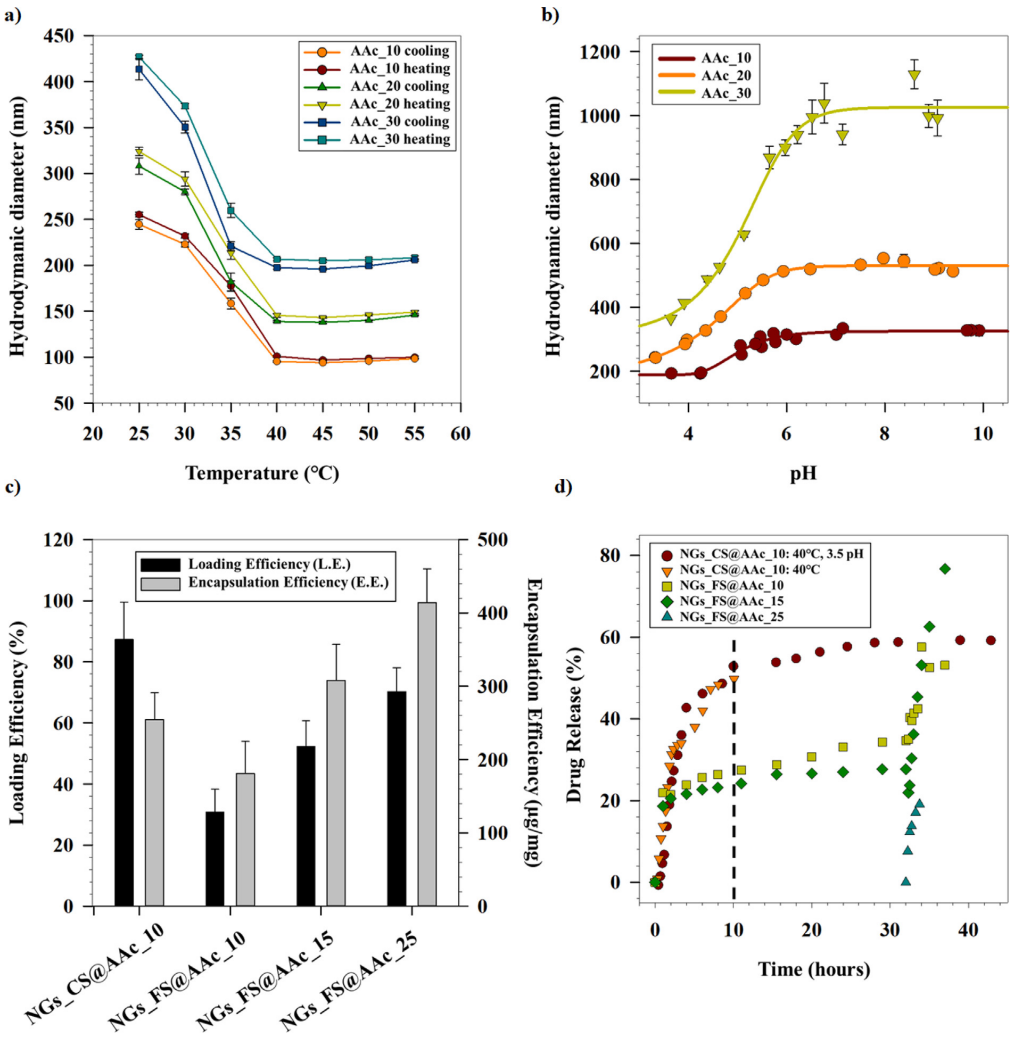

Fig. 4. Variation of the hydrodynamic diameter of AAc_10, AAc_20 and AAc_30 with respect to a) temperature and b) pH, showing decrease in size with increasing temperature and decreasing pH. c) Loading (L.E.) and encapsulation (E.E.) efficiencies of NGs_CS and NGs_FS, with the L.E. and E.E. for NGs_FS increasing with increasing AAc mole%. d) Release profiles of Cyt *C* from NGs_CS and NGs_FS at conditions of elevated temperature (>VPTT) and pH (acidic medium), mimicking cancerous microenvironment conditions. The error bars represent the standard deviation calculated from the triplicate measurement of the particular sample.

chains. Hence, pNIPAm chains with similar lengths will result in greater response (over a shorter range of temperature), whereas, NGs having different chain lengths of pNIPAm will have lower response (over a larger range of temperatures). Also, more responsive collapse of the NGs might be caused by the increased amounts of crosslinker (BIS) present in the samples with higher initial AAc mole % (Table 1). Larger number of crosslinker units will allow the NG to collapse to a larger extent thereby causing a greater hydrophilic to hydrophobic response. A similar sharp transition is observed with AAc_30, showing the sharpest variation in size when going from acidic to basic medium (Fig. 4b). Additionally, the increase in size for AAc_30 and AAc_20 occurs even at pH below 4, whereas AAc_10 only shows an increase after pH = 4.5. As can be seen from Fig. 3b, there is a slight increase in the zeta potential of the NGs with increasing basicity, which might indicate more AAc units being present on the surface of the NGs. Therefore, it can be argued that the early response to change in pH is seen for AAc_30 and AAc_20 owing to more AAc units present on the surface. The hydrodynamic diameter for AAc_30 also seems to plateau off (size stops increasing with further increase in pH) at higher pH values than its counterparts (Fig. 4b). Deprotonation of AAc units might start from the NG's surface towards the core as the units present on the surface will be exposed first. Hence, as AAc_30 has the more AAc units present on the surface (along with more units in the overall NG matrix), size increases with increasing pH, as the change in stimuli is registered by them with the NG matrix swelling and imbibing water. Since NGs_CS and NGs_FS showed similar sizes and VCEs, drug loading and release studies, using Cyt *C*, were performed on these systems to further compare these two systems.

3.3. Drug loading and release

Fig. 4c shows the loading (L.E.) and encapsulation efficiencies (E.E.) of the NGs synthesized via the continuous-stirring and the flashing-stirring methods, with varying concentrations of AAc. The L.E. and E.E. for AAc_10 is higher for NGs_CS than the NGs_FS when using Cyt *C*. Although, it can be seen that the L.E. and E.E. increases with increasing amounts of AAc for NGs_FS, the L.E. remains lower than for NGs_CS system at AAc_10. The increase in the L.E. with increasing AAc content might be owing to the increase in NG particle size. Breathing-in technique was used to load Cyt *C*, where NGs with larger sizes have the capacity to imbibe more drug inside their matrix as they swell on coming in contact with drug solution. Previous research has shown that the heme ligand, located in the lysine-rich region of Cyt *C*, interacts with the negatively charged hydrogel units via Coulombic forces, resulting in polymer-protein complex formation [49,50]. Therefore, increasing number of carboxylic groups (as more AAc units are incorporated in the NG matrix) might lead to higher number of binding sites for Cyt *C* thereby increasing drug loading.

Owing to an increase in metabolism, cancer cells thrive in acidic medium. Hence, to mimic cancerous regions and elevated body temperatures, the release of Cyt *C* from the NGs was observed at conditions of 40 °C and acidic pH as shown in Fig. 4d. NGs_CS particles were continuously exposed to 40 °C, while NGs_FS particles were first subjected to pH = 3 for 30 h, followed by 40 °C and pH = 3. In the case of NGs_CS samples, the Cyt *C* release profiles at 40 °C and at 40 °C with pH = 3.5 coincided to a significant extent. It was seen that NGs_FS followed the release profile of NGs_CS for the initial part and almost plateaued out after a couple of hours. Drug release from NGs_CS was observed to be faster than NGs_FS with 50% of Cyt *C* being released in the first 10 h as opposed to 27% and 24% for NGs_FS@AAc_10 and NGs_FS@AAc_15 respectively. The high release could be attributed to a higher amount of Cyt *C* in NGs_CS (L.E. = 84.8 ± 12.2) resulting in a larger drive for diffusion because of higher concentration gradient. It is observed that temperature induces a greater collapse in the NGs as compared to pH, as shown in Table 4. Therefore, as the release for NGs_CS is induced by temperature and pH, there is a higher driving force (expelling the drug from the NG matrix) owing to greater NG collapse. On the contrary, no Cyt *C* release is seen for NGs_FS@AAc_25 when the system is exposed to just acidic pH condition, even though the system had higher L.E.. The release from this system occurs only after the temperature is raised above VPTT, to 40 °C. This fact, together with the similar release profiles for NGs_CS (40 °C and at 40 °C with pH = 3.5), further support the hypothesis that temperature has a greater impact on drug release than pH. Furthermore, the diffusion of Cyt *C* progresses in three probable zones. The first being transport of the drug from the NG matrix to the NG surface, second being transport of the drug from the NG's surface to the dialysis membrane, and the third, diffusion across the dialysis membrane into the sink. Owing to the larger size of the AAc_25 NGs, the drug needs to travel a greater distance (than AAc_10 and AAc_15) to reach the NG surface before it can diffuse out of the NG matrix. Thus, an excess push is needed to drive the drug out of the NG matrix, provided by the temperature stimuli.

Even though, the continuous and the flashing methods result in NGs having similar physico-chemical properties, the continuous method produces particles with a narrower size distribution with higher drug loading capacity. Furthermore, as NGs_CS had the highest VCE (91.9 ± 0.7) (Table 3), as well as L.E. (Fig. 4c), this system was selected for biocompatibility studies.

3.4. Whole blood responses

Cell viability of monocytes and granulocytes in human whole blood was maintained after exposure to the NGs, as compared to the PBS control and heat-killed cells (Fig. 5a)). Complement activation was examined by measuring soluble TCC formation (Fig. 5b). NG exposure did not significantly increase the formation of TCC in human whole blood cells or activation of CR3 (Fig. S7). Therefore, it appears that the NGs neither significantly activate the complement system in human whole blood during the conditions examined, nor was production of the cytokines IL-1β, IL-6, IL-8 and TNF-α strongly affected compared to the baseline (PBS) values and positive controls. However, a minor, but not significant induction of IL-6 was noted with the highest NG dose, and minimal but statistical significant reduction in IL-8 and TNF-α was found for the intermediate NG doses. Previous research have reported similar data using other cell based models [34,35,51], however, whether the minimal decrease in IL-8 and TNF-α relative to the PBS control is biologically relevant can not be determined without vastly increasing number of donors to exclude potential statistical sampling errors. Minimal effects on complement activation, cytotoxicity and production of pro-inflammatory cytokines in human whole blood suggest that the NGs have good biocompatibility. On the other hand, there could be molecular processes induced by the NGs that are not accounted for by this model, such as production of other cytokines or increased cellular stress mechanisms, coagulation effects and tissue reactions during prolonged exposure *in vivo*. Thus, further investigations of these properties may be considered in order to fully develop these NGs as drug carriers.

4. Conclusion

Based on previous studies [10,4,24,25,38] new methods were developed to synthesize pNIPAm-pAAc-based nanogels (NGs), with varying degrees of physico-chemical properties. The physico-chemical properties of the NGs are influenced by various parameters including reactant concentrations, temperature and reaction atmosphere. SDS has been shown to act as a stabilizing agent that affects particle size. The sizes of NGs reduced on increasing the concentration of SDS from 2.1 mM to 4.2 mM owing to the stabilization of the precursor particles during nucleation, as well as, a denser packing around the nucleation centres thereby preventing growth. In addition, the effect of reaction atmosphere (nitrogen) on the growth of the NGs was investigated using continuous and flashing techniques (with different stirring modes), namely – continuous-stirring (NGs_CS), flashing-stirring (NGs_FS) and flashing-impeller (NGs_FI). Although flashing methods produced uniform VCE_{temp} on varying SDS, the NGs with the highest VCE_{temp} were produced with the process having continuous supply of nitrogen to the reaction medium and highest SDS concentration (VCE_{temp} = 92 ± 0%).

Furthermore, the pH responsiveness of NGs_CS was studied by varying AAc mole% during synthesis and the degree of pAAc incorporation in the NG matrix was confirmed by NMR. The size of NGs increased with increasing amounts of pAAc in the NG matrix and that also resulted in increased Cyt *C* loading efficiency (L.E.). L.E. was the highest for NGs_CS (L.E. = 87.4 ± 12.2%) compared to NGs_FS (L.E. = 30.8 ± 7.4%), for 10 mol% AAc. This study showed release of Cyt *C* with temp and pH, while controlling the particle size in nano-range. NGs_CS also showed biocompatibility, investigated by studying the activation of the complement system, and induced little or no release of pro-inflammatory cytokines/chemokines in a human whole blood model. Further investigations, specifying the degree of incorporation of different monomer units in the NG matrix, along with studies on molecular processes

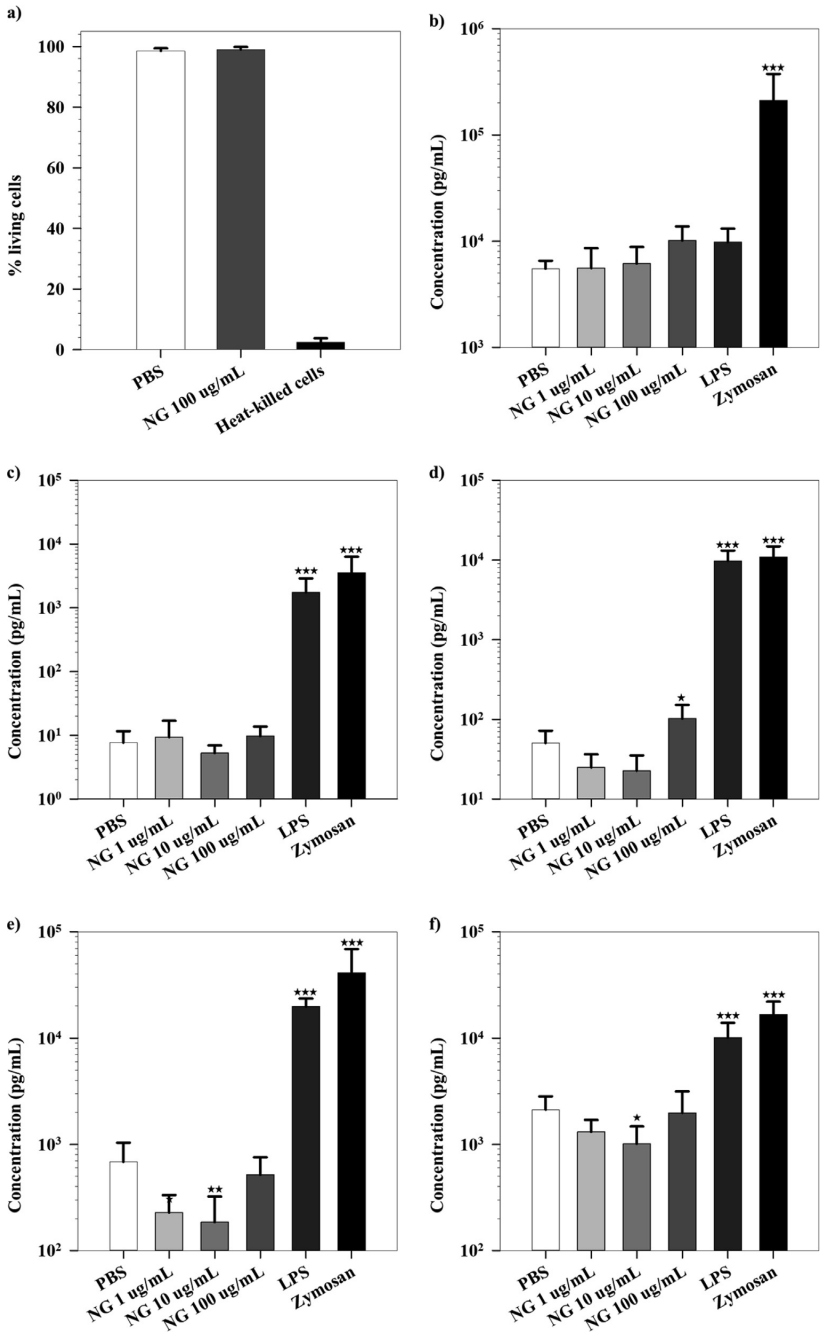

Fig. 5. a) Cell viability of monocytes and granulocytes was maintained after NG incubation in human whole blood. Loss of cell viability is accompanied by disruption of plasma membrane integrity and increased PI permeability and nuclear staining. Quantification of dead versus viable cells (PI intensity) was done by flow cytometry with gating for the respective cell types. b) There was no significant increase in TCC formation during incubation of NGs in blood, as determined by ELISA for soluble TCC in the plasma. c-f) Plasma levels of pro-inflammatory cytokines c) IL-1β, d) IL-6, e) TNF-α, and f) chemokine IL-8 were not significantly increased during NG incubation in blood, as determined by multiplex ELISA. For all subfigures: Error bars represent standard deviations. Statistical significance (*P<0.05, **P<0.01, ***P<0.001) compared to the PBS control found by 1way RM-ANOVA on log-transformed data (assuming log-normal distribution) with the Dunette post-test. N = 5 consecutive experiments.

induced in human blood, can help develop these NGs as drug carriers. Such drug carries can further incorporate metallic NPs, such as, gold, silver and iron-oxide, to impart optical and magnetic properties.

Ethics

The use of whole blood for these experiments was approved by the Regional Committee for Medical and Health Research Ethics in Central Norway (REC Central), The Norwegian Ministry of Education and Research, 2009/2245. Experiments were conducted according to their regulations and guidelines. Informed written consent was obtained from each voluntary donor prior to blood sampling.

Funding

Jørgen Stenvik is financed by the Research Council of Norway Grant 223255/F50 through its Centers of Excellence funding scheme.

Author's Contributions

All the NG synthesis, characterization and functionalization experiments have been performed at the Norwegian University of Science and Technology (NTNU), Norway.

CRediT authorship contribution statement

Anuvansh Sharma: Conceptualization, Methodology, Software, Validation, Investigation, Resources, Visualization, Writing – original draft, Writing – review & editing. **Karthik Raghunathan:** Conceptualization, Software, Validation, Investigation, Resources, Visualization, Writing – original draft, Writing – review & editing. **Helene Solhaug:** Conceptualization, Methodology, Validation, Investigation, Resources, Visualization, Writing – original draft, Writing – review & editing. **Jibin Antony:** Software, Validation, Investigation, Visualization. **Jørgen Stenvik:** Conceptualization, Methodology, Validation, Writing – original draft, Visualization, Supervision, Writing – review & editing. **Asbjørn Magne Nilsen:** Conceptualization, Methodology, Validation, Writing – original draft, Visualization, Supervision, Writing – review & editing. **Mari-Ann Einarsrud:** Validation, Visualization, Supervision, Writing – original draft. **Sulalit Bandyopadhyay:** Conceptualization, Methodology, Validation, Visualization, Supervision, Writing – original draft, Writing – review & editing.

Declaration of Competing Interest

The authors declare that they have no known competing financial interests or personal relationships that could have appeared to influence the work reported in this paper.

Acknowledgement

We thank the Functional Materials and Materials Chemistry (FACET) group for all the valuable insights and discussions. The authors would like to thank NorFab for the financial support in connection to the use of NTNU Nanolab and the Faculty of Natural Sciences and Technology, NTNU, for the financial support. We thank the Department of Material Sciences and Engineering (NTNU), Department of Clinical and Molecular Medicine (NTNU), NORTEM/ Gemini Centre (NTNU) and Nanolab (NTNU), for all their financial, technical and laboratory support. Mr. Romit Chakrborty and Mr. Abhishek Banerjee are thanked for conducting preliminary NG synthesis, drug loading and release experiments. We extend our ø, Department of Biotechnology and Food Science, for performing NMR measurements for this study. We also want to thank Liv Ryan at Centre for Molecular Inflammation Research (CEMIR) for technical and laboratory suppSort. The electron microscopy work was performed at the Cellular and Molecular Imaging Core Facility (CMIC) EM lab, Norwegian University of Science and Technology (NTNU) at St.Olavs Hospital, and a specific thanks to Nan T. Skogaker.

Appendix A. Supplementary material

Supplementary data associated with this article can be found, in the online version, at https://doi.org/10.1016/j.jcis.2021.07.139.

References

[1] L. Zha, B. Banik, F. Alexis, Soft Matter 7 (2011) 5908–5916.
[2] A.H. Bacelar, I.F. Cengiz, J. Silva-Correia, R.A. Sousa, J.M. Oliveira, R.L. Reisa, Handbook of intelligent scaffolds for tissue engineering and regenerative medicine 2 (2017) 327–361.
[3] N.K. Preman, R.R. Barki, A. Vijayan, S.G. Sanjeeva, R.P. Johnson, Eur. J. Pharm. Biopharm. (2020).
[4] R. Raju, S. Bandyopadhyay, A. Sharma, S.V. Gonzalez, P.H. Carlsen, O.R. Gautun, W.R. Glomm, Polymers 10 (2018) 309.
[5] W. Liwinska, I. Stanislawska, M. Lyp, Z. Stojek, E. Zabost, RSC Adv. 9 (2019) 13736–13748.
[6] A.S. Vikulina, S.T. Aleed, T. Paulraj, Y.A. Vladimirov, C. Duschl, R. Von Klitzing, D. Volodkin, PCCP 17 (2015) 12771–12777.
[7] Nothdurft, K., Muller, D. H., Murtz, S. D., Meyer, A. A., Guerzoni, L. P., Jans, A., Kuhne, A. J., De Laporte, L., Brands, T., Bardow, A., et al. Is the Microgel Collapse a Two-Step Process? Exploiting Cononsolvency to Probe the Collapse Dynamics of Poly-N-isopropylacrylamide (pNIPAM). The Journal of Physical Chemistry B 125 (2021) 1503–1512.
[8] T. Trongsatitkul, B.M. Budhlall, Colloids Surf., B 103 (2013) 244–252.
[9] I. Sanzari, E. Buratti, R. Huang, C.G. Tusan, F. Dinelli, N.D. Evans, T. Prodromakis, M. Bertoldo, Sci. Rep. 10 (2020) 1–14.
[10] S. Bandyopadhyay, M.K. Andersen, M.A.A. Alvi, A. Sharma, R. Raju, B.H. McDonagh, W.R. Glomm, Colloid Polym. Sci. 294 (2016) 1929–1942.
[11] Z. Meng, M.H. Smith, L.A. Lyon, Colloid Polym. Sci. 287 (2009) 277–285.
[12] G.R. Hendrickson, L.A. Lyon, Angew. Chem. Int. Ed. 49 (2010) 2193–2197.
[13] W. McPhee, K.C. Tam, R. Pelton, J. Colloid Interface Sci. 156 (1993) 24–30.
[14] B. Wedel, T. Brandel, J. Bookhold, T. Hellweg, ACS Omega 2 (2017) 84–90.
[15] W.H. Blackburn, L.A. Lyon, Colloid Polym. Sci. 286 (2008) 563–569.
[16] J.M. Knipe, N.A. Peppas, Regenerative Biomater. 1 (2014) 57–65.
[17] C. Decker, K. Moussa, Rapid Commun. 11 (1990) 159–167.
[18] C.W. Miller, C.E. Hoyle, S. Jönsson, C. Nason, T. Lee, W. Kuang, K. Viswanathan, N-vinylamides and Reduction of Oxygen Inhibition in Photopolymerization of Simple Acrylate Formulations, ACS Publications, 2003.
[19] V.V. Krongauz, C.P. Chawla, J. Dupre, Oxygen and Radical Photopolymerization in Films, ACS Publications, 2003.
[20] X. Xia, Z. Hu, Langmuir 20 (2004) 2094–2098.
[21] Y.K. Kim, E.-J. Kim, J.H. Lim, H.K. Cho, W.J. Hong, H.H. Jeon, B.G. Chung, Nanoscale Res. Lett. 14 (2019) 1–9.
[22] K. Kratz, T. Hellweg, W. Eimer, Colloids Surf., A 170 (2000) 137–149.
[23] V. Nigro, R. Angelini, B. Rosi, M. Bertoldo, E. Buratti, S. Casciardi, S. Sennato, B. Ruzicka, J. Colloid Interface Sci. 545 (2019) 210–219.
[24] S. Bandyopadhyay, A. Sharma, W.R. Glomm, Gels 3 (2017) 42.
[25] S. Bandyopadhyay, M.A.A. Alvi, A. Sharma, K. Zhu, A.-L. Kjøniksen, B. Nyström, W.R. Glomm, Colloid Polym. Sci. 295 (2017) 391–402.
[26] M.H. Smith, L.A. Lyon, Macromolecules 44 (2011) 8154–8160.
[27] A. Prasannan, H.-C. Tsai, Y.-S. Chen, G.-H. Hsiue, J. Mater. Chem. B 2 (2014) 1988–1997.
[28] D. Li, C.F. van Nostrum, E. Mastrobattista, T. Vermonden, W.E. Hennink, J. Controlled Release 259 (2017) 16–28.
[29] H. Zhang, Y. Zhai, J. Wang, G. Zhai, Mater. Sci. Eng.: C 60 (2016) 560–568.
[30] I. Neamtu, A.G. Rusu, A. Diaconu, L.E. Nita, A.P. Chiriac, Drug Deliv. 24 (2017) 539–557.
[31] Merkel, T. J., Jones, S. W., Herlihy, K. P., Kersey, F. R., Shields, A. R., Napier, M., Luft, J. C., Wu, H., Zamboni, W. C., Wang, A. Z., et al. Using mechanobiological mimicry of red blood cells to extend circulation times of hydrogel microparticles. Pro- ceedings of the National Academy of Sciences 2011, 108, 586–591.
[32] Halperin, J. A., Taratuska, A., Nicholson-Weller, A., et al. Terminal complement complex C5b-9 stimulates mitogenesis in 3T3 cells. The Journal of clinical investigation 1993, 91, 1974–1978.
[33] A. Fara, Z. Mitrev, R.A. Rosalia, B.M. Assas, Open Biol. 10 (2020) 200160.
[34] R.L. Bartlett, A. Panitch, Biomacromolecules 13 (2012) 2578–2584.
[35] Bridges AW, Singh N, Burns KL, Babensee JE, Andrew Lyon L, García AJ. Reduced acute inflammatory responses to microgel conformal coatings. Biomaterials.

2008 Dec;29(35):4605-15. https://doi.org/10.1016/j.biomaterials.2008.08.015. Epub 2008 Sep 19. PMID: 18804859; PMCID: PMC2585524.
[36] T.E. Mollnes, O.-L. Brekke, M. Fung, H. Fure, D. Christiansen, G. Bergseth, V. Videm, K.T. Lappegård, J. Kohl, J.D. Blood Lambris, J. Am. Soc. Hematol. 100 (2002) 1869–1877.
[37] M. Elsabahy, K.L. Wooley, Chem. Soc. Rev. 42 (2013) 5552–5576.
[38] S. Bandyopadhyay, A. Sharma, M.A.A. Alvi, R. Raju, W.R. Glomm, RSC Adv. 7 (2017) 53192–53202.
[39] K.S. Soppimath, L.-H. Liu, W.Y. Seow, S.-Q. Liu, R. Powell, P. Chan, Y.Y. Yang, Adv. Funct. Mater. 17 (2007) 355–362.
[40] Y. Chen, Y. Gao, L.P. da Silva, R.P. Pirraco, M. Ma, L. Yang, R.L. Reis, J. Chen, Polym. Chem. 9 (2018) 4063–4072.
[41] T.-Y. Liu, K.-H. Liu, D.-M. Liu, S.-Y. Chen, I.-W. Chen, Adv. Funct. Mater. 19 (2009) 616–623.
[42] H. Grüll, S. Langereis, J. Controlled Release 161 (2012) 317–327.
[43] Y. Kato, S. Ozawa, C. Miyamoto, Y. Maehata, A. Suzuki, T. Maeda, Y. Baba, Cancer Cell Int. 13 (2013) 1–8.
[44] E. Boedtkjer, S.F. Pedersen, Annual Rev. Physiol. 82 (2020) 103–126.
[45] L. Feng, Z. Dong, D. Tao, Y. Zhang, Z. Liu, National Sci. Rev. 5 (2018) 269–286.
[46] M.H. Smith, L.A. Lyon, Accounts Chem. Res. 45 (2012) 985–993.
[47] P. Pusey, J. Physique 48 (1987) 709–712.
[50] X. Gao, Y. Cao, X. Song, Z. Zhang, C. Xiao, C. He, X. Chen, J. Mater. Chem. B 1 (2013) 5578–5587.
[51] P.K. Jain, K.S. Lee, I.H. El-Sayed, M.A. El-Sayed, J. Phys. Chem. B 110 (2006) 7238–7248.
[52] V. Skobeleva, A. Zinchenko, V. Rogacheva, A. Zezin, Kabanov (2001) 43.
[53] M. Giulbudagian, G. Yealland, S. Hönzke, A. Edlich, B. Geisendörfer, B. Kleuser, S. Hedtrich, M. Calderón, Theranostics 8 (2018) 450.

8.3 Manuscript III

Sharma, A., 2021. Growth Kinetics of Iron-Oxide – Silver Dimeric Nanoparticles & Their Potential Biomedical Applications.

Growth Kinetics of Iron-Oxide – Silver Dimeric Nanoparticles & Their Potential Biomedical Applications

Abstract

Magneto-plasmonic nanoparticles (NPs) have gained increased interest in the field of biomedicine for applications, such as, drug delivery, biosensing and imaging. Iron and silver, are few of the many nanomaterials, that are used for the purpose of imparting superparamagnetic and plasmonic properties to the magneto-plasmonic NPs, respectively. At nanoscale, the physico-chemical properties of the magneto-plasmonic are dependant size and surface effects, and understanding the formation of these NPs is, therefore, critical in comprehending the resulting property of the particle. Studies with respect to these have mostly been performed using gold NPs and few with silver. Herein, we investigate the formation of magneto-plasmonic dimeric NPs (DNPs) by performing time-based study to analyse the growth of silver on iron-oxide NPs (IONPs). The studies reveal formation of satellite/raspberry-type morphology in the initial stages of the reaction suggesting nucleation of Ag on multiple sites on the surface of IONPs. However, the DNPs attain dumbbell-like morphology at the end of the reaction by reorientation of Ag on the surface of IONPs through surface diffusion and Ostwald ripening. Furthermore, the effect of silver precursor on the physico-chemical properties of the DNPs has been evaluated. The applicability of these particles as biosensors has been explored using the concept of magnetophoresis.

Keywords: Magnetophoresis, Dimeric Nanoparticles, Iron-Oxide, Silver, Growth Kinetics, Biosensing.

Introduction

Magneto-plasmonic nanoparticles (NPs) combine the worlds of magnetism and photonics at nanoscale, thereby exhibiting plasmonic and magnetic phenomenon simultaneously.[1] Besides their popular application in magnetic hyperthermia (MHT),[2–5] magnetic NPs provide other functions such as contrast for magnetic resonance imaging (MRI)[6,7] or magnetic-based targeting and drug delivery.[8,9] On the other hand, plasmonic NPs present optical sensing ability for applications as biosensors,[10,11] and imaging agents.[12–14] From a theranostics approach, the magneto-plasmonic association has gathered particular attention over the past few years due to its multifunctional potential for biomedical applications.[2] Magneto-plasmonic NPs, thus, combine complementary theranostic strategies in a unique structure, including multimodal photothermal therapy,[15] biosensing,[16] magnetic separation[17] and targeted therapy,[18] with magnetic and plasmonic features.

At nanoscale, size and surface effects play a key role in shaping NP properties that are affected by interparticle electromagnetic or magnetic dipolar interactions and intraparticle chemical, structural and electronic couplings. Studies have shown that the magnetic and plasmonic properties differ in hybrid NPs and their bare counterparts.[19–22] Usually, a decrease in the magnetisation is seen in the magneto-plasmonic NPs compared to the bare NPs resulting from a '*dead layer*' or magnetic disordered layer, at the free surface or the interface of the NPs.[23–28] Thus, understanding the formation of magneto-plasmonic NPs is critical in understanding their combined magnetic and plasmonic properties. The above mentioned studies have been performed mostly with Au, however, AgNPs have been shown to have better sensitivity (LSPR shift) compared to AuNPs, thereby making them suitable candidates for the application of biosensing.[29]

The formation magneto-plasmonic NPs takes place via epitaxial growth of the growth species on the seed (the other species), resulting in heterogeneous nucleation.[30] The morphology of the magneto-plasmonic NPs can be controlled by various reaction parameters, such as, seed size, seed concentration, solvent polarity, concentration of growth species, reaction temperature and crystalline lattice spacing, that might result in core-shell, dumbbell, flower-like morphology.[30–34] Growth of a crystalline specie (Ag) on another crystalline NP (IONP) would result in a dumbbell NP given that there is a large enough lattice mismatch.[30,35]

Magnetophoresis technique can be used for biosensing applications using magnetic NPs that have high surface functionality. Magnetic NPs move in the direction of applied magnetic field and the time of separation depends on factors such as solvent viscosity, NP size and magnetic field strength. For a constant field and solvent viscosity, the velocity of separation varies directly with magnetic NP size. These NPs can be functionalized with a ligand having complementary antigen functional groups enabling attachment of the antigen to the magnetic NPs, thereby resulting in NP self-assembly. Once the self-assembled NPs are exposed to the

magnetic field, they begin to separate out with a slower particle velocity than non-self-assembled NPs, due to the drag. Also, the overall magnetic component in the self-assembled particle reduces owing to the attachment of foreign body. The increase in separation time with respect to the control indicates the presence of the antigen. The separation velocities, in our study have been, measured indirectly using UV-Vis spectrophotometry, conducted for 24 h for a sample.

Experimental Section

Silver acetate (AgAc, $\geq$ 99.0%), iron(0) pentacarbonyl ($Fe(CO)_5$, > 99.99%), methanol ($\geq$ 99.8%), oleic acid (OA, $\geq$ 99.0%), sodium citrate dihydrate (NaCit, $\geq$ 99.0%), oleylamine (99.0%), hexane ($\geq$ 99.0%) and 1-Octadecene (ODE, 90.0%) were purchased from Sigma Aldrich®. Hexadecyltrimethylammonium bromide (CTAB, > 99.0%) and iron(III)chloride hexahydrate ($FeCl_3.6H_2O$, $\geq$ 99.0%) was purchased from Acros Organics®. Toluene (technical grade), isopropanol (technical grade) and acetone (technical grade) were purchased from VWR chemicals®. Sodium Oleate (NaOl, $\geq$ 97.0%) was purchased from Tokyo Chemical Industry®. All the chemicals were used as received without any further purification or modification. All solutions in aqueous phase were prepared using MilliQ water), having a resistivity ~18.2 MΩ.cm at 25°C, taken from Simplicity® Millipore (Darmstadt, Germany) water purification system.

NP Synthesis

Spherical and cubic iron-oxide nanoparticles (IONPs) were synthesised using thermal decomposition of iron-oleate precursor at elevated temperatures in inert (argon) atmosphere. The temperature of the reaction was raised using a temperature controller (MRC® Heating mantle 100 mL with analog control and Digital 4 programs × 16 segment programmer) for precise control of the heating rate.

Iron Oleate Synthesis

The iron-oleate complex was prepared using our previously reported protocol by our group.[36] Typically, 5.40 g of $FeCl_3{\cdot}6H_2O$ and 18.25 g of sodium oleate were dissolved in a mixture of solvents consisting of 40 mL ethanol, 30 mL MilliQ water and 70 mL hexane, in 250 mL round bottom flask. The resulting solution was refluxed at 70°C for 4 h with vigorous stirring using a bar magnet. The resulting dark red organic phase, containing iron oleate complex, was transferred to a separator funnel and washed three times with MilliQ water. The remaining solution was evaporated in a Heidolph rotary evaporator (T = 70°C) to yield a highly viscous dark red liquid of iron oleate.

Synthesis of Spherical Iron-Oxide NPs (SNPs)

The synthesis protocol, adapted and modified from previous works conducted by our group, involved mixing 1.6 g of iron oleate, 600 µL OA and 25 mL 1-octadecene (ODE) in a three-necked glass reactor, placed over a heating mantle fitted with a cooling water condenser.[36] The reaction was carried out under argon atmosphere and the temperature of the reactor was ramped from room temperature to 320°C at 3°C/min. The reaction was maintained at 320°C for 45 min after which the solution was cooled down to room temperature. NPs were then washed using hexane and precipitated out using a mixture of isopropanol and hexane. The particles were magnetically separated and washed thrice using acetone before finally redispersing in a known volume of toluene.

Synthesis of Cubic Iron-Oxide NPs (CNPs)

Adapted and modified from our group's work, in a typical synthesis, 0.833 g of iron oleate, 213 mg sodium oleate and 14 mL ODE were heated in a three-necked glass reactor placed on a heating mantle, fitted with a cooling water condenser, to 325°C at 2.8°C/min under argon atmosphere.[36] The reaction was maintained at 325°C for 45 min after which the NPs were cooled to room temperature. NPs were then washed using hexane and precipitated out using a mixture of isopropanol and hexane. The particles were magnetically separated and washed thrice using acetone before finally redispersing in a known volume of toluene.

Synthesis of Iron-Oxide – Silver Dimeric NPs (DNPs)

Both, SNPs and CNPs, have been used as seeds for the growth of Ag on the surface of IONPs. DNPs, synthesised using SNPs and CNPs, are referred to *'Ag@SNPs'* and *'Ag@CNPs'*, respectively in this study. The seed-mediated synthesis of DNPs used in this project is modified from the procedure reported by Zhang *et al.*[30] In a typical synthesis, 10 mg of IONPs, 354 µL of oleylamine, 10 mL toluene and silver acetate were mixed in a round bottom flask. The amount of silver acetate was varied according to Table 1. The mixture was heated to 72°C under inert (argon) atmosphere and the reaction was carried out overnight. The product was allowed to cool down to room temperature before adding methanol in order to precipitate the particles. The particles were washed with acetone before finally redispersing them in 10 mL of toluene.

Table 1: Varying amount of Silver Acetate for the synthesis of DNPs.

Seed	IONP (mg)	AgAc (mg)
SNP	10	7.7
SNP	10	11.2
SNP	10	15.7
CNP	10	11.2

Dimeric NP Growth Studies

In order to investigate the growth of silver on the surface of IONPs, samples were taken from the reaction mixture after particular time intervals of the start of the reaction. These are then examined under S(T)EM and TEM, where the grids were prepared by dropping a few drops of the mixture on them for analysis. Additionally, EDS measurements were also performed to locate iron-oxide and silver in the DNPs.

Dimeric NP Phase Transfer

As the DNPs are synthesised and stored in toluene, they need to be phase transferred to aqueous phase before they can be utilized for biomedical applications. CTAB was used to transfer the DNPs from toluene to water following a modified procedure previously reported by Kim *et al.*[37] In a typical process, 10 mL of the DNP solution was added to a glass vial and precipitated out by the addition of 40 mL of methanol. A disc magnet was kept on the side of the vial causing the particles to separate from the solution. The supernatant was discarded and the particles were washed thrice with acetone, to ensure removal of any residual solvent, and left to dry. Separately, 1 g of CTAB and 20 mL of MQ-water was added to a 100 mL single-necked round bottom flask resulting in a milky-white mixture. The solution was stirred vigorously while heated to 40°C to properly dissolve CTAB, that caused the liquid to turn transparent. 2 mL of chloroform was added to the dry DNPs and redispersed by ultra-sonication. The chloroform solution was then added to the CTAB solution in the round bottom flask and stirred magnetically for 30 min to ensure proper mixing. The mixture was heated up to 60°C and maintained for 10 min under stirring to evaporate the chloroform. The reaction solution was then cooled to room temperature, transferred to a glass vial and the CTAB-capped nanoparticles were separated using a disc magnet. The supernatant was discarded and the particles were washed 3 times with MilliQ water to remove any excess CTAB. The particles were finally redispersed in 5 mL MilliQ water for magnetophoresis analysis.

Characterization Techniques

Ultraviolet-Visible Spectroscopy (UV-Vis)

Transmission Electron Microscopy (TEM)

High resolution images were taken using the JEOL 2100 transmission electron microscope (Tokyo, Japan) operating at 200 kV. TEM grids were prepared by placing several drops of the dilute solution on a Formvar carboncoated copper grid (Electron Microscopy Sciences) and wiping immediately with Kimberly-Clark wipes to prevent further aggregation owing to evaporation at room temperature.

Energy-Dispersive X-ray Spectroscopy (EDS)

TEM was performed using a Jeol JEM 2100F equipped with a field emission gun operated at 200 kV. High-angle annular dark-field scanning TEM (HAADF-STEM) images were acquired using a beam semi-convergence angle of ?? mrad, and a collection angle of ??-?? mrad. Energy-dispersive X-ray spectroscopy (EDS) was performed using Oxford X-Max 80 SDD detector attached to the TEM.

Results and Discussion

We first report the growth of dimeric NPs (DNPs), followed by their potential biomedical application of biosensing, using the magnetophoresis technique.

Magneto–Plasmoic DNPs

DNPs have been synthesized using SNPs and CNPs as seed for the growth of Ag on the surface of IONPs resulting in *Janus*-structured particles. Figures 1a and b show the TEM images of Ag@SNPs and Ag@CNPs respectively. The lighter contrast represents IONPs, whereas the darker contrast is for Ag owing to the higher atomic number of Ag thereby having a darker contrast. To investigate the effect of AgAc concentration on the physico-chemical properties of the DNPs, varying concentrations (7.5, 11.2 and 15. 7 mg) of AgAc were used. The DNPs were characterized using VSM and UV-Vis spectroscopy as shown in Figures 1c) and d), respectively. VSM data suggests a decreasing saturation magnetization trend with increasing AgAc content, whereas, an increase in the UV-Vis absorbance peak is seen with greater AgAc content. These results indicate a higher degree of Ag deposition on IONPs, forming more dimeric NPs, as more AgAc is used during synthesis. A decrease in saturation magnetization (M_s), between the bare IONPs and their dimeric counterparts is seen as

represented in Table 2. The decrease is most probably caused due to the addition of non-magnetic Ag onto the IONP surface that only adds to the weight of the particle but not to M_s. Therefore, higher the amount of AgAc, greater is the decrease in M_s, and simultaneously, the plasmonic response of the particles increases due to more Ag deposition. A balance between the magnetic and plasmonic properties needs to be established to exploit the benefits of both the components of DNPs. Therefore, 11.2 mg Ag Acetate salt concentration was selected for further experiments of growth kinetics as well as biosensing application.

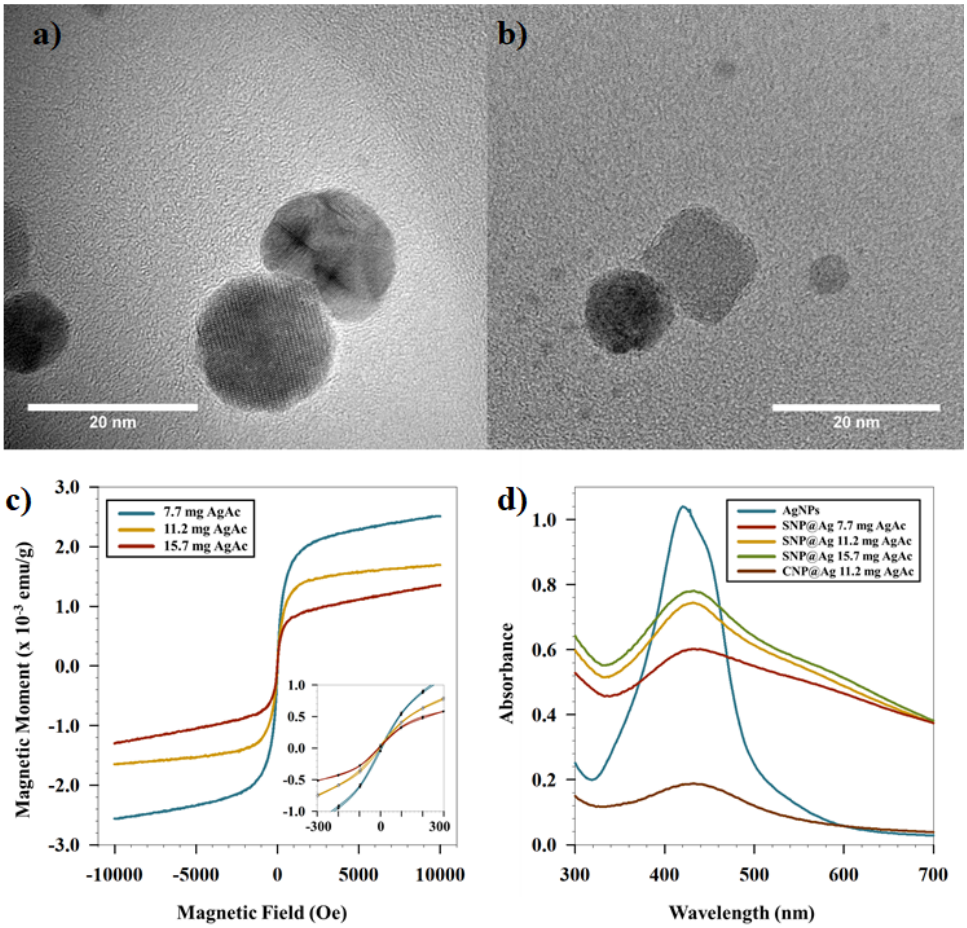

Figure 1: a) TEM image of Ag@SNPs and b) Ag@CNPs. c) VSM and d) UV-Vis of IONPs and DNPs with varying amounts of AgAc content.

Table 2: Saturation magnetisation and LSPR peak of IONPs and DNPs.

Particles	M_s emu/g	LSPR Peak nm
SNPs	74.33	-
CNPs	3.57	-
AgNPs	-	442
Ag@SNP 7.7 AgAc	25.13	431
Ag@SNP 11.2 AgAc	16.88	432
Ag@SNP 15.7 AgAc	13.6	432
Ag@CNP 11.2 AgAc	-	432

Growth Kinetics of DNPs

To perform growth studies, aliquots of the reaction samples were taken at intervals of 1, 3, 5, 7, 10 and 12 h, and were examined under TEM/SEM, as shown in Figures 2a–f. The deposition of Ag on the surface of IONPs is also tracked using EDS measurements and shown in Figures 2g–i. Figure 2g shows the EDS elemental mapping data after 1 h of reaction, marking Fe, O_2 and Ag regions. During the initial stages of the reaction, SNPs are seen with no dimeric growth of Ag, however, small Ag particles are scattered over IONP surfaces, across the sample. Multiple small nodes of Ag start being visible around the SNPs, after 3 h reaction, as seen in Figure 2h. EDS line profiling for Ag@SNPs also confirms the presence of two clear regions of SNP and Ag respectively (Figure S2). The occurrence of these nodes indicates that Ag is not present as a single island but, forms multiple small islands on the surface of SNPs indicating multiple regions of deposition in contrast to one particular site (Figure 2h). These nodes grow further as Ag deposits on them via surface diffusion, as well as, diffusion of Ag from the solvent to the particle. Figures 2d–f show the TEM images of the obtained Ag@SNPs after 7, 10 and 12 h of reaction, respectively. There is a homogeneous distribution of SNPs, whereas Ag nodes seem to exist in different sizes over the SNPs. The disappearance of smaller Ag nodes and growth of bigger ones cab be credited to Ostwald ripening, prevalent at the later stages of the reaction. However, it should be noted that though there is surface diffusion, Ag from smaller nodes might also redissolve in the solution only to be redeposited on another SNP. Additionally, as all the particles are in continuously in rigorous state of motion, Ag nodes diffusing into the solvent may contribute to different Ag@SNPs in their constantly changing vicinity. Thus, there is a highly non-homogeneous distribution of Ag on the SNPs.

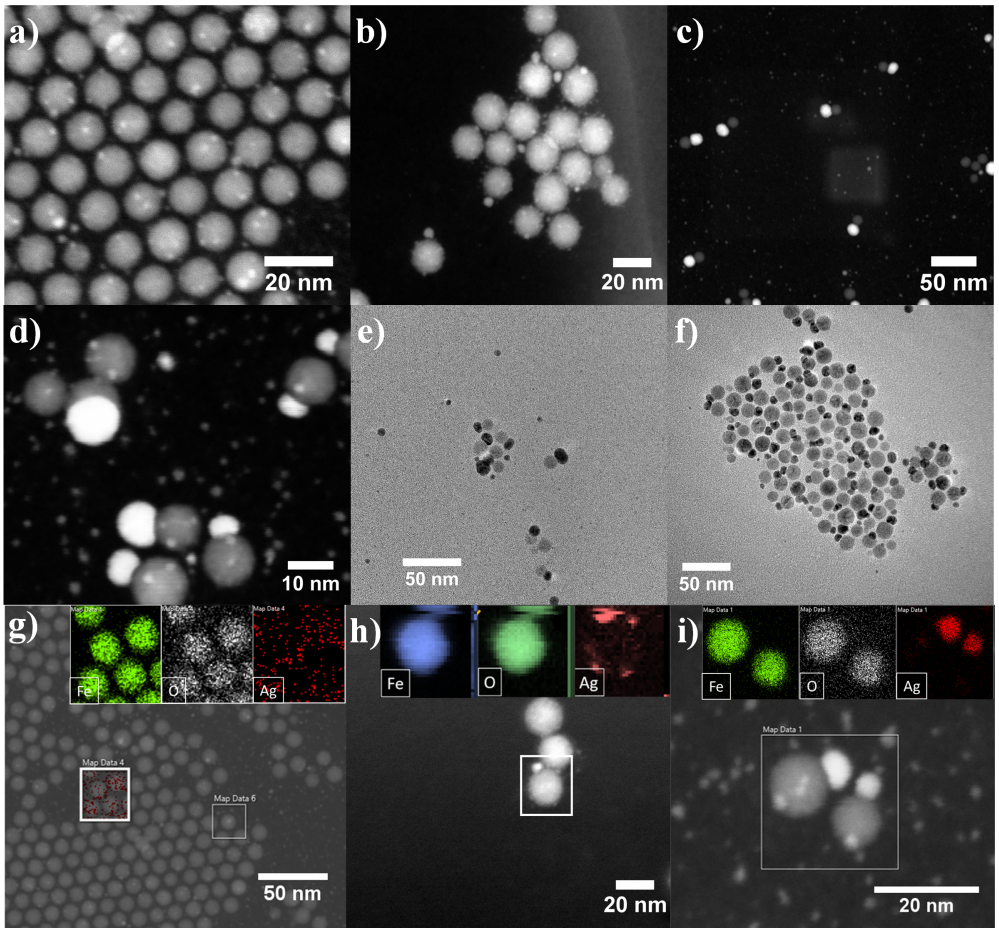

Figure 2: . SEM/TEM images of Ag@SNPs taken at time = a) 1 h, b) 3 h, c) 5 h, d) 7 h, e) 10 h and f) 12 h. EDS elemental mapping for Ag@SNPs at time g) 1 h, h) 3 h and i) 5 h.

Magnetophoresis and Biosensing

Due to the constant magnetic field gradient generated by the magnetophoretic instrument, the magnetic Ag@SNPs get attracted and start separating in the UV-Vis cuvette, as shown in Figure 3b. As the NPs start to separate, their UV-Vis absorbance starts to decrease simultaneously, thereby further confirming NP separation in the presence of the magnetic field (Figures 3c and d). The UV-Vis based separation study is performed at two different wavelengths of 350 and 450 nm, to check for the preciseness of the technique and any ambiguity that might arise in the separation profiles. Similar separation profiles were obtained

at 350 and 450 nm, having two distinct separation zones (Zone 1 and Zone 2), whereby Zone 2 appearing ∼1 h after exposure to the magnetic field. The magnetic field acts greater on larger particles, thus pulling them with greater velocities as compared to smaller ones. Therefore, larger particles will have lower separation times than smaller particles, that have lower separation velocities. Hence, over a period of time, the UV-Vis separation spectra forms two distinct zones as seen in Figures 3 c and d, resulting in two distinct set of NP population consisting of larger (Figure 3e) and smaller NPs (Figures 3f), found in Zones 1 and 2 respectively.

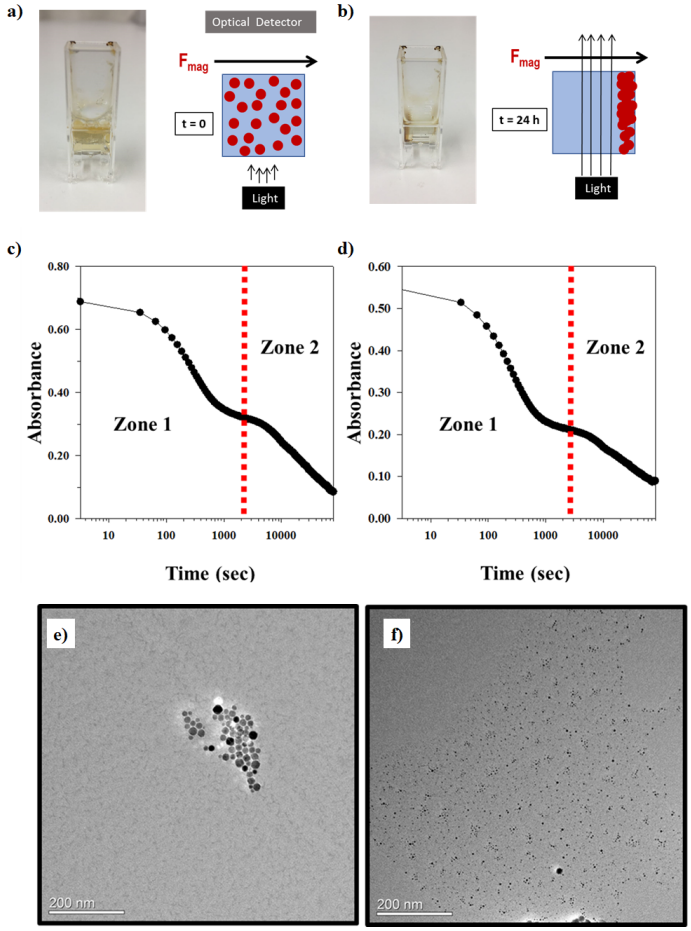

Figure 3: Ag@SNPs a) before and b) after being exposed to the magnetophoretic setup. UV-Vis spectra of Ag@SNPs measured over 24 h at c) 350 nm and d) 450 nm. TEM images of Ag@SNPs taken from magnetophoresis study at 450 nm in e) Zone 1 and f) Zone 2.

Conclusion

Herein, magneto-plasmonic DNPs have been synthesised for the purpose of using them for biosensing application. The magnetic and plasmonic properties are imparted by iron-oxide and silver NPs. Silver is grown on IONPs via epitaxial growth, using the latter as seed moieties. Time-based growth studies, performed using TEM and EDS, reveal nucleation of silver on multiple sites on the IONPs forming satellite/raspberry-type morphology. However, as the reaction proceeds, dumbbell-shaped DNPs are formed owing to reorganisation of silver on the surface of IONPs through surface diffusion and Ostwald ripening. Increasing AgAc concentration during synthesis results in increase in plasmon response as measured by UV-Vis, and a simultaneous decrease in magnetisation as measured by VSM.

The potential applicability of these DNPs as biosensing devices is tested by performing magnetophoretic separation, in conjunction with UV-Vis. The particles were exposed to the external magnetic field for 24 h and the UV-Vis specta was measured and two distinct wavelengths of 350 and 450 nm. The analysis showed separation of particle population, with bigger particles separating in the first 10 h. The smaller particles had lower separation velocities and can be seen separating even after 24 h. However, the bigger particles seem like promising candidates for biosensing devices as they might show variation in separation times with co-operative magnetophoresis (antigen bound to the particles).

Acknowledgement

We thank the Functional Materials and Materials Chemistry (FACET) group for all the valuable insights and discussions. The authors would like to thank NorFab for the financial support in connection to the use of NTNU Nanolab and the Faculty of Natural Sciences and Technology, NTNU, for the financial support. We thank the Department of Material Sciences and Engineering (NTNU), Department of Clinical and Molecular Medicine (NTNU), NORTEM/ Gemini Centre (NTNU) and Nanolab (NTNU), for all their financial, technical and laboratory support. We would like to thank Inger-Emma Nylund (PhD candidate, Department of Materials Science and Engineering, NTNU), for conducting measurements growth studies of magneto-plasmonic dimeric nanoparticles on transmission electron microscopy (TEM) and energy dispersive X-ray spectroscopy (EDS), along with Abhishek Banerjee (M.Sc., Department of Materials Science and Engineering, NTNU) and Helena Olivia Karlsen Ramsvik (M.Sc., Department of Biophysics, NTNU) for synthesizing, functionalizing and VSM characterization on the IONPS and DNPs.

Competing Interests

The authors declare that they have no competing interests.

References

(1) de Julián Fernández, C.; Pineider, F. *New Trends in Nanoparticle Magnetism*; Springer, 2021; pp 107–136.

(2) Espinosa, A.; Reguera, J.; Curcio, A.; Muñoz-Noval, Á.; Kuttner, C.; Van de Walle, A.; Liz-Marzán, L. M.; Wilhelm, C. Janus Magnetic-Plasmonic Nanoparticles for Magnetically Guided and Thermally Activated Cancer Therapy. *Small* **2020**, *16*, 1904960.

(3) Kowalik, P.; Mikulski, J.; Borodziuk, A.; Duda, M.; Kaminska, I.; Zajdel, K.; Rybusinski, J.; Szczytko, J.; Wojciechowski, T.; Sobczak, K., et al. Yttrium-doped iron oxide nanoparticles for magnetic hyperthermia applications. *The Journal of Physical Chemistry C* **2020**, *124*, 6871–6883.

(4) Soleymani, M.; Velashjerdi, M.; Shaterabadi, Z.; Barati, A. One-pot preparation of hyaluronic acid-coated iron oxide nanoparticles for magnetic hyperthermia therapy and targeting CD44-overexpressing cancer cells. *Carbohydrate polymers* **2020**, *237*, 116130.

(5) Chauhan, A.; Midha, S.; Kumar, R.; Meena, R.; Singh, P.; Jha, S. K.; Kuanr, B. K. Rapid tumor inhibition via magnetic hyperthermia regulated by caspase 3 with time-dependent clearance of iron oxide nanoparticles. *Biomaterials science* **2021**,

(6) Deh, K.; Zaman, M.; Vedvyas, Y.; Liu, Z.; Gillen, K. M.; O'Malley, P.; Bedretdinova, D.; Nguyen, T.; Lee, R.; Spincemaille, P., et al. Validation of MRI quantitative susceptibility mapping of superparamagnetic iron oxide nanoparticles for hyperthermia applications in live subjects. *Scientific reports* **2020**, *10*, 1–11.

(7) Jeon, M.; Halbert, M. V.; Stephen, Z. R.; Zhang, M. Iron oxide nanoparticles as T1 contrast agents for magnetic resonance imaging: fundamentals, challenges, applications, and prospectives. *Advanced Materials* **2020**, 1906539.

(8) Norouzi, M.; Yathindranath, V.; Thliveris, J. A.; Kopec, B. M.; Siahaan, T. J.; Miller, D. W. Doxorubicin-loaded iron oxide nanoparticles for glioblastoma therapy: A combinational approach for enhanced delivery of nanoparticles. *Scientific reports* **2020**, *10*, 1–18.

(9) Zhi, D.; Yang, T.; Yang, J.; Fu, S.; Zhang, S. Targeting strategies for superparamagnetic iron oxide nanoparticles in cancer therapy. *Acta biomaterialia* **2020**, *102*, 13–34.

(10) Wang, X.; Hou, T.; Lin, H.; Lv, W.; Li, H.; Li, F. In situ template generation of silver nanoparticles as amplification tags for ultrasensitive surface plasmon resonance biosensing of microRNA. *Biosensors and Bioelectronics* **2019**, *137*, 82–87.

(11) Fan, M.; Thompson, M.; Andrade, M. L.; Brolo, A. G. Silver nanoparticles on a plastic platform for localized surface plasmon resonance biosensing. *Analytical chemistry* **2010**, *82*, 6350–6352.

(12) Wu, Y.; Ali, M. R.; Chen, K.; Fang, N.; El-Sayed, M. A. Gold nanoparticles in biological optical imaging. *Nano Today* **2019**, *24*, 120–140.

(13) Caro, C.; Castillo, P. M.; Klippstein, R.; Pozo, D.; Zaderenko, A. P. Silver nanoparticles: sensing and imaging applications. *Silver nanoparticles* **2010**, 201–223.

(14) Stensberg, M. C.; Wei, Q.; McLamore, E. S.; Porterfield, D. M.; Wei, A.; Sepúlveda, M. S. Toxicological studies on silver nanoparticles: challenges and opportunities in assessment, monitoring and imaging. *Nanomedicine* **2011**, *6*, 879–898.

(15) Magadla, A.; Oluwole, D. O.; Managa, M.; Nyokong, T. Physicochemical and antimicrobial photodynamic chemotherapy (against E. coli) by indium phthalocyanines in the presence of silver–iron bimetallic nanoparticles. *Polyhedron* **2019**, *162*, 30–38.

(16) Chen, Y.; Xianyu, Y.; Dong, M.; Zhang, J.; Zheng, W.; Qian, Z.; Jiang, X. Cascade reaction-mediated assembly of magnetic/silver nanoparticles for amplified magnetic biosensing. *Analytical chemistry* **2018**, *90*, 6906–6912.

(17) Hola, K.; Markova, Z.; Zoppellaro, G.; Tucek, J.; Zboril, R. Tailored functionalization of iron oxide nanoparticles for MRI, drug delivery, magnetic separation and immobilization of biosubstances. *Biotechnology advances* **2015**, *33*, 1162–1176.

(18) Prucek, R.; Tuček, J.; Kilianová, M.; Panáček, A.; Kvítek, L.; Filip, J.; Kolář, M.; Tománková, K.; Zbořil, R. The targeted antibacterial and antifungal properties of magnetic nanocomposite of iron oxide and silver nanoparticles. *Biomaterials* **2011**, *32*, 4704–4713.

(19) Vita, F.; Innocenti, C.; Secchi, A.; Albertini, F.; Grillo, V.; Fiore, A.; Cozzoli, P. D.; de Julián Fernández, C. Colloidal Au/iron oxide nanocrystal heterostructures: magnetic, plasmonic and magnetic hyperthermia properties. *Journal of Materials Chemistry C* **2018**, *6*, 12329–12340.

(20) Lee, Y.; Garcia, M. A.; Frey Huls, N. A.; Sun, S. Synthetic tuning of the catalytic properties of Au-Fe3O4 nanoparticles. *Angewandte Chemie International Edition* **2010**, *49*, 1271–1274.

(21) Wang, C.; Wei, Y.; Jiang, H.; Sun, S. Tug-of-War in Nanoparticles: Competitive Growth of Au on Au- Fe3O4 Nanoparticles. *Nano letters* **2009**, *9*, 4544–4547.

(22) George, C.; Genovese, A.; Qiao, F.; Korobchevskaya, K.; Comin, A.; Falqui, A.; Marras, S.; Roig, A.; Zhang, Y.; Krahne, R., et al. Optical and electrical properties of colloidal (spherical Au)-(spinel ferrite nanorod) heterostructures. *Nanoscale* **2011**, *3*, 4647–4654.

(23) Liu, L.; Cheng, S.; Qi, B.; Xi, Z.; Dong, D. Precision limit of atomic magnetometers in the presence of spin-destruction collisions. *Journal of Physics B: Atomic, Molecular and Optical Physics* **2015**, *48*, 035502.

(24) Kodama, R. H.; Berkowitz, A. E.; McNiff Jr, E.; Foner, S. Surface spin disorder in NiFe 2 O 4 nanoparticles. *Physical Review Letters* **1996**, *77*, 394.

(25) Martínez-Boubeta, C.; Simeonidis, K.; Angelakeris, M.; Pazos-Pérez, N.; Giersig, M.; Delimitis, A.; Nalbandian, L.; Alexandrakis, V.; Niarchos, D. Critical radius for exchange bias in naturally oxidized Fe nanoparticles. *Physical Review B* **2006**, *74*, 054430.

(26) Chandra, S.; Huls, N. F.; Phan, M.-H.; Srinath, S.; Garcia, M.; Lee, Y.; Wang, C.; Sun, S.; Iglesias, O.; Srikanth, H. Exchange bias effect in Au-Fe3O4 nanocomposites. *Nanotechnology* **2014**, *25*, 055702.

(27) Luchini, A.; Vitiello, G.; Rossi, F.; De Ballesteros, O. R.; Radulescu, A.; D'Errico, G.; Montesarchio, D.; de Julián Fernández, C.; Paduano, L. Developing functionalized Fe 3 O 4–Au nanoparticles: a physico-chemical insight. *Physical Chemistry Chemical Physics* **2015**, *17*, 6087–6097.

(28) Zhu, L.; Deng, X.; Hu, Y.; Liu, J.; Ma, H.; Zhang, J.; Fu, J.; He, S.; Wang, J.; Wang, B., et al. Atomic-scale imaging of the ferrimagnetic/diamagnetic interface in Au-Fe 3 O 4 nanodimers and correlated exchange-bias origin. *Nanoscale* **2018**, *10*, 21499–21508.

(29) Rycenga, M.; Cobley, C. M.; Zeng, J.; Li, W.; Moran, C. H.; Zhang, Q.; Qin, D.; Xia, Y. Controlling the synthesis and assembly of silver nanostructures for plasmonic applications. *Chemical reviews* **2011**, *111*, 3669–3712.

(30) Zhang, L.; Dou, Y.-H.; Gu, H.-C. Synthesis of Ag–Fe3O4 heterodimeric nanoparticles. *Journal of colloid and interface science* **2006**, *297*, 660–664.

(31) Muraca, D.; Sharma, S.; Socolovsky, L.; De Siervo, A.; Lopes, G.; Pirota, K. Influence of silver concentrations on structural and magnetic properties of Ag-Fe3O4 heterodimer nanoparticles. *Journal of nanoscience and nanotechnology* **2012**, *12*, 6961–6967.

(32) Yu, H.; Chen, M.; Rice, P. M.; Wang, S. X.; White, R.; Sun, S. Dumbbell-like bifunctional Au- Fe3O4 nanoparticles. *Nano letters* **2005**, *5*, 379–382.

(33) Li, Y.; Yang, S.; Lu, X.; Duan, W.; Moriga, T. Synthesis and evaluation of the SERS effect of Fe 3 O 4–Ag Janus composite materials for separable, highly sensitive substrates. *RSC advances* **2019**, *9*, 2877–2884.

(34) Moscoso-Londono, O.; Muraca, D.; Tancredi, P.; Cosio-Castaneda, C.; Pirota, K. R.; Socolovsky, L. M. Physicochemical studies of complex silver–magnetite nanoheterodimers with controlled morphology. *The Journal of Physical Chemistry C* **2014**, *118*, 13168–13176.

(35) Sun, Y. Interfaced heterogeneous nanodimers. *National Science Review* **2015**, *2*, 329–348.

(36) Sharma, A.; Foppen, J. W.; Banerjee, A.; Sawssen, S.; Bachhar, N.; Peddis, D.; Bandyopadhyay, S. Magnetic Nanoparticles to Unique DNA Tracers: Effect of Functionalization on Physico-chemical Properties. *Nanoscale research letters* **2021**, *16*, 1–16.

(37) Kim, J.; Kim, H. S.; Lee, N.; Kim, T.; Kim, H.; Yu, T.; Song, I. C.; Moon, W. K.; Hyeon, T. Multifunctional uniform nanoparticles composed of a magnetite nanocrystal core and a mesoporous silica shell for magnetic resonance and fluorescence imaging and for drug delivery. *Angewandte Chemie* **2008**, *120*, 8566–8569.

"It always seems impossible until it's done."

– Nelson Mandela

"...when you have eliminated the impossible, whatever remains, however improbable, must be the truth."

– Sherlock Holmes

9 Conclusion

This work focuses on two kinds of NPs, namely inorganic NPs and stimuli-responsive NGs, that have been tailored for the use as hydrological tracers, sensors and targeted drug delivery vehicles. The former are comprised of superparamagnetic IONPs and magneto-plasmonic Ag@IONPs, while the latter refer to pNIPAm-pAAc-based NGs that show temperature and pH-based stimuli response.

Using DNA as the tracer moiety overcomes the limitations of conventional tracers and enables production of an infinite number of unique tracers. Incorporating magnetic IONPs to the DNA favours easier magnetic separation and recovery of the tracers during application. The IONPs were synthesised using co-precipitation and thermal decomposition routes, yielding particles with different shapes and sizes, referred as '*Mag*' (9.2 ± 2.3 nm), '*SNP* (spheres, 19 ± 2 nm) and '*CNP*' (cubes, 11.6 ± 1.1 nm). These particles were functionalised with different ligands (CTAB, TMAH, Na-Citrate and TMAPS) to modify their surface charge and functionality, before functionalising them with DNA and encapsulation in silica. Three different DNA (T21, GM5 and GM6) were used to prove the concept of forming different unique tracers, each having its own distinct tag (sequence). Successful functionalisation is confirmed by zeta potential (surface charge), that altered from positive for TMAPS, to negative after incorporation of DNA and stayed negative after silica coating. Effective DNA encapsulation was measured using qPCR with DNA from all the systems detected even at 30-fold dilution, stating the high ultrasensitivity of the system to overcome dilution challenges.

SNPs were further used to grow silver on their surface, resulting in DNPs that showed superparamagnetism and plasmonic response. Nucleation and growth of silver, studied using TEM and EDS by analysing reaction aliquots at different reaction time-points, revealed that silver nucleates on multiple sites on the surface of the IONP, forming nodes in a raspberry or satellite-like morphology. However, as the reaction continued, Ag nodes continuously diffused in and out of the solvent, and subsequently deposited on the growing Ag nodes by surface diffusion and Ostwald's ripening. By the end of the

reaction, the particle attains a dumbbell-like morphology with two distinct iron-oxide and silver particles attached at the interface. The physico-chemical properties were affected by varying the amount of added silver precursor – silver acetate, during the reaction. A decrease in magnetism was seen with increasing AgAc amounts, whereas, the plasmon response increased with increasing AgAc amounts. Due to the magnetic nature of these particles, separation studies were conducted on DNPs using a magnetophoresis set-up, in collaboration with UV-Vis. The study showed that the separation times of the particles depended on particle size, with larger particles separating faster than smaller ones. Therefore, if the particles are functionalised with an appropriate ligand to attach to the desired antigen, they can be used for biosensing applications, using the magnetophoresis technique.

pNIPAm-pAAc-based NGs were prepared using precipitation polymerisation to yield thermo- and pH-responsive NGs. The effect of surfactant concentration (SDS) and reaction atmosphere, on the physico-chemical properties of the NGs were examined. NG size decreased with increasing SDS concentration, owing to higher stabilization and colloidal stability of the precursor particles during the nucleation step. Additionally, high concentration of SDS led to denser packing around nucleation centres, thereby, limiting particle growth. Reaction atmosphere also influenced the size and PDI of NGs, as larger sizes and low PDI (NGs_CS = 0.2 ± 0.0) were observed for NGs under a continuous nitrogen environment compared to an intermittent nitrogen environment (NGs_FS = 0.7 ± 0.1, NGs_FI = 0.6 ± 0.2), as oxygen renders the initiator (KPS) inert by reacting with it, resulting in ineffective polymerisation. The mole% of AAc was varied to investigate the effect on the physico-chemical properties of the NG. The size of NGs increased with increasing AAc mole%. ^{1}NMR measurements showed an increase in chemical shift (δ) for pAAc in the regions, δ = 2.2 and 1.8. Drug loading and release studies were conducted using Cyt C at different conditions of temperature and pH. NGs_CS@AAc_10 showed higher loading (L.E.) and encapsulation (E.E.) efficiency (L.E. = 87.4 ± 12.2 %, E.E. = 254.5 ± 36.4 μg/mg) in contrast to NGs_FC@AAc_10 (L.E. = 30.8 ± 7.4 %, E.E. = 181.0 ± 44.0 μg/mg). However, L.E. and E.E. increased for NGs_FS AAc mole% of 15 (L.E. = 52.4 ± 8.4 %, E.E. = 308.0 ± 49.0 μg/mg) and 25 (L.E. = 70.3 ± 7.8 %, E.E. = 414.0 ± 46.0 μg/mg). To explore the possibility of using these NGs in biomedical applications, cell viability studies were performed using a whole blood model. The NGs showed excellent cell viability, did not activate the complement system and induced little or no release of pro-inflammatory cytokines/chemokines in a human whole blood model, suggesting good biocompatibility and potential as a candidate for drug delivery vehicles.

The key, enabling NPs to be used in various applications, lies in precisely producing monodisperse populations. However, reproducibility and repeatability are major challenges in NP formation that limit their use. Therefore, conducting multiple sets of experiments is important as it reduces uncertainties regarding product quality and aids in optimising the synthesis process, thereby ensuring similar particle quality. Another challenge faced in NP synthesis is scale-up of processes from laboratory to industrial scale. Recent advances, such as, in the field of microfluidics, aim at tackling these issues in an attempt to precisely produce narrow particle size distributions in bulk, thereby saving time, energy and resources.

"Science never solves a problem without creating ten more."
– George Bernard Shaw

"Greed and stupidity are what will end the human race."
– Stephen Hawking

10
Future Work & Outlook

This work describes the successful synthesis of DNA-based magnetic NPs that can be utilised as tracers for hydrology applications, however, further studies can be performed to test the stability of these particles in conditions mimicking those of natural water sources. These studies could test the particles in conditions by varying pH, salt concentration and flows through sand/soil beds. Furthermore, magnetic separation studies could be conducted by flowing the tracer solution through pipe/tubing channels over a magnet. Separation profiles can then be traced by plotting concentration vs flow rates for various tracer solutions.

In another instance, the IONPs can be incorporated in the stimuli-responsive NGs for the purpose of magnetically triggered drug release. These IONP functionalised NGs can be tested against alternating magnetic fields (AMF) at different frequencies to obtain heat generated collapse, thereby, releasing the payload. Additionally, incorporating magneto-plasmonic DNPs in the NGs could enable diagnostic and imaging due to the plasmonic silver moiety.

Two different populations of the magneto-plasmonic DNPs could be functionalised with ligands having complementary functional groups, that will result in self-assembly of the NPs on mixing. UV-Vis-based magnetophoretic studies can then be performed to evaluate separation velocities of the non-assembled and self-assembled particle group. The sensitivity of the system can also be tested against potential LSPR shift arising due to the silver component present in the particles.

Even though NPs possess numerous advantages, their use still remains debatable. Nanomaterials have been increasingly incorporated into uncountable consumer and industrial products, which has resulted in expanding research on these materials for their potential effects to the environment and human health. This research is essential and will continue to last long into the future to understand the potential threats of incorporating NPs in our lives and steps that can be taken to minimize potential negative effects. Having said that, the responsibility lies with each researcher to question the morality of the work.

A

List of Abbreviations

List of Abbreviations

AAc	Acrylic Acid.
AFM	Atomic Force Microscopy.
AgAc	Silver Acetate.
ATR-FTIR	Attenuated Total Reflection-Fourier Transform Infrared.
AuNP	Gold Nanoparticle.
BIS	N,N′-Methylenebis(acrylamide).
BOE	Buffered Oxide Etc.
CNP	Cubic Iron-Oxide Nanoparticles.
CR3	Complement Receptor 3.
CS	Continuous-Stirring.
CTAB	Cetyltrimethylammonium Bromide.
Cyt C	Cytochrome C.
DNA	Deoxyribonucleic Acid.
DNP	Dimeric Nanoparticles.
E.E.	Encapsulation Efficiency.
EDS	Energy Dispersive X-Ray Spectroscopy.
FI	Flashing-Impeller.
FS	Flashing-Stirring.
IONP	Iron-Oxide Nanoparticle.
KPS	Pottasium Persulphate.
L.E.	Loading Efficiency.
LCST	Lower Critical Solution Temperature.
LPS	Lipopolysaccharide.
LSPR	Localised Surface Plasmon Resonance.
MACS	Magnetic-activated Cell Sorting.
Mag	Magnetite Nanoparticles.
MNP	Magnetic Nanoparticles.
MRI	Magnetic Resonance Imaging.
MWCO	Molecular Weight Cut-Off.
Na-citrate	Sodium Citrate.

Na-oleate	Sodium Oleate.
NG	Nanogel.
NIPAm	N-Isopropylacrylamide.
NP	Nanoparticle.
NTC	Negative Control.
OA	Oleic Acid.
ODE	Octadecene.
pAAc	poly-Acrylic Acid.
PBS	Phosphate Buffered Saline.
PDI	Polydispersity Index.
PEG	Poly-ethylene Glycol.
PNC	Pre-nucleation Clusters.
pNIPAm	poly-N-Isopropylacrylamide.
PSD	Particle Size Distribution.
PVP	Polyvinylpyrrolidone.
qPCR	Quantitative Polymerase Chain Reaction.
RT	Room Temperature.
Rxn	Reaction.
SAXS	Small-angle X-ray Scattering.
SDS	Sodium Dodecyl Sulphate.
SEM	Scanning Electron Microscopy.
SNP	Spherical Iron-Oxide Nanoparticles.
TCC	Terminal Complement Complex.
TEM	Transmission Electron Microscopy.
TEOS	Tetraethyl orthosilicate.
TMAH	Tetramethylammonium Hydroxide.
TMAPS	Trimethoxysilylpropyl-N,N,N-trimethylammonium Chloride.
UV-Vis	Ultraviolet Visible Spectrophotometry.
VPTT	Volume Phase Transition Temperature.
VSM	Vibration Sample Magnetometry.
WAXS	Wide-angle X-ray Scattering.

B

List of Symbols

List of Symbols

A	Surface area
A_{bound}	UV-Vis absorbance of Cyt C after dialysis at 409 nm
A_{total}	UV-Vis absorbance of Cyt C before dialysis at 409 nm
a	Solute activity in an arbitrary state
a^*	Solute activity at equilibrium
C	Solute concentration in the supersaturated solution
C_i	Solute concentration in the solution at the crystal-solution interface
C^*	Equilibrium saturation concentration
C_t	Cycle Threshold
d	Separation Distance
E_d	Dipolar Energy
H_c	Coercivity
K	Kelvin
K_a	Anistropic Constant
K_B	Boltzmann Constant
k_d	Mass transfer coefficient based on diffusion
k_r	Rate constant for surface reaction process,
M_{NG}	Mass of NG (mg)
M_{drug}	Mass of Cyt C (µg)
M_r	Remanence Magnetisation
M_s	Saturation Magnetisation
m	Mass
S	Supersaturation
T	Temperature
t	Time
V	Mean Particle Volume
V_p	Volume of NPs
δ	^{1}H NMR Chemical Shifts
δm	Interparticle Interaction Intensity
μ_0	Permeability
μ_p	Average Magnetic Moment
τ_R	Relaxation Time
τ_m	Measurement Time

C

Supplementary Information for Papers & Manuscripts

C.1 Paper I

Sharma, A., Foppen, J.W., Banerjee, A., Sawssen, S., Bachhar, N., Peddis, D., Bandyopadhyay, S., 2021. Magnetic Nanoparticles to Unique DNA Tracers: Effect of Functionalization on Physico-chemical Properties. Nanoscale research letters, 16(1), pp.1-16. https://doi.org/10.1186/s11671-021-03483-5

Supporting Information

Magnetic Nanoparticles to Unique DNA Tracers – Effect of Functionalization on Physico-Chemical Properties.

Anuvansh Sharma[1], Jan Willem Foppen[2], Abhishek Banerjee[1], Slimani Sawssen[3,4], Nirmalya Bachhar[5], Davide Peddis[3,4], Sulalit Bandyopadhyay[6,7]*

1 Department of Materials Science and Engineering, NTNU Norwegian University of Science and technology, N-7491 Trondheim, Norway.

2 Water Science and Engineering, IHE Delft Institute for Water Education, Delft, Netherlands.

3 Dipartimento di Chimica e Chimica Industriale, Università di Genova, Genova, Italy

4 Istituto di Struttura della Materia – CNR, Area della Ricerca di Roma1, Monterondo Scalo, RM 00015, Italy

5 Department of Chemical Engineering, Indian Institute of Technology Jodhpur, Jodhpur 342037, India.

6 Department of Water Management, Delft University of Technology (TU Delft), Netherlands.

7 Department of Chemical Engineering, NTNU Norwegian University of Science and technology, N-7491 Trondheim, Norway.

* *Correspondence: sulalit.bandyopadhyay@ntnu.no Tel.: +47-45071041*

1. Materials and Methods

The following dsDNA strands were used for the studies.

1.1. T21

Sense: 5'–*CTG GAT GAT GCG AAT CGA ATC ACA CAC GTA GAG TTC GAA TGT GAT GGC CTA AAA GGA TGA GCA ATA GAG GAG CCT AAA GG–3'*

Antisense: 5'–*CCT TTA GGC TCC TCT ATT GCT CAT CCT TTT AGG CCA TCA CAT TCG AAC TCT ACG TGT GTG ATT CGA TTC GCA TCA TCC AG–3'*

1.2. GM5

Sense: *5'–TTC GGA CAA TCC TTT CCA TAT TAC GCT CTG AAG GCT ACT ACT CCT TCT TAT TAA CTG GGT CTC GTT T–3'*

Antisense: *5'–AAA CGA GAC CCA GTT AAT AAG AAG GAG TAG TAG CCT TCA GAG CGT AAT ATG GAA AGG ATT GTC CGA A–3'*

1.3. GM6

Sense: *5'–TTC TCT GCC CTT ACG TTT ATC TTA AGG GCC GGT CCA CCA GTT GAA CAC GAA CAA ACC TCT TT–3'*

Antisense: *5'–AAA GAG GTT TGT TCG TGT TCA ACT GGT GGA CCG GCC CTT AAG ATA AAC GTA AGG GCA GAG AA–3'*

2. Model and simulation of particle formation and growth

2.1. Nucleation

In our model, we assume homogeneous nucleation to take place during thermal decomposition and the nucleation frequency, (f_n), can be calculated by classical nucleation theory as:

$$f_n = \begin{cases} 0 & \text{if, } \lambda_l < 1 \\ VA \exp\left(\dfrac{-16\pi\sigma^3 V_m^2}{3(k_B T)^3 \ln(\lambda_l)^2} \right) & \text{if, } \lambda_l \geq 1 \end{cases} \quad \text{(S1)}$$

where, λ_l is the degree of supersaturation, defined by:

$$\lambda_l = \frac{C(l)}{S} \quad \text{(S2)}$$

and V, A, σ, k_B, T, S, $C(l)$ and V_m are total volume of liquid solution, pre-exponential factor, interfacial tension between solid nuclei and the surrounding liquid, Boltzmann constant, temperature, solubility of product molecule (Fe_3O_4), concentration of Fe_3O_4 in liquid phase and Fe_3O_4 molecular volume, respectively.[1] The values of all model and experimental parameters are given in **Table S1**. For critical nuclei size we considered the smallest possible cluster ($l_c = 2$ molecules, the smallest cluster) in our simulation, since a critical number of 2 is often used for nucleation of a sparingly soluble product.[2-4]

2.2. Diffusion controlled growth

The growth of nanoparticles by diffusion transport of molecules to its surface consists of two steps: (i) diffusion of solute molecule through a boundary layer (diffusion layer) from the bulk to the solid surface and (ii) surface-reaction of solute molecules that bind it to the nanoparticle. Generally, surface-reaction of molecules on the particle surface are very fast, therefore we ignore this step in our model. Hence, diffusion transport driven growth rate of iron oxide nanoparticles can be written as,

$$\frac{dr}{dt} = \frac{D_m V_m N_A C(l)}{r} \quad \text{(S3)}$$

where D_m, N_A and r, are molecular diffusivity of solute molecule, Avogadro's number and radius of particle, respectively.[5, 6] Diffusivity of Fe_3O_4 molecules in octadecene has been estimated by the Wilke-Chang correlation for molecular diffusion.[7]

2.3. Coagulation

Brownian collisions of the nanoparticles which result in complete coalescence (coagulation), leading to primary particle growth. The coagulation driven growth rate of a nanoparticle is therefore estimated using the Brownian collision frequency (q_p) modified by a coagulation efficiency, β.[1] The efficiency β is the ratio of the number of successful Brownian collisions (leading to coagulation), against the total number of Brownian collisions. q_p is given by Smoluchowski's equation:

$$q_p = \frac{2k_B T}{3\mu}\left[2 + \frac{r_1}{r_2} + \frac{r_2}{r_1}\right] \quad \text{(S4)}$$

where r_1 and r_2 are radii of colliding particles and μ is viscosity of the solvent.[8, 9] The coagulation frequency is hence calculated as:

$$f_c = \frac{1}{2}\beta V q_p N^2 \qquad \text{(S5)}$$

where N is the number density of nanoparticles.

2.4. Ostwald ripening

The timescale of Ostwald Ripening (OR) is large compared to all other formation and growth processes. The rate constant of OR, k_{OR} can be written as,

$$k_{OR} = \frac{8\sigma D_m (V_m N_A)^2 S}{9RT} \qquad \text{(S6)}$$

where R is universal gas constant (8.314 $JK^{-1}mol^{-1}$). Oskam *et al.* have shown by linearizing the Gibbs-Thomson equation, that the condition $\frac{4\sigma V_m}{k_B T} << \bar{d}_p$ must be valid, to have Ostwald ripening take place in a system.[10] Based on our parameter values of Fe_3O_4 nanoparticle, $2\alpha = \frac{4\sigma V_m}{k_B T} = 12$ nm. Therefore, we assume the onset point of OR in our system is 12 nm. The rate of the corresponding coarsening process can be given as:

$$\frac{dr}{dt} = \frac{3\alpha D_m V_m N_A S}{r^2}\left(\frac{r}{r_c} - 1\right) \qquad \text{(S7)}$$

where dr/dt represents the growth or decay in particle radius depending on whether r/r_c is greater or less than 1, respectively.[11] The rate equation of OR implies that in the PSD, particles larger than r_c will grow while smaller particles dissolve. Here critical radius r_c is given by, $r_c = \alpha / \theta(t)$, where, $\theta(t) = [C(l)\text{-}S]/S$, is a dimensionless concentration.[11] We have arbitrarily fitted $\theta(t)$ to be 1 to match the PSD.

Table S1. List of input parameters in the simulation.

Parameter	Value	Source
$C(l)_{t=0}$	23.7 mol m^{-3}	our experiment
V	2.5×10^{-5} m^3	our experiment
V_b	2.8×10^{-19} m^3	our simulation
T	593 K	our experiment
μ	0.3 kg.$m^{-1}s^{-1}$	obtained from literature
D_m	2.28×10^{-8} m^2s^{-1}	Estimated using Wilke-Chang correlation [7]
l_c	2	obtained from literature [4]
A	10^{34} $m^{-3}s^{-1}$	obtained from literature [4]
σ	0.1 J.m^{-2}	obtained from literature [4]
V_m	7.39×10^{-29} m^3	calculated using molar mass, density, and Avogadro Number
S	10^{-6} mol m^{-3}	-
β	2.5×10^{-5}	Our simulation
r_c	6 nm	Our simulation
$\theta(t)$	1	Our simulation

2.5. Simulation methodology

We formulated our kinetic Monte Carlo (kMC) simulation following Bachhar *et al*., by adopting the technique of interval of quiescence.[5, 6] There are four events in the simulation, namely, nucleation, diffusion-growth, coagulation-growth and Ostwald ripening. The interval of quiescence is defined as the time interval between two consecutive, discrete random events (nucleation or coagulation in the present case). During this interval, other continuous events (diffusion-growth and Ostwald ripening, estimated by their respective rate equations) occur. We start our simulation using a simplified growth model, with n_m number of Fe_3O_4 molecules (which at $t = 0$ is 4×10^6) and no nanoparticle to start with ($N_p = 0$). We used a discrete–continuous kMC simulation following Bachhar *et al.* [5, 6]

3. *Phase transfer of SNPs*

3.1. CTAB

The method has been adapted and modified by previous work of Kim et al. and 10 mM of CTAB solutions were made in 20 mL MilliQ water.[12] 5 and 10 mg of SNPs synthesized from thermal decomposition route were separately precipitated from toluene using methanol and cleaned thrice with acetone. Each precipitated SNP sample was redispersed in 2 mL chloroform before adding it dropwise to 20 mL of 1 and 10 mM CTAB solutions preheated to 60 °C over an oil bath under constant stirring. The reaction was left for 30 min after which the phase transferred SNPs were magnetically separated and washed thrice with MilliQ water before suspending them in 5 mL MilliQ water.

3.2. Sodium citrate

The procedure is taken and modified from works of Bandyopadhyay et al.[13] 10 and 50 mM of sodium citrate (Na-citrate) solutions were prepared in 10 mL MilliQ water. 5 and 10 mg SNPs were separately precipitated from toluene using methanol and cleaned thrice with acetone. 10 ml Na-citrate solution was added to the precipitated SNPs and the suspension was sonicated for 2 hours in a bath sonicator. Afterwards, the nanoparticles were magnetically separated and cleaned thrice with MilliQ water before redispersing them in 10 mL MilliQ water.

3.3. TMAH

Phase transfer of SNPs and CNPs using TMAH was performed by modifying a previously developed method.[14] Typically, 50 mg of SNPs and 25 mg of CNPs were separately precipitated from toluene using methanol and washed thrice with acetone in a glass vial. 2 mL and 1 mL TMAH solution was added to the SNPs and CNPs respectively and the vials were placed in a bath sonicator for 10 minutes. Afterwards, the vials were put on shaking at 300 rpm for 2 hours after which the particles were magnetically separated and cleaned thrice with water. Finally, the phase transferred IONPs were redispersed in 1 mL MilliQ water in an Eppendorf tube.

Table S2. SNPs from different precursors with different ligands

SNPs precursor	SNPs mass (mg)	Ligands	Ligand concentration (mM)
Iron oleate: SNPs spheres	5	CTAB	1
	10		1
	5		10
	10		10
Iron Oleate: SNPs spheres	5	Sodium citrate	10
	10		10
	5		50
	10		50

4. Results and discussion

4.1. Controlling the Particle Size and Shape

Based on the TEM analysis an experimental PSD has been constructed as reported in **Figures S1a and S1b**, where the relative frequency (%) of each size are plotted against particle diameter. Our model can capture the mean and the mode of the PSD however the standard deviation and other higher moments of the distributions are not accurately captured. A much more detailed model with OR might need to be considered for this process. The only additional adjustable parameter in this simulation was the coagulation efficiency which we found to be 2.5×10^{-5}. It is observed that the simulation data matches well with OR included. In this case the coagulation efficiency is found to be 8.5×10^{-6}. A detailed model of coagulation based on interparticle interaction[6] might give us better understanding of the process.

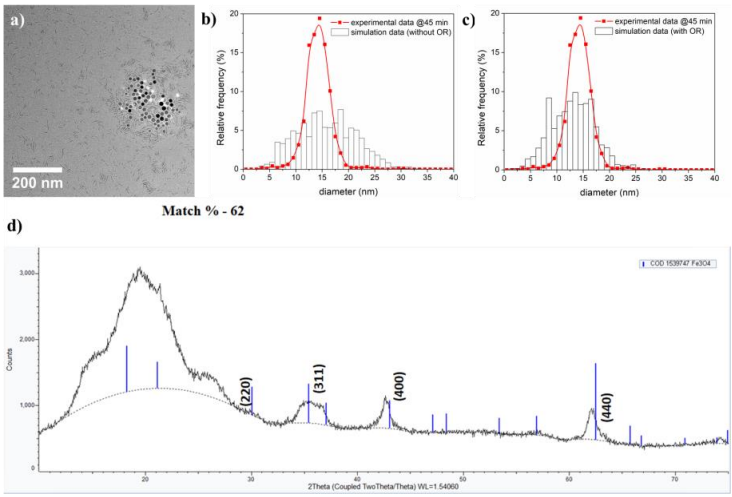

Figure S1 a) HRTEM image of growth evolution of IONPs at 250 ºC. Comparison between kMC simulation vs. experimental PSD of iron oxide formed through thermal decomposition route after 45 min of aging at 320 ˚C, b) without OR and c) with OR. d) XRD pattern of SNPs.

4.2. Phase transfer and Functionalization of IONPs

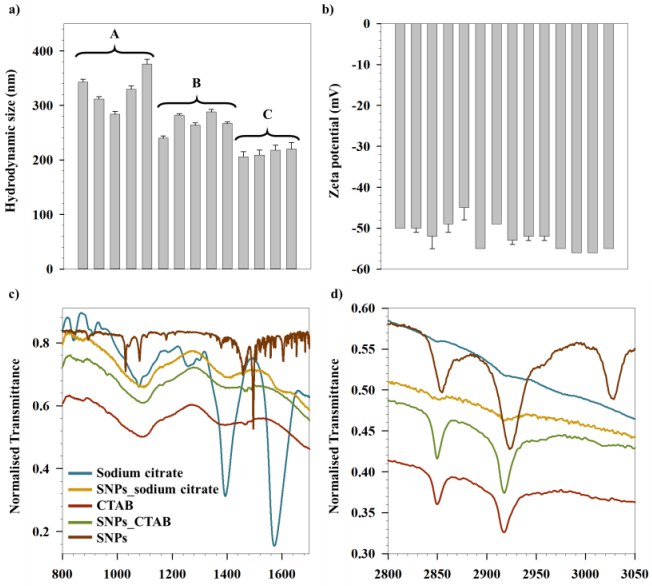

Figure S2. a) Size and b) zeta potential of SNPs phase transferred with Na-Citrate. ATR-FTIR spectra of sodium citrate, SNPs with sodium citrate, CTAB, SNPs with CTAB and SNPs in c) region 800-1600 cm-1 and d) region 2800-3200 cm-1.

4.3. Influence of Magnetic Properties upon Functionalization

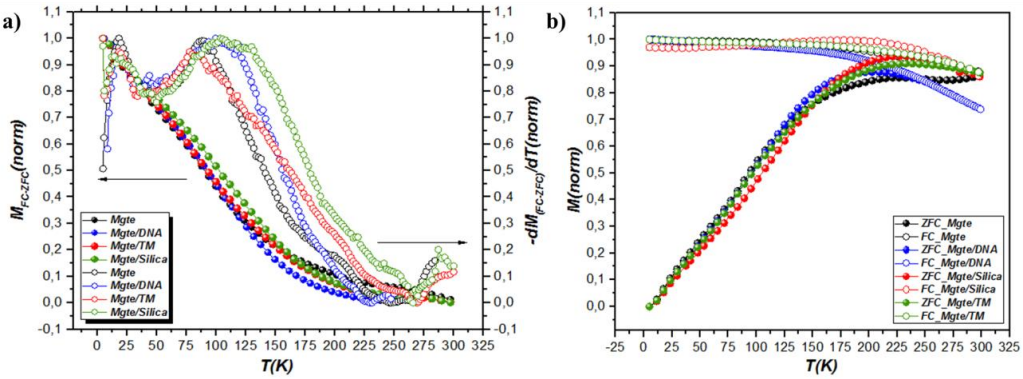

Figure S3. a) $M_{FC} - M_{ZFC}$ and ($dM_{FC} - M_{ZFC}/dT$) curves. b) ZFC/FC curves for Mag, Mag_DNA, Mag_TM and Mag_Silica.

In order to investigate magnetic nanoparticle interactions, low temperature remnant magnetization (5K) is carried out by the direct current demagnetization (DCD) and isothermal remnant magnetization (IRM) protocols (**Figure S4**).[15, 16] In a typical DCD measurement, the sample is saturated in an external field of −5 T, then the external field is removed, and the remanence magnetization is recorded. The sample is then exposed to a reverse positive field (H_{rev}) to invert the magnetization; so H_{rev} is removed and the remanence magnetization is recorded. The process is repeated several times, each time with a higher H_{rev}, up to 5 T. IRM protocol is similar to DCD protocol but starting with the sample in a demagnetized state.[17]
$M_r^{IRM}(H)$ and $M_r^{DCD}(H)$ represent the same energy barriers in the case of an ensemble of non-interacting monodomain particles with uniaxial anisotropy. This is clearly expressed by the so-called Wohlfarth relationship:

$$M_r^{DCD}(H) = 1 - 2M_r^{IRM}(H) \qquad \text{(S8)}$$

Kelly et al. rewrote the Wohlfarth's relationship in order to show more clearly the deviation of a real system from the non-interacting case:

$$\delta M(H) = M_r^{DCD} - [1 - 2M_r^{IRM}] \qquad \text{(S9)}$$

where the δM parameter has zero value for a non-interacting system.[18, 19] Interactions promoting the magnetized state such as exchange and other positive interactions lead to a

positive value of δM parameter whereas negative deviation are due to demagnetizing interactions (e.g. dipole–dipole interactions).[17]

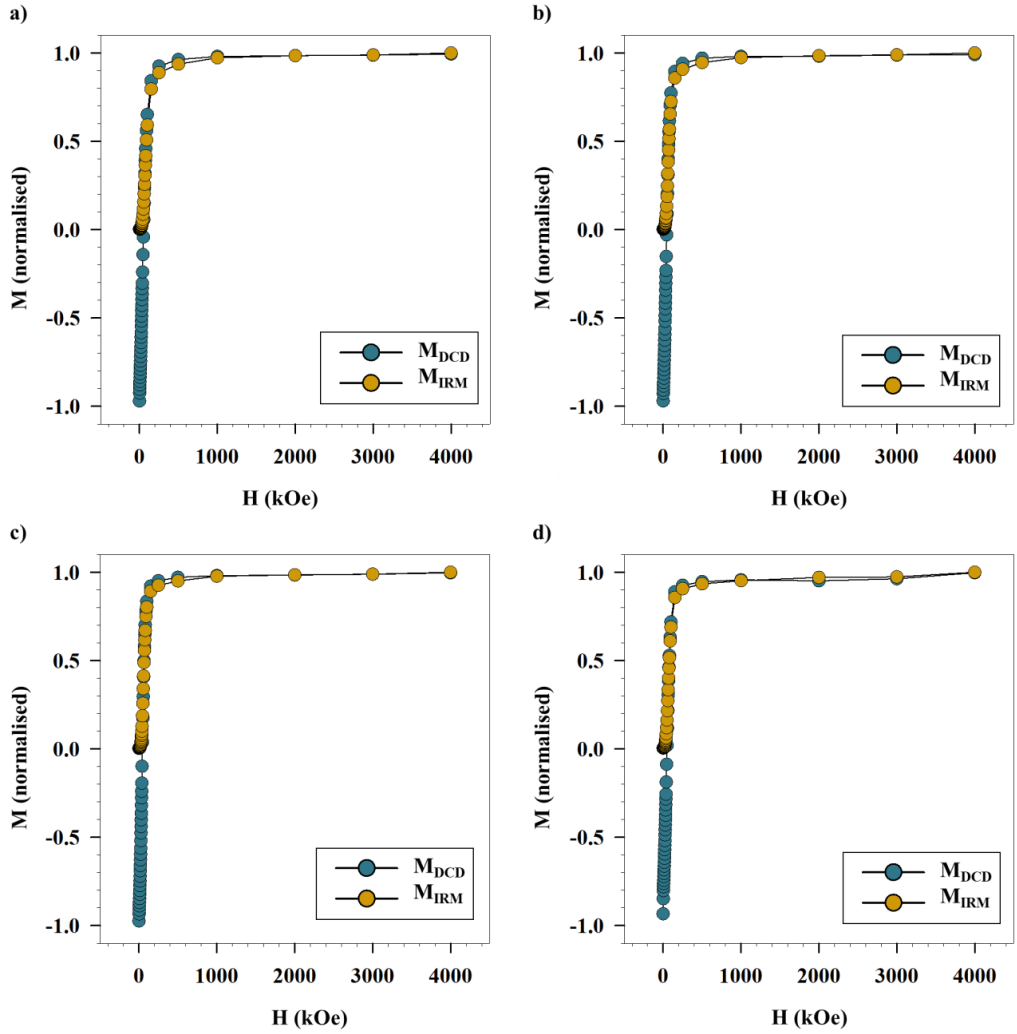

Figure S4. DCD and IRM curves for a) Mag, b) Mag_TMAPS, c) Mag_DNA amd d) Mag_Silica

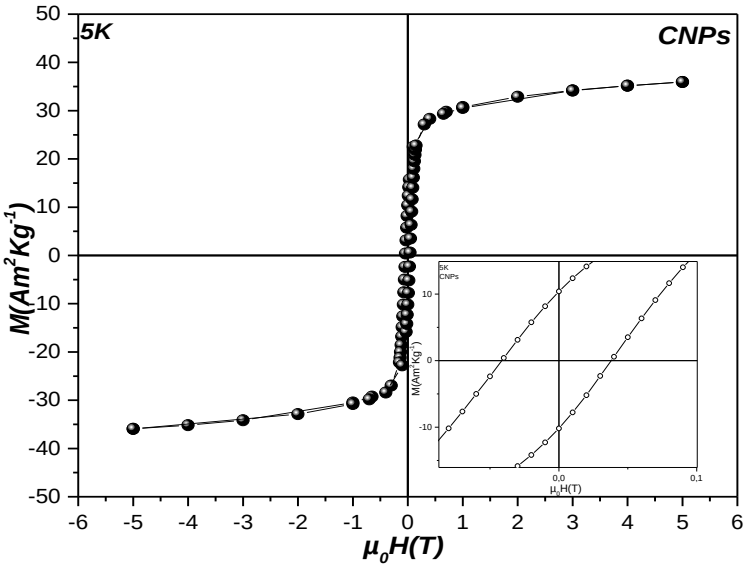

Figure S5. Field dependence of magnetization recorded at 5K for CNPs.

References

1. Randolph, A., *Theory of particulate processes: analysis and techniques of continuous crystallization*. 2012: Elsevier.
2. Bandyopadhyaya, R., R. Kumar, and K. Gandhi, *Simulation of precipitation reactions in reverse micelles.* Langmuir, 2000. **16**(18): p. 7139-7149.
3. Ethayaraja, M., C. Ravikumar, D. Muthukumaran, K. Dutta, and R. Bandyopadhyaya, *CdS− ZnS Core− Shell Nanoparticle Formation: Experiment, Mechanism, and Simulation.* The Journal of Physical Chemistry C, 2007. **111**(8): p. 3246-3252.
4. Layek, A., G. Mishra, A. Sharma, M. Spasova, S. Dhar, A. Chowdhury, and R. Bandyopadhyaya, *A generalized three-stage mechanism of ZnO nanoparticle formation in homogeneous liquid medium.* The Journal of Physical Chemistry C, 2012. **116**(46): p. 24757-24769.
5. Bachhar, N. and R. Bandyopadhyaya, *Role of coating agent in iron oxide nanoparticle formation in an aqueous dispersion: Experiments and simulation.* Journal of colloid and interface science, 2016. **464**: p. 254-263.
6. Bachhar, N. and R. Bandyopadhyaya, *Predicting complete size distribution of nanoparticles based on interparticle potential: experiments and simulation.* The Journal of Physical Chemistry C, 2016. **120**(8): p. 4612-4622.
7. Treybal, R.E., *Mass transfer operations.* New York, 1980. **466**.
8. Friedlander, S.K., *Smoke, dust, and haze*. Vol. 198. 2000: Oxford University Press New York.

9. Kestin, J., M. Sokolov, and W.A. Wakeham, *Viscosity of liquid water in the range− 8 C to 150 C.* Journal of Physical and Chemical Reference Data, 1978. **7**(3): p. 941-948.
10. Oskam, G., Z. Hu, R.L. Penn, N. Pesika, and P.C. Searson, *Coarsening of metal oxide nanoparticles.* Physical Review E, 2002. **66**(1): p. 011403.
11. Kabalnov, A.S. and E. Schchukin, *Ostwald ripening theory: applications to fluorocarbon emulsion stability.* Advances in colloid and interface science, 1992. **38**: p. 69-97.
12. Kim, J., H.S. Kim, N. Lee, T. Kim, H. Kim, T. Yu, I.C. Song, W.K. Moon, and T. Hyeon, *Multifunctional uniform nanoparticles composed of a magnetite nanocrystal core and a mesoporous silica shell for magnetic resonance and fluorescence imaging and for drug delivery.* Angewandte Chemie International Edition, 2008. **47**(44): p. 8438-8441.
13. Bandyopadhyay, S., M.K. Andersen, M.A.A. Alvi, A. Sharma, R. Raju, B.H. McDonagh, and W.R. Glomm, *Incorporation of Fe@ Au nanoparticles into multiresponsive pNIPAM-AAc colloidal gels modulates drug uptake and release.* Colloid and Polymer Science, 2016. **294**(12): p. 1929-1942.
14. Peeters, K., G. Lespes, T. Zuliani, J. Ščančar, and R. Milačič, *The fate of iron nanoparticles in environmental waters treated with nanoscale zero-valent iron, FeONPs and Fe3O4NPs.* Water research, 2016. **94**: p. 315-327.
15. Laureti, S., G. Varvaro, A. Testa, D. Fiorani, E. Agostinelli, G. Piccaluga, A. Musinu, A. Ardu, and D. Peddis, *Magnetic interactions in silica coated nanoporous assemblies of CoFe2O4 nanoparticles with cubic magnetic anisotropy.* Nanotechnology, 2010. **21**(31): p. 315701.
16. Muscas, G., N. Yaacoub, G. Concas, F. Sayed, R.S. Hassan, J.-M. Greneche, C. Cannas, A. Musinu, V. Foglietti, and S. Casciardi, *Evolution of the magnetic structure with chemical composition in spinel iron oxide nanoparticles.* Nanoscale, 2015. **7**(32): p. 13576-13585.
17. Peddis, D., P.E. Jönsson, S. Laureti, and G. Varvaro, *Magnetic interactions: A tool to modify the magnetic properties of materials based on nanoparticles*, in *Frontiers of Nanoscience*. 2014, Elsevier. p. 129-188.
18. Wohlfarth, E.P., *Relations between different modes of acquisition of the remanent magnetization of ferromagnetic particles.* Journal of Applied Physics, 1958. **29**(3): p. 595-596.
19. Kelly, P., K. O'grady, P. Mayo, and R. Chantrell, *Switching mechanisms in cobalt-phosphorus thin films.* IEEE Transactions on Magnetics, 1989. **25**(5): p. 3881-3883.

C.2 Paper II

Sharma, A., Raghunathan, K., Solhaug, H., Antony J., Stenvik J., Nilsen A.M., Einarsrud M-A., Bandyopadhyay S., 2021. Modulating Acrylic Acid Content of Nanogels for Drug Delivery Biocompatibility Studies. Journal of Colloid and Interface Science. https://doi.org/10.1016/j.jcis.2021.07.139

Modulating Acrylic Acid Content of Nanogels for Drug Delivery & Biocompatibility Studies

Anuvansh Sharma,[†] Karthik Raghunathan,[‡] Helene Solhaug,[¶] Jibin Antony,[‡] Jrgen Stenvik,[§] Asbjrn Magne Nilsen,[‖] Mari-Ann Einarsrud,[†] and Sulalit Bandyopadhyay[*,‡]

Department of Materials Science and Engineering, NTNU Norwegian University of Science and Technology, Norway, Department of Chemical Engineering, NTNU Norwegian University of Science and Technology, Norway, Department of Clinical and Molecular Medicine, Faculty of Medicine and Health Sciences, NTNU Norwegian University of Science and Technology, Trondheim, Norway, Centre of Molecular Inflammation Research, NTNU Norwegian University of Science and Technology, Trondheim, Norway and Department of Clinical and Molecular Medicine, NTNU Norwegian University of Science and Technology, Trondheim, Norway, and Department of Clinical and Molecular Medicine, NTNU Norwegian University of Science and Technology, Trondheim, Norway

E-mail: sulalit.bandyopadhyay@ntnu.no

[*]To whom correspondence should be addressed

[†]Department of Materials Science and Engineering, NTNU Norwegian University of Science and Technology, Norway

[‡]Department of Chemical Engineering, NTNU Norwegian University of Science and Technology, Norway

[¶]Department of Clinical and Molecular Medicine, Faculty of Medicine and Health Sciences, NTNU Norwegian University of Science and Technology, Trondheim, Norway

[§]Centre of Molecular Inflammation Research, NTNU Norwegian University of Science and Technology, Trondheim, Norway and Department of Clinical and Molecular Medicine, NTNU Norwegian University of Science and Technology, Trondheim, Norway

[‖]Department of Clinical and Molecular Medicine, NTNU Norwegian University of Science and Technology, Trondheim, Norway

Supporting Information Available

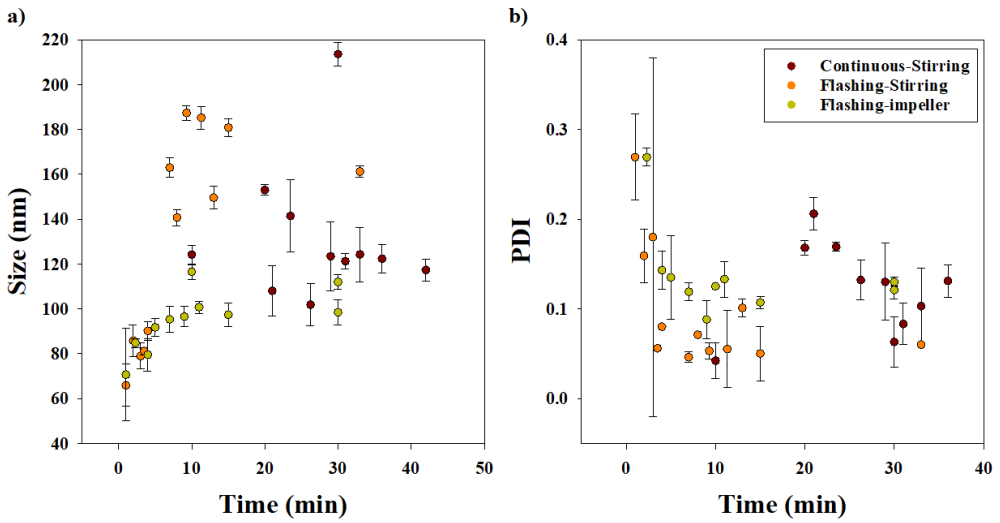

Figure S1: a) Size and b) polydispersity index (PDI) of NG samples prepared using Continuous-Stirring, Flashing-Stirring and Flashing-Impeller methods. (The error bars represent the standard deviation calculated from the triplicate measurement of the particular sample).

Figures S1a and b show the size and PDI of the NGs synthesised by the continuous-stirring, flashing-stirring and flashing-impeller methods, respectively. An initial increase in size is seen, for all the methods, before stabilizing to the final particle size. Whereas, for PDI, a decrease is seen as the reaction proceeds signaling the samples achieving a monodisperse population at the end of the reaction.

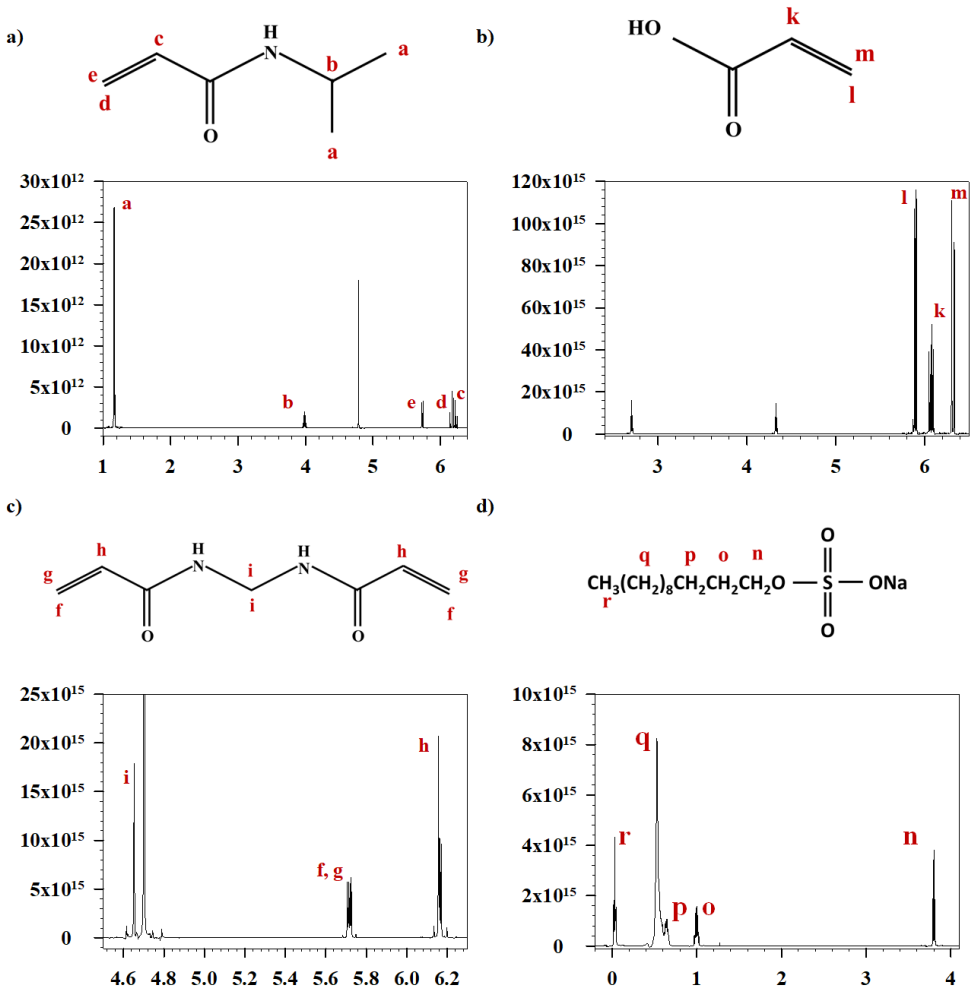

Figure S2: ^{1}H NMR spectra of nascent reagents, used to synthesise stimuli-responsive NGs, showing their respective proton peaks. a) NIPAm, b) AAc, c) BIS, d) SDS.

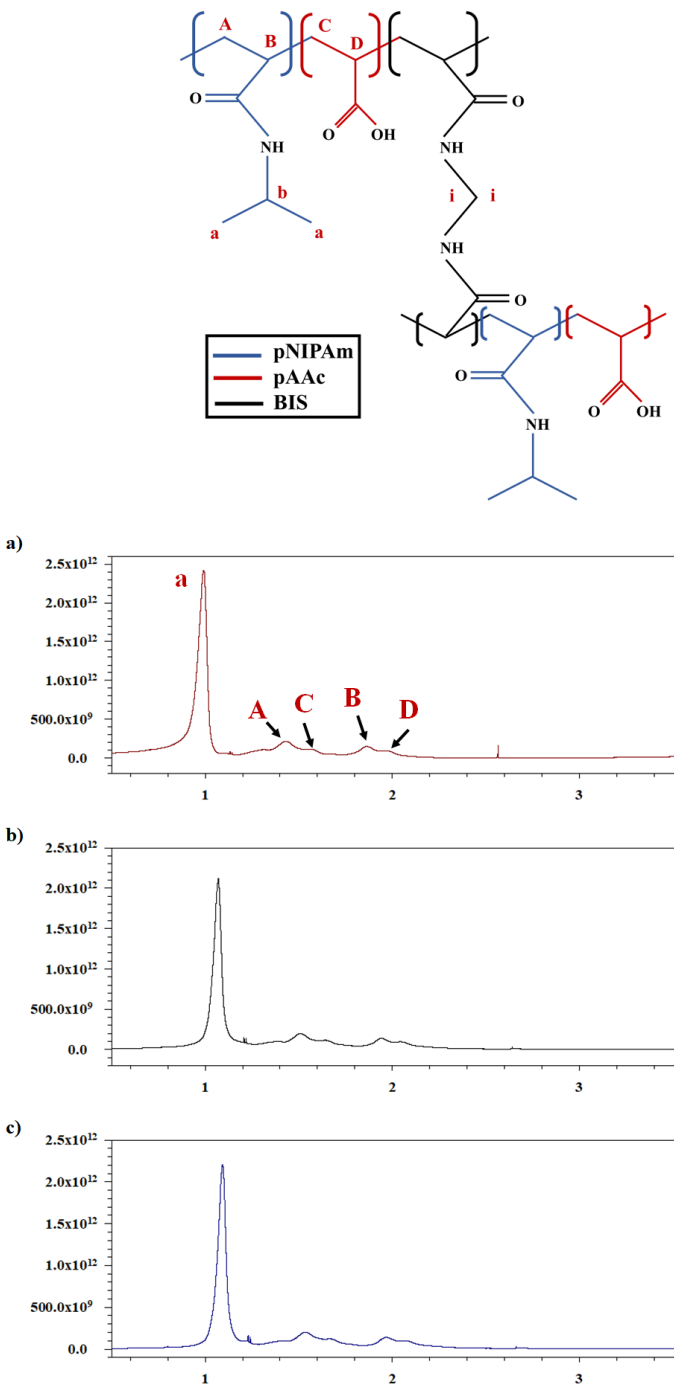

Figure S3: ^{1}H NMR spectra of NGs synthesized using a) Continuous-Stirring, b) Flashing-Stirring and c) Flashing-Impeller, showing the spectra for pNIPAm and pAAc incorporated withing the NGs.

Figures S3a, b and c show the ^{1}H NMR spectra of NGs synthesized using continuous-stirring, flashing-stirring and flashing-impeller. NGs, synthesised by the three methods, have peaks in the region 1.0 – 2.2 ppm, showing similar NG structure.

Table S1: VPTT of NGs_CS synthesized using different AAc mole%.

NG_CS	VPTT (°C)
AAc_10	36.3 ± 0.3
AAc_12.5	35.8 ± 0.4
AAc_15	36.3 ± 0.3
AAc_17.5	35.3 ± 0.4
AAc_20	35.3 ± 0.5
AAc_22.5	35.4 ± 0.5
AAc_25	34.4 ± 0.5
AAc_27.5	35.4 ± 0.5
AAc_30	34.4 ± 0.6

Similar to NGs_CS, NGs_FS show an increase size trend with increase AAc mole%, as shown in Figure S4a. Figure S4b shows the variation in size and zeta potential of NGs_FS with respect to AAc mole%. The NG size and zeta potential increases on increasing the pH of the system due to the deprotonation of AAc at higher pH.

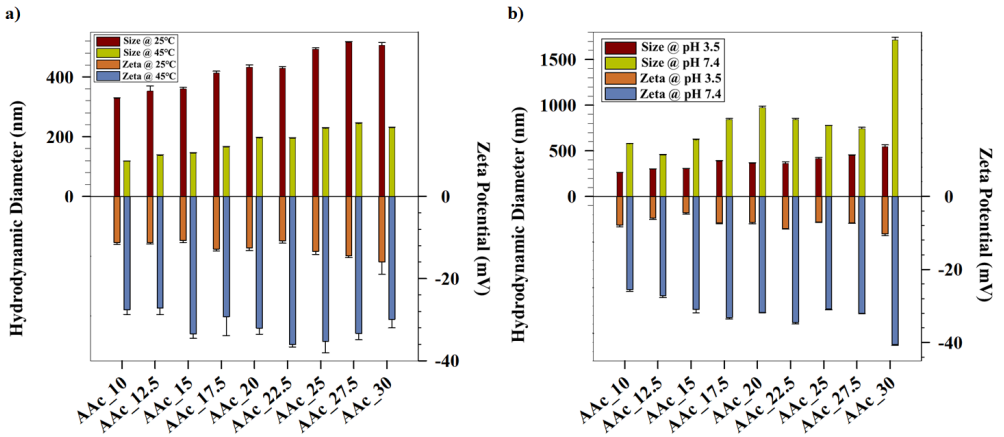

Figure S4: Hydrodynamic diameter and zeta potentials of the NGs_FS at a) 25 and 45°C, and b) pH = 3.5 and 7.4, showing decrease in size with increasing temperature and decreasing pH. (The error bars represent the standard deviation calculated from the triplicate measurement of the particular sample).

As can be seen from Figure S5, the VCE_{temp} decreases with increasing AAc mole%, similar to NGs_CS. However, VCE_{pH} for NGs_FS has a random distribution with varying AAc mole% suggesting non-uniform incorporation of pAAc between pNIPAm units inside the NG matrix, thereby resulting in inconsistent pH-dependent swelling behaviour.

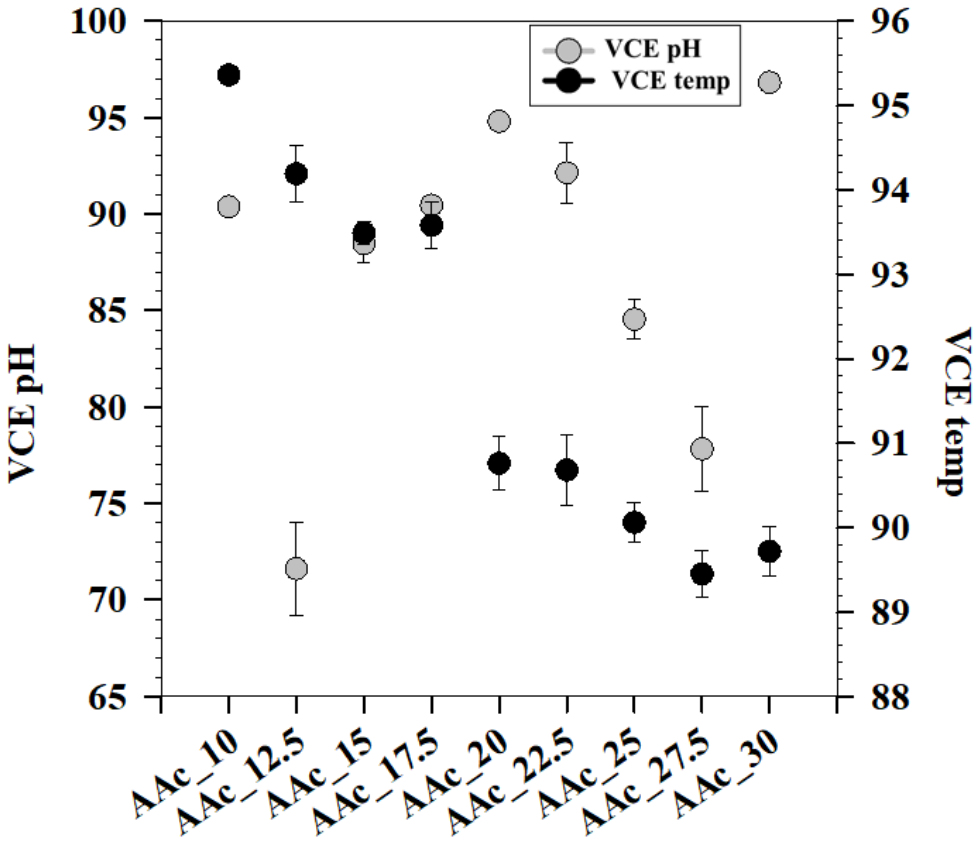

Figure S5: Volumetric swelling with respect to pH and temperature for NGs_FS, synthesized using different AAc mole%. (The error bars represent the standard deviation calculated from the triplicate measurement of the particular sample).

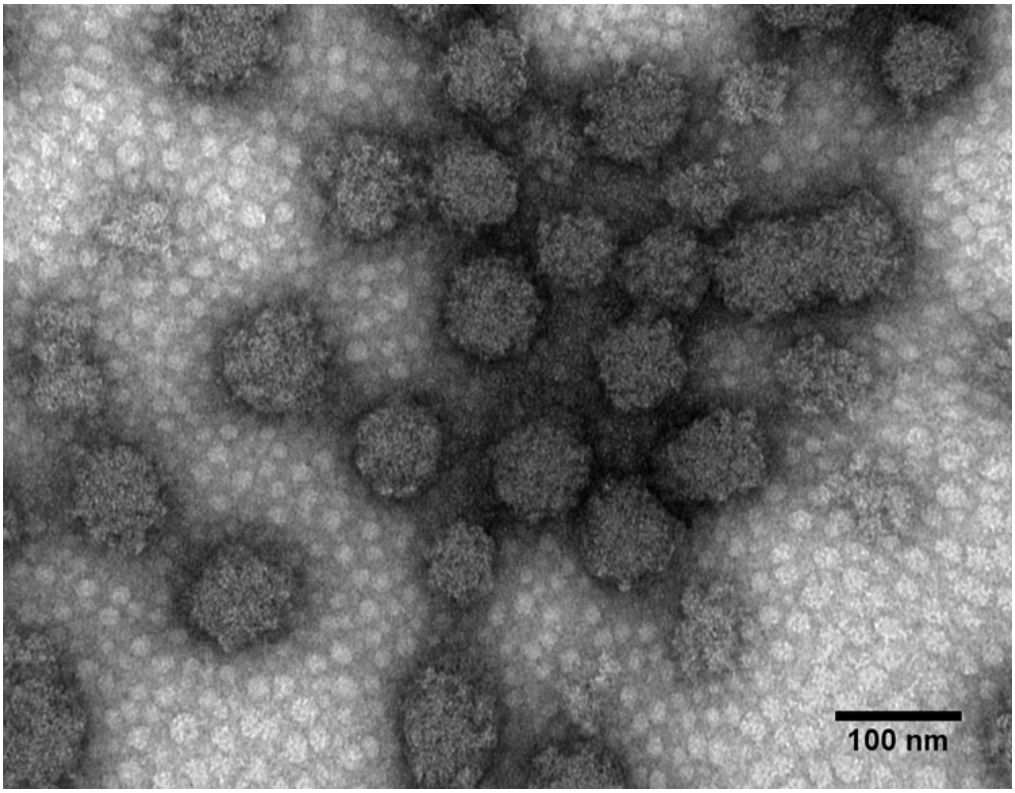

Figure S6: TEM image of NGs_CS synthesized using 10 mole% AAc.

Figure S6 shows TEM image of the dried NGs synthesized by the continuous method (10 mole% AAc) having a size of 85 ± 13 nm.

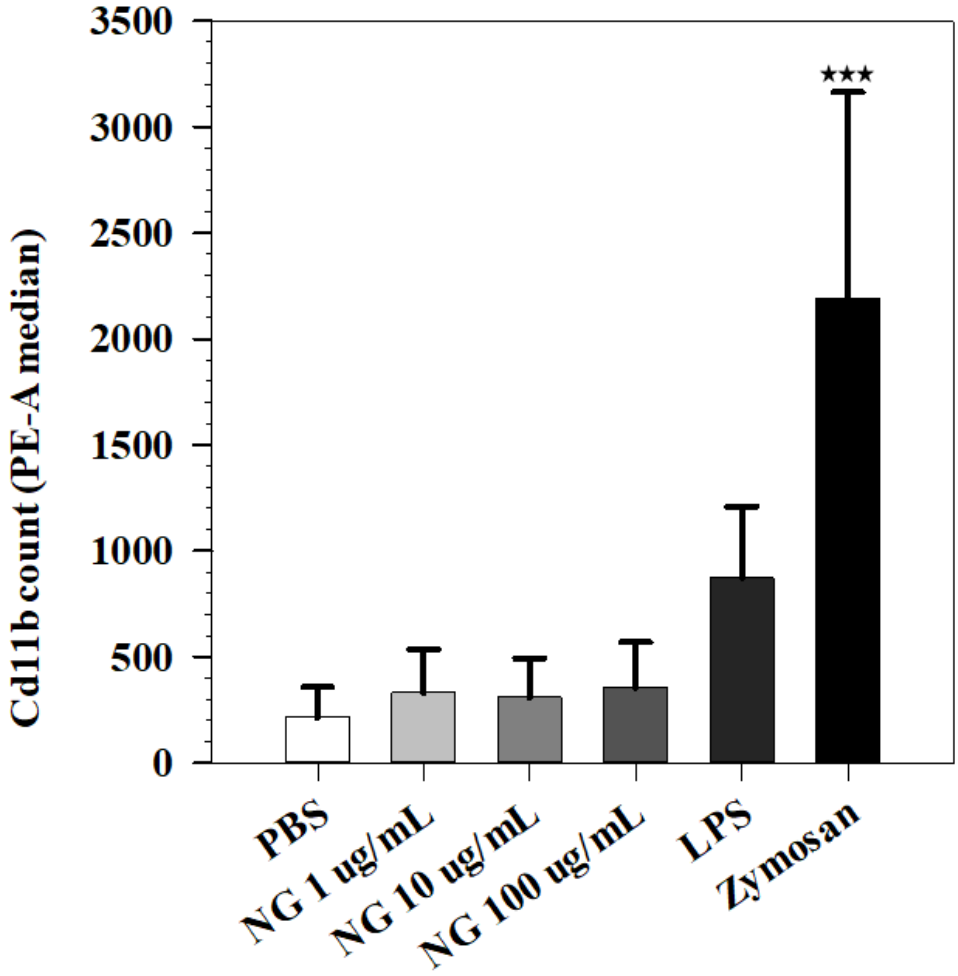

Figure S7: Assessment of CR3 activation in human whole blood by NGs as determined by Cd11b count. Error bars represent standard deviation, statistical significance (***P<0.001) compared to the PBS control found by one-way ANOVA. (N=5 consecutive experiments)

Method description for Figure S7: 15 min after exposure to NGs and controls, 25 µL was transferred to a 96-well polypropylene plate. Samples were fixated by adding 25 µL 1% paraformaldehyde (PFA). Then 2.5µL of anti-CD11b PE were added, a fluorescent marker for

activated CR3, was added followed by 15 min incubation. 150µL lysis buffer was added and samples were transferred to flow vials containing 600µL lysis buffer before further incubation in dark at room temperature for 15 minutes. The vials were then centrifuged at 720 x g for 4 minutes and the cell pellet was dissolved in 500µL PBS without Ca^{2+}/Mg^{2+}. The samples were kept on ice until flow cytometry measurements using BD FACSCanto II (BD BioSciences, Franklin Lakes, NJ, USA). NG induced activation of CR3 in monocytes and granulocytes was quantified by first gating cell populations exposed to Zymosan (positive control) and PBS (negative control) according to their forward- and side scatter, and then using the same gating for the NG treated samples. This data analysis was done using FlowJo software (BD BioSciences).

This material is available free of charge via the Internet at `http://pubs.acs.org/`.

C.3 Manuscript III

Sharma, A., 2021. Growth Kinetics of Iron-Oxide – Silver Dimeric Nanoparticles & Their Potential Biomedical Applications.

Supporting Information Available

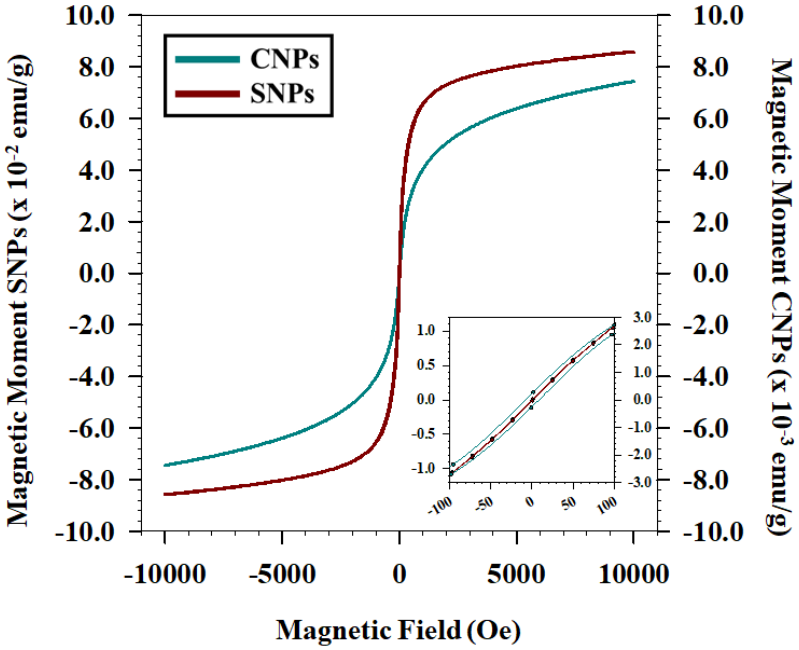

Figure S1: Hysteresis curves of SNPs and CNPs measured using VSM.

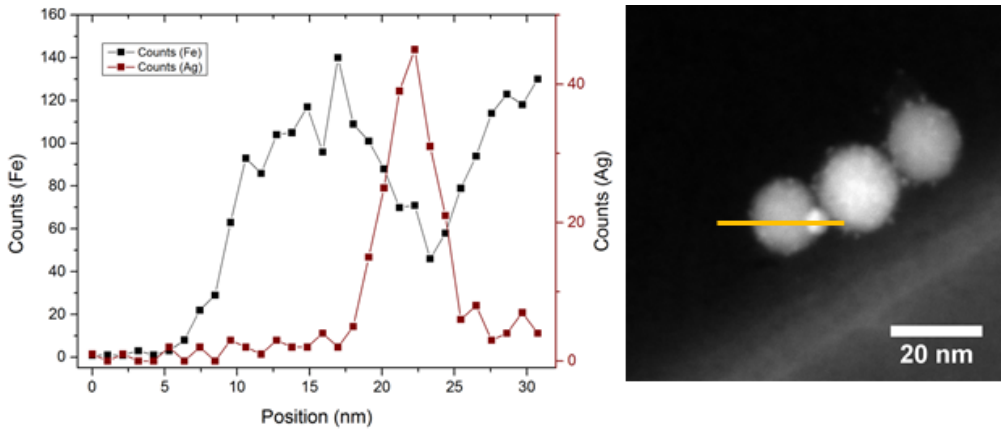

Figure S2: EDS profiling of Ag@SNPs after 3 h of reaction, showing the presence of iron-oxide and silver.

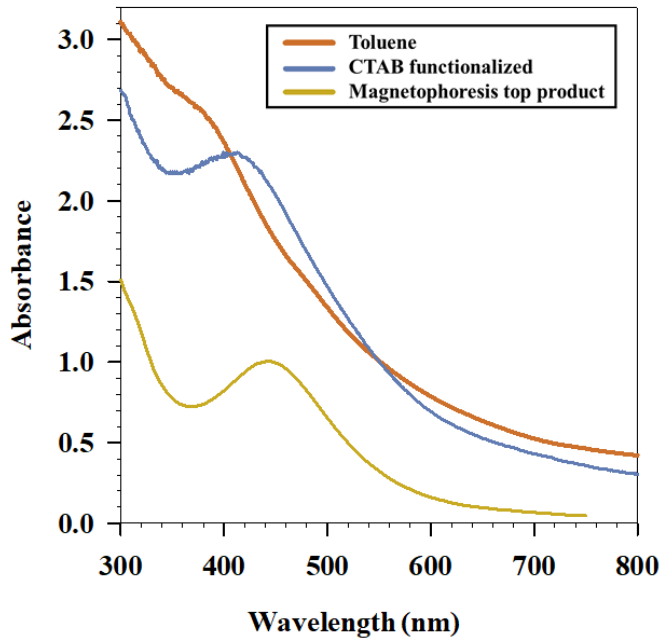

Figure S3: UV-Vis of Ag@SNPs in toluene, phase transferred with CTAB and the top product from the magnetophoretically separated sample (over 24 h).

ISBN 978-82-326-6926-4 (printed ver.)
ISBN 978-82-326-5819-0 (electronic ver.)
ISSN 1503-8181 (printed ver.)
ISSN 2703-8084 (online ver.)

NTNU
Norwegian University of
Science and Technology